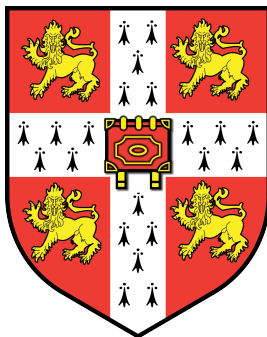


BLACK HOLE MASSES AND OUTFLOWS IN HIGH REDSHIFT QUASARS

LIAM COATMAN

Institute of Astronomy & Robinson College
University of Cambridge



A dissertation submitted to the
University of Cambridge for the degree of
DOCTOR OF PHILOSOPHY

Under the supervision of
PROF. PAUL C. HEWETT
& DR. MANDA BANERJI

April 2017

SUMMARY

Short summary of the contents in English...a great guide by Kent Beck how to write good abstracts can be found here:

<https://plg.uwaterloo.ca/~migod/research/beck00PSLA.html>

DECLARATION

This dissertation is the result of my own work and includes nothing which is the outcome of work done in collaboration except as declared in the Preface and specified in the text. It is not substantially the same as any that I have submitted, or, is being concurrently submitted for a degree or diploma or other qualification at the University of Cambridge or any other University or similar institution except as declared in the Preface and specified in the text. I further state that no substantial part of my dissertation has already been submitted, or, is being concurrently submitted for any such degree, diploma or other qualification at the University of Cambridge or any other University or similar institution except as declared in the Preface and specified in the text. The use of 'we' in the main text is a stylistic choice.

This thesis has used material from the following publications.

- Chapter 3 uses material from Coatman et al., (2016) and Coatman et al., (2017).

Liam Coatman

ACKNOWLEDGMENTS

Put your acknowledgments here.

CONTENTS

1	INTRODUCTION	1
1.1	Discovery	1
1.2	Basic structure	1
1.2.1	The broad line region	2
1.2.2	The dusty torus	2
1.2.3	The narrow line region	3
1.3	Winds and outflows in AGN	3
1.4	SDSS and the era of survey astronomy	4
1.5	The AGN-host galaxy connection	4
1.6	Measuring black hole masses	5
1.6.1	Reverberation mapping	5
1.6.2	Single-epoch virial estimates	7
1.7	SEDs	9
1.8	Summary / what I need to get across	9
1.9	Overview of thesis	10
1.9.1	A near-infrared spectroscopic database of high-redshift quasars	10
1.9.2	Black Hole Masses	10
1.9.3	Narrow line region properties	11
1.9.4	SED Properties	11
2	A NEAR-INFRARED SPECTROSCOPIC DATABASE OF HIGH-REDSHIFT QUASARS	13
2.1	Introduction	13
2.2	Data	14
2.2.1	Coatman et al. (2016) Quasars	14
2.2.2	Shen & Liu (2012) and Shen (2016) Quasars	18
2.2.3	Quasar Pairs	19
2.2.4	VLT SINFONI Quasars	19
2.2.5	ESO NTT SOFI Quasars	20
2.2.6	Hale TripleSpec Quasars	21
2.3	Instrumental broadening	21
2.3.1	Optical spectra	21
2.3.2	Flux calibration of spectra	22
2.3.3	Quasar monochromatic luminosity	23
2.4	Description of catalogue	27
3	BLACK HOLE MASSES	29

3.1	Introduction	29
3.2	Quasar Sample	33
3.2.1	Spectroscopic data	33
3.3	Spectral Measurements	33
3.3.1	CIV	35
3.3.2	H α	36
3.3.3	H β and [O III]	38
3.3.4	Fitting procedure	39
3.3.5	Spectra removed from sample	42
3.3.6	Emission-line parameter uncertainties	44
3.3.7	Contemporaneity of spectra	44
3.3.8	Quasar monochromatic luminosity	45
3.3.9	Characterising the emission-line widths	45
3.4	An empirical correction to C IV-based virial BH-mass estimates	49
3.4.1	H α /H β FWHM comparison	49
3.4.2	Measuring the quasar systemic redshift	53
3.4.3	Balmer/C IV line widths as a function of C IV-blueshift	55
3.4.4	C IV based virial BH mass estimates	58
3.4.5	C IV-derived BH masses at low C IV blueshift	61
3.5	Practical application of the C IV-based correction to virial BH-mass estimates	62
3.5.1	Recipe for unbiased C IV based BH masses	62
3.5.2	Systematic trends in residuals	68
3.5.3	Effectiveness of the C IV blueshift based correction to BH masses	70
3.5.4	Comparison to previous prescriptions	74
3.6	Population trends with C IV blueshift	78
3.6.1	Systematic biases in Balmer-based masses	79
3.6.2	The BAL parent population	81
3.6.3	The frequency of quasars with high accretion rates	82
3.7	Conclusions	83
3.8	Future work	83
3.9	Description of catalogue	84

4 NARROW LINE REGION PROPERTIES	87
4.1 Introduction	87
4.2 Quasar Sample	88
4.3 Parametric model fits	89
4.3.1 Redshift transformation	90
4.3.2 Removal of Fe II emission	90
4.3.3 Modelling Hβ/[O III]	93
4.3.4 Deriving upper limits on the [O III] EQW	94
4.3.5 Modelling Hα	94
4.3.6 Derived parameters	95
4.3.7 Deriving uncertainties on parameters	99
4.3.8 The significance of [O III] detections	99
4.3.9 Low EQW [O III]	100
4.3.10 Reliability of redshift estimates	100
4.4 Results	102
4.4.1 Luminosity/redshift-evolution of [O III] properties	104
4.4.2 Velocity width	105
4.5 Eigenvector 1 correlations	106
4.5.1 EV1 trends exist in high-redshift quasars	106
4.5.2 Extending EV1 parameter space	108
4.6 Extreme [O III] emitters	108
4.6.1 [O III] and C IV outflows are linked	112
4.7 Discussion	114
4.7.1 Static NLR is removed by outflows	114
4.8 Independent Component Analysis	115
4.8.1 The technique	115
4.8.2 Quality of fits	116
4.8.3 Physical interpretation of ICA components	117
4.8.4 ICA fits	119
4.8.5 Future work	124
5 SED PROPERTIES	125
5.1 Introduction	125
5.2 Data	126
5.2.1 SDSS DR7	126
5.2.2 UKIDSS Large Area Survey	127
5.2.3 WISE All-WISE Survey	128

5.2.4	Galactic extinction correction	128
5.2.5	Cross-matching	128
5.2.6	Completeness	128
5.2.7	Generating the quasar catalogue	129
5.3	Quasar SED	129
5.4	SED Model	131
5.4.1	Accretion Disc	131
5.4.2	Balmer Continuum	131
5.4.3	Hot Dust	131
5.4.4	Emission Lines	131
5.4.5	Host Galaxy	132
5.4.6	Dust Extinction	133
5.4.7	Empirical Correction	134
5.5	The ‘Standard’ SED Model	134
5.6	Results	136
5.7	Discussion of Fit	139
5.8	Hot Dust	139
5.8.1	Parametrising the hot dust emission	141
5.8.2	Sample	141
5.8.3	Diversity in hot dust properties	143
5.9	Fitting procedure	144
5.10	Results	145
5.10.1	Correlations with quasar properties	146
5.11	Discussion	149
5.11.1	Eddington ratio	153
5.11.2	Spectral properties	154
5.12	Further work	154
5.12.1	Hot-Dust-Poor Quasars	154
6	CONCLUSIONS / FUTURE WORK	157
6.1	Future: Red quasars	157
	BIBLIOGRAPHY	159

LIST OF FIGURES

- Figure 1.1 Illustration of the physical structure of an AGN in a simple orientation-based unification model. 2
- Figure 2.1 The ranges in redshift and luminosity covered by our sample, relative to the redshift-luminosity distribution of the SDSS DR7 quasar catalogue. 15
- Figure 3.1 Composite spectra of the C_{IV}-emission line as a function of C_{IV} blueshift for SDSS DR7 quasars. 31
- Figure 3.2 Demonstration of the effectiveness of our line parameter estimation scheme via a comparison of the C_{IV} FWHM with Shen et al., (2011). 37
- Figure 3.3 Demonstration of the effectiveness of our line parameter estimation scheme via a comparison of the H α FWHM with Shen and Liu, (2012). 38
- Figure 3.4 Demonstration of the effectiveness of our line parameter estimation scheme via a comparison of the H β FWHM with Shen, (2016). 39
- Figure 3.5 Model fits to continuum-subtracted H α , H β , and C_{IV} emission in four quasars, chosen to represent the range of S/N and line shapes present in the catalogue. 41
- Figure 3.6 The redshift and luminosity distributions of the spectra removed from our H α /C_{IV} (a, b) and H β /C_{IV} (c, d) samples. 43
- Figure 3.7 The FWHM, dispersion (σ) and shape (FWHM/ σ) of C_{IV} as a function of the C_{IV} blueshift. 46
- Figure 3.8 Comparison of the C_{IV} line profiles of SDSSJ1236+1129 and SDSSJ1525+0426. 48

- Figure 3.9 Comparison of H α and H β FWHM measurements for 99 quasars. 49
- Figure 3.10 One- and two-dimensional projections of the MCMC sampling of the posterior distribution from the fit in Fig. 3.9. 52
- Figure 3.11 The H α (blue) and H β (red) emission line regions in the median composite spectrum, shown as function of the velocity shift from the respective predicted line peak wavelengths. 53
- Figure 3.12 C IV FWHM relative to H α FWHM (a), and C IV based BH mass (BHM) compared to H α based mass (b), both as a function of the C IV blueshift. 56
- Figure 3.13 C IV FWHM relative to H β FWHM (a), and C IV based BH mass (BHM) compared to H β based mass (b), both as a function of the C IV blueshift. 57
- Figure 3.14 One- and two-dimensional projections of the MCMC sample of the posterior distribution for a linear fit to the FWHM C IV/H α ratio as a function of the C IV blueshift. 59
- Figure 3.15 The distribution of the orthogonal displacement of each data point from the best-fitting linear relationship in the fit to FWHM(C IV)/FWHM(H α) as a function of the C IV blueshift. 60
- Figure 3.16 Rest-frame EW versus blueshift of the broad C IV-emission line for 32,157 SDSS DR7 quasars at $1.6 < z < 3.0$. 64
- Figure 3.17 Same as Fig. 3.12a, with the marker colour representing the H α FWHM. 70
- Figure 3.18 Rest-frame EW versus blueshift of the broad C IV-emission line for 32,157 SDSS DR7 quasars at $1.6 < z < 3.0$ and our sample. 71
- Figure 3.19 Comparison of the C IV- and H α -based BH masses before and after applying the C IV blueshift-based correction to the C IV FWHM. 72

Figure 3.20	Comparison of the C IV and H α line dispersion, σ . 73
Figure 3.21	Comparison of BH mass estimates derived from C IV and H α as a function of the C IV blueshift. 75
Figure 3.22	The FWHM, dispersion (σ) and shape (FWHM/ σ) of H α as a function of the C IV blueshift. 77
Figure 3.23	H α -derived Eddington ratio versus C IV blueshift. 78
Figure 4.1	Spectra of the 24 objects for which significant Fe II emission is still visible following our Fe II-subtraction procedure. 91
Figure 4.1	Continued. 92
Figure 4.2	Model fits to the continuum- and Fe II-subtracted H β /[O III] emission in 15 quasars, chosen at random. 96
Figure 4.3	Uncertainty in v_{10} as a function of the EQW, for [O III]. 100
Figure 4.4	Comparison of systemic redshift estimates using [O III], broad H β and broad H α . 101
Figure 4.5	Correlations between the line width w_{80} , asymmetry R and EQW of [O III]. 103
Figure 4.6	The [O III] EQW as a function of the quasar bolometric luminosity for the sample presented in this chapter (blue circles) and the low- z SDSS sample (grey points and contours). 105
Figure 4.7	The [O III] velocity-width, characterised by w_{80} , as a function the [O III] luminosity and the quasar redshift. 106
Figure 4.8	EV1 parameter space. 107
Figure 4.9	The high-redshift EV1 parameter space of C IV blueshift and EQW. 109
Figure 4.10	[O III] EQW as a function of the C IV blueshift. 110
Figure 4.11	Model fits to the continuum- and Fe II-subtracted H β /[O III] emission in 18 quasars with extreme [O III] emission profiles. 111

- Figure 4.13 The relation between the blueshifts of C_{IV} and [O III]. [113](#)
- Figure 4.14 H β /[O III] emission J002952+020607. The ICA reconstruction is shown in black, and the spectrum in grey. The first three components, and the sum of components four, five and six are shown individually. [117](#)
- Figure 4.15 [O III] emission in J002952+020607. [118](#)
- Figure 4.16 The relative weight in each of the six positive ICA components for the high-luminosity and low luminosity samples. [120](#)
- Figure 4.17 The relative weight in the three ICA components corresponding to [O III] emission and the relative weight of the component most closely related to blueshifted [O III] emission relative to all three [O III] components. [121](#)
- Figure 4.18 Weight in the [O III] wing relative to the weight in the [O III] core emission versus the strength of the core [O III] emission. [121](#)
- Figure 4.19 The ICA component weight w_4 , which is a proxy for the strength of core [O III], as a function of the C_{IV} blueshift. [122](#)
- Figure 4.20 Median ICA-reconstructed spectra as a function of the C_{IV} blueshift. [122](#)
- Figure 5.1 Median radio-loud SED from Shang et al., [\(2011\)](#). [126](#)
- Figure 5.2 Distribution of our sample in the redshift-luminosity plane. [129](#)
- Figure 5.3 Model quasar spectrum at $z = 1$, showing the contributions to the total flux from the blue power-law slope, red power-law slope, Balmer continuum, blackbody, emission line spectrum and host galaxy. [130](#)
- Figure 5.4 Model quasar spectrum at three different redshifts, and throughput functions for SDSS, UKIDSS and WISE band-passes. [135](#)

Figure 5.5	Colours of median quasar SED and best-fitting model, with and without correction. 137
Figure 5.6	Colours of median quasar SED, individual objects, best-fitting model as a function of redshift. 138
Figure 5.7	Residuals from fit as a function of rest-frame wavelength. 140
Figure 5.8	$W_1 - W_2$ colours of sample as a function of redshift. 140
Figure 5.9	$i - K$ colours of non-BALQSO DR7Q quasars with $i > 19.1$ as a function of redshift. 144
Figure 5.10	Ratio of NIR to UV luminosity ($R_{\text{NIR/UV}}$) against temperature (T_{BB}) for low- z sample. 145
Figure 5.11	Ratio of NIR to UV luminosity ($R_{\text{NIR/UV}}$) against temperature (T_{BB}). 146
Figure 5.12	Best-fit blackbody temperature against UV luminosity, black-hole mass and Eddington ratio. 147
Figure 5.13	Composite SDSS spectra for objects at $z \sim 0.7$. 148
Figure 5.14	Hot dust abundance as a function of rest-frame EQW and blueshift of the CIV line. 150
Figure 5.15	Hot dust abundance as a function of rest-frame EQW and blueshift of the CIV line. 151
Figure 5.16	152

LIST OF TABLES

Table 2.1	Summary of near-infrared spectroscopic database. 16
Table 2.2	Measured spectral resolutions of the spectrographs used in this thesis. 21

Table 2.3	Quasars in our near-infrared spectroscopic database. Only the first 15 entries are shown. The full table (including 462 objects) is available online. Columns are as follows: (1) identifier, (2) unique catalogue name, (3) date near-infrared spectra acquired, (4)-(5) coordinates, (6) instrument/telescope, (7) wavelength coverage, (8) velocity per pixel, (9) S/N per pixel, (10) redshift. 26
Table 3.1	The numbers of quasars with reliable H α and H β line measurements, and the spectrographs and telescopes used to obtain the near-infrared spectra 34
Table 3.2	The format of the table containing the emission line properties from our parametric model fits. The table is available in machine-readable form in the online version of Coatman et al., (2017). 40
Table 3.3	The number of spectra removed from our sample by the cuts described in Section 3.3.5. 42
Table 3.4	The fractional error on the corrected BH mass as a function of C IV blueshift for different uncertainties in the quasar systemic redshift. 65
Table 4.1	The numbers of quasars with [O III] line measurements and the spectrographs and telescopes used to obtain the near-infrared spectra. 89
Table 4.2	Summary of models used to fit the H α emission, and the number of quasars each model is applied to. 95
Table 4.3	The format of the table containing the emission line properties from our parametric model fits. 97
Table 4.4	Physical interpretation of the ICA components. 117
Table 5.1	Available photometry, effective wavelength, Vega to AB magnitude offsets, conversion from E(B – V) to extinction. 127
Table 5.2	Model parameters. 139

Table 5.3 Summary of sub-samples. [142](#)

ACRONYMS

- AGN Active Galactic Nuclei
NLR Narrow Line Region
BLR Broad Line Region
EV₁ Eigenvector 1
ICA Independent Component Analysis
PCA Principal Component Analysis
SDSS Sloan Digital Sky Survey
BOSS Baryon Oscillation Spectroscopic Survey
UV Ultra-Violet
EQW Equivalent Qidrh
S/N Signal-to-noise
BH Black Hole
SED Spectral Energy Distribution
IR Infrared
NIR Near-infrared
FWHM Full-Width-at-Half-Maximum

INTRODUCTION

1.1 DISCOVERY

The first quasar was discovered when it was found that the star-like, thirteenth magnitude object associated with the radio source 3C 273 was at a cosmological distance ($z = 0.158$; Schmidt, 1963). This implied an enormous luminosity ($4 \times 10^{12} L_\odot$) for such a compact object and it was quickly realised that energy source was the release of gravitational potential energy as mass is accreted onto a super-massive black hole (BH) at the centre of a galaxy (e.g. Hoyle and Fowler, 1963; Salpeter, 1964; Lynden-Bell, 1969; Lynden-Bell and Rees, 1971).

*Super-massive:
 $10^{6-9} M_\odot$*

1.2 BASIC STRUCTURE

An Active Galactic Nucleus¹ (AGN) is significantly more compact than a cubic parsec, and yet can outshine the starlight from an entire galaxy. The basic features of the current paradigm explaining this phenomenon are essentially unchanged from Salpeter, (1964), although many of the details remain unclear. Material is pulled towards a super-massive BH and sheds angular momentum through viscous and turbulent processes in a hot accretion disc (e.g. Begelman, 1985). The accretion disc reaches temperatures of $\sim 10^6$ K, and radiates primarily at ultraviolet (UV) to soft-X-ray wavelengths. Hard X-ray emission originates in a hot corona near the BH, emission lines are produced in rapidly moving clouds of ionised gas and infrared emission is dominated by thermal emission from a dusty, parsec-scale structure. Collimated jets of relativistic plasma and/or associated lobes are also seen in the 10 per cent of quasars that are radio-loud (e.g. Peterson, 1997).

¹ Throughout this thesis we use the terms ‘quasar’ and ‘Active Galactic Nucleus (AGN)’ interchangeably to describe active supermassive black holes, although the term quasar is generally reserved for the luminous ($L_{\text{Bol}} > 10^{12} L_\odot$) subset of AGNs.

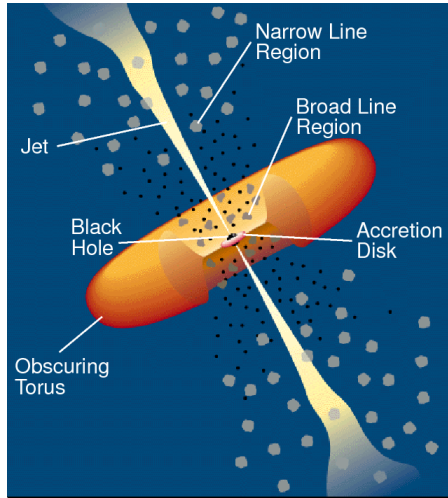


Figure 1.1: Illustration of the physical structure of an AGN in a simple orientation-based unification model. Figure taken from Urry and Padovani, (1995).

1.2.1 *The broad line region*

One of the pre-eminent features of many AGN spectra are broad optical and UV emission lines produced in the *broad line region (BLR)*. The BLR consists of gas clouds at distances from several light-days to several light-months that are photo-ionised by the ultraviolet continuum emission emanating from the accretion disc. Because of the close proximity to the central super-massive BH, bulk motions are dominated by gravity and radiation pressure. The very broad emission line widths are assumed to Doppler-broadened, and imply line-of-sight velocities of many thousands of km s^{-1} .

1.2.2 *The dusty torus*

Further out are dusty, molecular clouds which are co-planar with the accretion disc. These dusty clouds are generally referred to as the ‘torus’. In a Type II AGN, the accretion disc is observed in an edge-on configuration and, as a result, emission from the accretion and BLR is obscured by the dusty torus (e.g. Antonucci, 1993). Although this simple picture (shown in Figure 1.1) is a useful starting point, the idea of a torus as a static, doughnut-like structure is almost certainly incorrect. For example, the problem of maintaining the thickness of such a structure has long been recognized. In one alternative scenario, the torus is the dusty part of an accretion disc wind that extends be-

yond the dust-sublimation radius (e.g. Konigl and Kartje, 1994; Everett, Gallagher, and Keating, 2009; Gallagher et al., 2012; Everett, 2005; Keating et al., 2012; Elitzur and Shlosman, 2006).

1.2.3 *The narrow line region*

Further away from the central BH and beyond the dusty torus is the narrow emission line region (NLR). Like the BLR, the NLR is ionised by radiation from the central source. Unlike the BLR, densities in the NLR are low enough that forbidden transitions are not collisionally suppressed. Emission line widths are typically hundreds of km s^{-1} in the NLR. The NLR is sufficiently extended to be spatially resolved.

Extent: ask
Paul/Manda

1.3 WINDS AND OUTFLOWS IN AGN

Quasars are very powerful sources of radiation, and are embedded in matter-rich environments at the centres of galaxies. Strong winds, driven by some combination of gas pressure, radiation pressure due to dust or lines, and magnetic forces, are to be expected under these conditions (e.g. Blandford and Payne, 1982; Proga, Stone, and Kallman, 2000; Everett, 2005). In line with these expectations, evidence for outflows is common in the spectra of quasars.

Perhaps the most dramatic evidence of outflows is seen in broad absorption line quasars (BALQSOs; Weymann et al., 1991). BALQSOs are characterised by broad absorption features in the ultra-violet resonance lines of highly ionised N v , C iv and Si iv . The absorption is always blueshifted, and is evidence for fast outflows with velocities as large as 60 000 km s^{-1} (e.g. Turnshek, 1988). The observed C iv BALQSO fraction in radio-quiet quasars is ~ 15 per cent (e.g. Hewett and Foltz, 2003; Reichard et al., 2003) and the intrinsic fraction has been estimated at 40 per cent (Allen et al., 2011). The blueshifting of high-ionisation lines in the BLR (including C iv) also appears to be nearly ubiquitous in the quasar population (e.g. Richards et al., 2002; Richards et al., 2011), suggesting winds are even more common. Outflows are also used to explain narrow UV and X-ray absorption lines (NALs) which are seen in ~ 60 per cent of Seyfert 1 galaxies (Crenshaw et al., 1999) and some quasars (e.g. Hamann et al., 1997). The wide range of emission and absorption line phenomena can be explained in disc wind models

(e.g. Murray et al., 1995; Elvis, 2000; Proga, Stone, and Kallman, 2000; Everett, 2005)

1.4 SDSS AND THE ERA OF SURVEY ASTRONOMY

Emphasise the range of data now available and this allows us to do

1.5 THE AGN-HOST GALAXY CONNECTION

The space density of quasars was much greater at $z \gtrsim 2$, and declines steeply to $z = 0$. The existence of inactive BHs at the centres of massive galaxies is therefore a fundamental test of the quasar paradigm. Significant resources have been devoted to searching for these BHs, which are now known to exist in the centres of many nearby massive galaxies (e.g. Kormendy and Richstone, 1995; Ferrarese and Ford, 2005; Kormendy and Ho, 2013). Remarkably, given the sphere-of-influence of the BH is many orders of magnitude smaller than the size of the galaxy, the BH mass and mass of the host galaxy spheroid are strongly correlated (Ferrarese and Merritt, 2000; Gebhardt et al., 2000; Graham et al., 2001; Tremaine et al., 2002; Marconi and Hunt, 2003; Aller and Richstone, 2007; Gultekin et al., 2009). Although any underlying causal mechanism(s) responsible for the correlation is yet to be conclusively identified, there is considerable observational and theoretical support for a ‘feedback’ relationship in which the energy output from rapidly accreting BHs (in a quasar phase) couples with the gas in the host galaxy and quenches star formation (e.g. Silk and Rees, 1998; King, 2003; Di Matteo, Springel, and Hernquist, 2005; King and Pounds, 2015).

Models of galaxy evolution that invoke AGN feedback require these outflows to reach galactic scales and quench star formation in the AGN host galaxies. In recent years, a huge amount of resources have been devoted to searching for observational evidence of these galaxy-wide, AGN-driven outflows. This has resulted in recent detections of outflows in AGN-host galaxies using tracers of atomic, molecular, and ionised gas with enough power to sweep their host galaxies clear of gas (e.g. Nesvadba et al., 2006; Arav et al., 2008; Nesvadba et al., 2008; Moe et al., 2009; Dunn et al., 2010; Alexander et al., 2010; Harrison et al., 2012; Harrison et al., 2014; Nesvadba et al., 2010; Rupke and Veilleux, 2013; Veilleux et al., 2013; Nardini et al.,

2015; Feruglio et al., 2010; Alatalo et al., 2011; Cimatti et al., 2013; Cicone et al., 2014).

Quasar feedback has also been invoked to explain the similarity of the cosmic BH accretion and star formation histories. The number density of quasars, which evolves strongly with redshift, peaks at redshifts $2 \lesssim z \lesssim 3$ (e.g. Brandt and Hasinger, 2005; Richards et al., 2006b) and the most massive ($M_\bullet \gtrsim 10^9 M_\odot$) present-day BHs experienced much of their growth during this epoch. The star formation rate, which closely follows the cosmological evolution of the quasar luminosity function, also peaks during this epoch (e.g. Boyle and Terlevich, 1998). Quantifying the growth-rate of massive BHs at $2 \lesssim z \lesssim 3$ would therefore help significantly in understanding the role quasars play in galaxy evolution.

1.6 MEASURING BLACK HOLE MASSES

As one of just two fundamental quantities describing a BH on astrophysical scales, the mass is of crucial importance to virtually all areas of quasar science, including the evolution and phenomenology of quasars, and accretion physics. The power output of quasars is directly proportional to the BH mass. There is much debate regarding what effect the energy output by quasars has on the evolution and structure of the host galaxy.

The masses of BHs in many local, inactive galaxies have been measured by dynamical modelling spatially resolved kinematics. However, this requires the sphere-of-influence of the BH, R_{BH} , to be resolved. With BH masses only ~ 0.1 per cent of the stellar mass of the host galaxies, $R_{\text{BH}} \sim 1 - 100$ pc. With current instrumentation, resolving this region is only possible in very close by galaxies.

$$R_{\text{BH}} = \frac{2GM_{\text{BH}}}{\sigma_*^2}$$

The reverberation mapping method, first proposed by Blandford and McKee, (1982), uses the time delay between continuum variations and emission-line variations to estimate the size of the BLR, and hence the BH mass. Because it depends on temporal resolution rather than spatial resolution, this technique can be applied out to much greater distances.

1.6.1 Reverberation mapping

Continuum variability is a common characteristic of quasars, owing to the stochastic nature of the accretion process. Because the BLR is photo-ionized by the continuum, the broad emis-

sion lines also vary with some characteristic lag, which is related to the light travel time across the BLR. The reverberation mapping technique uses the time lag between variations in the continuum emission and correlated variations in the broad line emission to measure the typical size of the BLR (e.g. Peterson, 1993; Netzer and Peterson, 1997; Peterson, 2014).

Under the assumptions that the BLR dynamics are virialised and the gravitational potential is dominated by the BH, the BH mass is given by:

$$M_{\text{BH}} = f \left(\frac{\Delta V^2 R}{G} \right) \quad (1.1)$$

where ΔV is the line-width and R is the reverberation BLR radius. In practice, reverberation mapping relies on dense spectrophotometric monitoring campaigns which span many years. The typical velocity in the BLR is measured from the width of the broad H β line. Since the structure and geometry of the BLR is unknown, a virial coefficient f is introduced to transform the observed line-of-sight velocity inferred from the line width into a virial velocity. In practice, the value of f is empirically determined by requiring that the derived masses are consistent with those predicted from the M- σ relation for local inactive galaxies. Although the reverberation mapping technique has proved to be effective, because it relies on resource-intensive spectrophotometric monitoring campaigns, lags have been measured for only ~ 50 AGN (e.g. Kaspi et al., 2000; Peterson et al., 2004; Kaspi et al., 2007; Bentz et al., 2009; Denney et al., 2010; Barth et al., 2011; Grier et al., 2012). This sample is strongly biased to low luminosity Seyfert 1 galaxies, and the maximum redshift is just $z \sim 0.3$.

The full width at half maximum (FWHM) or dispersion (σ ; derived from the second moment) velocity of the prominent broad emission line of H β (4862.7Å)² is used as an indicator of the virial velocity, with extensions to other low-ionization emission lines such as H α (6564.6Å) and Mg II $\lambda\lambda 2796.4, 2803.5$ (e.g. Vestergaard, 2002; McLure and Jarvis, 2002; Wu et al., 2004; Kollmeier et al., 2006; Onken and Kollmeier, 2008; Wang et al., 2009; Rafiee and Hall, 2011).

The virial theorem states...

σ : velocity dispersion of galaxy

Seyfert 1:

FWHM: Full width of the line profile at half of maximum intensity

² Vacuum wavelengths are employed throughout the thesis.

1.6.2 Single-epoch virial estimates

Reverberation mapping campaigns have also revealed a tight relationship between the radius of the BLR and the quasar optical (or ultraviolet) luminosity (the R – L relation; e.g. Kaspi et al., 2000; Kaspi et al., 2007). A slope of $\simeq 0.5$ is found, which consistent with the naive prediction (e.g. Peterson, 1997). An advantage of the technique is that it is inexpensive in telescope time. A single spectrum yields a mass measurement. This relation provides a much less expensive method of measuring the BLR radius, and large-scale studies of AGN and quasar demographics have thus become possible through the calibration of single-epoch virial-mass estimators using the reverberation-derived BH masses (e.g. Greene and Ho, 2005b; Vestergaard and Peterson, 2006; Vestergaard and Osmer, 2009; Shen et al., 2011; Shen and Liu, 2012; Trakhtenbrot and Netzer, 2012). Single-epoch virial BH mass estimates normally take the form

$$M_{\text{BH}} = 10^a \left(\frac{\Delta V}{1000 \text{ km s}^{-1}} \right)^b \left[\frac{L_\lambda}{10^{44} \text{ erg s}^{-1}} \right]^c \quad (1.2)$$

where ΔV is a measure of the line width (from either the FWHM or dispersion), L_λ is the monochromatic continuum luminosity at wavelength λ , and a , b , and c are coefficients, determined via calibration against a sample of AGN with reverberation-mapping BH mass estimates. Several calibrations have been derived using different lines (e.g. H β , Mg II, C IV) and different measures of the line width (FWHM or dispersion) (e.g. Vestergaard, 2002; McLure and Jarvis, 2002; Vestergaard and Peterson, 2006; McGill et al., 2008; Wang et al., 2009; Rafiee and Hall, 2011; Park et al., 2013).

The uncertainties in reverberation mapped BH masses are estimated to be ~ 0.4 dex (e.g. Peterson, 2010), and the uncertainties in virial masses are similar (e.g. Vestergaard and Peterson, 2006). Since the structure and geometry of the BLR is unknown, a virial coefficient f is introduced to transform the observed line-of-sight velocity inferred from the line width in to a virial velocity. This simplification accounts for a significant part of the uncertainty in virial BH masses (in addition to, for example, describing the BLR with a single radius R and scatter in the R – L relation; Shen, 2013). By far the biggest uncertainty is the virial coefficient f . It is unknown, and it probably varies from source to source. A spherical distribution of clouds on random, isotropic orbits has $f = 3/4$ for $\Delta V = \text{FWHM}$ and $f = 3$ for

$\Delta V = \sigma$ (Netzer 1990). Furthermore, if the BLR is anisotropic (for example, in a flattened disk; e.g. Jarvis and McLure, 2006) then the line width will be orientation-dependent (e.g. Runnoe et al., 2013b; Shen and Ho, 2014; Brotherton et al., 2015).

The main progress in this area in recent years, that enables comprehensive statistical studies of active black holes (BHs), is the success of the large reverberation mapping project. This allows reliable estimates of broad line region (BLR) sizes and BH masses. The main concern and the biggest unknown is the extension of the method to high redshifts where H β measurements are no longer available. Something we will explore in Chapter 3.

For example, single epoch estimates have been used to calculate black hole masses in the highest redshift quasars to study the growth of SMBHs. This figure shows a compilation of SE mass estimates for quasars over a wide redshift range from different studies. These studies show that massive, 10^9 BHs are probably already in place by $z \sim 7$, when the age of the Universe is less than 1 Gyr. The fact that a SMBH exists in a quasar at such high redshift is of great importance in physics. The high redshift means that it was already there when our universe was very young, only about 800 million years old. And the fact that a SMBH was able to grow up in such a short time put some very tight constraints upon both the cosmological parameters and the accretion history of the SMBH itself (Willott et al. 2003).

Single epoch masses have also been used to study the distribution of quasars in the BH mass-luminosity plane, which conveys important information about the accretion process of these active black holes (e.g. Kollmeier et al. 2016). Redshift evolution of BH-bulge scaling relations (e.g. Bennert et al. 2011). Clustering (Shen & Ho 2014; Timins et al.?). With the R-L relationship, we are able to explore the black hole mass function, not only locally but at high redshift, enabling us to trace the history of black hole growth. Some exploratory work has been done on this and in fact there are claims that the M-sigma relation evolves over time. Estimates of such masses are important with respect to the relation between the MBH in the center of a stellar spheroid and the velocity dispersion.

We emphasize that application of single-epoch spectroscopy to quasars rests on the untested assumption that machinery which is calibrated for sub-Eddington BHs with $M \sim 10^7$ still works for BHs with masses up to 10^{10} that radiate near the

Eddington limit. Refer forward to problems with C IV (Chapter 3)

1.7 SEDS

AGN emit strongly over many decades in frequency. To first order SEDs are remarkably similar over many decades in luminosity and redshift. Significant diversity is observed in the SEDs of individual objects. However, the systematic study of the dependence of the SED shape on physical parameters has, until very recently, been limited by the difficulty in obtaining a large sample of quasars with good multi-wavelength coverage and large dynamic range in luminosity and redshift. However, we are able to take advantage of a number of recent, sensitive, wide-field photometric surveys, including SDSS (in the UV/optical), UKIDSS (in the NIR) and WISE (in the mid-infrared).

1.8 SUMMARY / WHAT I NEED TO GET ACROSS

It's a data rich time. SDSS has been revolutionary - shown the power of large surveys. We have wide-field photometry in a number of bands - important because AGN emit strongly over many decades in frequency. With spectra from SDSS we can derive BH masses and outflow properties from optical lines. But these are shifted to infrared wavelengths at redshifts > 1 , when things get interesting. Increasing availability of infrared-spectra. Looking to the future, huge spectroscopic surveys - WEAVE, 4MOST.

Quasar black hole masses: Shen, (2013), Peterson, (2010), Peterson, (2011), Vestergaard et al., (2011), Marziani and Sulentic, (2012). This has motivated a considerable amount of observational work searching for feedback signatures (for recent reviews, see Alexander and Hickox, 2012; Fabian, 2012; Heckman and Best, 2014).

Throughout this thesis we adopt a Λ CDM cosmology with $h_0 = 0.71$, $\Omega_M = 0.27$, and $\Omega_\Lambda = 0.73$. All wavelengths and equivalent width measurements are given in the quasar rest-frame, and all emission line wavelengths are given as measured in vacuum.

Get across:

Quasars are not all the same! There is a large range of continuum, emission, and absorption properties among quasars,

which demands that quasars cannot be fully described by a single, static picture.

1.9 OVERVIEW OF THESIS

Describe thesis in one chapter.

1.9.1 *A near-infrared spectroscopic database of high-redshift quasars*

1.9.2 *Black Hole Masses*

Black-hole masses are crucial to understanding the physics of the connection between quasars and their host galaxies and measuring cosmic black hole-growth. At high redshift, $z \gtrsim 2.1$, black hole masses are normally derived using the velocity-width of the $\text{CIV}\lambda\lambda 1548, 1550$ broad emission line, based on the assumption that the observed velocity-widths arise from virial-induced motions. In many quasars, the CIV-emission line exhibits significant blue asymmetries ('blueshifts') with the line centroid displaced by up to thousands of km s^{-1} to the blue. These blueshifts almost certainly signal the presence of strong outflows, most likely originating in a disc wind. We have obtained near-infrared spectra, including the $\text{H}\alpha \lambda 6565$ emission line, for 19 luminous ($L_{\text{Bol}} = 46.5 - 47.5 \text{ erg s}^{-1}$) Sloan Digital Sky Survey quasars, at redshifts $2 < z < 2.7$, with CIV emission lines spanning the full-range of blueshifts present in the population. A strong correlation between CIV-velocity width and blueshift is found and, at large blueshifts, $>2000 \text{ km s}^{-1}$, the velocity-widths appear to be dominated by non-virial motions. Black-hole masses, based on the full width at half maximum of the CIV-emission line, can be overestimated by a factor of five at large blueshifts. A larger sample of quasar spectra with both CIV and H β , or H α , emission lines will allow quantitative corrections to CIV-based black-hole masses as a function of blueshift to be derived. We find that quasars with large CIV blueshifts possess high Eddington luminosity ratios and that the fraction of high-blueshift quasars in a flux-limited sample is enhanced by a factor of approximately four relative to a sample limited by black hole mass.

The $\text{CIV}\lambda\lambda 1498, 1501$ broad emission line is visible in optical spectra to redshifts exceeding $z \sim 5$. CIV has long been known to exhibit significant displacements to the blue and these 'blueshifts' almost certainly signal the presence of strong

outflows. As a consequence, single-epoch virial black hole (BH) mass estimates derived from C_{IV} velocity-widths are known to be systematically biased compared to masses from the hydrogen Balmer lines. Using a large sample of 230 high-luminosity ($L_{\text{Bol}} = 10^{45.5} - 10^{48} \text{ erg s}^{-1}$), redshift $1.5 < z < 4.0$ quasars with both C_{IV} and Balmer line spectra, we have quantified the bias in C_{IV} BH masses as a function of the C_{IV} blueshift. C_{IV} BH masses are shown to be a factor of five larger than the corresponding Balmer-line masses at C_{IV} blueshifts of 3000 km s^{-1} and are over-estimated by almost an order of magnitude at the most extreme blueshifts, $\gtrsim 5000 \text{ km s}^{-1}$. Using the monotonically increasing relationship between the C_{IV} blueshift and the mass ratio $\text{BH(C}_4\text{V)/BH(H}\alpha\text{)}$ we derive an empirical correction to all C_{IV} BH-masses. The scatter between the corrected C_{IV} masses and the Balmer masses is 0.24 dex at low C_{IV} blueshifts ($\sim 0 \text{ km s}^{-1}$) and just 0.10 dex at high blueshifts ($\sim 3000 \text{ km s}^{-1}$), compared to 0.40 dex before the correction. The correction depends only on the C_{IV} line properties - i.e. full-width at half maximum and blueshift - and can therefore be applied to all quasars where C_{IV} emission line properties have been measured, enabling the derivation of un-biased virial BH mass estimates for the majority of high-luminosity, high-redshift, spectroscopically confirmed quasars in the literature.

1.9.3 *Narrow line region properties*

1.9.4 *SED Properties*

2

A NEAR-INFRARED SPECTROSCOPIC DATABASE OF HIGH-REDSHIFT QUASARS

2.1 INTRODUCTION

With the exception of a handful of very nearby objects, the inner regions of AGN cannot be resolved. Spectroscopic data is therefore invaluable to all AGN-related science. The optical region includes a number of strong emission features, including the broad lines of $\text{H}\alpha\lambda6565$ and $\text{H}\beta\lambda4863$ and the narrow $[\text{O III}]\lambda\lambda4960,5008$ doublet. As we will see in Chapter 3, the low-ionisation Balmer lines are routinely used to derive black hole masses and quasar accretion rates. As the strongest narrow emission line, $[\text{O III}]$ is used to measure the systemic redshift, and to probe quasar-driven outflows on galactic scales (see Chapter 4).

Large optical surveys have provided spectra for hundreds of thousands of AGN and quasars. With its twelfth data release in 2016, the number of quasar spectra in the Sloan Digital Sky Survey (SDSS; York et al., 2000) catalogue alone reached almost 300,000. However, the rest-frame optical region is redshifted beyond the reach of optical spectrographs at redshifts $z \gtrsim 0.4$ and, at redshifts $z \sim 2$, near-infrared spectroscopy is required in order to access the rest-frame optical lines.

The number density of quasars in the Universe rises sharply as a function of redshift, and peaks at redshifts $2 \lesssim z \lesssim 4$. The star formation rate follows a similar evolutionary path. Therefore, understanding supermassive black hole accretion over cosmic time and quasar feedback critically depends on the availability of near-infrared spectra for high-redshift quasars. Spectroscopic observations are more challenging at infrared wavelengths than in the optical. The Earth's atmosphere is both bright and highly variable at infrared wavelengths. As a result, the number of high-redshift quasars with near-infrared spectra is limited. Previous investigations of the rest-frame optical spectra of quasars at redshifts $z \sim 2$ have typically used samples of a few dozen (e.g. Shen and Liu, 2012; Shen, 2016).

In this chapter I will describe how I have constructed a database containing 462 high-redshift quasars. In later chap-

*Other references?
Sulentic?*

ters, I will describe how I have used this data to derive unbiased virial black hole mass estimates for quasars at redshifts $z \gtrsim 2$ (Chapter 3) and to study quasar-drive galaxy-wide outflows (Chapter 4). The unprecedented size and quality of this dataset make a number of other exciting investigations possible, some of which are described in Section 6.

In Fig. 2.1 we show the luminosities and redshifts of the quasar sample relative to the redshift-luminosity distribution for the Seventh Data Release (DR7; Schneider et al., 2010) of the SDSS spectroscopic quasar catalogue. Our sample spans a redshift range $1.5 < z < 4.0$ and a bolometric luminosity range $10^{45.5} - 10^{48} \text{ erg s}^{-1}$. Spectra were obtained within one or more of the JHK pass-bands and the gaps in our sample coverage at $z \sim 1.8$ and $z \sim 3$ are due to the presence of atmospheric absorption. Obtaining near-infrared spectra of adequate resolution and signal-to-noise ratio (S/N) of even moderately bright quasars remains resource intensive. As a consequence, at fixed redshift, the luminosities of the quasars are brighter than the average luminosity of the SDSS sample, although the dynamic range in luminosity is a full 1.5 decades.

2.2 DATA

The near-infrared spectra in our database are taken from published catalogues, by downloading and reducing archival spectra, and by reducing spectra acquired in programmes led by Prof. J. Hennawi (UCSB) and Prof. X. Prochaska (UCO/LICK). As the P.I. of two programmes, I filled in an under-sampled region of the C_{IV} blueshift parameter space by targeting quasars with the most extreme C_{IV} blueshifts. The telescopes and instruments used to observe these spectra are summarised in Table 2.1 and the information on the individual spectra is provided in Table 2.3. In the remainder of this chapter I will describe each of these sub-samples in turn.

2.2.1 Coatman et al. (2016) Quasars

2.2.1.1 Defining sample

We selected quasars from the SDSS DR7 spectroscopic quasar catalogue. The sample was restricted to objects with redshifts $2.14 < z < 2.51$ (7,258 quasars), to ensure that the H β and H α emission lines fall within the H- and K-bands respectively,

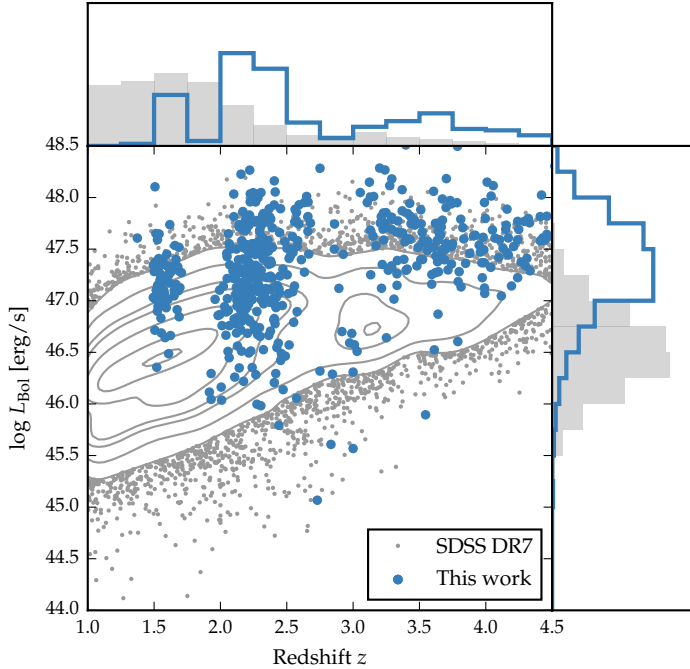


Figure 2.1: The ranges in redshift and luminosity covered by our sample, relative to the redshift-luminosity distribution of the SDSS DR7 quasar catalogue. In regions of high point-density, contours show equally-spaced lines of constant probability density generated using a Gaussian kernel-density estimator. For the SDSS sample we use Hewett and Wild, (2010) redshifts and bolometric luminosities measured by Shen et al., (2011). For the quasars in our sample the redshift is defined using the peak of the H α /H β emission and the luminosity is measured in the continuum at 1350Å and converted to a bolometric quantity using the same conversion factor employed by Shen et al., (2011). Eight objects are missing because we do not have enough information to calculate the bolometric luminosity.

Table 2.1: Summary of near-infrared spectroscopic database.

Instrument	Number
FIRE/Magellan	36
GNIRS/Gemini	29
ISAAC/VLT	13
LIRIS/WHT	21
NIRI/Gemini	31
NIRSPEC/Keck	3
SINFONI/VLT	84
SofI/NTT	111
TRIPLESPEC/ARC	38
TRIPLESPEC/Hale	60
XSHOOTER/VLT	36
Total	462

allowing us to observe both simultaneously with the appropriate grism configuration. Given the limited number of quasars for which near-infrared spectra could be obtained, the quasar sample was further restricted to objects that are radio-quiet (5,980 quasars), show no evidence of broad absorption lines (BALs) in their spectra (5,299 quasars), and are free from significant dust extinction. We removed radio-loud objects from our sample using the same radio-loud classification as Shen et al., (2011), and BAL quasars using the classifications of both Shen et al., (2011) and Allen et al., (2011). The removal of quasars with significant dust extinction was achieved by identifying quasars with $i - K$ colours redder than a parametric spectral energy distributions (SED) model + SMC-like extinction curve with $E(B - V) = 0.05$ (the SED model is described in Chapter 5).

The K-magnitude was taken from the UKIRT Infrared Deep Sky Survey (UKIDSS; Lawrence et al., 2007) Large Area Survey (ULAS). The requirement to be in the ULAS footprint and have reliable K band photometry reduced our sample of possible targets to 1,683, and the $E(B - V)$ cut left 1,204 in our sample. Finally, a flux-limit of $K < 18.5$ (AB) was applied to ensure that spectra of sufficient signal-to-noise ratio (S/N) could be obtained (412 quasars).

We were able to obtain new infra-red spectra for 19 quasars from this sample of 412 possible targets. The quasars included in this sub-sample were selected to have C IV-emission shapes

which span the full range observed in the population. Reliably quantifying the distribution of C IV-emission shapes has been made possible thanks to improvements in the estimation of systemic redshifts from ultraviolet spectra. The Allen & Hewett (2017, *in preparation*) redshift estimation algorithm generates redshifts which are independent of the C IV-emission shape. This has been a crucial factor in allowing us to quantify the distribution of C IV-blueshifts in the observed quasar population as a whole, and thus select a sample of quasars with a range of C IV blueshifts (see Section XX).

This paragraph could be more succinct

2.2.1.2 Observations

Near-infrared spectra were obtained with the Long-slit Intermediate Resolution Infrared Spectrograph (LIRIS; Manchado et al., 1998) mounted on the 4.2m William Herschel Telescope (WHT) at the Observatorio del Roque de los Muchachos (La Palma, Spain). Observations took place over four non-contiguous nights from 2015 March 31 to April 4. Approximately one night was lost due to poor weather and a further half-night was affected by poor transparency due to cloud. A one arcsecond slit-width was employed and the LIRIS H + K low-resolution grism was selected, which covers the spectral ranges 1.53–1.79 μm and 2.07–2.44 μm with a dispersion of 9.7 $\text{\AA}/\text{pixel}$. The spatial scale of the instrument is 0.25 arcsec/pixel. Observations were divided into 60 s sub-exposures and performed in an ABBA nodding pattern, with the object placed at two positions along the slit 12 arcsec apart. Bright A0–5V stars were observed at similar air-masses to the targets in order to provide both telluric absorption corrections and a flux calibration of the quasar spectra.

2.2.1.3 Data reduction

The raw LIRIS data frames incorporate a known ‘pixel shift’ which was first removed from all frames using the LIRIS data reduction package LIRISDR. Subsequent data reduction was undertaken with standard IRAF¹ procedures. The flat-field images, which were taken at the beginning of each night via illumination of the dome, were averaged and normalised to

¹ IRAF is distributed by the National Optical Astronomy Observatory, which is operated by the Association of Universities for Research in Astronomy (AURA) under a cooperative agreement with the National Science Foundation.

remove any wavelength-dependent signature. Each individual two-dimensional spectrum was then flat-field corrected. Consecutive AB and BA pairs of two-dimensional spectra were subtracted to remove the sky background. All the subtracted AB/BA-pairs for a target were then averaged to give the final two-dimensional spectrum.

The size of the one-dimensional spectrum extraction windows, in the slit direction, varied from 6–10 pixels. To increase the S/N, optimal variance-weighted extraction with sigma clipping was employed. For the fainter objects in our sample we were unable to trace the spectrum across the dispersion axis reliably and the trace from a telluric standard-star observation, observed at a similar air mass and time, was used instead. The wavelength calibration, using argon and xenon lamp exposures, resulted in root mean square errors in the range 1.01–1.71 Å, with a mean of 1.47 Å. The telluric standard star observations were reduced using the same steps described above. The stellar continuum was divided out of the standard star spectrum, which was then divided into the quasar spectrum to remove telluric absorption features. The spectral type and magnitude of the standard star were used to flux calibrate the quasar spectrum both in a relative and absolute sense. Variable atmospheric conditions combined with the narrow slit width resulted in a significant level of uncertainty in the absolute flux calibration for the quasar observations. The use of the UKIDSS broadband magnitudes (H and K) to normalise the spectra results in a significantly improved calibration.²

2.2.2 *Shen & Liu (2012) and Shen (2016) Quasars*

Shen, (2016) and Shen and Liu, (2012) obtained near-infrared spectroscopy for a sample of 74 luminous, $1.5 < z < 3.5$ quasars selected from the SDSS DR7 quasar catalogue. Targets had to possess good optical spectra covering the C IV line and have redshifts $z \sim 1.5$, 2.1, and 3.3 to ensure that the H β -[O III] region was covered in one of the near-infrared JHK bands. Thirty-eight of the quasars were observed with TripleSpec (Wilson et al., 2004) on the Astrophysics Research Consortium (ARC) 3.5 m telescope, and 36 with the Folded-port InfraRed Echelle (FIRE; Simcoe et al., 2010) on the 6.5 m Magellan-Baade

² The data reduction pipeline is available at github.com/liamcoatman/SpectraTools

telescope. The reduction of the spectra is described in Shen, (2016) and Shen and Liu, (2012).

2.2.3 Quasar Pairs

A large part of our catalogue was observed as part of an ongoing effort to identify quasar pairs at very close projected separations (Quasars Probing Quasars³ (QPQ); Hennawi et al., 2006a; Hennawi et al., 2010). The primary science driver of this work is to study the circum-galactic medium of the foreground quasars in absorption (Hennawi et al., 2006b). Very accurate systemic redshift measurements are a requirement and a large amount of effort has gone into obtaining near-infrared spectra which cover low-ionisation broad lines or features from the quasar narrow line region (Prochaska and Hennawi, 2009; Lau, Prochaska, and Hennawi, 2016; Hennawi et al., 2015). Twenty-nine quasars were observed with the Gemini Near-Infrared Spectrograph (GNIRS; Elias et al., 2006) on the 8.1 m Gemini North telescope, thirteen using the Infrared Spectrometer And Array Camera (ISAAC; Moorwood et al., 1998) on the European Southern Observatory (ESO) Very Large Telescope (VLT), thirty-one with the Near InfraRed Imager and Spectrometer (NIRI; Hodapp et al., 2003) also on Gemini North and thirty-six with XSHOOTER (Vernet et al., 2011), again, on the VLT.

The XSHOOTER spectra were reduced with a custom software package developed by George Becker (for details, see Lau, Prochaska, and Hennawi, 2016). The remaining data was processed with algorithms in the LowRedux⁴ package (see Prochaska and Hennawi, 2009).

2.2.4 VLT SINFONI Quasars

We performed a search of the ESO archive for high-redshift quasars observed with the SINFONI integral field spectrograph (Eisenhauer et al., 2003; Bonnet et al., 2004) at VLT/UT4. We found 79 quasars with redshifts $1.5 < z < 3.7$ which have H and/or K SINFONI spectroscopy, covering the H β and H α lines respectively. Seventy-two of the quasars are from a large programme led by L. Wisotzki (programme 083.B-0456(A)) to study the mass function and Eddington ratios of active BHs at

³ www.ucolick.org/~xavier/QPQ/Quasars_Probing_Quasars

⁴ www.ucolick.org/~xavier/LowRedux

redshifts $z \sim 2$ drawn from the Hamburg/ESO survey (Wisotzki et al., 2000). A further seven SINFONI spectra are from a programme led by J. D. Kurk (programme 090.B-0674(B)) to obtain reliable BH mass estimates from $\text{H}\alpha/\text{H}\beta$ for a sample of radio-loud/radio-quiet SDSS quasars.

The SINFONI spectra were reduced using the package EASYSINF⁵. The package, which is based on the ESO-SINFONI pipeline, is described in Williams et al., (2016).

2.2.5 ESO NTT SOFI Quasars

One quarter of the quasar catalogue derives from a large programme (programme 187.A-0645; PI: J. Hennawi) to combine near-infrared spectra from SOFI (Moorwood, Cuby, and Lidman, 1998) on the 3.6 m New Technology Telescope (NTT) with archival high-resolution optical spectra from the UV-Visual Echelle Spectrograph (UVES; Dekker et al., 2000) at VLT/UT2 and the High Resolution Echelle Spectrometer (HIRES; Vogt et al., 1994) at Keck to construct a legacy database of bright, high-redshift ($2 < z < 4$) quasars with both rest-frame optical spectra, covering the $\text{H}\beta\text{-}[\text{O III}]$ complex, and high-resolution rest-frame ultraviolet spectra. The main science goal is to obtain precise systemic redshifts which are crucial for the study of absorption line systems. Observations were undertaken over 16 nights from September 2011 to March 2013. I reduced these spectra using a custom pipeline using algorithms in the LowRedux package and, in Coatman et al., (2017), published a subset of the data for the first time.

Over five nights from 2015 August 31 to September 4 we obtained near-infrared SOFI spectra for a further 26 quasars (programme 095.B-0644(A); PI: L. Coatman). These quasars were selected from the SDSS DR7 quasar catalogue using criteria very similar to those described above for the WHT sample. In particular, we selected quasars with large C IV blueshifts to improve the statistics in this region of the C IV emission-line parameter space. The spectra were reduced using the same LowRedux pipeline.

Expand section?

⁵ www.mrao.cam.ac.uk/~rw480/easysinf

Table 2.2: Measured spectral resolutions of the spectrographs used in this thesis.

Spectrograph	FWHM [km s ⁻¹]
FIRE	59
GNIRS	136
ISAAC	46
LIRIS	477
NIRI	465
NIRSPEC	122
SINFONI	124
SOFI (MR)	323
SOFI (LR)	535
P200 TRIPLESPEC	88
ARC TRIPLESPEC	97
XSHOOTER	25

2.2.6 Hale TripleSpec Quasars

A further sixty quasars in our catalogue are bright SDSS quasars which were observed with the TRIPLESPEC spectrograph on the Palomar 200-inch Hale telescope (P200). The objects were observed with the same science goals as the SOFI NTT large programme. The spectra were reduced using a custom pipeline, again using algorithms in the LowRedux package.

2.3 INSTRUMENTAL BROADENING

Throughout this thesis, reported line-width measures are corrected for instrumental broadening by subtracting the resolution of the spectrograph in quadrature. The spectrograph resolutions, which we estimate from the line widths in the observed sky spectra, are given in Table 2.2.

2.3.1 Optical spectra

Optical SDSS DR7 spectra are employed for 70 quasars in the full catalogue. The SDSS DR7 spectra are moderate resolution ($R \approx 2000$) and S/N ($S/N \approx 20$) and cover the observed-frame wavelength interval $\sim 3800 - 9180 \text{ \AA}$. Many of the quasars in the

*Numbers reflect
chapter 3. Need to
update*

SDSS DR7 catalogue have been re-observed as part of the Sloan Digital Sky Survey-III: Baryon Oscillation Spectroscopic Survey (SDSS-III/BOSS; Dawson et al., 2013). As the BOSS-spectra typically have higher S/N than the SDSS DR7 spectra, we have used the BOSS spectra when available (126 quasars). We also use optical spectra from the Hamburg/ESO survey (15 quasars), and high-resolution spectra taken with VLT/UVES (11 quasars) and VLT/XSHOOTER (8 quasars). The Hamburg/ESO optical spectra have a typical $\sim 400 \text{ km s}^{-1}$ spectral resolution and $S/N \gtrsim 10$ per pixel. The reduced and fluxed UVES spectra were made available to us by A. Dall'Aglio (a description of the reduction procedure is contained in Dall'Aglio, Wisotzki, and Worseck, (2008)). The spectral resolution of the UVES observations is very high ($R \sim 40\,000$) and the S/N of the spectra re-binned to a resolution of $\simeq 2000$ is $S/N \simeq 300$. The XSHOOTER spectra are moderate resolution (~ 6000) and cover the full optical-near-infrared spectral region ($0.30 - 2.50 \mu\text{m}$).

2.3.2 Flux calibration of spectra

*Ask Manda: (1+z)
in luminosity
calculation.*

When NIR photometric data is available, the absolute flux scale of the spectra may be established by ensuring that broad-band magnitudes measured from the spectra are consistent with the photometry. Because this information is unavailable for a sizeable fraction of our sample, we consider two alternative approaches.

In the first approach, we leverage the excellent flux-calibration of the SDSS/BOSS spectra, which are available for XX objects in our sample. We use our standard quasar SED model (Chapter 5) to bridge the gap between the wavelength coverage of the NIR and optical SDSS/BOSS spectra. The quasar SED model is first fit to the SDSS/BOSS spectra, with the normalisation and extinction E(B-V) as free parameters. The NIR spectra are then fit to the normalised SED model. The second approach is identical, except that the SED model is first fit to the available optical (SDSS) and NIR (VHS, Viking, UKIDSS or 2MASS) photometric data⁶.

⁶ We are unable to verify the absolute flux calibration of the near-infrared spectra for XX objects () because neither SDSS/BOSS spectra nor optical/near-infrared data is available.

2.3.3 Quasar monochromatic luminosity

Relative flux-calibration of the infrared spectra as a function of wavelength has been achieved through observations of appropriate flux standards. The absolute flux levels, however, can be in error by large factors due to variable atmospheric conditions combined with the narrow slit widths. For the majority of the quasars we have, therefore, established the absolute flux scale for each near-infrared spectrum by fitting an SED-model to the optical-infrared photometry. The SED model, described in Chapter 5, gives a very good fit to the SDSS and UKIDSS magnitudes of SDSS DR7 quasars, reproducing the individual magnitudes with a $\sigma < 0.1$ mag. For 207 quasars, (Y)JHK passband magnitudes from the UKIRT Infrared Deep Sky Survey (UKIDSS; Lawrence et al., 2007) Large Area Survey, the Two Micron All Sky Survey (2MASS; Skrutskie et al., 2006) and the Visible and Infrared Survey Telescope for Astronomy (VISTA) Hemisphere Survey (VHS; McMahon et al., 2013) and Kilo-Degree Infrared Galaxy (VIKING; Edge et al., 2013) survey are available. The SED model was fit to the infrared magnitudes; integrating the SED model through the pass-band transmission functions, to give model magnitudes, and performing a variance weighted least-squares fit to the observed magnitudes. The flux at 5100 Å was then taken from the normalised model.

For 19 of the remaining 23 quasars, where near-infrared photometry was not available, the quasar SED model was fit to the SDSS spectra, the flux calibration of which are known to be excellent. The fit was done using a simple variance-weighted chi-squared minimisation procedure in emission line-free intervals of the optical spectra. The model includes a reddening, $E(B - V)$, based on a Small Magellanic Cloud-like extinction curve and described in detail in Section 5.4.6, and an overall normalisation as free parameters. In practice, the quasars possess only very modest reddening, with $E(B - V) \approx 0.0\text{--}0.1$. The flux at 5100 Å was then, again, taken from the normalised SED model.

For the four remaining quasars, which possess neither near-infrared photometry nor SDSS DR7 spectra, we fit the SED model to the BOSS DR12 spectra. To avoid the known issues in the flux calibration of the BOSS DR12 quasar spectra at observed-frame blue wavelengths (Lee et al., 2013), our fitting was confined to rest-frame wavelengths long-ward of 1275 Å.

*Numbers reflect
chapter 3 sample
only, and so need
updating*

The monochromatic luminosity at 1350\AA was also measured by fitting our quasar SED model to the SDSS/BOSS spectra. For 26 quasars in the catalogue the optical spectra come from surveys other than SDSS/BOSS and optical magnitudes from recent epochs are not available. In order to obtain an estimate of the luminosity at 1350\AA for the 26 quasars, we normalise the quasar SED model to the near-infrared photometric data, and read off the flux at 1350\AA .

Comparison of the 5100\AA luminosity, computed using the photometry- and spectrum-based methods for 177 quasars, showed a scatter of just ~ 0.1 dex. We therefore assume 0.1 dex to be the measurement uncertainty on the 5100\AA luminosities. We expect the uncertainties on the 1350\AA luminosities to be at similar level. For all the catalogue quasars, the optical and near-infrared spectra as well as the near-infrared photometry were obtained at different epochs, with rest-frame time differences of up to ~ 5 years. Intrinsic quasar photometric variability in the rest-frame ultraviolet and optical will therefore add additional scatter of ~ 0.2 mag (e.g. MacLeod et al., 2010) to the derived 1350- and 5100\AA -luminosities.

We matched our catalogue to the AllWISE release from WISE with a $5''$ matching radius. Out of 498 quasars, matches were found for 482. We did a linear interpolation through the WISE SED to find the flux at rest-frame $5\mu\text{m}$, which we then convert in to a monochromatic luminosity. $5\mu\text{m}$ luminosities were derived in this way for 414 quasars up to redshift $z = 3.4$. At higher redshifts, the longest wavelength WISE pass-band (W4) is at $< 5\mu\text{m}$ in the quasar rest-frame.

Table 2.3: Quasars in our near-infrared spectroscopic database. Only the first 15 entries are shown. The full table (including 462 objects) is available online. Columns are as follows: (1) identifier, (2) unique catalogue name, (3) date near-infrared spectra acquired, (4)-(5) coordinates, (6) instrument/telescope, (7) wavelength coverage, (8) velocity per pixel, (9) S/N per pixel, (10) redshift.

ID (1)	Cat. Name (2)	Date (3)	Ra (4)	Dec (5)	Instr. (6)	$\Delta\lambda$ [μm] (7)	Δv [km s ⁻¹] (8)	S/N (9)	z (10)
J000039-001804	QSO460	2015-09-02	+00h00m39.00s	-00d18m03.90s	SofI/NTT	1.50-2.54	154.0	4.9	2.14
J000345-232353	QSO552	2009-07-07	+00h03m45.00s	-23d23m53.40s	SINFONI/VLT	1.44-1.87	36.0	12.7	2.27
J000345-232353	QSO330	2011-09-18	+00h03m45.00s	-23d23m53.40s	SofI/NTT	1.48-1.83	63.0	36.0	2.26
J000451-084450	QSO290	2013-07-12	+00h04m50.66s	-08d44m49.63s	XSHOOTER/VLT	0.31-2.28	15.0	10.3	3.00
J000451-084452	QSO289	2013-08-08	+00h04m50.91s	-08d44m51.98s	XSHOOTER/VLT	0.31-2.28	15.0	5.4	3.00
J000500-003348	QSO454	2015-09-01	+00h05m00.42s	-00d33m48.20s	SofI/NTT	1.50-2.54	154.0	8.2	2.18
J000501+010221	QSO459	2015-09-02	+00h05m00.53s	+01d02m20.80s	SofI/NTT	1.50-2.54	154.0	6.8	2.13
J001016+001228	QSO475	2015-09-04	+00h10m16.49s	+00d12m27.60s	SofI/NTT	1.50-2.54	154.0	8.9	2.28
J001247+001239	QSO082	2013-06-06	+00h12m47.12s	+00d12m39.49s	ISAAC/VLT	1.52-1.60	15.0	19.1	2.16
J001708+813508	QSO107	2012-08-04	+00h17m08.48s	+81d35m08.10s	TRIPLESPEC/Hale	0.94-2.80	39.0	36.5	3.40
J001919+010152	QSO476	2015-09-04	+00h19m19.31s	+01d01m52.20s	SofI/NTT	1.50-2.54	154.0	6.5	2.32
J001955-091316	QSO001	2004-11-26	+00h19m54.67s	-09d13m16.45s	GNIRS/Gemini	0.60-2.61	88.0	9.9	2.12
J002018-233654	QSO553	2009-07-07	+00h20m18.41s	-23d36m53.80s	SINFONI/VLT	1.44-1.87	36.0	16.9	2.30
J002023-414639	QSO554	2009-07-08	+00h20m23.38s	-41d46m38.90s	SINFONI/VLT	1.09-1.41	35.0	33.4	1.57
J002111-242247	QSO555	2009-07-16	+00h21m10.90s	-24d22m47.20s	SINFONI/VLT	1.44-1.86	36.0	11.1	2.26

2.4 DESCRIPTION OF CATALOGUE

We have tabulated supplementary information for our spectroscopic catalogue. This information is used extensively throughout this thesis. Here, we describe the format of this extended catalogue.

- 1 ID: Jhhmmss+ddmmss (J₂₀₀₀; truncated coordinates).
- 2-3 ID: RA and DEC (in decimal degrees; J_{2000.0}).
- 4 Origin of optical spectra, if applicable.
- 5 BAL flag. -1 = no optical spectrum, o = non-BAL, 1 = BAL. BAL quasars are identified using flags from Shen et al., (2011), Allen et al., (2011) and Pâris et al., (2017), and by visual inspection.
- 6 Radio flag (-1 = not in FIRST footprint, o=FIRST undetected, 1=core dominant, 2=lobe dominant) from matching out sample to the FIRST radio catalogue (White et al., 1997). Following Shen et al., (2011), we classify quasars with matches within 5 arcseconds as core-dominated, while, if multiple matches were found within 30 arcseconds, quasars are classified as lobe-dominated.
- 2-11 SDSS DR9 ugriz magnitudes, and their errors.
- 12-14 SuperCosmos bri magnitudes.
- 15-20 2MASS JHK magnitudes, and their errors.
- 21-26 UKIDSS DR10 YJHK magnitudes, and their errors.
- 27-34 VHS YJHK magnitudes, and their errors.
- 35-44 Viking ZYJHK magnitudes, and their errors.
- 45-52 WISE W1W2W3W4 magnitudes.

LogL₅₁₀₀

LogL₁₃₅₀

$5\mu\text{m}$ luminosity, in erg s^{-1} . Luminosity is derived by linearly interpolating between WISE magnitudes.

3

BLACK HOLE MASSES

3.1 INTRODUCTION

The goal of better understanding the origin of the correlation between the masses of super-massive black holes (BHs) and the masses of host-galaxy spheroids has led to much work focussing on the properties of quasars and active galactic nuclei (AGN) at relatively high redshifts, $z \gtrsim 2$. Extensive reverberation-mapping campaigns have been used to calibrate single-epoch virial-mass estimates which use the velocity widths of the hydrogen Balmer emission lines and the nuclear continuum luminosity to provide reliable BH masses. Single-epoch virial BH mass estimates using H β are possible up to redshifts $z \sim 0.7$, and the technique has been extended to redshifts $z \sim 1.9$ via the calibration of the broad Mg II $\lambda\lambda 2796, 2803$ emission line (McLure and Jarvis, 2002; Onken and Kollmeier, 2008; Wang et al., 2009; Rafiee and Hall, 2011). At redshifts $z \gtrsim 2$, however, ground-based statistical studies of the quasar population generally have no access to the rest-frame optical and near-ultraviolet spectral regions.

The C IV $\lambda\lambda 1548, 1550$ emission doublet is both relatively strong in the majority of quasars and visible in modern optical spectra, such as those provided by the Sloan Digital Sky Survey (SDSS), to redshifts exceeding $z \sim 5$. C IV-derived BH masses have therefore become the standard (e.g. Vestergaard and Peterson, 2006; Park et al., 2013) for both individual quasars and in studies of quasar population demographics.

Currently, the number of reverberation mapped quasars is small (~ 50 quasars; Park et al., 2013) and restricted to low redshifts and luminosities. The luminosities of quasars at redshifts $z \gtrsim 2$ are much greater than in the reverberation mapped sample, and the reliability of the existing calibration involving C IV FWHM velocity measurements and ultraviolet luminosity is not established definitively when extrapolating to high-redshifts and luminosities. While some authors have found good agreement between BH mass-estimates based on C IV and H β (e.g. Vestergaard and Peterson, 2006; Assef et al., 2011; Tilton and Shull, 2013), others have questioned the consistency

(e.g. Baskin and Laor, 2005a; Trakhtenbrot and Netzer, 2012; Shen and Liu, 2012).

In contrast to a number of low-ionisation emission lines, such as Mg II, the C IV emission has long been known to exhibit significant asymmetric structure, with an excess of flux to the blue of the predicted rest-frame transition wavelength (Gaskell, 1982). More recent work (e.g. Sulentic, Marziani, and Dultzin-Hacyan, 2000; Richards et al., 2011) has established that the extent of ‘blueshifts’ in the C IV emission correlates with a number of properties of quasar spectral energy distributions (SEDs). A fundamental assumption on which single-epoch virial BH-mass estimates are based is that the widths of the broad emission lines are directly related to the virial motions of the emitting clouds moving in the gravitational potential of the central BH. While the physical origin of the blueshifted emission has not been established there is a consensus that the associated gas is not tracing virial-induced velocities. A favoured interpretation associates the blueshifted emission with out-flowing material (see Netzer, 2015, for a recent review), reaching velocities significantly larger than virial-induced velocities associated with the BH (e.g. Sulentic et al., 2007; Richards et al., 2011). These outflows, most likely, result from the presence of a radiation line-driven accretion-disc wind (e.g. Konigl and Kartje, 1994; Murray et al., 1995; Proga, Stone, and Kallman, 2000; Everett, 2005; Gallagher et al., 2015; Higginbottom and Proga, 2015).

Excess emission-line flux in the blue wing of the C IV emission increases commonly employed measures of the line-width, notably the full-width at half maximum (FWHM) and the line dispersion (σ). In general, researchers studying quasar demographics at high-redshift adopt estimates of BH masses based on the width of C IV-emission, without reference to the blueshift of the C IV-emission (e.g. Vestergaard, 2004; Kollmeier et al., 2006; Gavignaud et al., 2008; Vestergaard et al., 2008; Vestergaard and Osmer, 2009; Kelly et al., 2010; Kelly and Shen, 2013). Figure 3.1 shows the shape of the C IV-emission in composite spectra constructed from SDSS DR7 quasars as a function of C IV blueshift. The profiles show how, at large values of blueshift ($\gtrsim 2000 \text{ km s}^{-1}$) the C IV-profile is displaced to the blue by amounts comparable to the FWHM of the profile. This indicates that non-virial motions, very likely due to outflows, are having a significant effect on the observed C IV emission velocity profile (e.g. Gaskell, 1982; Baskin and Laor, 2005a; Su-

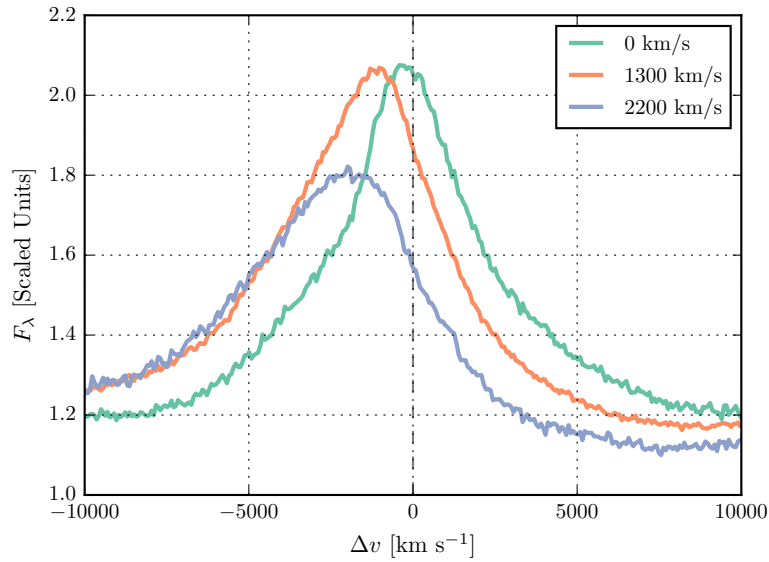


Figure 3.1: Composite spectra of the CIV-emission line as a function of CIV blueshift for SDSS DR7 quasars. Quasars classified as BALs, or possessing strong associated absorbers have been excluded, and the composite-spectra shown are derived using an arithmetic mean of a minimum of 200 spectra at each blueshift. Virtually the entire CIV-profile appears to shift blueward and the change in line shape is not simply an enhancement of flux in the blue wing of a still identifiable symmetric component. In order of increasing CIV blueshift, the composite spectra have FWHM 4870, 5610, and 6770 km s⁻¹ and EW 33.1, 31.6, and 28.8 Å.

lentic et al., 2007; Richards et al., 2011; Wang et al., 2013). At fixed emission-line EW, virtually the entire C IV-profile appears to shift blueward and the change in line shape is not simply an enhancement of flux in the blue wing of a still identifiable symmetric component. While gravity almost certainly plays a key role, determining the escape velocity for out-flowing material for example, it is clear that the virial assumption, on which single-epoch BH-mass measurements are predicated, is not straightforwardly applicable for the C IV-emission line in quasars exhibiting large blueshifts. As a consequence, BH-masses derived from C IV emission line velocity-widths are systematically biased compared to masses from the Balmer lines (e.g. Shen et al., 2008; Shen and Liu, 2012; Coatman et al., 2016).

As highlighted by Richards et al., (2011), the sample of reverberation mapped quasars includes a restricted range of the C IV emission line shapes seen in the quasar population. In particular, the reverberation mapped objects generally possess high C IV equivalent widths and low C IV-blueshifts. Nevertheless, the derived scaling relations based on the reverberation-mapped sample are regularly applied to the quasar population with low C IV EWs and/or large C IV-blueshifts, where any non-virial outflow-related contribution to the dynamics is significant.

In recent literature, attempts have been made to minimise the influence of the systematic non-virial contribution to the C IV emission on estimates of the BH mass. Strategies include (i) significantly reducing the dependence of the derived masses on the emission-line velocity width (e.g. from the V^2 dependence predicted assuming a virialized broad line region to just $V^{0.56}$ in Park et al. 2013; see also Shen and Liu 2012), (ii) adopting a measure of emission-line velocity-width that is relatively insensitive to changes in the core of the emission-line profile (e.g. Denney et al., 2013) and (iii) estimating the amplitude of the non-virial contribution to the C IV emission-line via comparison with other ultraviolet emission lines (e.g. Si IV+O IV $\lambda 1400$ in Runnoe et al. 2013a and Brotherton et al. 2015). The increased number of quasars with high-quality spectra that cover both the observed-frame optical (where the redshifted C IV appears) and near-infrared (where H β and H α lie) enables us to take a rather different approach in this chapter. We will use properties of the C IV emission line itself to reduce, or even remove, the systematic bias in the BH-mass estimates. Specifically, using the low-ionisation Balmer lines H α and H β as reliable proxies

for the virial velocity, we will measure empirically the systematic bias in C IV-based virial BH mass estimates as a function of the C IV emission-line blueshift.

3.2 QUASAR SAMPLE

We have compiled a sample of 307 quasars at redshifts $1.5 < z < 4$ with both optical and near-infrared spectra. Reliable emission line properties were measured for 230 quasars (Section 3.3.5), with 164 possessing H α line measurements and 144 H β line measurements. This will allow us to directly compare virial BH mass estimates based on the C IV line-width with estimates based on the line-widths of the low-ionisation Balmer lines H α and H β . The sample is considerably larger than previous studies of the rest-frame optical spectra of high- z quasars (e.g. Shen and Liu, 2012). As we demonstrate in Section 3.5.3, the quasars have C IV blueshifts of up to $\sim 5000 \text{ km s}^{-1}$, and span the full range observed in the population.

3.2.1 Spectroscopic data

The near-infrared data has been described in Chapter 2 and the telescopes/spectrographs used are summarised in Table 3.1. Corresponding optical spectroscopy was obtained from the SDSS (70 quasars), BOSS (126 quasars) and Hamburg/ESO surveys (15 quasars), and with VLT/UVES (11 quasars) and VLT/XSHOOTER (8 quasars). Once more, further details are provided in Chapter 2. We have sub-divided our sample into two overlapping groups: quasars with reliable H α line measurements (the ‘H α sample’) and quasars with reliable H β measurements (the ‘H β sample’).

3.3 SPECTRAL MEASUREMENTS

Conventionally, single-epoch virial estimates of the BH mass are a function of the line-of-sight velocity width of a broad emission line and the quasar luminosity. The velocity width is a proxy for the virial velocity in the broad line region (BLR) and, as revealed in reverberation-mapping studies, the luminosity is a proxy for the typical size of the BLR (the R – L relation; e.g. Kaspi et al., 2000; Kaspi et al., 2007). Most reverberation mapping campaigns have employed H β time-lags and velocity

Table 3.1: The numbers of quasars with reliable H α and H β line measurements, and the spectrographs and telescopes used to obtain the near-infrared spectra

Spectrograph	Telescope	H α Sample	H β Sample
FIRE	MAGELLAN	18	19
GNIRS	GEMINI-N	22	17
ISAAC	VLT	0	4
LIRIS	WHT	15	0
NIRI	GEMINI-N	0	12
SINFONI	VLT	2	25
SOFI	NTT	47	23
TRIPLESPEC	ARC-3.5m	33	20
TRIPLESPEC	P200	23	19
XSHOOTER	VLT	4	7
Total		164	144

widths, but the line-widths of H α and Mg II $\lambda\lambda2800$ have been shown to yield consistent BH masses (e.g. McLure and Jarvis, 2002; Greene and Ho, 2005b; Onken and Kollmeier, 2008; Shen et al., 2008; Wang et al., 2009; Rafiee and Hall, 2011; Mejía-Restrepo et al., 2016). In Section 3.4.1 we verify that the H α and H β line-widths yield consistent BH for the 99 quasars in our sample with measurements of both.

In our work, a robust measure of the C IV emission-line ‘blueshift’ provides the basis for the corrected C IV velocity-width measurements, and hence BH masses. The effectiveness of the scheme is validated via a direct comparison of the C IV velocity-widths to the Balmer emission velocity-widths in the same quasars. Our process is as follows. First, an accurate measure of the quasar’s systemic redshift is required, for which we adopt the centre of the Balmer emission, where the centre, λ_{half} , is the wavelength that bisects the cumulative total flux. Balmer emission centroids are available for all quasars in the catalogue but we verify that the measure is relatively unbiased through a comparison of the centroids to the wavelengths of the peak of the narrow [O III] $\lambda\lambda4960,5008$ doublet for the subset of spectra where both are available (Section 3.4.2). Second, the blueshift of the C IV emission line is determined. Again, we adopt the line centroid to provide a robust measure of the C IV emission blueshift. The blueshift (in km s $^{-1}$) is defined as $c \times (1549.48 - \lambda_{\text{half}}) / 1549.48$ where c is the velocity of light and

1549.48\AA is the rest-frame wavelength for the C_{IV} doublet¹. Positive blueshift values indicate an excess of emitting material moving towards the observer and hence out-flowing from the quasar.

Emission-line velocity widths are derived from the full-width-at-half-maximum (FWHM) of the lines but we also compute the line dispersion (calculated from the flux-weighted second moment of the velocity distribution) as some authors have claimed this provides a better estimate of the virial velocity (Denney et al., 2013).

To minimise the impact of the finite S/N of the quasar spectra and the presence of absorption features superposed on the broad emission lines we first fit a parametric model to the continuum and the emission lines. The particular form of the model parametrizations is not important and the fits are used only to provide robust line parameters, such as the centroid λ_{half} , and FWHM, which are measured non-parameterically from the best-fitting model. The models used and the fitting procedure are described below. The issues involved in deriving parameters for broad emission lines from spectra of modest S/N – for example, subtraction of narrow line emission, subtraction of Fe II emission – have been covered comprehensively by other authors (e.g. Shen et al., 2011; Shen and Liu, 2012; Denney et al., 2013; Shen, 2016) and, as far as possible, we follow standard procedures described in the literature.

3.3.1 C_{IV}

We first define a power-law continuum, $f(\lambda) \propto \lambda^{-\alpha}$, with the slope, α , determined using the median values of the flux in two continuum windows at 1445–1465 and 1700–1705 \AA . The continuum emission is subtracted from the spectra, which is then transformed from wavelength units into units of velocity relative to the rest-frame line-transition wavelength for the C_{IV} doublet. The parametric model is ordinarily fit within the wavelength interval 1500–1600 \AA (corresponding to approximately $\pm 10\,000\text{ km s}^{-1}$ from the rest-frame transition wavelength), a recipe that is commonly adopted (e.g. Denney et al., 2013). The line-window was extended if more than 5 per cent of the total

¹ The adopted C_{IV} rest-frame wavelength assumes an optically thick BLR, in which case the contribution from each component is equal. Adopting a 2:1 ratio (appropriate for an optically thin BLR) changes the blueshifts by $\sim 80\text{ km s}^{-1}$.

flux in the profile was present blueward of the short wavelength limit. Narrow absorption features, which are frequently found superimposed on C_{IV} emission, were masked out during the fit.

The C_{IV} emission was fit with sixth-order Gauss-Hermite (GH) polynomials, using the normalisation of van der Marel and Franx, (1993) and the functional forms of Cappellari et al., (2002). We allowed up to six components, but in many cases a lower order was sufficient (40 and 45 per cent were fit with second- and fourth-order GH polynomials respectively). GH polynomials were chosen because they are flexible enough to model the often very asymmetric C_{IV} line profile. The flip-side of this flexibility, however, is that the model has a tendency to over-fit when spectra possess low S/N. The fits were therefore carefully checked visually and the number of components reduced if over-fitting was evident.

We find that using the commonly employed three-Gaussian component model, rather than the GH polynomials, resulted in only marginal differences in the line parameters. Our best-fit parameters are also in good agreement with Shen et al., (2011), who employ a multi-Gaussian parametrization. In Fig. 3.2 we compare our measurements of the C_{IV} FWHM from the 71 SDSS DR7 spectra in our sample with the measurements published in Shen et al., (2011). There is a very strong agreement between our measurements, with a scatter of 0.05 dex (200 km s⁻¹).

3.3.2 H α

A power-law continuum is fit using two continuum windows at 6000–6250 and 6800–7000 Å. The continuum-subtracted flux is then fit in the wavelength interval 6400–6800 Å. We adopt a rest-frame transition wavelength of 6564.89 Å to transform wavelengths into equivalent Doppler velocities. The broad component of H α is fit using one or two Gaussians, constrained to have a minimum FWHM of 1200 km s⁻¹. When two Gaussians are used, the velocity centroids are constrained to be the same.

The emission-line profiles of both H β and H α frequently include a significant narrow component from the physically more extended narrow line region (NLR). Additional Gaussian components were included in our parametric model to fit the narrow component of H α as well as [N II] $\lambda\lambda$ 6548,6584 and [S II] $\lambda\lambda$ 6717,6731. This resulted in a better fit to the observed flux in 50 per cent of cases. We impose a 1200 km s⁻¹ upper limit

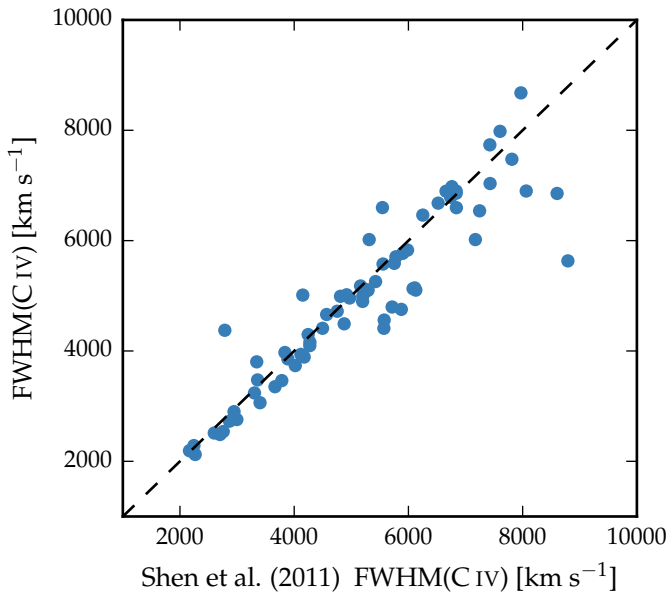


Figure 3.2: Demonstration of the effectiveness of our line parameter estimation scheme via a comparison of the C IV FWHM with Shen et al., (2011).

on the FWHM of all narrow lines and the amplitudes of all components must be non-negative. The relative flux ratio of the two [N II] components is also fixed at the expected value of 2.96. In 70 per cent of the spectra the [O III] $\lambda\lambda 4960, 5008$ doublet is detected at moderate S/N in the H β region. In these cases the peak of the [O III] is used to fix the velocity offsets and the FWHMs of the narrow line components in the H α region. For spectra where the [O III] doublet does not constrain the velocity and FWHM accurately, the narrow emission in the H α and H β regions are fitted independently but, for each region, the individual narrow-line velocity offsets and the FWHMs are constrained to be identical. In these objects the narrow line contribution is generally weak, and so does not have a large effect on the line parameters we measure for the broad component.

The model described above is very similar to the one described in Shen and Liu, (2012) and Shen et al., (2011), the only major differences being that we do not fit the H α and H β emission regions simultaneously and we fix the centroids of the Gaussian components used to fit the broad emission. In Fig. 3.3 we plot our H α FWHM measurements against the measurements published in Shen and Liu, (2012), for 51 quasars in

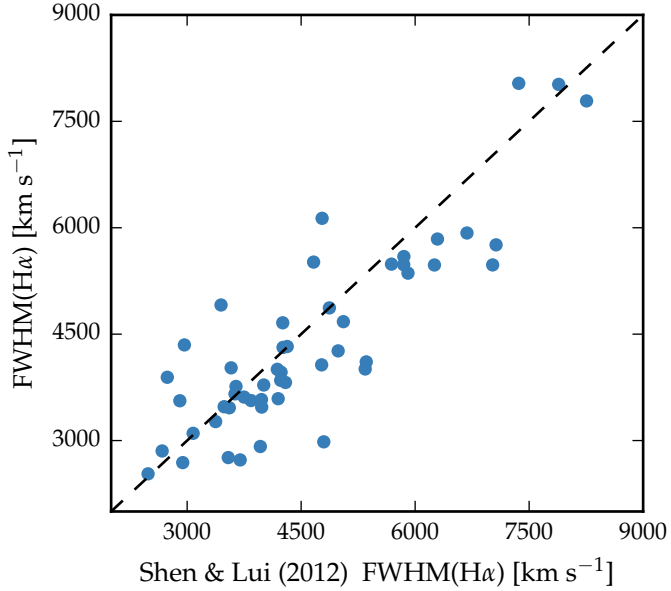


Figure 3.3: Demonstration of the effectiveness of our line parameter estimation scheme via a comparison of the H α FWHM with Shen and Liu, (2012).

common to both samples. There is a strong correlation and a scatter of just 0.07 dex.

3.3.3 $H\beta$ and [O III]

Emission from optical Fe II is generally strong in the vicinity of H β . We therefore fit a combination of a power-law continuum and an optical Fe II template – taken from Boroson and Green, (1992) – to two windows at 4435-4700 and 5100-5535 Å. The Fe II template is convolved with a Gaussian, and the width of this Gaussian, along with the normalisation and velocity offset of the Fe II template, are free variables in the pseudo-continuum fit. We use the same model to fit the broad and narrow components of H β as was used with H α . Each line in the [O III] doublet is fit with two Gaussians, to model both the systemic and any outflow contributions. The peak flux ratio of the [O III] 4960 Å and 5008 Å lines is fixed at 1:3. As for the fit to the narrow lines in the spectral region around H α , the width and velocity offsets of all the narrow components are set to be equal, and an upper limit of 1200 km s $^{-1}$ is placed on the FWHM.

The parametric model we fit to the H β /[O III] emission region was very similar to the model employed by Shen, (2016).

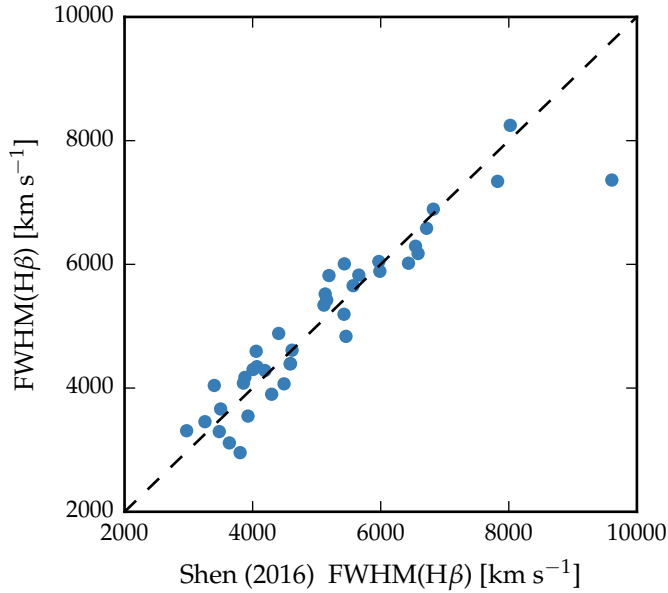


Figure 3.4: Demonstration of the effectiveness of our line parameter estimation scheme via a comparison of the H β FWHM with Shen, (2016).

In Fig. 3.4 we plot our H β FWHM measurements against the measurements published in Shen, (2016), for 39 quasars in common to both samples. As expected, we observe a very tight correlation, with a scatter of 0.04 dex.

3.3.4 Fitting procedure

Model parameters were derived using a standard variance-weighted least-squares minimisation procedure employing the Levenberg-Marquardt algorithm. Prior to the fit, the spectra were inspected visually and regions significantly affected by absorption or of low S/N were masked out.

In Fig. 3.5 we present our parametric fits to the C IV, H α and H β emission lines in a handful of quasars, which have been chosen to illustrate the range of spectrum S/N and line shapes in the sample. The Doppler velocities have been shifted so that the H α emission line centroid is at 0 km s $^{-1}$. The y-axes of the data-minus-model residual plots have been scaled by the spectrum flux errors. The mean reduced chi-squared values in our H α , H β and C IV fits are 1.69, 1.62, and 1.77 respectively and, in general, there are no strong features observable in the spectrum minus model residuals. The only significant features seen

Table 3.2: The format of the table containing the emission line properties from our parametric model fits. The table is available in machine-readable form in the online version of Coatman et al., (2017).

	Units	Description
NAME		Catalogue name
FWHM_BROAD_HA	km s^{-1}	FWHM of broad H α line
FWHM_BROAD_HA_ERR	km s^{-1}	
SIGMA_BROAD_HA	km s^{-1}	Dispersion of broad H α line
SIGMA_BROAD_HA_ERR	km s^{-1}	
Z_BROAD_HA		Redshift from broad H α line
FWHM_BROAD_HB	km s^{-1}	FWHM of broad H β line
FWHM_BROAD_HB_ERR	km s^{-1}	
SIGMA_BROAD_HB	km s^{-1}	Dispersion of broad H β line
SIGMA_BROAD_HB_ERR	km s^{-1}	
Z_BROAD_HB		Redshift from broad H β line
FWHM_CIV	km s^{-1}	FWHM of C IV doublet
FWHM_CIV_ERR	km s^{-1}	
SIGMA_CIV	km s^{-1}	Dispersion of C IV doublet
SIGMA_CIV_ERR	km s^{-1}	
BLUESHIFT_CIV_HA	km s^{-1}	Blueshift of C IV relative to H α
BLUESHIFT_CIV_HA_ERR	km s^{-1}	
BLUESHIFT_CIV_HB	km s^{-1}	Blueshift of C IV relative to H β
BLUESHIFT_CIV_HB_ERR	km s^{-1}	
LOGL ₅₁₀₀	erg s^{-1}	Luminosity at 5100Å
LOGL ₁₃₅₀	erg s^{-1}	Luminosity at 1350Å

in the residual C IV spectra correspond to the location of narrow absorption lines which were excluded in the fitting procedure.

Table 4.3 includes the line parameters of our best-fitting model for each line. The reported line-width measures are corrected for instrumental broadening by subtracting the resolution of the spectrograph in quadrature. The spectrograph resolutions, which we estimate from the line widths in the observed sky spectra, range from 25km s^{-1} for XSHOOTER to 477km s^{-1} for the low-resolution LIRIS grism and are therefore small relative to the quasar broad line widths.

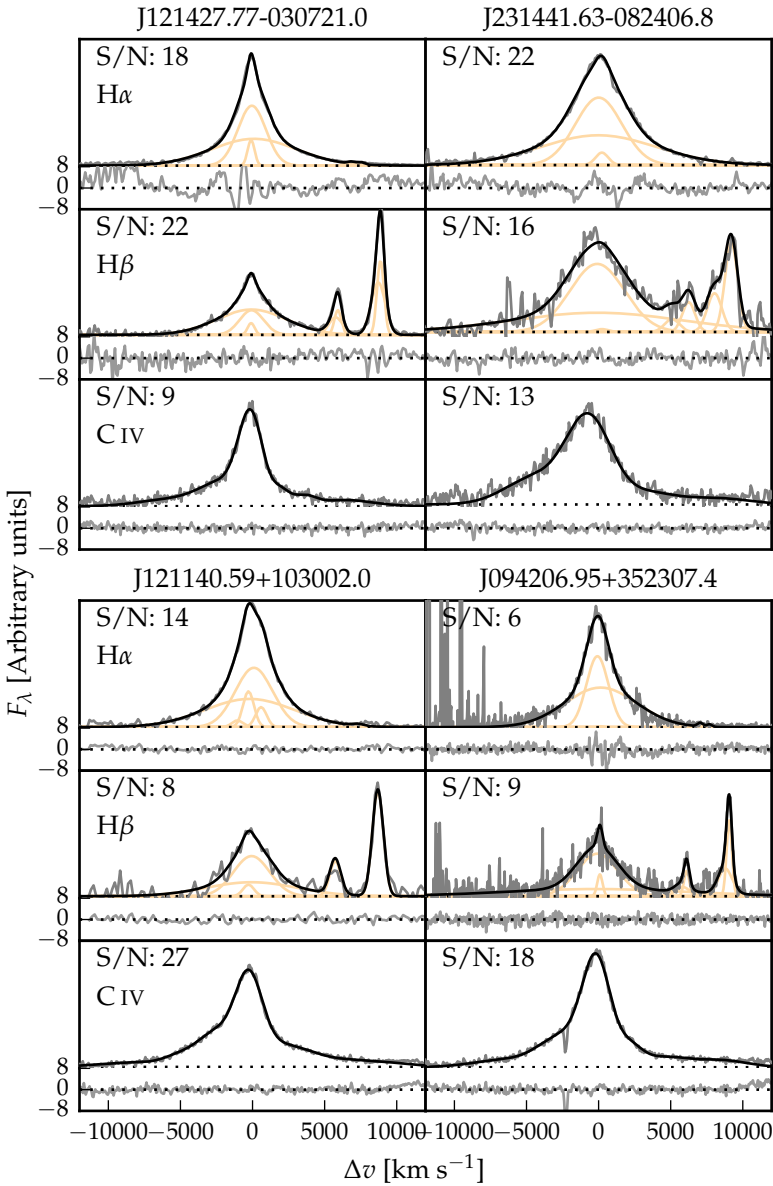


Figure 3.5: Model fits to continuum-subtracted $\text{H}\alpha$, $\text{H}\beta$, and CIV emission in four quasars, chosen to represent the range of S/N (indicated in the figure and given per 150km s^{-1} pixel in the continuum) and line shapes present in the catalogue. The data is shown in grey, the best-fitting parametric model in black, and the individual model components in orange. The centroid of the broad $\text{H}\alpha$ emission is used to set the redshift, and Δv is the velocity shift from the line rest-frame transition wavelength. Below each fit we plot the data minus model residuals, scaled by the errors on the fluxes.

Table 3.3: The number of spectra removed from our sample by the cuts described in Section 3.3.5.

	H α sample	H β sample
Total	194	279
H α /H β	Wavelength	6
	S/N	8
C IV	Wavelength	6
	S/N	4
	Absorption	6
Total remaining		164
		144

3.3.5 Spectra removed from sample

Through visual inspection we flagged and discarded the spectra of quasars for which reliable emission line parameters could not be obtained.

First, we flagged emission lines in spectra that possessed insufficient S/N. A single minimum S/N threshold was not entirely effective and, instead, spectra were flagged when it was judged conservatively that no meaningful constraints could be placed on the velocity centroid and/or width of the emission-line.

Second, we flagged emission lines where significant regions of the continuum and/or emission line fell outside of the wavelength coverage of the spectra. Reliable continuum definition and subtraction is not straightforward for emission lines so affected.

Third, we flagged C IV emission lines because of strong, narrow absorption close to the peak of the line where reliable interpolation across the absorption, using our parametric model, was not possible.

The number of spectra that are removed by each cut is given in Table 3.3 and the distribution in redshift and luminosity is shown in Fig. 3.6. Unsurprisingly, there is a preferential removal of intrinsically faint quasars, whose spectra can be of poorer S/N, and a loss of quasars at redshifts $z \sim 2.6$ where the H α emission falls at the edge of the K-band. H β is much weaker than H α , and the H β spectra are generally of lower S/N. As a result, the fraction of H β spectra that are flagged – 39 per cent – is particularly high.

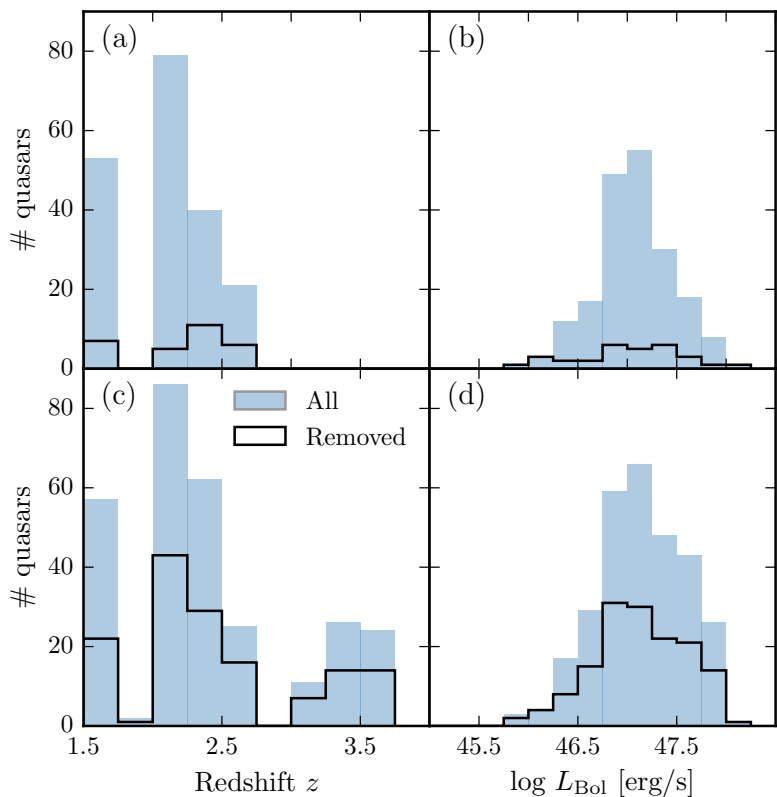


Figure 3.6: The redshift and luminosity distributions of the spectra removed from our $\text{H}\alpha/\text{C IV}$ (a, b) and $\text{H}\beta/\text{C IV}$ (c, d) samples.

3.3.6 Emission-line parameter uncertainties

The 1σ error bars calculated from the covariance matrix in least-squares minimisation will underestimate the true uncertainties on the line parameters, since they do not account for systematic errors such as the significant uncertainty introduced in the continuum subtraction procedure. To calculate more realistic uncertainties on our fitted variables we employed a Monte Carlo approach. One thousand artificial spectra were synthesised, with the flux at each wavelength drawn from a Normal distribution (mean equal to the measured flux and standard deviation equal to the known error). Our emission-line fitting recipe was then implemented on each of these mock spectra. The uncertainty in each parameter is given by the spread in the best-fitting values from the one thousand realisations of the fitting routine. In some cases the standard deviation of the parameter distribution was biased by extreme values caused by bad fits². We therefore chose to measure the spread in the parameter distribution by fitting a composite model with two Gaussian components – one to model uncertainty in the parameter and the other any possible outlier component. The uncertainty in each line parameter was then taken to be the width of the narrower Gaussian. The uncertainties on all derived quantities, such as the BH mass, are propagated through by assuming that the uncertainties are uncorrelated and independent.

3.3.7 Contemporaneity of spectra

The epochs of the near-infrared and optical spectra can differ by many years. For example, the NTT SOFI spectra were taken ~ 14 years after the SDSS spectra, and the VLT SINFONI spectra 20 years or more after the Hamburg/ESO observations³. If the broad emission line profiles varied significantly on these time-scales the relation between the C IV and Balmer line-width measurements could be blurred.

Cases do exist of dramatic changes in quasar spectra over short time-scales, but this phenomenon is rare (MacLeod et al., 2016). In our spectroscopic catalogue there are 112 SDSS DR7 quasars which are re-observed in BOSS and included in the DR12 quasar catalogue. The mean time elapsed between the

² In the analysis of the real spectra such fits are identified via visual inspection.

³ Time differences in the quasar rest-frame are reduced by a factor of $(1 + z)$.

two sets of observations is ~ 8 years. The root-mean-square difference in the C IV FWHM measured from the BOSS and SDSS spectra is a modest $\simeq 500 \text{ km s}^{-1}$. Differences in the S/N of the spectra will make a substantial contribution and the scatter due to true variations in the C IV velocity-width will be significantly smaller than 500 km s^{-1} . We conclude therefore that any intrinsic changes with time do not materially affect the emission line measurements.

3.3.8 Quasar monochromatic luminosity

Computing virial BH masses also requires the quasar luminosity in an emission-line free region of the continuum adjacent to the broad line being used. The luminosity is used as a proxy for the size of the BLR. The monochromatic continuum flux is generally measured at 1350 \AA for C IV and 5100 \AA for H α and H β . The calculation of these luminosities is described in Chapter 2.

As described in Chapter 2, we estimate the uncertainties on the monochromatic luminosities to be ~ 0.3 dex. Given that the luminosity enters into the calculation of BH-mass only as the square-root, the uncertainty on the luminosities does not make a large contribution to the uncertainties in the BH mass estimates.

3.3.9 Characterising the emission-line widths

There has been a considerable degree of attention paid to the effectiveness of different velocity-width measures of the C IV-emission; specifically, the line FWHM and the dispersion, σ , derived from the second-moment velocity (e.g. Assef et al., 2011; Denney et al., 2013). The FWHM and line dispersion trace different parts of the broad line velocity field, with the FWHM relatively more sensitive to any low-velocity core present and the line dispersion relatively more sensitive to the high velocity wings. In practice, the line dispersion is almost certainly a more robust velocity indicator when the assumptions underlying the virial-origin of the emission-line velocity width are true and the spectral S/N and resolution are adequate. This was demonstrated by Denney et al., (2013) for a sample of quasars possessing a significantly smaller range in C IV-blueshift than investigated here.

In reality, however, as highlighted by Denney, (2012), contributions to the C IV-emission line profile from gas where virial

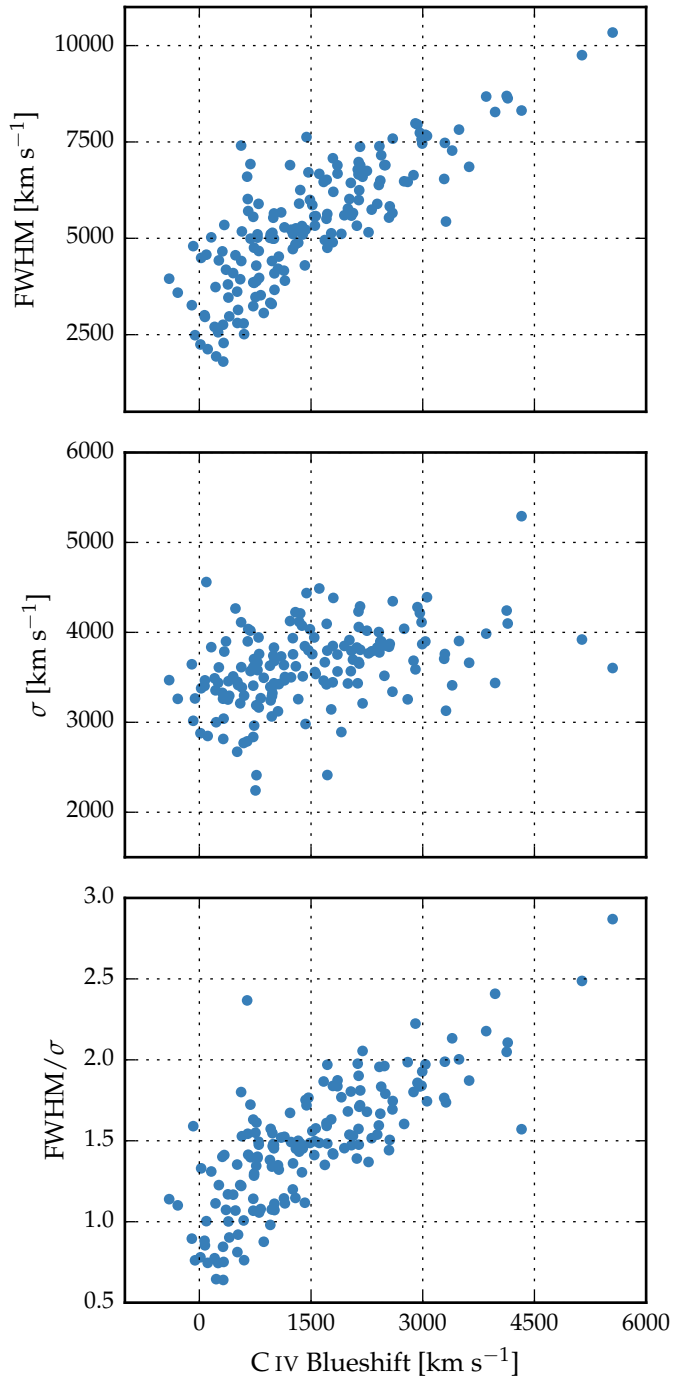


Figure 3.7: The FWHM, dispersion (σ) and shape (FWHM/ σ) of C IV as a function of the C IV blueshift.

motions do not dominate can be significant. Looking to the future, the results of the new reverberation-mapping projects (Shen et al., 2015; King et al., 2015) will show what fraction of the C IV-emission line, as a function of velocity, does reverberate for quasars with an extended range of C IV-emission shapes. The derivation of quantitative corrections to transform velocity-width measures from single-epoch to reverberation-only line profiles should then be possible.

As such information is not yet available, there is a strong rationale for investigating whether the systematic changes in the C IV-emission line profile can be used to improve the single-epoch BH-mass estimates derived using the C IV line. In Fig. 3.7 we show how the C IV FWHM, line dispersion, σ , and line shape, FWHM/ σ , vary as a function of the blueshift. The C IV FWHM is correlated with the blueshift, with the median FWHM of quasars with the largest blueshifts a factor of 2–3 higher than quasars with only moderate blueshifts. The dispersion, however, does not show a similarly strong systematic variation.

Without knowledge of the C IV-blueshifts, the dynamic range present in the FWHM and line dispersion measurements accords with the expectations from the study of Denney et al., (2013); the factor of $\simeq 4$ spread in the FWHM measurements indicating greater sensitivity to the emission-line profile shape than is the case for the dispersion, which varies by a factor of only $\lesssim 2$. Adopting a value of 1200 km s^{-1} to define ‘low’ and ‘high’ blueshift, the median C IV-emission dispersion for the low and high-blueshift samples differ by only 10 per cent. It follows, therefore, that while the dispersion provides a relatively line-profile independent measure of the velocity width for quasars where the underlying assumption regarding the virial-origin of the velocity width applies, quasars where the assumption is not true can be assigned apparently normal velocity-widths and hence potentially incorrect BH-masses.

To emphasise this point, in Fig. 3.8 we overlay the C IV line profiles of SDSSJ1236+1129 and SDSSJ1525+2928, whose dispersions are indistinguishable (4168 ± 271 and $4303 \pm 128 \text{ km s}^{-1}$ respectively). Notwithstanding the very similar dispersion values, the emission-line velocity fields differ dramatically and, therefore, the dispersion values cannot be measuring accurately the virial-induced velocity spread of the C IV emission in both quasars.

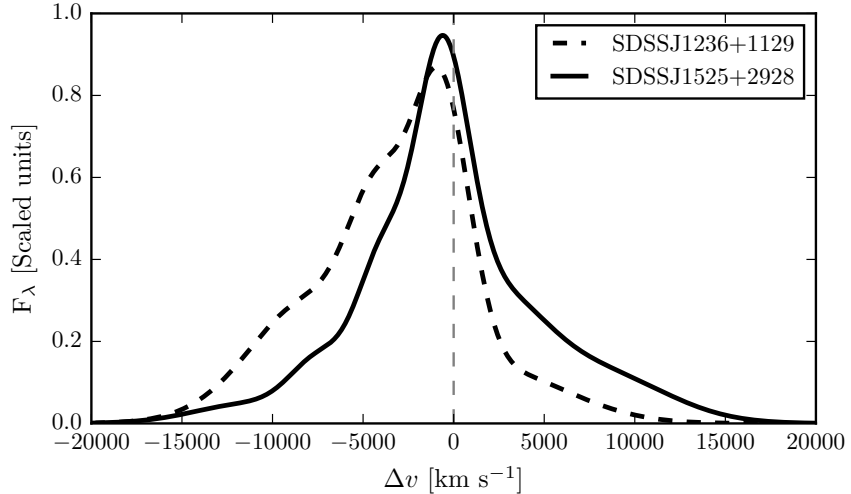


Figure 3.8: Comparison of the C IV line profiles of SDSSJ₁₂₃₆₊₁₁₂₉ and SDSSJ₁₅₂₅₊₀₄₂₆. Notwithstanding the essentially identical dispersion values, the emission-line velocity fields differ dramatically and, therefore, the dispersion values cannot be measuring accurately the virial-induced velocity spread of the C IV emission in both quasars.

The analysis here, building on earlier work (including Shen and Liu, 2012; Sulentic et al., 2007), confirms a link between C IV emission-line shape and blueshift, raising the prospect of developing a blueshift-dependent correction to single-epoch BH-mass estimates based on the C IV line. Expressed in another way, we are interested in testing if the significant systematic change in line shape as a function of C IV blueshift can be used to provide improved single-epoch BH-masses from the C IV emission line. The tightness of the correlation we observe between the C IV FWHM and blueshift implies that such an approach may be more effective than using the C IV emission-line velocity dispersion without reference to blueshifts. A further practical advantage is that, given the typical S/N of current survey-quality spectra, virial BH mass estimates for high-redshift quasars are usually based on the FWHM rather than the dispersion (e.g. Shen et al., 2011), which, being strongly affected by the continuum placement, is often found to be difficult to measure robustly (e.g. Mejía-Restrepo et al., 2016).

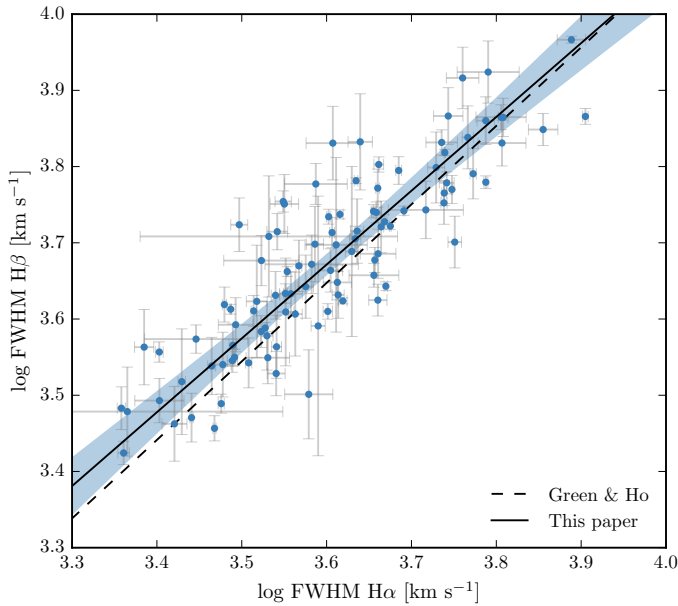


Figure 3.9: Comparison of H α and H β FWHM measurements for 99 quasars. The solid line is our best-fitting power-law model, and the blue-shaded region shows the 2- σ uncertainties on the model parameters. The dashed line is the relation found by Greene and Ho, (2005b) using a sample of $z < 0.35$ SDSS AGN.

3.4 AN EMPIRICAL CORRECTION TO C IV-BASED VIRIAL BH-MASS ESTIMATES

3.4.1 $H\alpha/H\beta$ FWHM comparison

BH-mass calibrations which use the width of the broad H β emission line as a proxy for the virial velocity are widely regarded as the most reliable, since most reverberation mapping employs the H β line and the R – L relation has been established using H β . When H β is not available, H α has been shown to be a reliable substitute (e.g. Greene and Ho, 2005b; Shen et al., 2011; Shen and Liu, 2012).

In our sample, we have 99 quasars with reliable measurements of both H α and H β lines. The 99 objects include 21 quasars which were excluded from the main 308-object catalogue because the CIV FWHM and/or blueshift could not be measured reliably. The line widths are compared in Fig. 3.9 and, as expected, a tight correlation is observed. Greene and Ho, (2005b), using a sample of 162 quasars with high S/N SDSS

spectra at $z < 0.35$, established the following relation between the H α and H β FWHMs

$$\text{FWHM}(\text{H}\beta) = (1.07 \pm 0.07) \times 10^3 \left(\frac{\text{FWHM}(\text{H}\alpha)}{10^3 \text{ km s}^{-1}} \right)^{(1.03 \pm 0.03)} \quad (3.1)$$

The relation is shown as the dashed line in Fig. 3.9. The root-mean-square scatter about this relation is 0.07 dex, compared to the ~ 0.1 dex found by Greene and Ho, (2005b). However, we find a systematic offset, in the sense that the H β line-widths we measure are on average larger by 270 km s^{-1} than predicted by the Greene and Ho, (2005b) relation. As our sample covers higher redshifts and luminosities than the sample in Greene and Ho, (2005b), we derive a new relation between the H α and H β FWHMs.

We assume a relation of the same form used by Greene and Ho, (2005b), i.e. a simple power-law, and infer the model parameters by fitting a linear model (with slope α and intercept β) in log-log space. The fit is performed within a Bayesian framework described by Hogg, Bovy, and Lang, (2010). Each data point is treated as being drawn from a distribution function that is a convolution of the projection of the point's covariance tensor, of variance Σ_i^2 , with a Gaussian of variance V representing the intrinsic variance in the data. The log-likelihood is then given by

$$\ln \mathcal{L} = - \sum_{i=1}^N \frac{1}{2} \ln \left[2\pi (\Sigma_i^2 + V) \right] - \sum_{i=1}^N \frac{\Delta_i^2}{2[\Sigma_i^2 + V]} \quad (3.2)$$

where Δ_i is the orthogonal displacement of each data point from the linear relationship. An advantage of this approach is that it allows a proper treatment of the measurement errors on both variables, which in this case are comparably large. The model also makes the reasonable assumption that there is an intrinsic scatter in the relationship between the variables that is independent of the measurement errors. Following the suggestion by Hogg, Bovy, and Lang, (2010), the linear model was parametrized in terms of (θ, b_\perp) , where θ is the angle the line makes with the horizontal axis and b_\perp is the perpendicular distance from the line to the origin. Uniform priors were placed on these parameters, and the Jeffreys prior (the inverse variance)

was placed on the intrinsic variance. The posterior distribution was sampled using a Markov Chain Monte Carlo (MCMC) method using the Python package emcee (Foreman-Mackey et al., 2013).

The one- and two-dimensional posterior distributions are shown in Fig. 3.10. The solid line in Fig. 3.9 is the maximum likelihood solution

$$\text{FWHM}(\text{H}\beta) = (1.23 \pm 0.10) \times 10^3 \left(\frac{\text{FWHM}(\text{H}\alpha)}{10^3 \text{km s}^{-1}} \right)^{0.97 \pm 0.05} \quad (3.3)$$

and the shaded region shows the 2σ uncertainties on the model parameters.

As discussed above, our relation is displaced to slightly higher H β FWHM than the Greene and Ho, (2005b) relation – the offset is 210km s^{-1} for a quasar with H α FWHM 4500km s^{-1} . We infer a power-law index that, although slightly shallower, is consistent with the Greene and Ho, (2005b) index within the quoted uncertainties. The intrinsic scatter in the data, σ_I , we infer from the fit is 0.04 dex. This is smaller than the total scatter seen in Fig. 3.9 (0.06 dex), which suggests that measurement errors make a significant contribution to the total scatter in the relation.

We constructed composite spectra of the H α and H β regions from 217 and 171 quasars respectively. Spectra were first de-redshifted to the quasar rest-frame, and then interpolated on to a common wavelength grid with a 1\AA resolution. The spectra were scaled by the mean flux in the interval $4700\text{-}5100\text{\AA}$ (H β) and $6400\text{-}6800\text{\AA}$ (H α). The composite was then defined as the median flux from all of the normalised spectra in each wavelength bin. The H α and H β lines in the composite spectra are shown in Fig. 3.11. The cores of the two lines are very similar, but H β has more flux in the wings of the line.

For 19 of the 99 quasars with H β and H α emission profiles, one of the two Gaussians used to reproduce the H β profiles has a FWHM greater than 2000km s^{-1} and a fractional contribution to the total H β broad line flux of >0.3 (Marziani et al., 2009; Marziani et al., 2013). Such a broad component is not seen in the H α profiles and the very broad H β -component may be an artifact of the fitting scheme. A particular issue for H β is the presence of Fe II emission, often at a significant level. Furthermore, additional lines could be contributing to the underlying continuum (e.g. the He I $\lambda\lambda 4922, 5017$ doublet; Véron, Gonçalves, and Véron-Cetty, 2002; Zamfir et al., 2010).

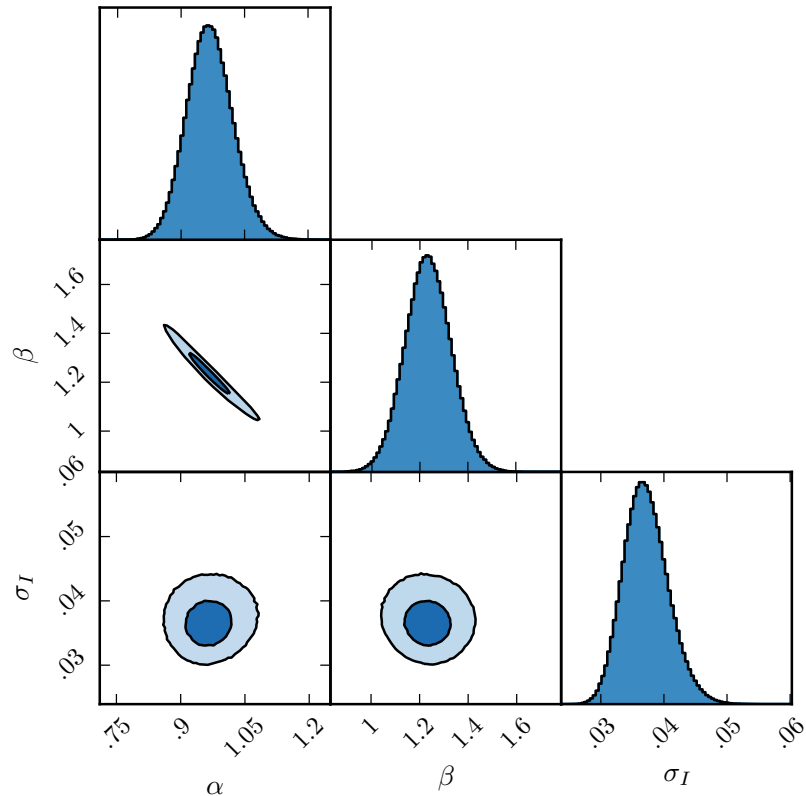


Figure 3.10: One- and two-dimensional projections of the MCMC sampling of the posterior distribution from the fit in Fig. 3.9. α is the power-law index, 10^β is the normalisation, and σ_I is the intrinsic scatter. In the two-dimensional projections, 1- and 2- σ contours are shown.

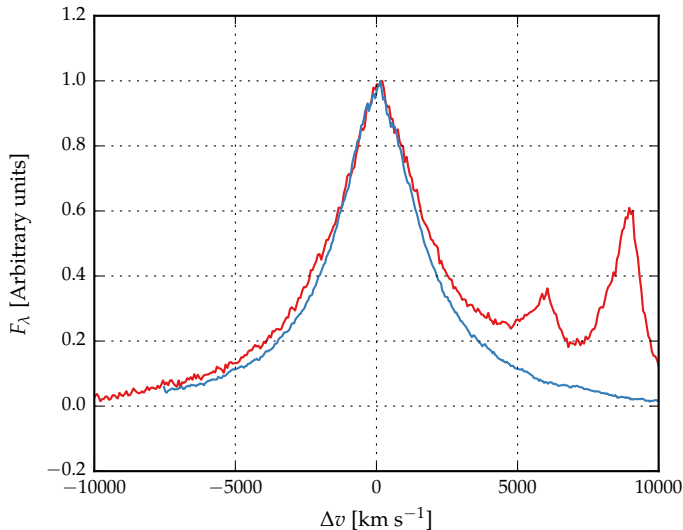


Figure 3.11: The H α (blue) and H β (red) emission line regions in the median composite spectrum, shown as function of the velocity shift from the respective predicted line peak wavelengths. The background continuum and optical Fe II emission has been modelled and subtracted. The line fluxes have been scaled in order for the profile shapes to be readily compared.

In Sec. 3.4.3 we use the whole of the H β profile to derive an un-biased BH mass. If, instead, the FWHM is calculated from the narrower of the two Gaussian components rather than the composite profile, then the H β FWHM decreases by 630km s^{-1} on average. This effectively removes the average offset to broad H β profiles evident in Fig. 3.9. This will enhance the C IV FWHM relative to the H α /H β FWHM by ~ 15 per cent and increase the size of the correction which must be applied to the C IV-based BH masses by ~ 30 per cent.

3.4.2 Measuring the quasar systemic redshift

An accurate measure of the quasar's systemic redshift is required in order for the blueshift of the C IV emission line to be determined. Balmer emission centroids are available for all quasars in the catalogue and so we use this to define the systemic redshift.

For 62 and 86 quasars in the H α and H β samples respectively narrow [O III] emission is also detected with sufficient S/N to measure the line properties. In the model fit to the H β region

the velocity centroids of the broad H β -line and the core component of the [O III] emission were deliberately determined separately. We find the intrinsic difference in the velocity centroids of the H α and H β emission and the narrow [O III] emission to have a dispersion of 300 and 400 km s $^{-1}$, which is very similar to the value found by Shen et al., (2016). However, the median velocity centroid of the narrow component of the [O III] emission is blueshifted by 250 km s $^{-1}$ relative to the centroid of the broad Balmer line. Applying our parametric model fitting routine to the composite spectrum from Hewett and Wild, (2010), which is constructed using relatively low redshift SDSS quasars with $L_{\text{Bol}} \sim 10^{44}$ erg s $^{-1}$, the centroids of the broad component of H β and the narrow component of [O III] are found to be at essentially identical velocities, suggesting that the blueshifting of narrow [O III] could be luminosity dependent.

As described in Section 3.3, the broad components of H α and H β were modelled with up to two Gaussians, with identical velocity centroids. If there is any significant asymmetry in these lines then the emission will be poorly fit by our model and the redshift derived from the peak of the best-fitting model could be biased. To investigate this possibility we relaxed the requirement for the centroids of the two broad Gaussians to be the same, and measured the systemic redshift from the peak of the composite profile. With this new, more flexible model, the mean absolute difference between the centroids of the two Gaussian components used to model H α and H β was 480 and 780 km s $^{-1}$ respectively. With these adjustments, we found the mean difference between the [O III]- and H α (H β) based redshift estimates to be -100(-120) km s $^{-1}$ and the scatter to be 290(320) km s $^{-1}$. Therefore, the shift between the Balmer and [O III] velocities is reduced, suggesting that there might be a \sim 100 km s $^{-1}$ systematic bias in our measurements of the quasar systemic redshift. Regardless, since both the systematic offset and the scatter are small in comparison to the dynamic range in C IV blueshifts, the blueshift-based empirical correction we will derive does not depend on whether the broad Balmer emission or the [O III] centroid is used to define the systemic redshift, or how the broad Balmer emission is parameterized.

Later, in section XX, we demonstrate how improvements in the estimation of systemic redshifts from ultraviolet quasar spectra means that it is now possible to quantify the distribution of C IV-blueshifts in the observed population as a whole.

Clearly, this is a crucial development in making a blueshift-based correction viable.

3.4.3 Balmer/C_{IV} line widths as a function of C_{IV}-blueshift

In this section we directly compare the C_{IV} and H α /H β line widths as a function of the C_{IV} blueshift. Because virial BH mass estimates are generally based on the H β FWHM, we first convert our H α FWHM measurements to equivalent H β FWHM using Eq. 3.3. In Figs. 3.12 and 3.13 we show the C_{IV} FWHM relative to both the (H β -scaled) H α FWHM and the H β FWHM, as a function of the C_{IV} blueshift.

Employing the same Bayesian fitting framework described in Section 3.4.1, we fit independent linear models to the C_{IV} FWHM relative to the H α and H β FWHM as a function of the C_{IV} blueshift. As before, our model has an additional parameter representing any intrinsic scatter in the relationship between the variables which is independent of measurement errors. We also tested a model where some fraction of the data points (which is free to vary) are drawn from an outlier distribution, represented by a broad Gaussian centered on the mean of the data. We found, however, that the inferred outlier fraction was very low (0.004, corresponding to ~ 0.7 data points) and so did not include such a component in our model.

In Fig. 3.14 we show the one- and two-dimensional projections of the posterior distribution from the linear fit to the FWHM C_{IV}/H α ratio. The projections from the FWHM C_{IV}/H β fit, which we do not show, have very similar appearances. In Fig. 3.12 we plot the maximum likelihood model and the 2σ uncertainties on the model parameters. The maximum likelihood line is given by

$$\text{FWHM}(\text{C}_{\text{IV}}, \text{Corr.}) = \frac{\text{FWHM}(\text{C}_{\text{IV}}, \text{Meas.})}{(0.41 \pm 0.02) \left(\frac{\text{C}_{\text{IV}} \text{Blueshift}}{10^3 \text{ km s}^{-1}} \right) + (0.62 \pm 0.04)} \quad (3.4)$$

for the C_{IV}/H α fit and

$$\text{FWHM}(\text{C}_{\text{IV}}, \text{Corr.}) = \frac{\text{FWHM}(\text{C}_{\text{IV}}, \text{Meas.})}{(0.36 \pm 0.03) \left(\frac{\text{C}_{\text{IV}} \text{Blueshift}}{10^3 \text{ km s}^{-1}} \right) + (0.61 \pm 0.04)} \quad (3.5)$$

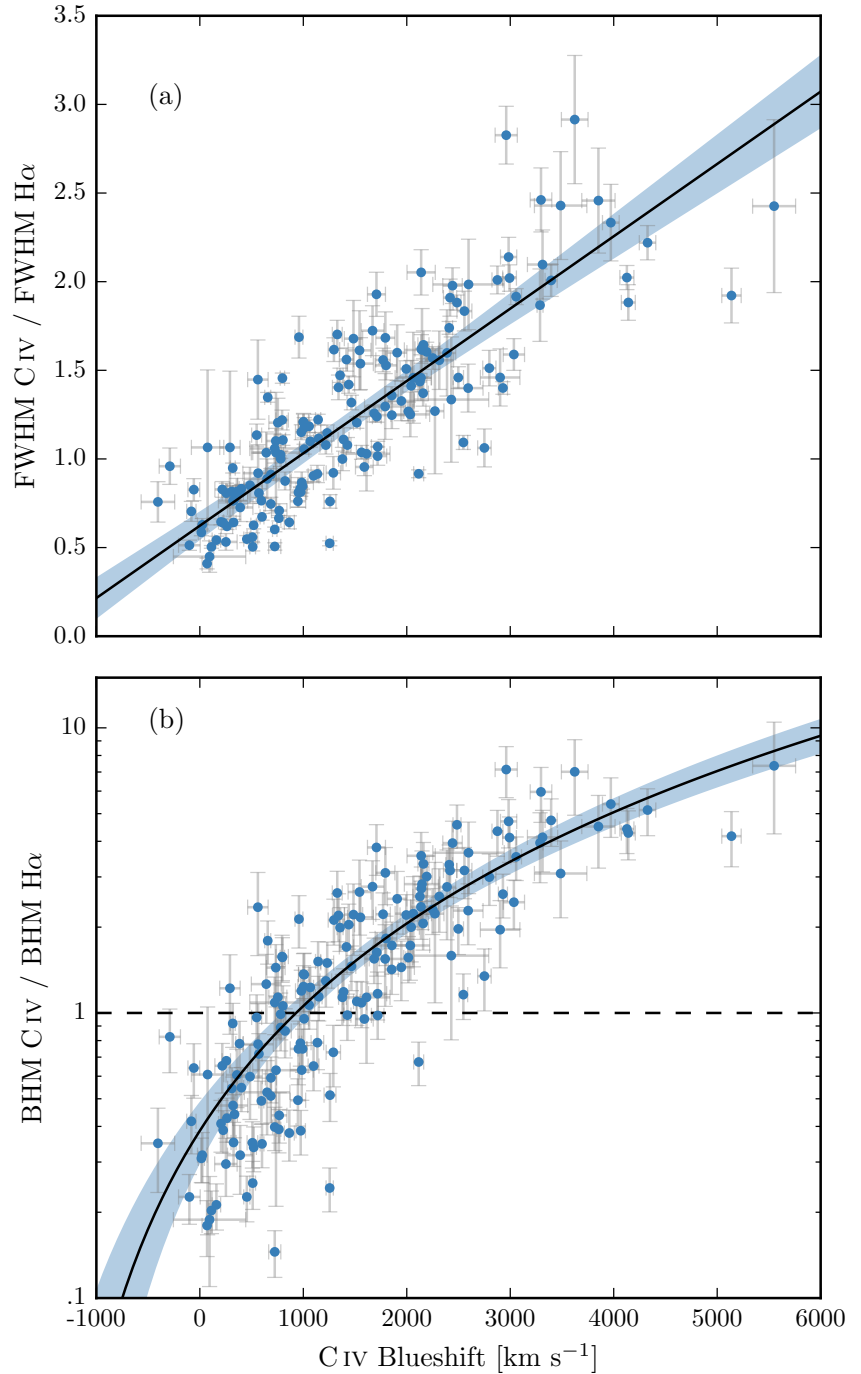


Figure 3.12: C IV FWHM relative to H α FWHM (a), and C IV based BH mass (BHM) compared to H α based mass (b), both as a function of the C IV blueshift. The black line is our best-fit linear model, and the shaded region shows the 2σ uncertainties on the slope and intercept. The H α FWHM have been scaled to match the H β FWHM using Eq. 3.3.

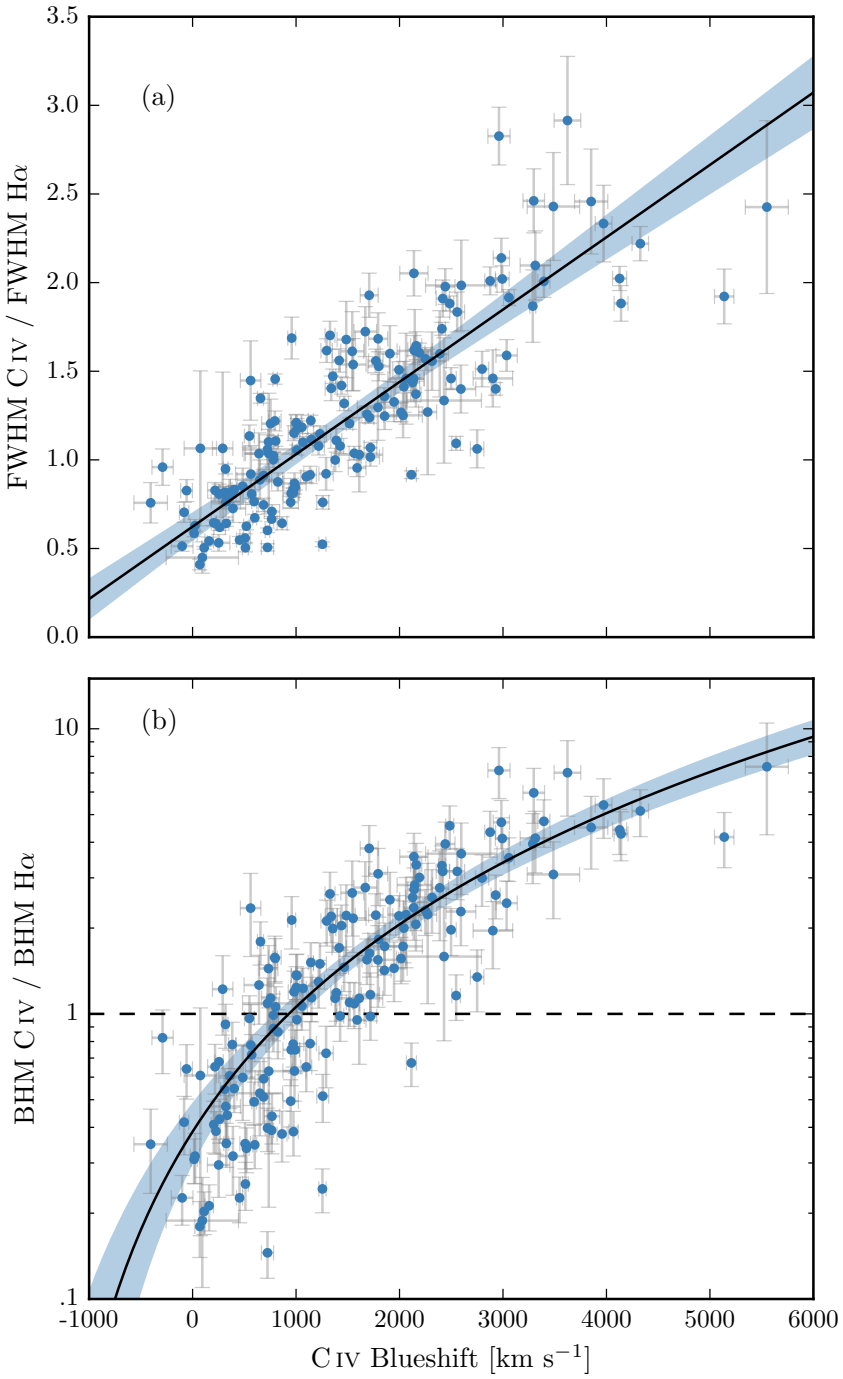


Figure 3.13: C IV FWHM relative to H β FWHM (a), and C IV based BH mass (BHM) compared to H β based mass (b), both as a function of the C IV blueshift.

for the C_{IV}/H β fit. The intercepts of the two relations are consistent, while the difference between the slopes is only marginally inconsistent given the quoted uncertainties.

The intrinsic scatter in the data about the linear relation we infer is 0.23 ± 0.02 and 0.25 ± 0.02 for the H α and H β fits respectively. The intrinsic scatter for the H α fit is represented by the Normal probability density distribution shown in Fig. 3.15. In the same figure we show the distribution of the orthogonal displacement of each data point from the best-fitting linear relationship. The two distributions are well-matched, which demonstrates that our model is a good representation of the data and the measurement errors on the data points are small relative to the intrinsic scatter.

The overall (intrinsic and measurement) scatter about the best-fitting model is slightly higher when the C_{IV} line-widths are compared to H β (0.12 dex) than when compared to H α (0.10 dex). This is likely due, at least in part, to the generally higher S/N of the H α emission. In addition, contributions from the strong [O III] doublet in the vicinity of H β make de-blending the H β emission more uncertain. As a consequence, for quasars where H α and H β are both measured, the mean uncertainty on the H α FWHM is 130km s^{-1} , compared to 340km s^{-1} for H β .

In the next section we use both the H α and H β lines to calculate unbiased BH masses. However, we use the H α measurements to derive an empirical C_{IV} blueshift based correction to the C_{IV} masses (Eq. 3.6) because of the issues related to the accurate modelling of the H β -profile just described. An extra advantage, which is evident in Figs. 3.12 and 3.13, is that the H α sample has a better C_{IV} blueshift coverage. However, as can be seen from the similarity of Equations 3.4 and 3.5, our results would not change significantly were we instead to use the H β sample.

3.4.4 C_{IV} based virial BH mass estimates

Virial BH masses were calculated using the widely adopted Vestergaard and Peterson, (2006) calibrations. The Vestergaard and Peterson, (2006) C_{IV} FWHM calibration uses the monochromatic continuum luminosity at 1350\AA to predict the BLR radius and corresponds to ($a = 6.66$, $b = 2$, $c = 0.53$) in Eq. 1.2. For the H β calibration, Vestergaard and Peterson, (2006) use the monochromatic continuum luminosity at 5100\AA and

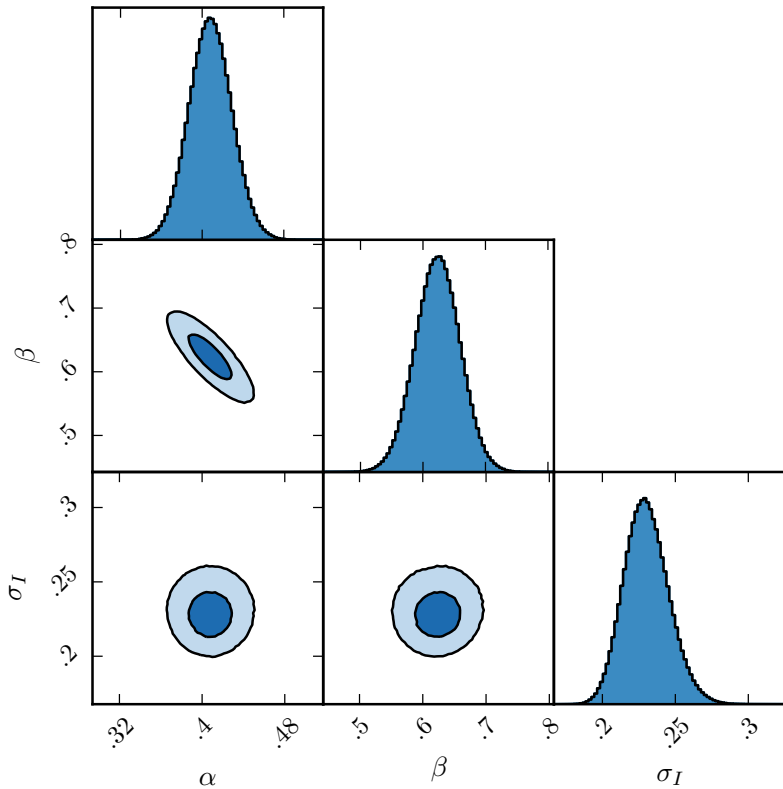


Figure 3.14: One- and two-dimensional projections of the MCMC sample of the posterior distribution for a linear fit to the FWHM C IV/H α ratio as a function of the C IV blueshift. In the two-dimensional projections we show 1- and 2- σ contours. The posterior distribution for the linear fit to the FWHM C IV/H β ratio, which we do not show, has a very similar appearance.

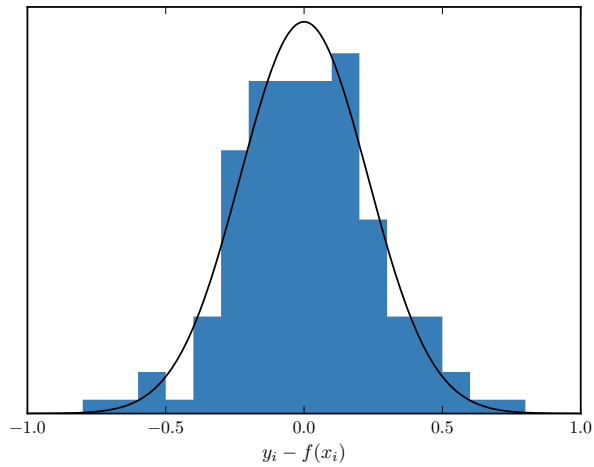


Figure 3.15: The distribution of the orthogonal displacement of each data point from the best-fitting linear relationship in the fit to $\text{FWHM}(\text{C IV})/\text{FWHM}(\text{H}\alpha)$ as a function of the C IV blueshift (blue histogram). The black curve is a Normal distribution with a width equal to the intrinsic scatter in the population inferred from the fit. The two distributions are well-matched, which demonstrates that our model is a good representation of the data and the measurement errors on the data points are small relative to the intrinsic scatter.

calibration coefficients corresponding to ($a = 6.91$, $b = 2$, $c = 0.5$). BH masses are computed using the line and continuum properties given in Table 4.3, and we convert our H α emission-line velocity-width measures to predicted H β widths using Eq. 3.3.

In the lower panels of Figs. 3.12 and 3.13 the C IV-based estimates are compared to the H α /H β estimates as a function of the C IV blueshift. There is a strong systematic error in the C IV-based masses as a function of blueshift, which is a direct consequence of the FWHM trend described in the previous section. The C IV emission-based BH-masses are in error by a factor of more than five at 3000km s^{-1} in C IV emission blueshift and the overestimate of the BH-masses reaches a factor of 10 for quasars exhibiting the most extreme blueshifts, $\gtrsim 5000\text{km s}^{-1}$.

The virial product is the product of the virial velocity squared and the BLR radius (e.g. Shen, 2013), and is proportional to the BH mass. We use the corrected C IV FWHM given by Eq. 3.4 as an indicator of the virial velocity, and adopt the same R – L relation for the 1350 Å continuum luminosity as Vestergaard and Peterson, (2006) (i.e. $R \propto L^{0.53}$). To find the constant scaling factor necessary to transform the virial product into a BH mass we compute the inverse-variance weighted mean difference between the virial products and the H α -based masses. The virial BH mass can then be expressed in terms of the corrected C IV FWHM and monochromatic continuum luminosity at 1350 Å

$$\text{MBH(C IV, Corr.)} = 10^{6.71} \left(\frac{\text{FWHM(C IV, Corr.)}}{10^3 \text{ km s}^{-1}} \right)^2 \left(\frac{\lambda L_\lambda(1350\text{\AA})}{10^{44} \text{ erg s}^{-1}} \right)^{0.53} \quad (3.6)$$

Given measured C IV emission line FWHM and blueshift, equations 4 and 6 can then be used to provide an unbiased estimate of the quasar BH mass.

3.4.5 C IV-derived BH masses at low C IV blueshift

In this section, we consider why the C IV based masses of quasars with modest C IV blueshifts ($\lesssim 1000\text{km s}^{-1}$) are systematically underestimated relative to masses derived from the Balmer lines (Figs. 3.12 and 3.13).

Might work better later in discussion.

Reverberation mapping measurements of nearby AGN have revealed the BLR to be stratified, with high-ionisation lines, including C IV, emitted closer to the BH than low-ionisation lines,

including H α and H β (e.g. Onken and Peterson, 2002). Vestergaard and Peterson, (2006) found that the C IV-emitting region is at approximately half the radius of the H β /H α emitting region. Given the $\Delta V \propto R_{\text{BLR}}^{-0.5}$ virial relation, this leads to the prediction that the C IV line widths should be $\simeq 1.4$ times broader than H α for a given BH mass. More recently, Denney, (2012) found that there is a significant contribution from gas at larger radii to the C IV emission line, enhancing the profile at lower-velocity and leading to smaller FWHM or dispersion values. The ratio of the line widths is therefore predicted to be lower than the factor of $\simeq 1.4$.

The H α and C IV FWHM of the 77 quasars with C IV blueshifts $< 1200 \text{ km s}^{-1}$ are linearly correlated, as expected if the dynamics of the BLR clouds are dominated by virial motions. The median C IV/H α FWHM ratio is 0.97 with standard deviation 0.31. Thus, as predicted by considering the contribution from low-velocity gas at large radii, the FWHM-based comparison results in a systematically lower median C IV/H α .

As a direct consequence of the empirically small C IV/H α FWHM ratio, the C IV-derived BH mass estimates are systematically lower than the corresponding H α -derived masses when the blueshift is small. This can be seen in Fig 3.12, where for almost every quasar with a C IV blueshift $< 1200 \text{ km s}^{-1}$, the C IV-derived BH mass is smaller than the corresponding H α -derived mass. The median fractional difference between the two estimates is 0.60.

3.5 PRACTICAL APPLICATION OF THE C IV-BASED CORRECTION TO VIRIAL BH-MASS ESTIMATES

3.5.1 Recipe for unbiased C IV based BH masses

3.5.1.1 Measuring the systemic redshift

Equations 4 and 6 together provide an un-biased estimate of the virial BH mass given the FWHM and blueshift of C IV, together with the continuum luminosity at 1350 Å. The FWHM is readily obtained, either directly from the data, or, via the fitting of a parametric model to the C IV-emission line. The blueshift – defined as the bisector of the cumulative line flux – is also straightforward to measure and our preferred procedure is described in Section 3.5.1.2. The only potential complication arises in establishing the quasar systemic redshift and hence defining

the zero-point for the C IV-blueshift measurement, since both the blueshift and the systemic redshift cannot be determined from C IV alone. In practice, when rest-frame optical lines are accessible, as is the case for the quasar sample here, an accurate systemic redshift can be obtained. The [O III] doublet and the Balmer lines all have velocity centroids very close to systemic, and the same is true for the broad Mg II doublet. For quasars at very high redshifts, $z \sim 6$, systemic redshifts can also be derived using the [C II] 158 μm emission in the sub-millimetre band (e.g. Venemans et al., 2016). However, in general, for example in determining the BH-masses of quasars at redshifts $z > 2$, if only the rest-frame ultraviolet region is available determining a reliable systemic redshift is non-trivial.

The SDSS DR7 pipeline redshifts are not sufficiently reliable to measure the C IV blueshift accurately because, in part, the C IV emission line itself contributes to the determination of the quasar redshifts. This is demonstrated in Fig. 3.16a, in which we plot the C IV-blueshift versus C IV-emission equivalent width (EW) using the SDSS pipeline redshifts and the blueshifts calculated by Shen et al., (2011). A strong trend in the blueshift values as a function of line EW is not evident in Fig. 3.16a; structure in the parameter space is being masked because the C IV emission line is itself being used in the determination of the quasar redshifts.

The redshift-determination scheme of Hewett and Wild, (2010) provided much improved redshifts, not least because the redshift estimates for the majority of quasars were derived using emission-lines other than the C IV-line itself. Figure 3.16b shows SDSS DR7 quasars in the same C IV parameter space as Figure 3.16a, but now using Hewett and Wild, (2010) redshifts. The improved redshift estimates are predominantly responsible for the differences seen in Fig. 3.16a and b; the appearance in Fig. 3.16b of the extension to high blueshift for quasars with low C IV EW is particularly evident.

Shen et al., (2016) and our own work shows that there is an intrinsic variation of $\sigma \approx 220 \text{ km s}^{-1}$ in the velocity centroids of the broad-line region relative to a systemic-frame defined by the quasar narrow-line regions. The redshifts for quasars in the SDSS DR10 and DR12 catalogues (Pâris et al., 2014; Pâris et al., 2017) possess errors of $\approx 500\text{-}750 \text{ km s}^{-1}$ (Pâris et al., 2012; Font-Ribera et al., 2013). The impact of low spectrum S/N for fainter quasars in all the SDSS data releases increases the uncertainty further. Table 3.4 includes the values for the fractional error

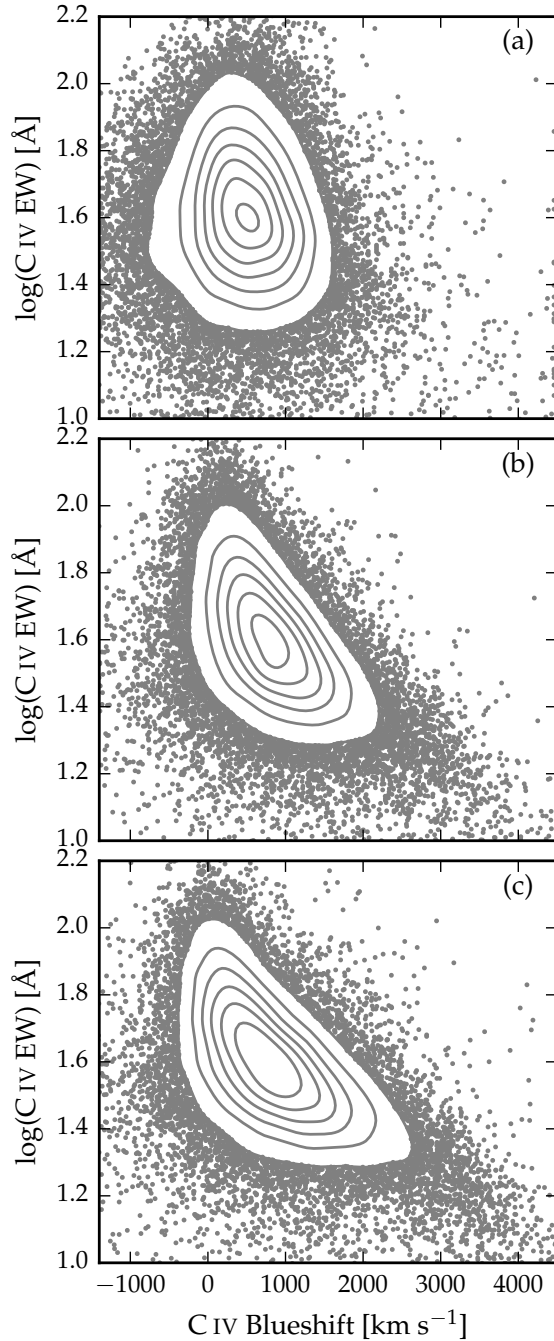


Figure 3.16: Rest-frame EW versus blueshift of the broad C_{IV} emission line for 32,157 SDSS DR7 quasars at $1.6 < z < 3.0$. Panel (a) uses C_{IV} line parameters from Shen et al., (2011) and SDSS pipeline systemic redshifts. Panels (b) and (c) use systemic redshifts from Hewett and Wild, (2010) and Allen & Hewett (2017, in preparation) respectively, and C_{IV} line measurements described in Sec. 3.5.1.2. In regions of high point-density, contours show equally-spaced lines of constant probability density generated using a Gaussian kernel-density estimator.

Table 3.4: The fractional error on the corrected BH mass as a function of C IV blueshift for different uncertainties in the quasar systemic redshift.

δv (km s^{-1})	C IV blueshift (km s^{-1})			
	0	1000	2000	4000
250	0.33	0.20	0.14	0.09
500	0.65	0.39	0.28	0.18
1000	1.30	0.79	0.57	0.36

in the corrected BH-mass that result from a given error in the determination of the systemic rest-frame. For example, the fractional error in the corrected BH mass is 0.39 for a quasar with a 1000 km s^{-1} C IV blueshift when there is a 500 km s^{-1} uncertainty in the quasar systemic redshift.

Of potentially more significance for studies of BH-masses as a function of quasar and host-galaxy properties are redshift errors that depend on the form of the quasar ultraviolet SED. The large systematic variation in the C IV emission-line profile within the population is evident from figures 11 and 12 of Richards et al., (2011). The plots and analysis in Richards et al., (2011) employ the quasar redshifts from Hewett and Wild, (2010) but, as is evident from the figures, the systematic variation in the C IV shape is correlated with changes in the quasar SEDs, including the strengths of the Si III $\lambda 1892$ and C III $\lambda 1908$ emission lines in the rest-frame ultraviolet. As a consequence, the redshifts from Hewett and Wild, (2010) still suffer from systematic errors that are correlated with the shape, and particularly the blueshift, of the C IV emission line. For the Hewett and Wild, (2010) redshifts, and ultraviolet emission-line based redshifts in general, quasars with large C IV EW and modest blueshifts have relatively small ($\simeq 300 \text{ km s}^{-1}$) SED-dependent redshift errors. Redshift uncertainties as large as $\simeq 1000 \text{ km s}^{-1}$ for such quasars are unusual and the large relative error in the corrected C IV BH-mass given in Table 3.4 is pessimistic.

Conversely, systematic redshift errors are greatest for quasars with large blueshifts, reaching $\sim 750 \text{ km s}^{-1}$ in the extreme for the Hewett and Wild, (2010) values. The associated error in the corrected C IV BH-masses is, however, mitigated somewhat due to the smaller gradient of the MBH(C IV)/MBH(Balmer) relation at large C IV blueshift (see Figs. 3.12 and 3.13). A definitive

quantification of any systematic SED-dependent errors present in the quasar redshifts contained in the SDSS DR12 catalogue is not yet available but the principal component analysis (PCA) based redshift estimates are expected to be largely free of SED-dependent systematics.

Using published redshift estimates, notably those from Hewett and Wild, (2010) for the SDSS DR7 quasars and the BOSS PCA-based redshifts from Pâris et al., (2017) for SDSS DR12, the correction formula given in Section 3.4.3 produces significant improvements to C_{IV}-based BH mass estimates. In a forthcoming work, Allen & Hewett (in preparation) will present a new redshift-estimation algorithm that produces redshifts independent of the C_{IV} blueshift and other variations in the ultraviolet SEDs of luminous quasars. The low-ionization emission lines visible in the rest-frame ultraviolet (over wavelengths from Mg II $\lambda\lambda 2796, 2803$ down to the O I $\lambda 1304$ +Si II $\lambda 1307$ blend) using the new redshift-algorithm are located at rest-frame wavelengths in excellent agreement with the systemic redshift defined using the rest-frame narrow-line optical O III doublet and broad-line H β and H α . SED-dependent systematic errors are below the apparent inherent dispersion of $\simeq 220 \text{ km s}^{-1}$ associated with broad emission line redshifts (Shen et al., 2016).

Figure 3.16c shows the C_{IV} emission line parameters calculated using the Allen & Hewett redshift-estimation algorithm. The systematic trends seen in Fig. 3.16b, in particular the extension to high blueshift at low C_{IV} EW, become more apparent in Fig. 3.16c, as expected from consideration of the known SED-related errors in the redshifts from Hewett and Wild, (2010). A population of quasars with only modest blueshifts and low EW is also apparently still present.

3.5.1.2 C_{IV} emission line blueshift measurements

The differences in the distribution of C_{IV} emission line properties seen in the three panels of Fig. 3.16 are due primarily to the change in the systemic redshift estimates. It is also necessary, however, to obtain a measure of the C_{IV} emission line ‘location’ in order to calculate the blueshifts. When working with moderately-sized samples, parametric fits to the emission-line profile may be undertaken using careful mask-definition to minimise the effect of absorption features on the profiles used

for the parametrization, and this is the approach we followed in Section 3.3.

Effective analysis of the tens of thousands of spectra from SDSS DR7, and now DR12, however, requires a more robust scheme to determine a C IV-blueshift estimate that is not very sensitive to the range of S/N among the spectra or the presence of narrow absorption systems within the C IV-emission profile. Shen et al., (2011) provide a discussion (their section 3) of the factors that effect the measurement of broad emission lines in quasar spectra of modest S/N. Their careful analysis of the C IV emission properties employed the results of parametric fits of three Gaussians to the spectra. Our own experiments in quantifying the C IV emission properties of SDSS spectra showed that a simple non-parametric measure of the C IV emission location reduced the number of outliers significantly. Visual inspection of spectra demonstrated that the improvement is due primarily to the identification of, and interpolation over, associated and outflow absorption systems, which forms part of the non-parametric measurement scheme.

We therefore chose to use a non-parametric scheme to measure the blueshift of the C IV line, which we will now describe. A continuum is first defined as a power-law of wavelength, $f(\lambda) \propto \lambda^{-\alpha}$, with the slope, α , determined using the median⁴ values of the flux in two continuum windows at 1445–1465 and 1700–1705Å (the same wavelengths as adopted by Shen et al., (2011)). The C IV emission line is taken to lie within the wavelength interval 1500–1600Å, a recipe that is commonly adopted (e.g. Shen et al., 2011; Denney et al., 2013). To reduce the impact of narrow absorption systems on the emission-line profile a ‘pseudo continuum’ is defined by applying a 41-pixel median filter to the quasar spectrum. Pixels within the C IV profile that lie more than 2σ below the pseudo-continuum are deemed to be affected by absorption and added to an ‘absorber’-mask. Two pixels on either side of each such pixel are also included in the mask. For each masked pixel, the flux values in the spectrum are replaced by values from the pseudo-continuum. The wavelength that bisects the cumulative total line flux is recorded and the blueshift is defined in exactly the same way as in Section 3.3.

Allen & Hewett will publish improved redshifts for all quasars in the SDSS DR7 and DR12 catalogues. At the same time we will publish catalogues of unbiased BH masses for both

⁴ The median is used to improve the robustness of the continuum estimate from the relatively small wavelength intervals.

SDSS DR7 and DR12 based on the Allen & Hewett redshifts. The components from the mean-field independent component analysis (see Allen et al., 2013, for an application to astronomical spectra) used in the Allen & Hewett redshift algorithm will also be published. With these components, if a rest-frame ultra-violet spectrum is available, it will be straightforward to determine the systemic redshift, via a simple optimisation procedure, and hence calculate the C IV blueshift.

3.5.2 Systematic trends in residuals

The scatter about the best-fitting line in the C IV/H α FWHM versus C IV-blueshift relation is ~ 0.1 dex, an order of magnitude smaller than the size of the C IV-blueshift dependent systematic but, nevertheless, still significant. With a view to reducing the scatter further, we searched for measurable parameters which correlate with the scatter at fixed C IV blueshift, including the luminosity, redshift, [O III] equivalent width (EW), and Fe II EW. The only significant correlation we find is with the H α FWHM (Fig. 3.17). Quasars with broad H α lines tend to lie below the relation while quasars with narrow H α tend to lie above it. One possibility is that this correlation is simply due to random scatter (either intrinsic or measurement error) in the H α FWHM which, with the other quasar properties fixed, would naturally produce a correlation between FWHM(C IV)/FWHM(H α) and FWHM(H α). However, the fact that we see no such correlation between the model residuals and the C IV FWHM suggests that the H α FWHM correlation could be revealing something more fundamental. The H α /H β FWHM is part of ‘eigenvector 1’ (EV1), the first eigenvector in a principal component analysis which originated from the work of Boroson and Green, (1992). While a number of parameters have been considered within the EV1 context (e.g. Brotherton and Francis, 1999), Fig. 3.17 suggests that part of the scatter between the Balmer and C IV velocity widths might be attributed to differences in the spectral properties which are correlated with EV1 (Marziani et al., 2013).

The shape of the line can be characterised by the ratio (FWHM/ σ , where σ is the dispersion, derived from the second moment velocity; e.g. Kollatschny and Zetzl, 2011; Kollatschny and Zetzl, 2013). FWHM/ $\sigma \simeq 2.35$ for a Gaussian pro-

file, while $\text{FWHM}/\sigma \simeq 1$ for a peakier Lorentzian profile⁵. In our sample, we find the residuals and the H α FWHM correlate with the shape of the line. The narrow lines are, on average, ‘peakier’ (with $\text{FWHM}/\sigma \simeq 1$) than the broader lines (with $\text{FWHM}/\sigma \simeq 2$). The origin of the Balmer-line shape correlation is not clear but one possibility is an orientation-dependence of the H α FWHM (e.g. Shen and Ho, 2014). In this scenario quasars with broader emission lines are more likely to be in an edge-on orientation relative to our line of sight.

At radio wavelengths, the morphology of the radio structure, parametrized in terms of ‘core dominance’ is believed, at least in a statistical sense, to be a proxy for the orientation of the accretion disk (e.g. Jackson and Browne, 1991). Twenty core- quasars and six lobe-dominated quasars were identified in our sample, but no statistically significant differences in the H α line-widths of the two samples were found. It should be noted that the sub-sample of radio-detected quasars is small and the effectiveness of the test is further compromised by the lack of radio-detected quasars at large blueshifts (see figure 14 of Richards et al., 2011, for example).

Maybe include: On the other hand, a concern is raised by the observation that the BLR structure changes with emission-line FWHM (Kollatschny & Zetzl 2011). They show that FWHM/σ is a strong, smooth function of FWHM. These changes in line profile shapes suggest that the balance between rotation, random velocities, and in- or outflow changes with line width. Hints of this were seen in earlier work (Collin et al. 2006; Marziani & Sulentic 2012).

There are currently very few reverberation-mapping measurements of quasars with large C IV blueshifts. Looking to the future, the results of the large on-going statistical reverberation mapping projects (e.g. Shen et al., 2015; King et al., 2015) for luminous quasars at high-redshift will shed new light on the Balmer line emitting region of the BLR for quasars with a range of C IV blueshifts and lead to a greater understanding of the relation between the Balmer line profile and the BH mass.

*I think I mentioned
this earlier so okay
to delete there.*

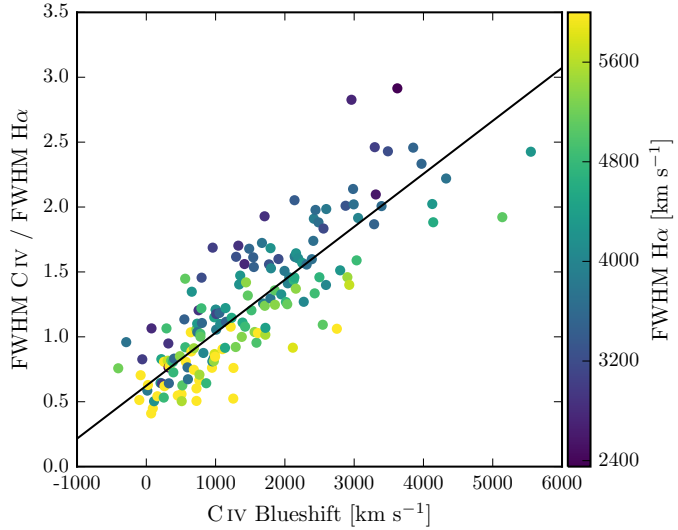


Figure 3.17: Same as Fig. 3.12a, with the marker colour representing the $\text{H}\alpha$ FWHM. At fixed CIV blueshift, there is a clear $\text{H}\alpha$ FWHM dependent systematic in the model residuals.

3.5.3 Effectiveness of the CIV blueshift based correction to BH masses

Figure 3.18 demonstrates that our sample has an excellent coverage of the EW-blueshift parameter space in relation to SDSS DR7 quasars at redshifts $1.6 < z < 3.0$. The systematic offset to higher CIV blueshifts for our catalogue relative to the SDSS quasars as a whole is a result of the higher mean luminosity relative to the SDSS sample (Fig. 2.1). Our sample includes 21 quasars with CIV blueshifts $> 3000 \text{ km s}^{-1}$, and extends to $\sim 5000 \text{ km s}^{-1}$, i.e. at the very extreme of what is observed in this redshift and luminosity range. Our investigation thus demonstrates that the CIV -blueshift based correction derived in this chapter is applicable to very high blueshifts. Conversely, there are no quasars in our catalogue with CIV blueshifts $\lesssim 0 \text{ km s}^{-1}$ and we caution against extrapolating the correction formula to negative blueshifts.

Figure 3.19 compares the CIV - and $\text{H}\alpha$ -based BH masses before and after applying the blueshift-based correction to the CIV FWHM. Before the correction, the correlation between the CIV - and $\text{H}\alpha$ -based BH masses is very weak, and the scatter

⁵ Strictly $\text{FWHM}/\sigma \rightarrow 0$ for a Lorentzian profile, but values close to unity are typical when the dispersion is calculated over a velocity range, $\simeq \pm 10000 \text{ km s}^{-1}$, used to parametrize broad emission lines in quasar spectra.

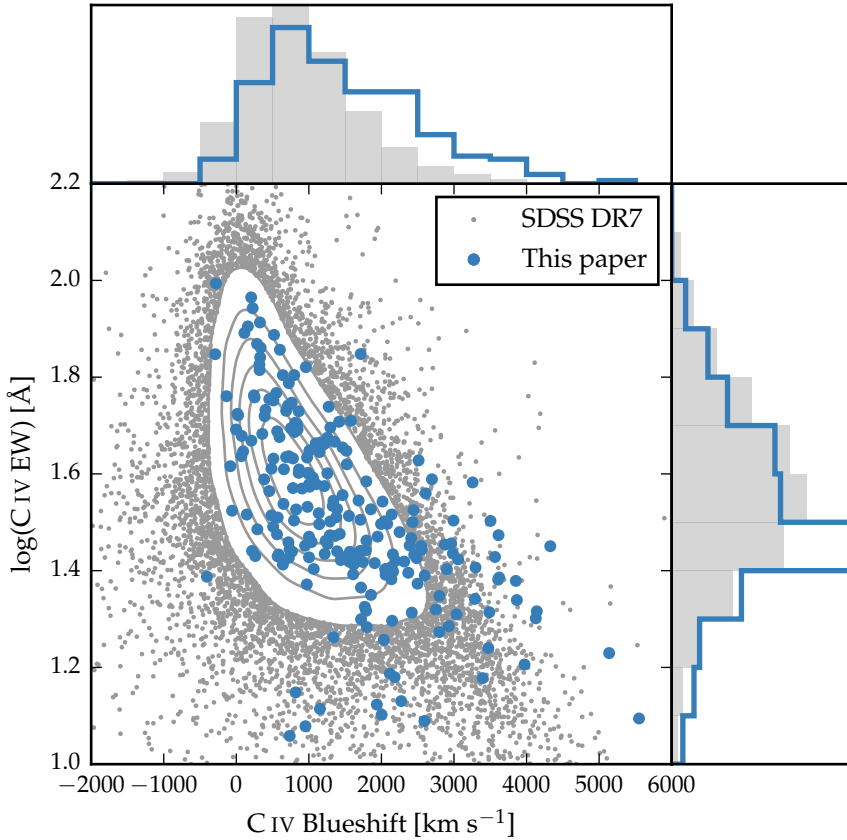


Figure 3.18: Rest-frame EW versus blueshift of the broad C_{IV}-emission line for 32,157 SDSS DR7 quasars at $1.6 < z < 3.0$ (grey) and our sample (blue). For the SDSS quasars, the systemic redshifts used to calculate the blueshifts are from Hewett and Wild, (2010) and C_{IV} emission properties are described in Paper I. In regions of high point-density, contours show equally-spaced lines of constant probability density generated using a Gaussian kernel-density estimator. Our sample has very good coverage; the shift to high blueshifts is a result of the high luminosity of our sample in relation to the SDSS sample and the correlation between luminosity and blueshift.

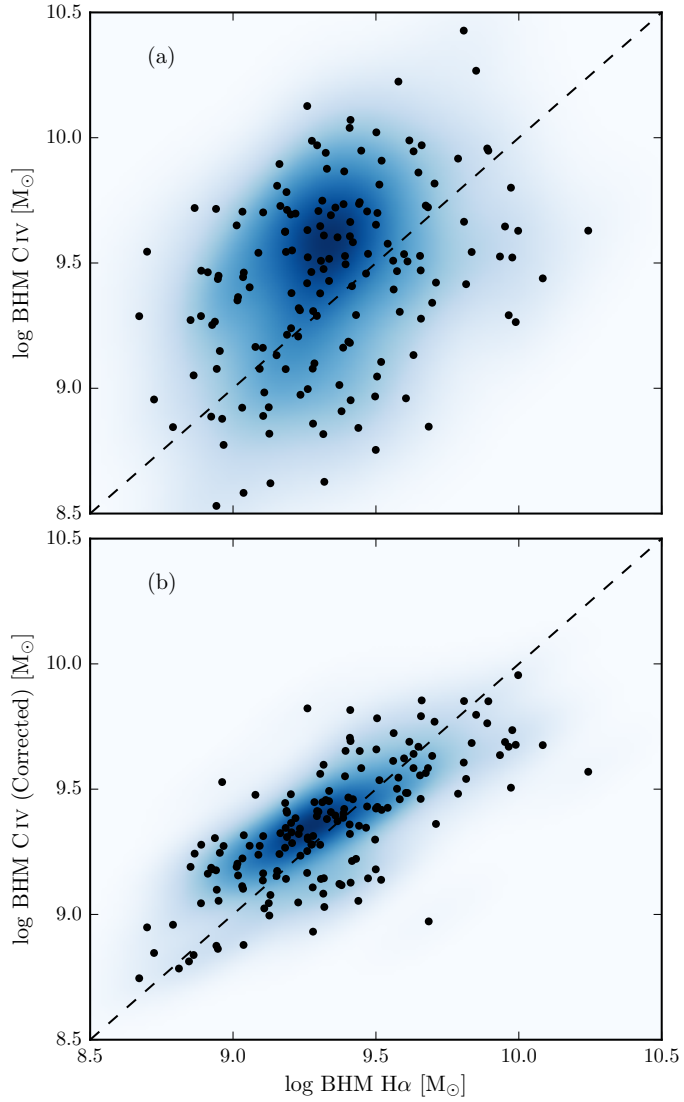


Figure 3.19: Comparison of the CIV- and H α -based BH masses before (a) and after (b) applying the CIV blueshift-based correction to the CIV FWHM. The density of the plotted points (estimated using a Gaussian kernel density estimator) is represented by the colour. The correction to the CIV BH masses decreases the scatter by from 0.4 to 0.2 dex. **Should definitely include some empirical validation of ICA redshifts since that is what we are telling people to use.**

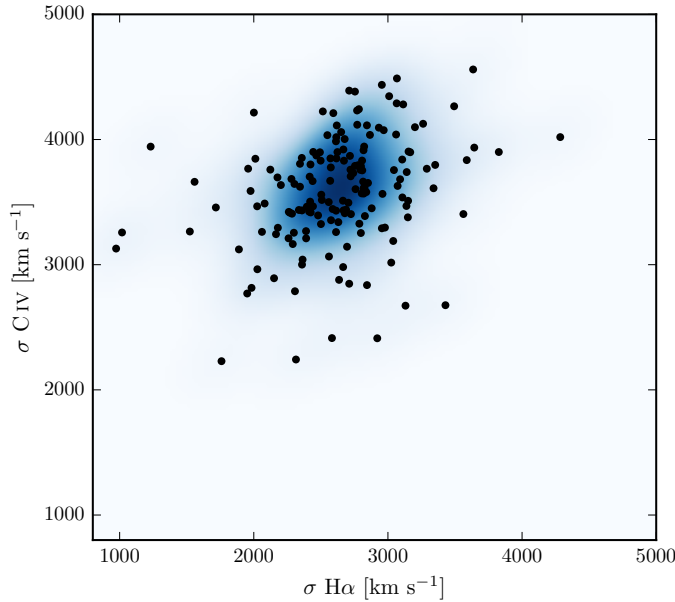


Figure 3.20: Comparison of the C_{IV} and H α line dispersion, σ . The density of the plotted points (estimated using a Gaussian kernel density estimator) is represented by the colour. Estimating a reliable BH mass from the C_{IV} FWHM and blueshift line is substantially more effective than using the C_{IV} line dispersion with, or without, the line blueshift. The C_{IV} dispersion values are larger than the corresponding H α measurements by a factor of 1.4 on average, which is consistent with reverberation mapping measurements (Vestergaard and Peterson, 2006).

between the masses is 0.4 dex. After correcting the C_{IV} FWHM for the non-virial contribution, the correlation improves dramatically. The scatter between the corrected C_{IV}-based masses and the H α -based masses is reduced to 0.2 dex. The scatter is 0.24 dex at low C_{IV} blueshifts ($\sim 0 \text{ km s}^{-1}$) and 0.10 dex at high blueshifts ($\sim 3000 \text{ km s}^{-1}$).

There has been a considerable amount of attention regarding the relative merits of using the FWHM or dispersion to characterise the velocity width (e.g. Denney et al., 2013). The existence of a trend in the C_{IV}-dispersion values with C_{IV} blueshift is evident from inspection of the bottom left panel of Fig. 3.7 but the systematic trend relative to the spread at fixed blueshift is significantly smaller than when using C_{IV} FWHM. Therefore, without the blueshift information, using the line dispersion would yield a more accurate BH mass than the FWHM (Fig. 3.20).

The correlation between the $H\alpha$ and $C\text{IV}$ line dispersion is, however, weak. The Pearson coefficient for the correlation is 0.36 (and just 0.15 when the $H\beta$ measurements are used in place of $H\alpha$). Furthermore, there is little dynamic range in the line dispersion: the scatter is just 480 and 460 km s^{-1} for $H\alpha$ and $C\text{IV}$ respectively. The observation suggests that the line dispersion does not fully trace the dynamic range in BH mass present in the quasar population. At least part of the reason is that the line dispersion is difficult to measure reliably in current survey-quality data, particularly because of the sensitivity to flux ascribed to the wings of the emission line (e.g. Mejía-Restrepo et al., 2016). Figures 3.19 and 3.20 demonstrate that estimating a reliable BH mass from the $C\text{IV}$ FWHM and blueshift line is substantially more effective than using the $C\text{IV}$ line dispersion with, or without, the line blueshift.

3.5.4 Comparison to previous prescriptions

In Fig. 3.21 we compare the $C\text{IV}$ blueshift-based correction presented in this chapter to various prescriptions which have been proposed in the literature to derive BH masses from the $C\text{IV}$ line which are consistent with the masses derived from the Balmer lines. In each case we compare the corrected $C\text{IV}$ -based masses to the $H\alpha$ -based masses as a function of the $C\text{IV}$ blueshift. The correction proposed by Runnoe et al., (2013a) is based on the spectral region at rest-frame wavelengths of $\sim 1400 \text{ \AA}$ (see below). Therefore, our analysis is based on the 123 quasars with spectra covering this region.

In Fig 3.21a the $C\text{IV}$ BH masses have been corrected using the $C\text{IV}$ shape (FWHM/σ) based correction proposed by Denney, (2012). Denney, (2012) found the level of contamination in single-epoch spectra from non-reverberating gas to be correlated with the shape (FWHM/σ) of the $C\text{IV}$ profile. In our sample, we observe a strong correlation between the shape of the $C\text{IV}$ line and its blueshift (Fig. 3.7); between the two extremes in the $C\text{IV}$ blueshift distribution the line shape changes from $\text{FWHM}/\sigma \sim 1$ to 2.5. The investigation of Denney, (2012) was based on a sample of reverberation mapped quasars, which have a narrow range of $C\text{IV}$ -emission line shapes, including the absence of any objects with large $C\text{IV}$ blueshifts. The correction is not applicable at large $C\text{IV}$ blueshifts. Therefore, while the consistency between the $H\alpha$ - and $C\text{IV}$ -based masses at low $C\text{IV}$

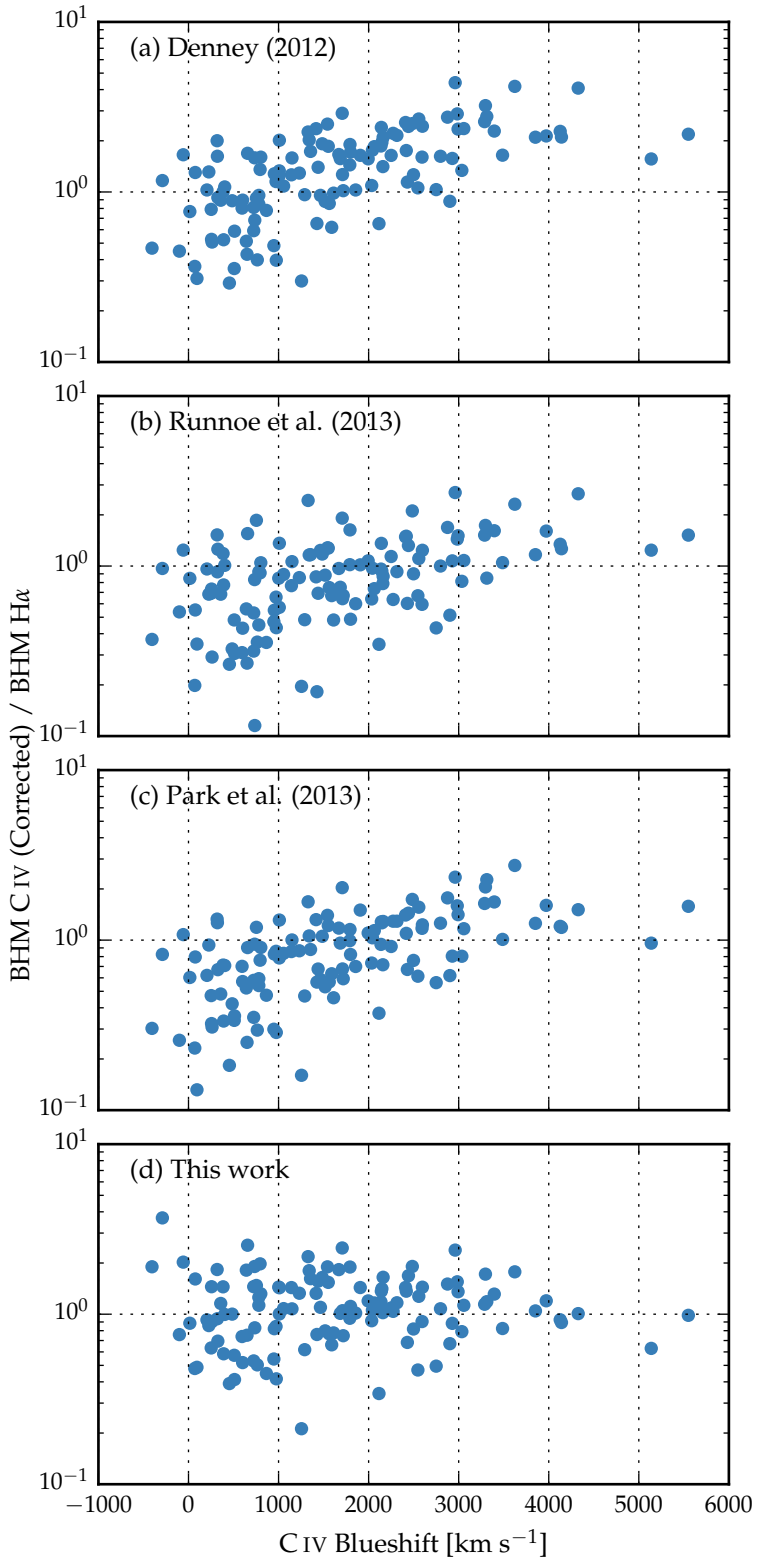


Figure 3.21: Comparison of BH mass estimates derived from C IV and H α as a function of the C IV blueshift. Corrections to the C IV-based masses have been applied based on the shape (FWHM/ σ) of the C IV emission line (a; Denney, 2012), the peak flux ratio of the Si IV+O IV blend relative to C IV (b; Runnoe et al., 2013a), by significantly reducing the dependence of the derived BH mass on the C IV velocity-width (c; Park et al., 2013), and based on the C IV blueshift (d; this chapter).

blueshifts is improved, at high C_{IV} blueshifts the C_{IV}-based masses remain seriously overestimated.

As explained above, reliably measuring the quasar systemic redshift from the UV region of the spectrum has proved difficult. However, the situation is improved dramatically by the new scheme developed by Allen & Hewett (2017, in preparation). Given the difficulty of measuring reliable C_{IV} blueshifts without the Allen & Hewett scheme, Runnoe et al., (2013a) opted instead to use the continuum-subtracted peak flux ratio of the ultraviolet emission-line blend of Si_{IV}+O_{IV} (at 1400 Å) to that of C_{IV} to correct for non-virial contributions to the C_{IV} velocity width. This parameter was chosen because it showed the strongest correlation with the FWHM C_{IV}/H β residuals, as well as with the strengths of optical O_{III} and Fe_{II}.

Following Runnoe et al., (2013a), we measure the peak flux by fitting a model with four Gaussian components (two for each emission line) to the continuum-subtracted flux. As is evident from Fig. 3.18, a correlation exists between the blueshift and equivalent width of C_{IV}: C_{IV} emission which is strongly blueshifted is typically weak. The Si_{IV}+O_{IV} emission-line blend, however, shows significantly less systematic variation. Therefore, the Si_{IV}+O_{IV}-based correction is quite effective in practice: the systematic bias in the C_{IV} BH masses at large C_{IV} blueshifts is reduced to a factor of ~ 2 (Fig. 3.21b). However, the C_{IV} based masses are still systematically overestimated at large C_{IV} blueshifts.

In contrast to the widely-used Vestergaard and Peterson, (2006) C_{IV}-based virial BH mass calibration, the more recent Park et al., (2013) calibration significantly reduces the dependence of the derived masses on the emission-line velocity width (from the V^2 dependence predicted assuming a virialized BLR to just $V^{0.56}$). As a consequence, the C_{IV} based masses of the quasars with large C_{IV} blueshifts are much reduced (Fig. 3.21c). However, the systematic error in the C_{IV}-based BH masses as a function of C_{IV} blueshift remains.

As a comparison, the C_{IV}-based masses shown in Fig 3.21d have been corrected using to the C_{IV} blueshift-based procedure presented in this chapter. No systematic in the BH masses as a function of the C_{IV} blueshift is evident.

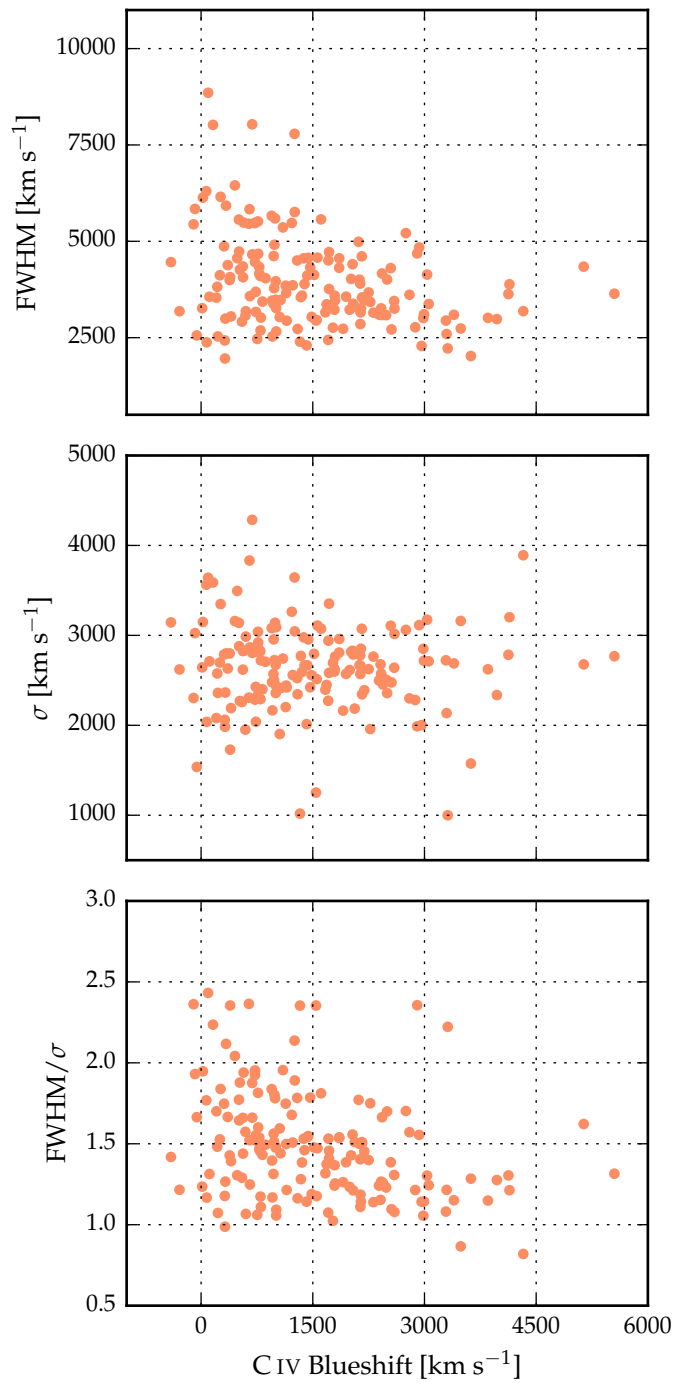


Figure 3.22: The FWHM, dispersion (σ) and shape (FWHM/ σ) of H α as a function of the C IV blueshift.

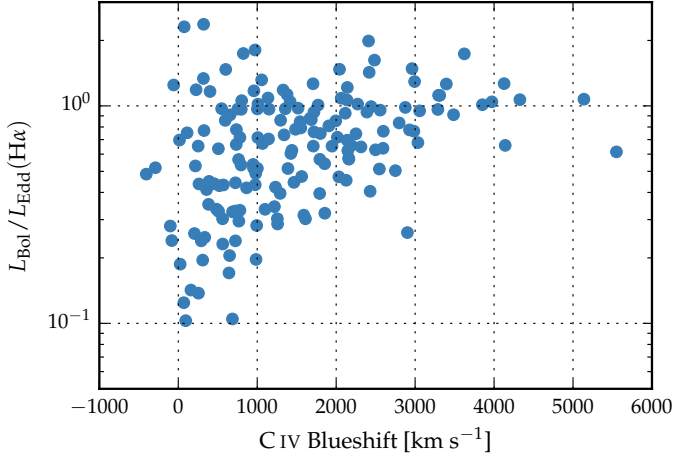


Figure 3.23: H α -derived Eddington ratio versus C IV blueshift. At blueshift $\gtrsim 2000 \text{ km s}^{-1}$ all quasars have high accretion rates ($L/L_{\text{Edd}} \simeq 1$). This is in agreement with Kratzer and Richards, (2015), but in contrast to what one would derive from naive use of C IV-based BH mass scaling relations.

3.6 POPULATION TRENDS WITH C IV BLUESHIFT

As shown in Fig. 3.22, there are systematic variations in the H α line profile as a function of the C IV blueshift. At C IV-blueshift $< 1200 \text{ km s}^{-1}$, the H α FWHM range is $\simeq 2000 - 8900 \text{ km s}^{-1}$, with mean $\simeq 4300 \text{ km s}^{-1}$. However, amongst the quasars with C IV-blueshift $> 2000 \text{ km s}^{-1}$, the mean H α FWHM = 3500 km s^{-1} , with a scatter of just 700 km s^{-1} . The apparent trend of peakier H α -emission, with FWHM/ σ close to unity, at large C IV-blueshift is enhanced by the modest increase in H α EW with blueshift. Amongst the low-C IV-blueshift population there are in addition quasars with broader and more Gaussian-like H α line profiles, with FWHM/ $\sigma \simeq 2$.

The change in the H α emission-line profiles as a function of C IV-blueshift means that the H α -FWHM derived BH masses at high-blueshift are smaller than the sample mean. We transformed the observed luminosity into a mass-normalised accretion rate (Eddington ratio). To convert the monochromatic luminosity, which is observed, in to a bolometric luminosity we use the bolometric correction factor given by Richards et al., (2006a) ($L_{\text{bol}} = 9.26L_{5100}$). Although there is evidence that the bolometric correction factor is a function of the luminosity, as well as of other parameters including the C IV blueshift (Krawczyk et

al., 2013), the differences are small over the parameter range covered by our sample, and for simplicity we adopt a constant factor.

The results, shown in Fig. 3.23, demonstrate that at large blueshifts quasars are accreting at around their Eddington limits (Fig. 3.23). This finding is in accord with our interpretation that the blueshifting of C IV is evidence for strong outflows resulting from the presence of a radiation-driven accretion-disc wind. Richards et al., (2002) found that quasars with large C IV blueshifts have weak He II. This is evidence for weak soft X-ray continuum emission (Leighly, 2004), which would allow a strong line-driven wind to form. The strength of such a wind is predicted to be related to the quasar far-ultraviolet SED, which, in turn, could be related to the mass-accretion rate.

All of the objects in our sample which exhibit large C IV blueshifts would be classified as population A in the Sulentic et al., (2000) scheme based on the H α FWHM. Our results therefore support the idea of the Sulentic et al., (2000) A/B division being driven by the Eddington ratio, with population A sources possessing higher accretion rates. However, we also observe a number of quasars which have high Eddington ratios but do not have line profiles suggestive of strong outflows in the C IV BLR. This suggests that a high accretion rate is a necessary but not sufficient condition for the existence of outflows (Baskin and Laor, 2005a).

The two-dimensional nature of the C IV emission line parametrization and the apparent anti-correlation between C IV EW and C IV blueshift suggests that the quasar population exhibits a continuum of properties. As such, more accurate C IV blueshift measurements for SDSS-quasars should allow an improved mapping between the C IV-emission properties and key physical parameters of the quasars. This includes improving our understanding of the origin of quasars with exceptionally weak, blueshifted C IV emission (weak emission line quasars; Luo et al., 2015) which could be exotic versions of wind-dominated quasars (Plotkin et al., 2015).

3.6.1 Systematic biases in Balmer-based masses

The interpretation described in the preceding section requires some caution since the emission-line shape (characterized by the value of FWHM/ σ) of H α is also changing as a function of the C IV blueshift (Fig. 3.22). At low C IV blueshifts there are

a range of shapes, but all of the quasars exhibiting large C_{IV} blueshifts have peaky H α profiles with FWHM/ $\sigma \simeq 1$. This raises the question of whether the H α FWHM is a reliable proxy for the virial-induced velocity dispersion for the full range of H α line shapes we have in our sample.

*Can move most of
this to earlier
section on residuals
and then refer back
to that.*

When calibrating the virial-product to masses derived independently using the BH mass – stellar velocity dispersion ($M_{\odot} - \sigma$) relation, Collin et al., (2006) find that the scaling factor, f , is a factor ~ 2 larger for their Population ‘1’ sources (with FWHM/ $\sigma < 2.35$ and essentially equivalent to population A of Sulentic and co-workers and to the high-blueshift quasars here) than for their Population 2 (with FWHM/ $\sigma > 2.35$). For single-epoch BH-mass estimates, assuming a constant value of f , as is normally done (e.g. Vestergaard and Peterson, 2006), means that Population 1 masses will be underestimated and Population 2 will be overestimated. In the context of this result from Collin et al., (2006), our high-blueshift objects all possess peaky H α -lines and, while our quasar sample probes much higher luminosities and masses, the true BH-masses may also be underestimated. Adopting such an interpretation, the amplitude of the trend seen in Figs. 3.12 and 3.13 might not be so pronounced.

As mentioned in Section 1 and discussed in Richards et al., (2011), quasars with current reverberation mapping measurements have a restricted range of C_{IV}-line shapes. There are currently very few reverberation-mapping measurements of quasars with large C_{IV} blueshifts but the results of the large on-going statistical reverberation mapping projects (e.g. Shen et al., 2015) for luminous quasars at high-redshift will go some way to establishing whether the quasar broad line regions producing Balmer emission look the same for objects with very different C_{IV}-emission blueshifts.

Although the EV1-trends (Sulentic et al., 2000; Shen and Ho, 2014) are most likely driven by the accretion rate, orientation may also have a role to play in determining the observed properties of the BLR. Shen and Ho, (2014) argue that a large part of the scatter observed in the H β FWHM relates not to a spread in BH masses, but rather to the orientation of the BLR relative to the line-of-sight. For this to be true, the BLR would need to be in a flattened disc-like geometry, in which case the observed line width would increase with the inclination of the disc relative to the line of sight. Brotherton, Singh, and Runnoe, (2015) found that the core-dominance of radio-loud quasars, which

is believed to be a reliable proxy for orientation, at least in a statistical sense, is significantly correlated with the H β FWHM and hence with the BH-mass estimates. This raises the question of whether the narrow H α emission lines observed in the quasars with the largest C IV blueshifts could be an orientation effect. However, there is no evidence that the C IV blueshift is dependent on the orientation (inferred from the radio core-dominance; Richards et al., 2011; Runnoe et al., 2014). Furthermore, Leighly, (2004) showed that the He II λ 1640 emission-line properties of quasars with large C IV blueshifts are more consistent with differences in the SED rather than differences in the orientation. Collin et al., (2006) showed that orientation effects were also sub-dominant to the Eddington ratio in determining the shape of the H β line and the H α line shape trend we observe is consistent with the finding of Marziani et al., (2003) that the H β emission profiles of high/low Eddington ratio low- z quasars and type 1 Seyfert nuclei are well fit by Lorentzian and double Gaussian profiles respectively. Overall, therefore, orientation does not appear to be the dominant effect in determining the C IV blueshift and correlated changes in the H α line profile.

3.6.2 *The BAL parent population*

Classical high-ionization BAL (HiBAL) quasars are also predominantly Population A objects in the scheme of Sulentic et al., (2000). There are no HiBAL quasars in our sample by design but it is generally accepted that quasars which show high-ionisation BALs are likely to be radiating with relatively high L/L_{Edd} (e.g. Zhang et al., 2014). We therefore propose that the subset of the quasar population that exhibits large C IV-emission blueshifts, with high-EW and narrow-H α emission lines, may be directly related to the HiBAL quasar population – perhaps even the ‘parent’ population (Richards, 2006). A prediction of such a linkage is that near-infrared observations of the rest-frame optical spectra of HiBAL quasars will show strong, relatively narrow, Balmer emission lines, very similar to those of the quasars with high C IV-blueshifts presented in this chapter (see Runnoe et al., 2013b, for such a study).

*Do I actually say
BALs are removed
from sample?*

*I must have a few
BALs. Make a
composite spectra of
Balmer lines of
BALs?*

3.6.3 *The frequency of quasars with high accretion rates*

Quantifying the frequency of quasars producing outflows as a function of key parameters, e.g. quasar luminosity, BH-mass, redshift,... will be important to constrain models of quasar-galaxy evolution. At fixed BH mass, the intrinsic and the observed fraction of quasars exhibiting properties that depend on the Eddington ratio can differ significantly. As an illustration, we consider the implications for the intrinsic fraction of quasars possessing large C IV blueshifts given the observed numbers in the $m_i < 19.1$ flux-limited sub-sample of the SDSS DR7 quasar catalogue. In order to estimate the size of the selection effect, we considered the detection probability for a much-simplified quasar population. We assume that all quasars with C IV blueshifts $> 1200 \text{ km s}^{-1}$ have enhanced accretion rates relative to the ‘normal’ population (with C IV blueshifts $< 1200 \text{ km s}^{-1}$). If the accretion rate of the high-blueshift population is double the rate of the low-blueshift population (which is true in an average sense – see Fig. 3.23), then the high-blueshift population will be brighter by $\simeq 0.75$ magnitude. Under the assumption that the BH mass distribution is independent of the C IV blueshift, the high-blueshift population will then be over-represented in a flux-limited sample. To estimate the size of the bias, we need to know how many more quasars, at redshifts $2 < z < 2.5$, there are with $m_i < 19.1 + 0.75 = 19.85$ relative to $m_i < 19.1$. This is the fraction of the population which, as a consequence of having enhanced accretion rates, are boosted above the survey flux limit. The main colour-selected SDSS DR7 quasar catalogue extends only to $m_i = 19.1$ and, assuming the luminosity function is continuous⁶ we thus use the number counts at $m_i < 19.1$ and $m_i < 18.35$, which differ by a factor of $\simeq 4$.

At redshifts $2 < z < 2.5$, there are 3,834 quasars with C IV blueshifts $< 1200 \text{ km s}^{-1}$ and 2,484 with blueshifts $> 1200 \text{ km s}^{-1}$ in the SDSS DR7 $m_i < 19.1$ quasar sample, a ratio of $\sim 2:1$. The above calculation, although much idealised, suggests that the intrinsic fraction of high-blueshift quasars is a factor of four smaller than in the flux-limited sample (i.e. ~ 15 per cent of the ultraviolet-selected non-BAL quasar population).

⁶ The luminosity function and number-counts vary only smoothly (e.g. Ross et al., 2013) for the magnitude and redshift range used here.

3.7 CONCLUSIONS

The main results of this chapter are as follows:

- We have analysed the spectra of 230 high-luminosity ($10^{45.5} - 10^{48}$ erg s $^{-1}$), redshift $1.5 < z < 4.0$ quasars for which spectra of the Balmer emission lines and the C IV emission line exist. The large number of quasars in our spectroscopic catalogue and the wide range in C IV blueshifts the quasars possess has allowed us to directly investigate biases in C IV-based BH mass estimates which stem from non-virial contributions to the C IV emission as a function of the C IV blueshift, which, in turn, depends directly on the form of the quasar ultraviolet SEDs (Richards et al., 2011).
- The C IV emission-based BH-masses are systematically in error by a factor of more than five at 3000 km s $^{-1}$ in C IV emission blueshift and the overestimate of the BH-masses reaches a factor of 10 for quasars exhibiting the most extreme blueshifts, $\gtrsim 5000$ km s $^{-1}$.
- We have derived an empirical correction formula for BH-mass estimates based on the C IV emission line FWHM and blueshift. The correction may be applied using equations 4 and 6 in Section 3.4.3. The large SED-dependent systematic error in C IV-based BH-masses is removed using the correction formulae. The remaining scatter between the corrected C IV-based masses and the H α -based masses is 0.24 dex at low C IV blueshifts (~ 0 km s $^{-1}$) and 0.10 dex at high blueshifts (~ 3000 km s $^{-1}$). This is a significant improvement on the 0.40 dex scatter observed between the un-corrected C IV and H α BH masses. The correction depends only on the C IV line properties - i.e. the FWHM and blueshift - and allows single-epoch virial BH mass estimates to be made from optical spectra, such as those provided by the SDSS, out to redshifts exceeding $z \sim 5$.

3.8 FUTURE WORK

- Clustering
- Data-driven mapping

3.9 DESCRIPTION OF CATALOGUE

2 Unique ID: QSOXXX.

LogMBH_Ha, LogMBH_Ha_Err

Edd_Ratio_Ha, Edd_Ratio_Ha_Err

LogMBH_Hb, LogMBH_Hb_Err

Edd_Ratio_Hb, Edd_Ratio_Hb_Err

LogMBH_CIV_VPo6, LogMBH_CIV_VPo6_Err

Edd_Ratio_CIV_VPo6, Edd_Ratio_CIV_VPo6_Err

Add corrected BH mass

FWHM_Broad_Ha, FWHM_Broad_Ha_Err

Sigma_Broad_Ha, Sigma_Broad_Ha_Err

EQW_Broad_Ha, EQW_Broad_Ha_Err

LogL_Broad_Ha, LogL_Broad_Ha_Err

FWHM_Broad_Hb, FWHM_Broad_Hb_Err

Sigma_Broad_Hb, Sigma_Broad_Hb_Err

EQW_Broad_Hb, EQW_Broad_Hb_Err

LogL_Broad_Hb, LogL_Broad_Hb_Err

z_Broad_Ha. Repeated in chapter 4 with slightly different model.

z_Broad_Hb. Repeated in chapter 4 with slightly different model.

WARN_Ha (Remove 2, just flag 1 as low S/N)

RedChi_Ha

WARN_Hb (Remove 2, just flag 1 as low S/N)

RedChi_Hb

FWHM_CIV_BEST, FWHM_CIV_BEST_Err (remove best, make sure it's clear where it comes from) (Just give BEST values then note of which optical spectrum was used).

Sigma_CIV_BEST, Sigma_CIV_BEST_Err

Median_CIV_BEST, Median_CIV_BEST_Err

EQW_CIV_BEST, EQW_CIV_BEST_Err

LogL_CIV_BEST, LogL_CIV_BEST_Err

Max_CIV_BEST, Max_CIV_BEST_Err

Max_1400_BEST, Max_1400_BEST_Err

1400_CIV_BEST, 1400_CIV_BEST_ERR

RedChi_CIV_BEST

WARN_CIV_BEST (will have removed warn=2, so should just be warn=1 low S/N flag)

WARN_1400_BEST (remove 1400 max if warn=2)

Blueshift_CIV_Ha, Blueshift_CIV_Ha_Err

Blueshift_CIV_Hb, Blueshift_CIV_Hb_Err

4

NARROW LINE REGION PROPERTIES

4.1 INTRODUCTION

X-ray and UV spectroscopy has revealed high velocity outflows to be nearly ubiquitous in high accretion rate AGN. Models of galaxy evolution that invoke AGN feedback require these outflows to reach galactic scales and quench star formation in the AGN host galaxies. In recent years, a huge amount of resources have been devoted to searching for observational evidence of these galaxy-wide, AGN-driven outflows. This has resulted in recent detections of outflows in AGN-host galaxies using tracers of atomic, molecular, and ionised gas (e.g. Nesvadba et al., 2006; Arav et al., 2008; Nesvadba et al., 2008; Moe et al., 2009; Dunn et al., 2010; Alexander et al., 2010; Harrison et al., 2012; Harrison et al., 2014; Nesvadba et al., 2010; Rupke and Veilleux, 2013; Veilleux et al., 2013; Nardini et al., 2015; Feruglio et al., 2010; Alatalo et al., 2011; Cimatti et al., 2013; Cicone et al., 2014).

One particularly successful technique has been observing forbidden emission lines, which trace warm ($T \sim 10^4$ K) ionised gas in the AGN NLR. Because of its high equivalent width, [O III] $\lambda 5008$ is the most studied of the narrow AGN emission lines. In general, the [O III] emission consists of two distinct components: a narrow, ‘core’ component, with a velocity close to the systemic redshift of the host galaxy, and a broader ‘wing’ component, which is normally blueshifted. The general consensus is that the core component traces the gravitational potential of the host galaxy, as the width correlates well with the stellar velocity dispersion. On the other hand, the broad, blueshifted wing is tracing outflowing gas. This emission appears blueshifted because the far-side of the outflow - that is, the side which is moving away from the line of sight - is obscured (e.g. Heckman et al., 1981; Vrtilek, 1985).

Observations of broad velocity-widths and blueshifts in narrow emission lines stretch back several decades (e.g. Weedman, 1970; Stockton, 1976; Heckman et al., 1981; Veron, 1981; Feldman et al., 1982; Heckman, Miley, and Green, 1984; Vrtilek, 1985; Whittle, 1985; Boroson and Green, 1992). However, these studies rely on small samples, which are often unrepresentative of

the properties of the population. More recently, the advent of large optical spectroscopic surveys (e.g. SDSS) have facilitated studies of the NLR in tens of thousands of AGN (e.g. Boroson, 2005; Greene and Ho, 2005a; Zhang et al., 2011; Mullaney et al., 2013; Zakamska and Greene, 2014; Shen and Ho, 2014). This has provided constraints on the prevalence and drivers of ionised outflows. At the same time, there is strong evidence from spatially resolved spectroscopic observations that these outflows are extended over galaxy scales (e.g. Greene et al., 2009; Greene et al., 2011; Hainline et al., 2013; Harrison et al., 2012; Harrison et al., 2014).

However, these studies do not cover the redshift range when star formation and BH accretion peaked, and consequently when feedback is predicted to be strongest. At these redshifts the bright optical emission lines are redshifted to near-infrared wavelengths, where observations are much more challenging. As a consequence, studies at high redshifts have typically relied on relatively small numbers of objects (e.g. Netzer et al., 2004; Sulentic et al., 2004; Shen, 2016). These studies find [O III] to be broader in more luminous AGN, suggesting that AGN efficiency in driving galaxy-wide outflows increases with luminosity (e.g. Netzer et al., 2004; Nesvadba et al., 2008; Kim et al., 2013; Brusa et al., 2015; Carniani et al., 2015; Perna et al., 2015; Bischetti et al., 2016). The fraction of objects with very weak [O III] emission also appears to increase with redshift and/or luminosity (e.g. Netzer et al., 2004).

Other recent studies have looked at the [O III] emission properties of extreme objects - e.g. heavily obscured quasars (Zakamska et al., 2016) and the most luminous quasars (Bischetti et al., 2016) - at redshifts $z \sim 2$. The [O III] emission in these objects is extremely broad and strongly blueshifted. These observations are consistent with galaxy formation models that predict AGN feedback to be strongest in luminous, dust-obscured quasars.

In this chapter we analyse the [O III] properties of a sample of 354 high-luminosity, redshift $1.5 < z < 4$ quasars. This is the largest study of the NLR properties of high redshift quasars ever undertaken.

4.2 QUASAR SAMPLE

From our near-infrared spectroscopic catalogue (Chapter 2), we have selected 354 quasars which have spectra covering the strong, narrow [O III] doublet. The broad Balmer H β line is

Table 4.1: The numbers of quasars with [O III] line measurements and the spectrographs and telescopes used to obtain the near-infrared spectra.

Spectrograph	Telescope	Number
FIRE	MAGELLAN	31
GNIRS	GEMINI-N	28
ISAAC	VLT	7
LIRIS	WHT	7
NIRI	GEMINI-N	29
NIRSPEC	Keck II	3
SINFONI	VLT	80
SOFI	NTT	76
TRIPLESPEC	ARC-3.5m	27
TRIPLESPEC	P200	45
XSHOOTER	VLT	21
Total		354

also observed for all but two of the sample. In 165, the spectra extend to the broad H α emission line at 6565Å, and in 260 optical spectra including C IV are also available (mostly from SDSS/BOSS). The sample covers a wide range in redshifts ($1.5 \lesssim z \lesssim 4$) and luminosities ($45.5 \lesssim \log L_{\text{Bol}} \lesssim 49$ erg s $^{-1}$). The spectrographs and telescopes used to obtain the near-infrared spectra are summarised in Table 4.1.

4.3 PARAMETRIC MODEL FITS

In this section, we describe how parameters of the [O III] emission are derived. Our approach is to model the spectra using a power-law continuum, an empirical Fe II template and multiple Gaussian components to model the emission from the broad and narrow components of H β and the [O III] doublet. Non-parametric emission line properties are then derived from the best-fitting model. This approach, which is commonly adopted in the literature (e.g. Shen et al., 2011; Shen and Liu, 2012; Shen, 2016), is more robust when analysing spectra with limited S/N (in comparison to measuring line properties directly from the data) and allows different emission lines to be de-blended.

The same approach was used to model the H β /[O III] complex in Chapter 3. However, a number of small adjustments have been made to the model (Section 4.3.3). H α emission line properties (used in this Chapter to estimate the quasar systemic redshift) are also re-derived using a slightly modified model (Section 4.3.5). C IV emission line properties (used to infer the strength of BLR outflows) are taken directly from Chapter 3.

4.3.1 Redshift transformation

Before a spectrum can be modelled, it must first be transformed to the quasar rest-frame. The redshift used in this transformation is either derived from the peak of the broad H α emission (\sim 40 per cent of our sample), from the peak of the broad H β emission (\sim 40 per cent) or from the peak of the narrow [O III] emission (20 per cent). The rest-frame transformation is only required to be accurate to within \sim 1000km s $^{-1}$ for our fitting procedure to work. In later sections, more precise estimates of the systemic redshift will be calculated using our parametric model fits.

4.3.2 Removal of Fe II emission

Fe II emission is generally strong in the vicinity of H β /[O III]. Therefore, before H β /[O III] is modelled, we first model and subtract the continuum and Fe II emission using the procedure described in Chapter 3.

We encountered 24 objects for which Fe II emission appears to be present in the spectrum even after the subtraction procedure (Figure ??). In these objects the relative strengths of the Fe II lines differ significantly from those of I Zw 1, on which the Fe II template we use is based. The residual Fe II emission is at rest-frame wavelengths very close to zero-velocity wavelengths of the [O III] doublet, which is generally very weak in these objects. The Gaussians we fit to the spectra to model [O III] are therefore strongly biased, and the [O III] emission properties we infer from the model are in error by large factors.

For example, J223819-092106 was analysed by Shen, (2016) using a very similar model. Shen, (2016) reported the [O III] emission in this object to be shifted by \sim 7500km s $^{-1}$ relative to the Hewett and Wild, (2010) systemic redshift. Our analysis suggests that emission which was modelled by Shen, (2016) as [O III] is more likely to be [poorly-subtracted Fe II emission.

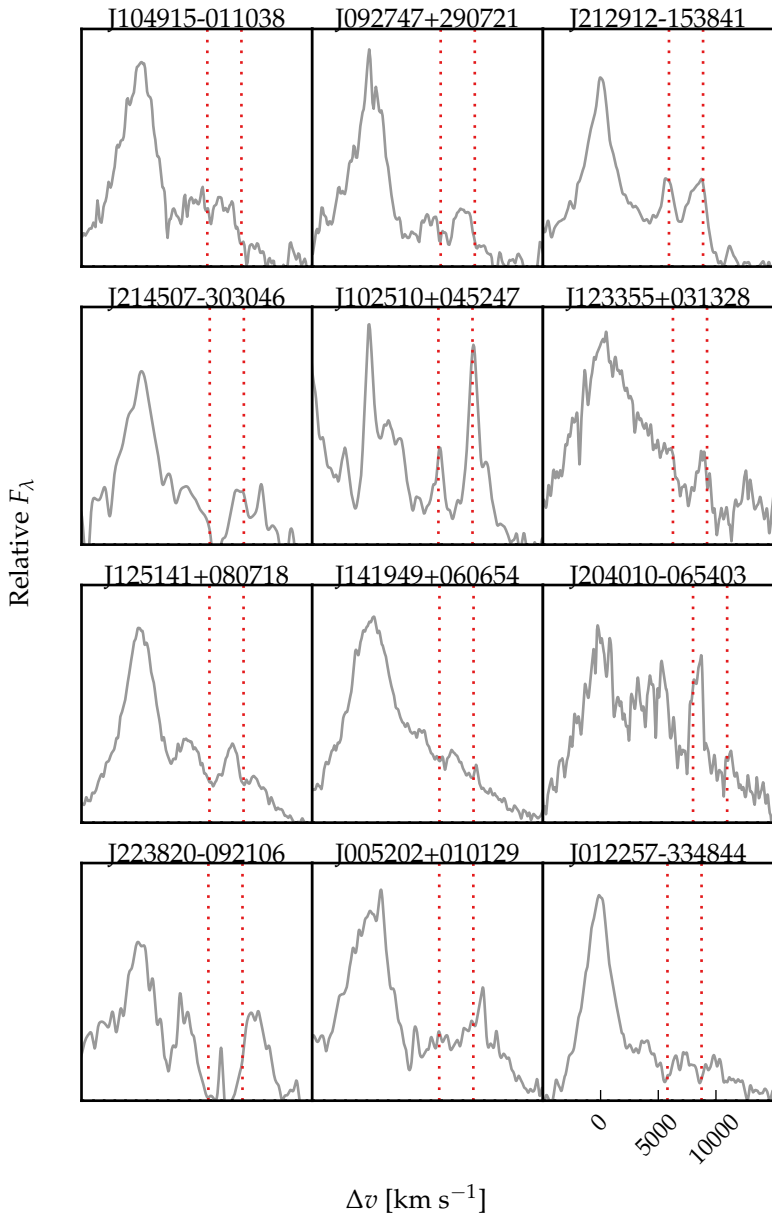


Figure 4.1: Spectra of the 24 objects for which significant Fe II emission is still visible following our Fe II-subtraction procedure. Spectra have been smoothed via convolution with a 100 km s^{-1} Gaussian kernel. The vertical lines indicate the expected positions of the [O III] doublet (which is generally very weak) with the systemic redshift defined using the peak of the broad H β emission.

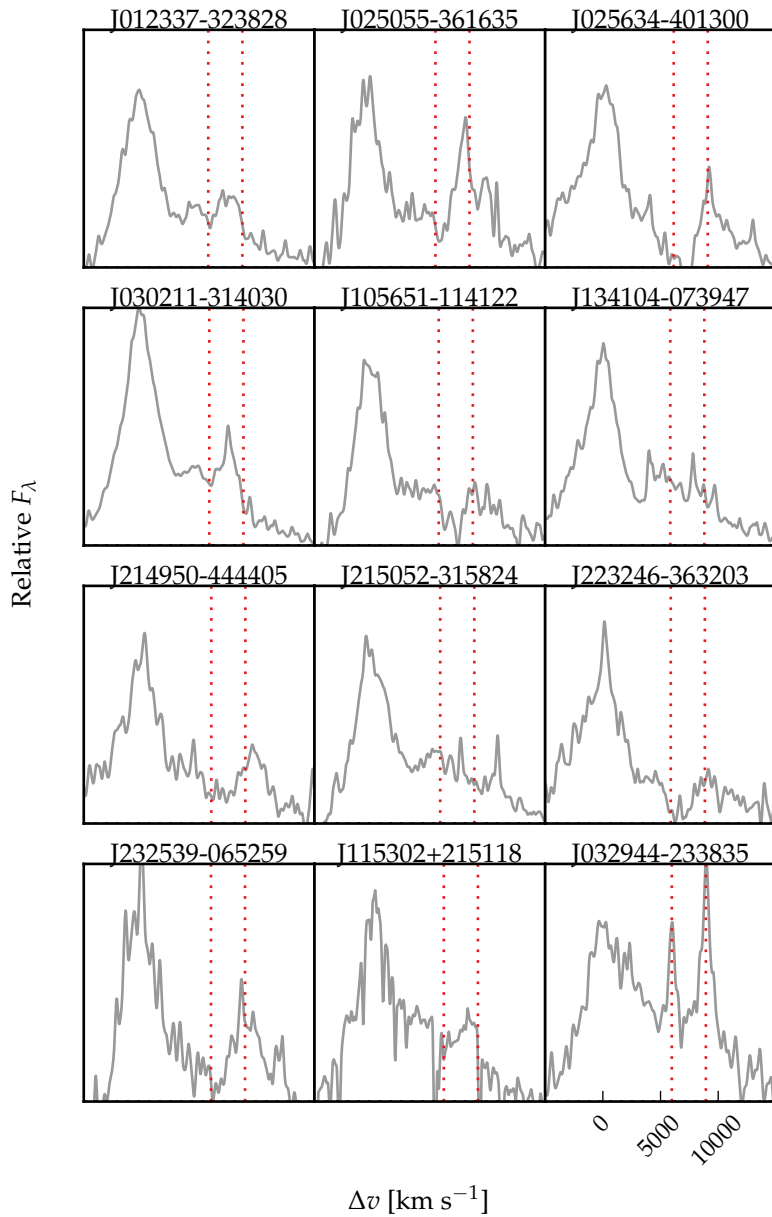


Figure 4.1: Continued.

Because the derived [O III] emission properties can be strongly biased in objects so-affected, these objects are flagged and are excluded from our analysis in the remainder of this chapter (leaving 330 objects).

4.3.3 Modelling H β /[O III]

The H β and [O III] emission is fit using the procedure described in Chapter 3. However, we make a number of modifications to the parametric model employed in the fit. The model employed in this Chapter is described in detail below.

In general, H β is modelled by two Gaussians with non-negative amplitudes and FWHM greater than 1200 km s $^{-1}$. In 10 objects H β is modelled with a single Gaussian and in 41 objects H β is modelled with two Gaussians, but the velocity centroids of the two Gaussians are constrained to be equal. These spectra generally have low S/N, and adding extra freedom to the model does not significantly decrease the reduced χ^2 . In addition there are cases where the blue wing of the H β emission is below the lower wavelength limit of the spectrograph; in these cases models with more freedom are insufficiently constrained by the data.

Contributions to the H β emission from the NLR is weak in the vast majority of our sample, and in general we do not include an additional Gaussian component to model this emission. In 9 objects features in the model - data residuals suggest that a narrow emission component is significant, and an additional narrow Gaussian is included for these quasars. It is likely that there is some not insignificant contribution from the NLR in other quasars in our sample. If this is the case then measures of the H β velocity width will be biased to lower values on average. However, measurements of the [O III] emission (the focus of this chapter) will not be affected by not decomposing H β into distinct broad and narrow components.

Each component of the [O III] doublet is fit with one or two Gaussians, depending on the fractional reduced χ^2 difference between the one- and two-component models. Concretely, if the addition of the second Gaussian decreases the reduced χ^2 by more than 5 per cent then the double-Gaussian model is accepted. One hundred and twenty-eight are fit with a single Gaussian and 140 with two Gaussians. The peak flux ratio of the [O III] 4960 Å and 5008 Å components are fixed at the ex-

pected 1:3 ratio and the width and velocity offsets are set to be equal¹.

In 62 objects with very weak [O III] (mean EQW $\sim 2\text{\AA}$) we found that the Gaussian model has a tendency to fit features of the noise. In some cases this can lead to large errors on the [O III] line properties. To avoid this problem, we instead fit a fixed [O III] template to the spectra, with the overall scaling the only free-parameter in the fit. This template is generated by running our line-fitting routine on a median composite spectrum of the 268 quasars with [O III] line measurements. The spectra used to construct the composite were first de-redshifted and continuum- and Fe II-subtracted.

In Figure 4.2 we show example fits to 15 objects, chosen at random. The mean reduced chi-squared value is 1.74 and, in general, there are no strong features observable in the spectrum minus model residuals.

4.3.4 Deriving upper limits on the [O III] EQW

Firstly, the best-fitting model comprising the continuum, Fe II, and H β emission is subtracted from the spectra, leaving behind only emission due to [O III]. These spectra are then smoothed by convolving with a Gaussian of width 200km s^{-1} . From each of these spectra we generate 100 mock spectra, with the flux at each wavelength randomly drawn from a Normal distribution with a mean equal to the smoothed flux and a width equal to the error on the flux. We then perform an error-weighted linear least-squares regression with the [O III] template described in the preceding section. The EQW and its error are then defined as the mean and root-mean-square error of the best-fitting EQW in the 100 realisations. We define the upper limit on the [O III] EQW as the mean plus the error.

*Paul: does this way
of deriving upper
limits make sense?*

4.3.5 Modelling H α

There are 217 quasars in our sample with spectra covering the H α emission line. Below, we use the peak of the H α emission as one estimate of the quasar systemic redshift. In this section we describe how the H α emission was modelled.

¹ For QSO176, a significantly better fit ($\Delta\chi^2_v \sim 25\%$) is obtained when the peak flux ratio constraint relaxed; the peak ratio of the best-fitting model is 0.47.

Table 4.2: Summary of models used to fit the H α emission, and the number of quasars each model is applied to.

Model	Components	Fix centroids?	Number
1	1 broad Gaussian	N/A	10
2	2 broad Gaussians	Yes	71
3	2 broad Gaussians	No	32
4	2 broad Gaussians + narrow Gaussians	Yes	51
5	2 broad Gaussians + narrow Gaussians	No	53

The continuum emission is first modeled and subtracted using the procedure described in Chapter 3. We then test five different models with increasing degrees of freedom to model the H α emission. The models are summarised in Table 4.2. They are (1) a single broad Gaussian; (2) two broad Gaussians with identical velocity centroids; (3) two broad Gaussians with different velocity centroids; (4) two broad Gaussians with identical velocity centroids, and additional narrower Gaussians to model narrow H α emission, and the narrow components of [N II] $\lambda\lambda 6548,6584$ and [S II] $\lambda\lambda 6717,6731$; (5) two broad Gaussians with different velocity centroids, and additional narrower Gaussians. If used, the width and velocity of all narrow components are set to be equal in the fit, and the relative flux ratio of the two [N II] components is fixed at the expected value of 2.96. The model we select is the simplest model for which the fractional change in the reduced χ^2 from the model with the lowest reduced χ^2 is less than ten per cent. The numbers of quasars on which each of the five models was applied are given in Table 4.2.

4.3.6 Derived parameters

All [O III] line properties are derived from the [O III] $\lambda 5008$ emission, but, as described above, the kinematics of [O III] $\lambda 4960$ are constrained by our fitting routine to be identical.

We do not attach any physical meaning to the individual Gaussian components used in the model. Decomposing the [O III] emission into a narrow component component at the systemic redshift and a lower-amplitude, blueshifted broad component is subject to large uncertainties and is highly dependent on the spectral S/N and resolution. Furthermore, there is no

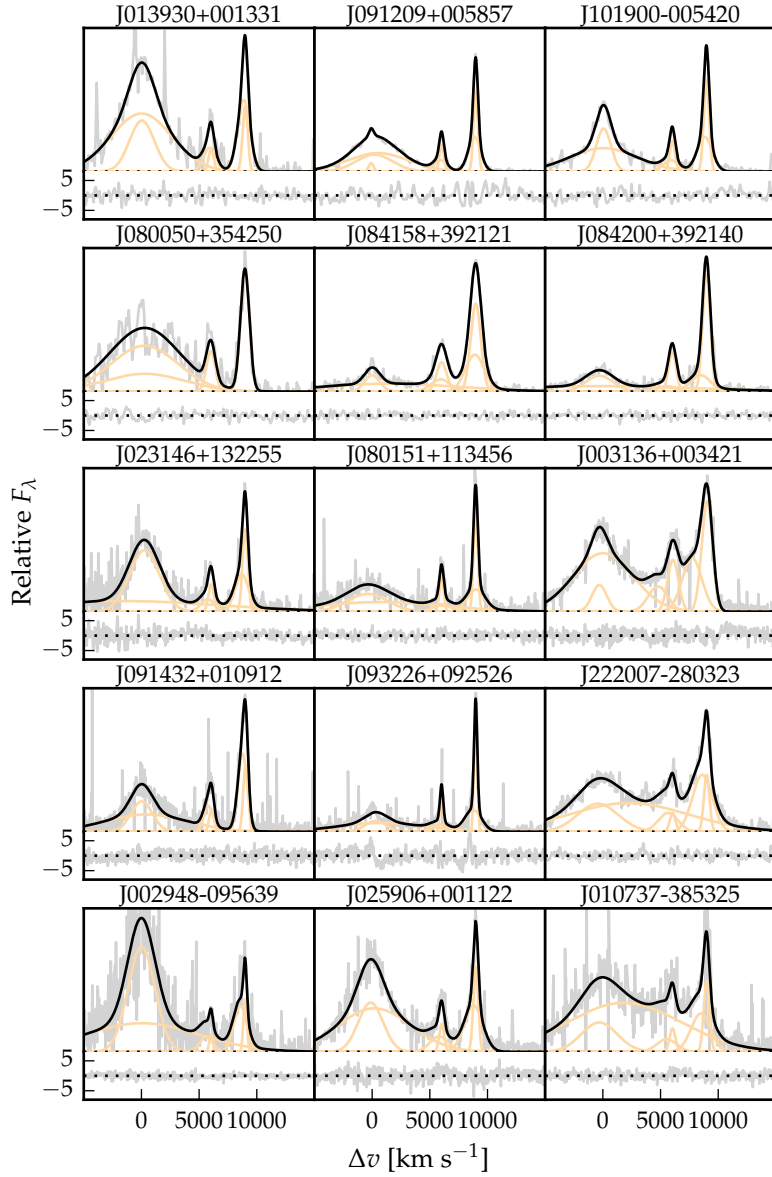


Figure 4.2: Model fits to the continuum- and Fe II-subtracted H β /[O III] emission in 15 quasars, chosen at random. The data is shown in grey, the best-fitting model in black, and the individual model components in orange. The peak of the [O III] emission is used to set the redshift, and Δv is the velocity shift from the rest-frame transition wavelength of H β . Below each spectrum we plot the data minus model residuals, scaled by the errors on the fluxes.

Table 4.3: The format of the table containing the emission line properties from our parametric model fits.

Column	Name	Units	Description
1	UID		Catalogue name
2	OIII_V5	km s^{-1}	[O III] v_5
3	OIII_V5_ERR	km s^{-1}	Uncertainty in v_5
4	OIII_V10	km s^{-1}	[O III] v_{10}
5	OIII_V10_ERR	km s^{-1}	Uncertainty in v_{10}
6	OIII_V25	km s^{-1}	[O III] v_{25}
7	OIII_V25_ERR	km s^{-1}	Uncertainty in v_{25}
8	OIII_V50	km s^{-1}	[O III] v_{50}
9	OIII_V50_ERR	km s^{-1}	Uncertainty in v_{50}
10	OIII_V75	km s^{-1}	[O III] v_{75}
11	OIII_V75_ERR	km s^{-1}	Uncertainty in v_{75}
12	OIII_V90	km s^{-1}	[O III] v_{90}
13	OIII_V90_ERR	km s^{-1}	Uncertainty in v_{90}
14	OIII_V95	km s^{-1}	[O III] v_{95}
15	OIII_V95_ERR	km s^{-1}	Uncertainty in v_{95}
16	z_OIII		[O III] redshift
17	z_OIII_ERR		Uncertainty in [O III] redshift
18	OIII_W50	km s^{-1}	[O III] w_{50}
19	OIII_W50_ERR	km s^{-1}	Uncertainty in [O III] w_{50}
20	OIII_W80	km s^{-1}	[O III] w_{80}
21	OIII_W80_ERR	km s^{-1}	Uncertainty in [O III] w_{80}
22	OIII_W90	km s^{-1}	[O III] w_{90}
23	OIII_W90_ERR	km s^{-1}	Uncertainty in [O III] w_{90}
24	OIII_A		[O III] asymmetry
25	OIII_A_ERR		Uncertainty in [O III] asymmetry
26	OIII_EQW	\AA	[O III] EQW
27	OIII_EQW_ERR	\AA	Uncertainty in [O III] EQW
28	OIII_LUM	erg s^{-1}	[O III] luminosity
29	OIII_LUM_ERR	erg s^{-1}	Uncertainty in [O III] luminosity
30	EQW_FE_4434_4684	\AA	Fe II EQW
31	EQW_FE_4434_4684_ERR	\AA	Uncertainty in Fe II EQW
32	HB_VPEAK	km s^{-1}	H β peak velocity
33	HB_VPEAK_ERR	km s^{-1}	Uncertainty in H β peak velocity
34	HA_VPEAK	km s^{-1}	H α peak velocity
35	HA_VPEAK_ERR	km s^{-1}	Uncertainty in H α peak velocity
36	HB_Z		H β redshift
37	HB_Z_ERR		Uncertainty in H β redshift
38	HA_Z		H α redshift
39	HA_Z_ERR		Uncertainty in H α redshift
40	OIII_REDCHI		Reduced- χ^2 in H β /[O III] fit
41	OIII_FE_FLAG		Bad Fe II subtraction
42	OIII_EXTREM_FLAG		Extreme [O III] emission
43	HA_REDCHI		Reduced- χ^2 in H α fit

theoretical justification that the broad component should have a Gaussian profile.

We therefore choose to characterize the [O III] line profile using a number of non-parametric measures, which are commonly used in the literature (e.g. Zakamska and Greene, 2014; Zakamska et al., 2016). A normalised cumulative velocity distribution is constructed from the best-fitting model, from which the velocities below which 5, 10, 25, 50, 75, 90, and 95 per cent of the total flux accumulates can be calculated. These velocities are then adjusted so that the peak of the [O III] emission is at 0 km s^{-1} .

The width of the emission line can then be defined using either w_{50} ($\equiv v_{75} - v_{25}$), w_{80} ($\equiv v_{90} - v_{10}$) or w_{90} ($\equiv v_{95} - v_5$). In terms of the FWHM, $w_{50} \simeq \text{FWHM}/1.746$, $w_{80} \simeq \text{FWHM}/0.919$, $w_{90} \simeq \text{FWHM}/0.716$. w_{90} is relatively more sensitive to the wings of the line profile, whereas w_{50} is relatively more sensitive to the core. We also define the relative asymmetry of the line as:

$$A = \frac{(v_{90} - v_{\text{peak}}) - (v_{\text{peak}} - v_{10})}{(v_{90} - v_{10})}. \quad (4.1)$$

Line-width measures are corrected for instrumental broadening by subtracting the resolution of the spectrograph (Table 2.2) in quadrature. Because the line profiles are typically non-Gaussian, this deconvolution procedure is only approximate. All of the derived parameters we have calculated are summarised in Table 4.3. The columns are as follows:

- 1 Unique ID: QSOXXX.
- 2-3 Systemic redshift measured at [O III] peak wavelength, and its error.
- 4-17 v_5 , v_{10} , v_{25} , v_{50} , v_{75} , v_{90} and v_{95} velocity of [O III], relative to [O III] peak, and their errors, in km s^{-1} .
- 18-23 w_{50} ($\equiv v_{75} - v_{25}$), w_{80} ($\equiv v_{90} - v_{10}$) and w_{90} ($\equiv v_{95} - v_5$) velocity width of [O III], and their errors, in km s^{-1} .
- 24-25 Dimensionless [O III] asymmetry A , and its error.
- 26-27 Rest-frame [O III] EQW, and its error, in \AA .
- 28-29 1- σ upper-limit on rest-frame [O III] EQW, in \AA .

- 30-31 [O III] luminosity, and its error, in erg s^{-1} .
- 32-33 4434-4684 Årest-frame Fe II EQW, and its error, in Å.
- 34-35 Velocity of H β peak, relative to [O III] peak, in km s^{-1} , and its error.
- 36-37 Velocity of H α peak, relative to [O III] peak, in km s^{-1} , and its error.
- 38-38 Redshift of H β peak, and its error.
- 40-41 Redshift of H α peak, and its error.
- 42 Reduced χ -squared from [O III]/H β fit.
- 43 Reduced χ -squared in fit to H α .
- 44 Fe II flag.
- 45 Extreme [O III] flag.
- 46-47 C IV v_{50} , relative to [O III] peak, in km s^{-1} , and its error.

4.3.7 *Deriving uncertainties on parameters*

Our method to estimate realistic uncertainties on emission line properties derived from the best-fitting model is very similar to the one describe in Chapter 3. Very briefly, random simulations of each spectrum are generated. Our fitting-procedure is run on each simulated spectrum, and the errors on the line parameters are estimated by looking at the distribution of values from the ensemble of simulations. In a slight modification of the procedure in Chapter 3, the error is defined using the 68 (84 - 16) percentile spread in the parameter values.

4.3.8 *The significance of [O III] detections*

We require a method of determining weather a measured EQW is significant or not. We measure the rms of the flux density in the emission-line free window between 4500 and 4600 Å. We multiply the rms by the wavelength per pixel, and then multiply this by the square root of the number of pixels in the full width at zero intensity of the [O III] profile, to get σ . A line flux is accepted as significant if it is $> 3\sigma$. We also adopt an EQW of 1Åas the lower detection limit to account for systematic errors.

σ not the same as upper limit derived above.

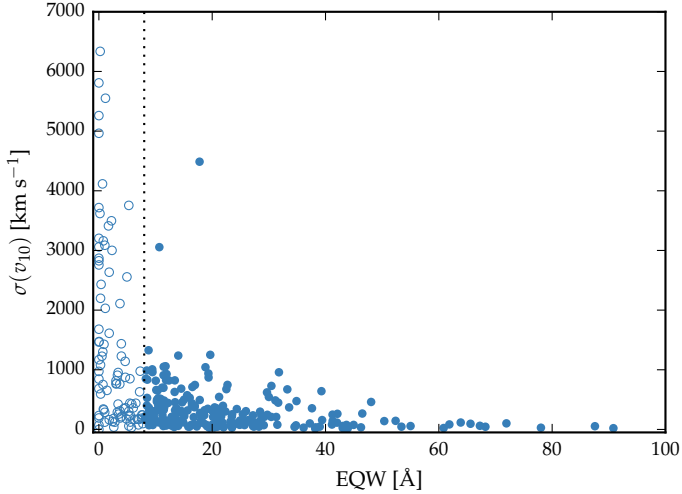


Figure 4.3: Uncertainty in v_{10} as a function of the EQW, for [O III]. Uncertainties in v_{10} are large to the left of the vertical line, at 8\AA . These objects are ignored in our subsequent analysis of the [O III] line shape.

4.3.9 Low EQW [O III]

In Figure 4.3 we show how the uncertainty in v_{10} depends on the EQW. As the strength of [O III] decreases, the average uncertainty in v_{10} increases. As the EQW drops below 8\AA , typical uncertainties in v_{10} become very large (exceeding 1000km s^{-1} in many objects). Clearly, the emission line is too weak for properties - in this case v_{10} - to be reliably measured in many of these objects. Therefore, when the [O III] line properties (e.g. velocity-width, centroid) are analysed in later sections, these objects with $\text{EQW} < 8\text{\AA}$ will be excluded. This leaves 226 quasars in the sample.

4.3.10 Reliability of redshift estimates

In this section, we compare systemic redshift estimates based on [O III], H β and H α . The wavelength of each of these lines is measured at the peak of the emission and this measurement is done on the best-fitting parameter model. In the case of the Balmer lines, this model includes both broad and (if present) narrow emission features.

We compare systemic redshift estimates based on [O III] and H β (Figure 4.4a), [O III] and H α (Figure 4.4b) and H β and H α (Figure 4.4c). [O III], H β and H α measurements are avail-

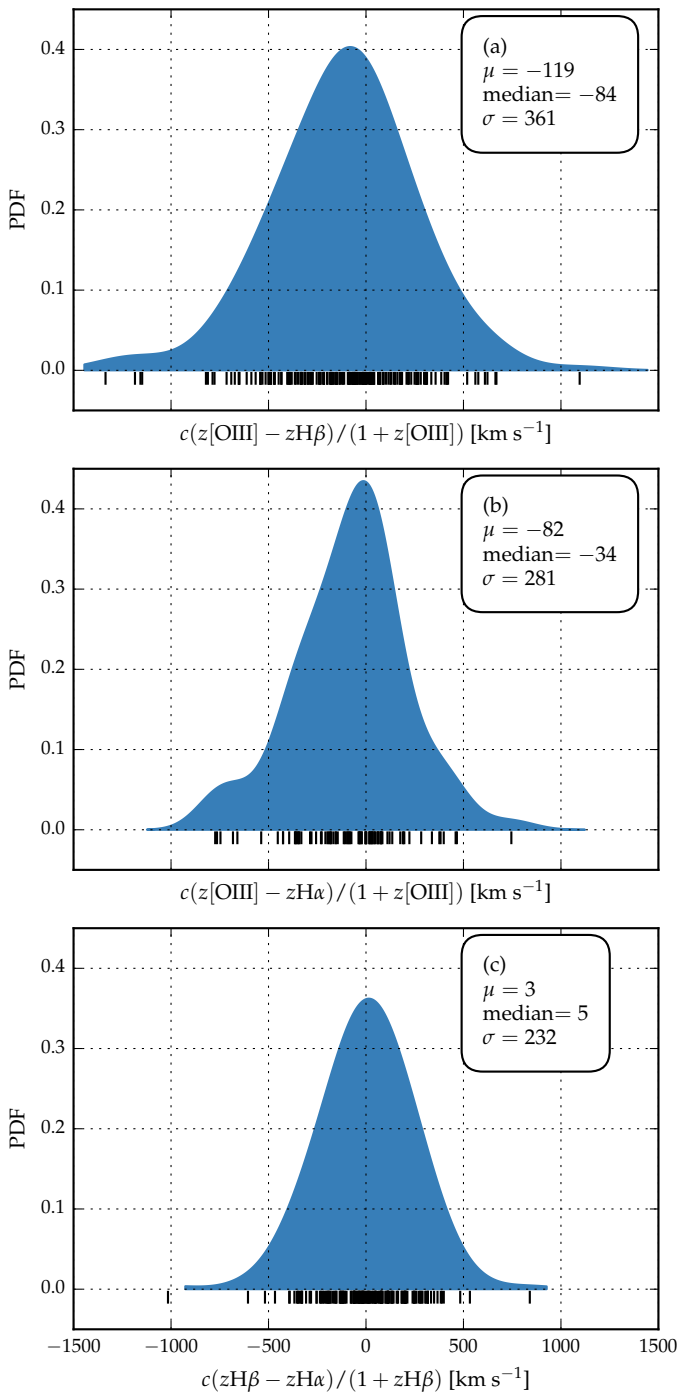


Figure 4.4: Comparison of systemic redshift estimates using [O III], broad H β and broad H α . The probability density functions are generated using a Gaussian kernel density estimator with a $\simeq 150 \text{ km s}^{-1}$ kernel width. The short black lines show the locations of the individual points.

able for 226, 418 and 226 objects. We exclude [O III], H β and H α measurements when the uncertainties on the peak velocities exceed 400, 600 and 400 km s $^{-1}$ respectively. This excludes 4, 6 and 12 per cent of the [O III], H β and H α measurements respectively. We also exclude [O III] measurements from 16 objects with very broad, blueshifted [O III] emission that is strongly blended with the red wing of H β (these objects are discussed in Section 4.6) because these redshifts are almost certainly strongly biased. After these cuts, there are 182, 85 and 162 objects being compared in (a), (b) and (c) respectively.

We generate probability density functions using a Gaussian kernel density estimator. The bandwidth, which is optimised using leave-one-out cross-validation, is 170, 120 and 140 km s $^{-1}$ for (a), (b) and (c) respectively. The systematic offset between the H α and H β estimates is consistent with being zero, and the scatter is 230 km s $^{-1}$. The scatter in these distributions is consistent with previous studies of redshift uncertainties from broad emission lines (e.g. Shen et al., 2016). The [O III] redshifts appear to be systematically offset in comparison to both H α and H β , in the sense that [O III] is blueshifted. This effect is strongest when [O III] is compared to H β , in which case [O III] is shifted by ~ 100 km s $^{-1}$ to the blue.

4.4 RESULTS

In our sample of 354 quasars, there is a huge diversity in [O III] emission properties (Fig. 4.2). In Figure ?? we present a sub-set of the measurements we have made of the [O III] line.

The [O III] EQW follows an approximately log-normal distribution, peaking at 17 Å. In 10 per cent of our sample [O III] is very weak, with EQW < 1 Å. The average [O III] strength is consistent with earlier studies on smaller samples (e.g. Sulentic et al., 2004; Netzer et al., 2004; Shen, 2016). The strength of [O III] depends on the covering factor of NLR gas, its density and ionisation parameter.

*Paul: Define
undetected as less
than 3 σ ?*

The mean and standard deviation of the line width (characterized by w_{80}) is 1535 ± 562 km s $^{-1}$, with a median of 1529, minimum of 206 and maximum of 3214. This is consistent with recent near-infrared spectroscopy of $z > 1.5$ quasars which often report velocity widths $\gtrsim 1000$ km s $^{-1}$ (e.g. Netzer et al., 2004; Kim et al., 2013; Brusa et al., 2015; Shen, 2016).

For gas discs rotating in the potential of the massive galaxies line widths do not exceed $w_{80} \simeq 600$ km s $^{-1}$ (Liu et al.,

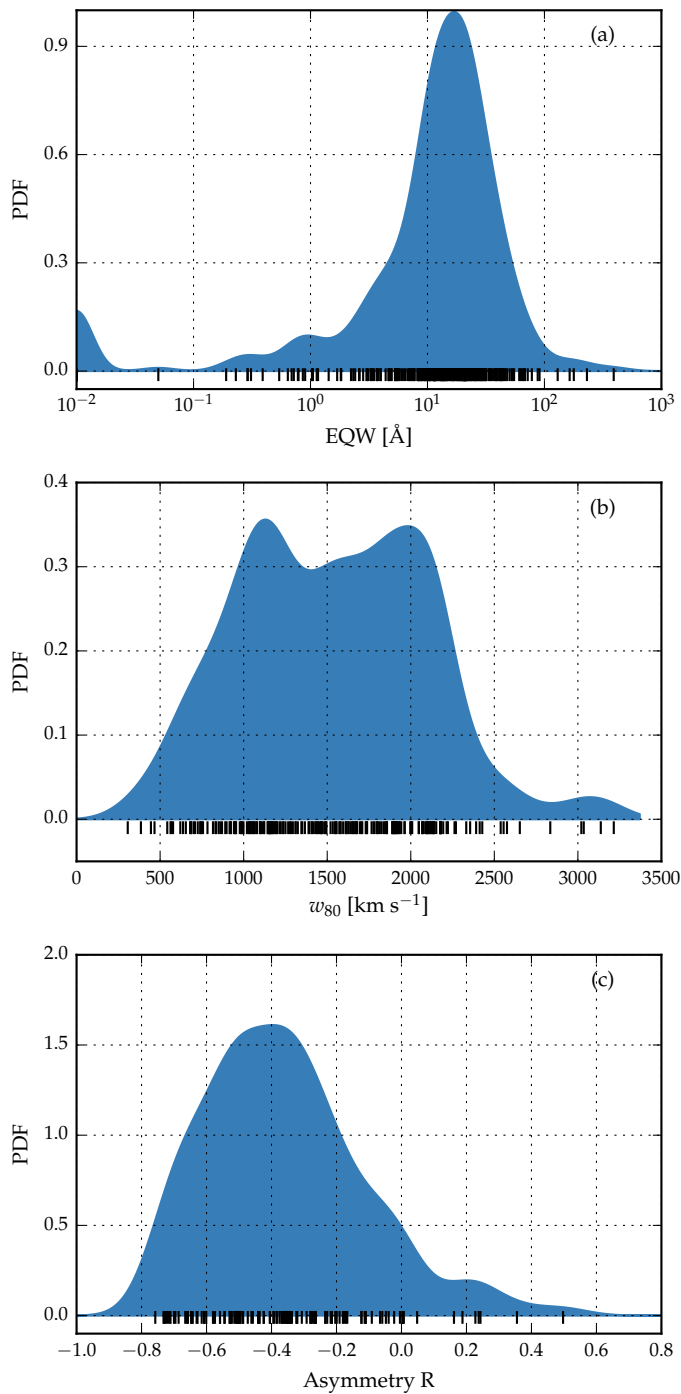


Figure 4.5: Correlations between the line width w_{80} , asymmetry R and EQW of [O III].

2013). Therefore the [O III] gas cannot be in dynamical equilibrium with the host galaxy. [O III] emission is suppressed by collisional de-excitation in higher-density environments, and so the large velocity widths cannot be due to the BLR. The 1200 km s^{-1} upper limit on the velocity width of the Gaussian functions used to model [O III] is responsible for the peak at 1200 km s^{-1} .

The [O III] asymmetry is shown in Figure 4.5c. In 40 per cent of the sample [O III] is fit with a single Gaussian. The asymmetry is zero in this model and so these objects are excluded. [O III] is blue-asymmetric in all but a handful of objects. This indicates that there is an outflow component in the [O III]-emitting gas. We also find that there is a correlation between w_{80} and the asymmetry: the broader lines are more blue-asymmetric.

4.4.1 Luminosity/redshift-evolution of [O III] properties

4.4.1.1 Comparison sample

We extend the dynamic range of our samples in terms of both luminosity and redshift by supplementing our sample with quasars presented by Mullaney et al., (2013) and Harrison et al., (2016). The Mullaney et al., (2013) catalogue contains [O III] line measurements for $\sim 25\,000$ optically-selected AGN with SDSS spectra at $z < 0.4$. Mullaney et al., (2013) fit [O III] with one or two Gaussians, and then used similar non-parametric measures to the ones we adopt. We select only the Type I AGN from the Mullaney et al., (2013) catalogue. The Harrison et al., (2016) sample contains 40 quasars at intermediate redshifts ($1.1 \leq z \leq 1.7$).

We also use the SDSS DR7 quasar catalogue, with properties derived by Shen et al., (2011). [O III] is visible in SDSS spectra up to redshifts $z = 0.84$. There are 20,663 quasars in the Shen et al., (2011) catalogue with $[\text{O III}] \text{ EQW} > 0 \text{\AA}$.

4.4.1.2 Equivalent width

In Fig. 4.6 we show the [O III] EQW as a function of the quasar bolometric luminosity. Bolometric luminosity is estimated from the monochromatic continuum luminosity at 5100\AA , using the correction factor given by Richards et al., (2006a). For comparison, we also show the low- z sample from Shen et al., (2011).

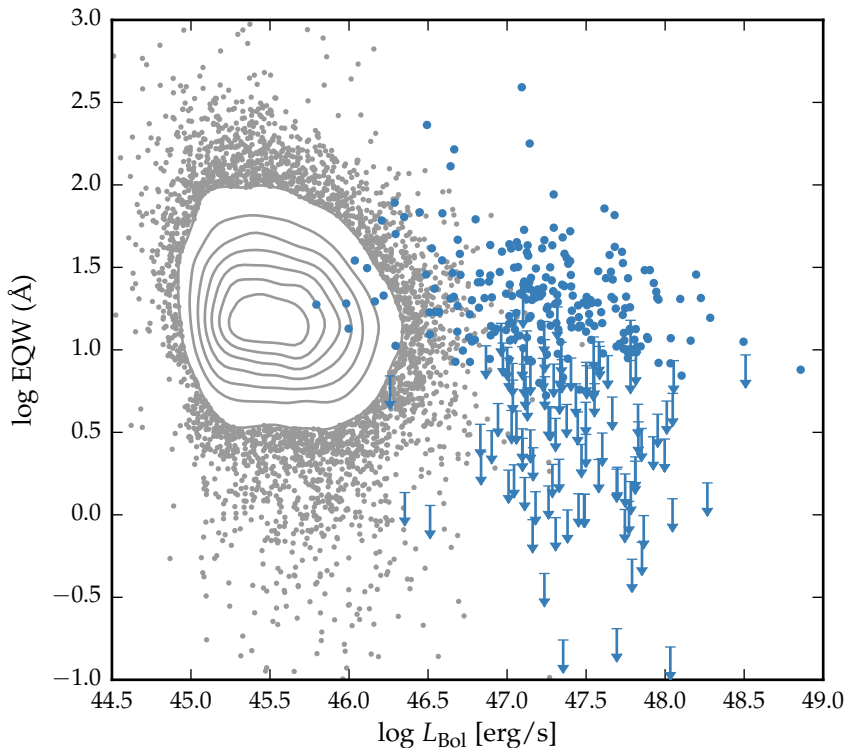


Figure 4.6: The [O III] EQW as a function of the quasar bolometric luminosity for the sample presented in this chapter (blue circles) and the low- z SDSS sample (grey points and contours). Upper limits are denoted by the downward arrows.

Use upper limit when EQW less than 3σ ?

We find that [O III] EQW is fairly constant as a function of quasar luminosity in the objects with prominent [O III] emission. We find that [O III] is undetected/very weak in XX per cent of our sample, which is very similar to the fraction reported by Netzer et al., (2004) based on a much smaller sample. In contrast, quasars with weak [O III] are very rare in nearby AGN. As a result, the mean [O III] EQW decreases as a function of luminosity (e.g. Brotherton, 1996; Netzer et al., 2004; Sulentic et al., 2004; Baskin and Laor, 2005b). This trend is known as the Baldwin effect for [O III] (e.g. Baldwin, 1977; Brotherton, 1996; Zhang et al., 2011; Stern and Laor, 2012).

4.4.2 Velocity width

In Figure 4.7 we show the [O III] velocity width as a function of the [O III] luminosity and the quasar redshift. The lack of any

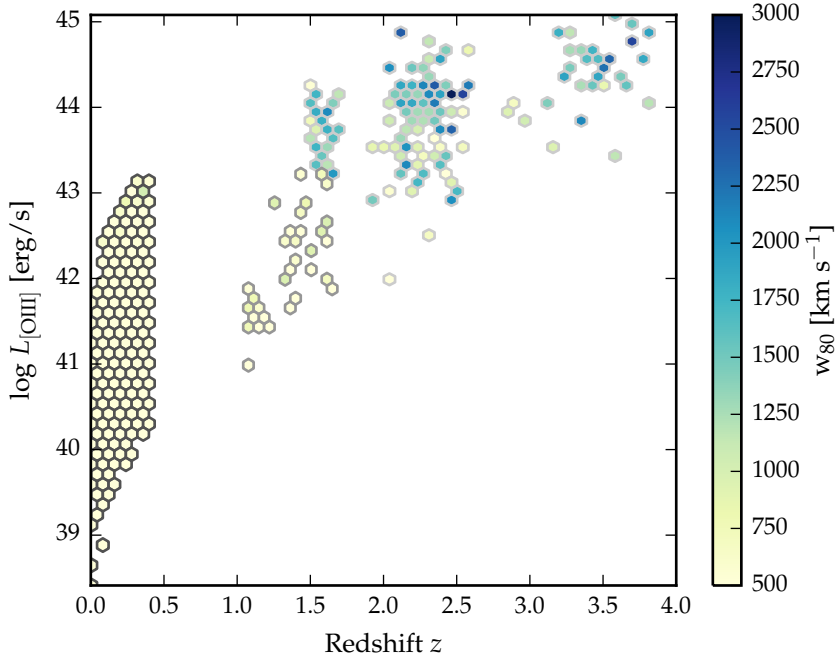


Figure 4.7: The [O III] velocity-width, characterised by w_{80} , as a function the [O III] luminosity and the quasar redshift. The colour of each hexagon denotes the mean w_{80} for the objects in that luminosity-redshift bin. Objects at redshifts $z < 0.5$ are from Mullaney et al., (2013), lower-luminosity objects at redshifts $z \sim 1.5$ (with a darker grey border) are from Harrison et al., (2016), and objects with a light grey border at $z \gtrsim 1.5$ are from this Chapter.

redshift-evolution between $z = 0$ and $z = 1.5$ was reported by Harrison et al., (2016). The kinematics of high redshift quasars are similar to those at lower redshifts with similar luminosities. On the other hand, at fixed redshift, we see a significant correlation between the [O III] velocity width and the luminosity.

4.5 EIGENVECTOR 1 CORRELATIONS

4.5.1 *EV1 trends exist in high-redshift quasars*

The FWHM of the broad H β emission line and the relative strengths of optical Fe II and H β have been identified as the features responsible for the largest variance in the spectra of AGN. These parameters form part of EV1, the first eigenvector in a PCA which originated from the work of Boroson and Green, (1992). The underlying driver behind EV1 is thought to

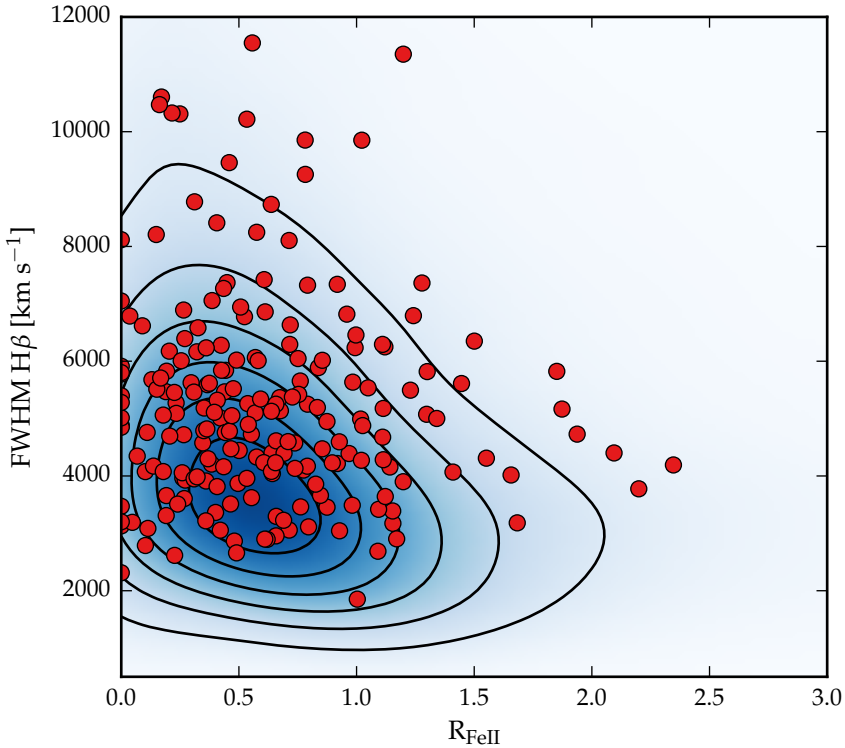


Figure 4.8: EV1 parameter space. The contours and shading show low-redshift, low-luminosity SDSS AGN (with measurements taken from Shen et al., (2011)) and the red circles show the high-redshift, high-luminosity objects presented in this chapter.

be the Eddington ratio (e.g. Sulentic et al., 2000; Shen and Ho, 2014).

In Figure 4.8 we show the [O III] EQW as a function of the H β FWHM and the optical Fe II strength. The optical Fe II strength is defined as the ratio of the Fe II and H β EQW, where the Fe II EQW is measured between 4434 and 4684Å. Measurements of the H β line properties are taken from Chapter 3. In our sample, these parameters follow very similar correlations to what is observed at low-z. In particular, we observe a strong anti-correlation between the [O III] and Fe II EQW. The H β FWHM are displaced to higher values, which is consistent with the high-redshift, high-luminosity sample having larger BH masses. Thus, we confirm earlier results using much smaller samples that suggest that the same EV1 correlations exist in high-redshift quasars (e.g. Sulentic et al., 2004; Sulentic et al., 2006; Runnoe et al., 2013a; Shen, 2016).

4.5.2 Extending EV1 parameter space

The C_{IV} blueshift and EQW is a diagnostic that similarly spans the diversity of broad emission line properties in high redshift quasars (Sulentic et al., 2007; Richards et al., 2011). C_{IV} is dominated by a virialized component at one extreme, and is dominated by outflows at the other (see Chapter 3 for details). The similarity of the C_{IV} EQW-blueshift parameter space at high redshift to EV1 parameter space at low redshift suggests that these trends are connected.

Optical spectra are available for XXX quasars in our catalogue, and cover the broad C_{IV} doublet. In Chapter 3, we demonstrated that the quasars in our sample cover the full range of C_{IV} blueshifts seen in the SDSS quasar population. This means that we can use our quasar sample to understand how the low-redshift EV1 parameter space maps to the high-redshift C_{IV} parameter space. In Figure 4.9 we show how the EV1 parameters change as a function of position in the C_{IV} EQW-blueshift parameter space.

Two hundred and fourteen objects are shown in Figure 4.9. Objects for which the H β or C_{IV} line properties could not be measured reliably (see Section 3.3.5) have also been removed. We consider only objects for which the C_{IV} EQW exceeds 15Å. The C_{IV} blueshift is measured relative to the redshift determined from the peak of [O III], H β or H α .

Most of the diversity in C_{IV} properties is correlated with the [O III] EQW. This is seen more clearly in Fig. 4.10, in which we plot the [O III] EQW as a function of the C_{IV} blueshift. On the other hand, the C_{IV} blueshift and EQW cannot be used to predict the H β FWHM. This is consistent with what we found in Chapter 3: objects with large C_{IV} blueshifts have narrow Balmer emission lines, but objects with modest C_{IV} blueshifts have a wide range of Balmer line widths.

4.6 EXTREME [O III] EMITTERS

Figure 4.11 shows the spectra of 18 objects which we visually identified as having exceptionally broad [O III] emission profiles. These objects are defined as having very broad [O III] emission (although not necessarily the broadest in our sample) and heavily blended emission in between the zero-velocity wavelengths of H β and [O III]. Because the emission is so heavily-blended, it is difficult to determine unambiguously what com-

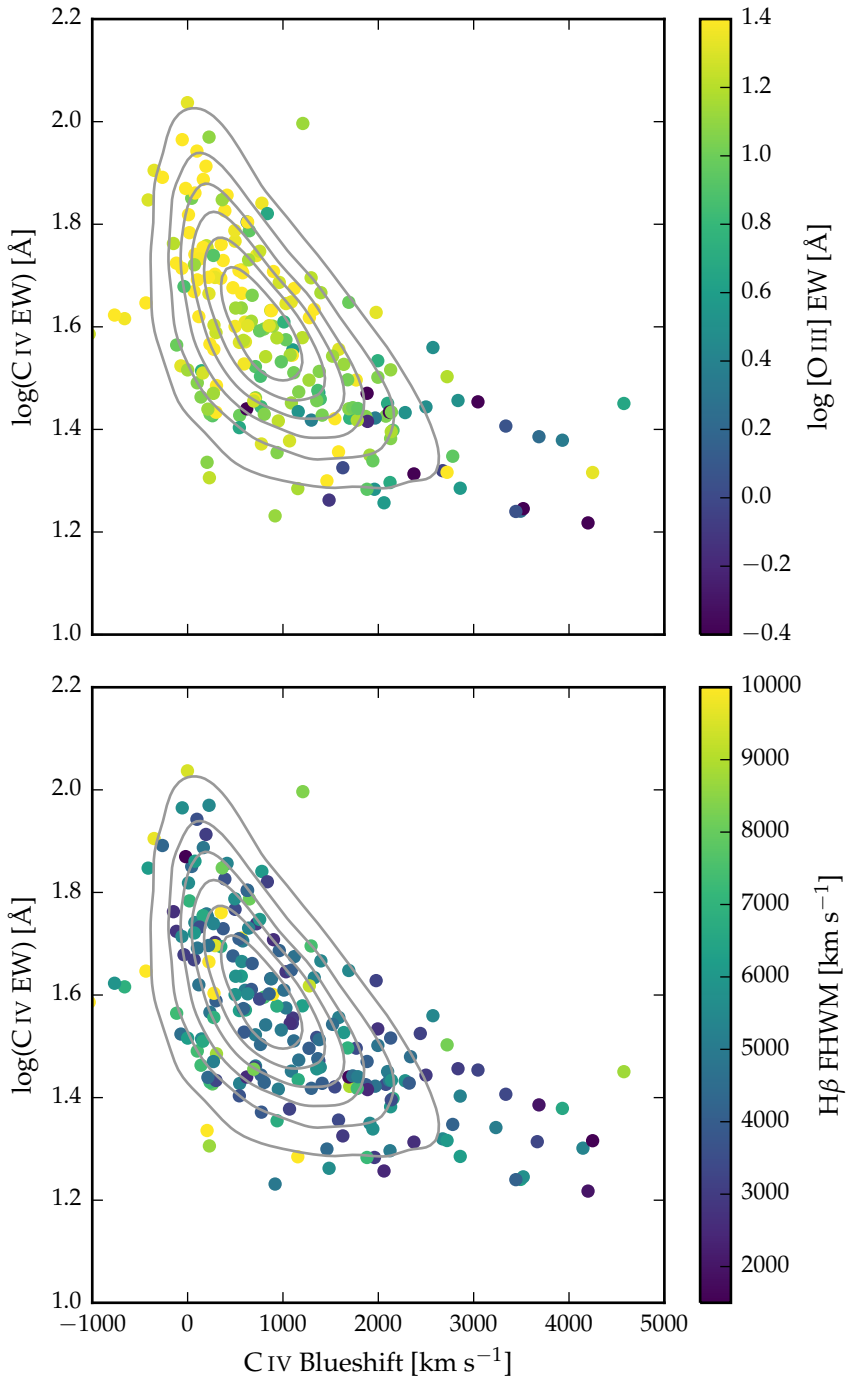


Figure 4.9: The high-redshift EV1 parameter space of CIV blueshift and EQW. Our sample is shown with points, and quasars from the full SDSS catalogue are shown with grey contours. The [O III] EQW varies systematically with position in the CIV blueshift-EQW parameter space (a) but the H β FWHM shows significantly less systematic variation (b).

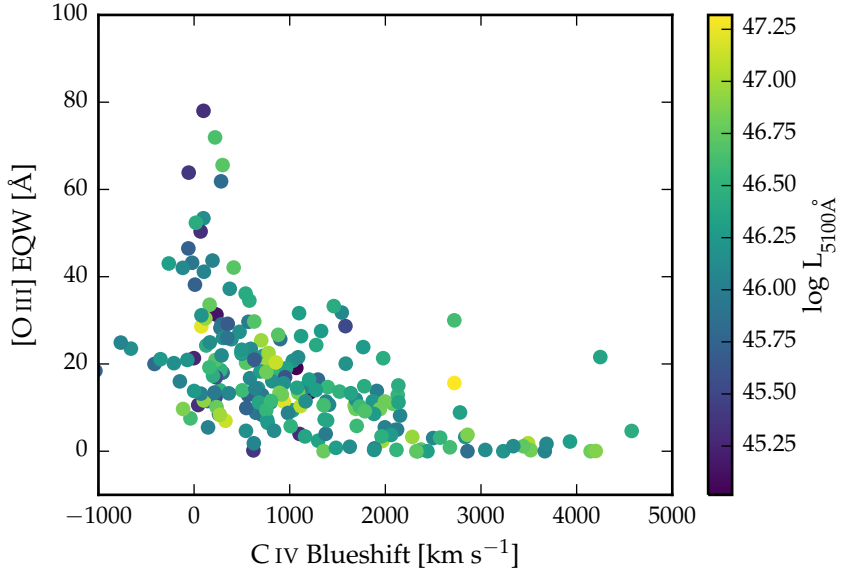


Figure 4.10: [O III] EQW as a function of the C IV blueshift.

bination of H β , [O III] and Fe II is responsible for the unusual plateau-like emission observed in these objects. Therefore, uncertainties on the [O III] emission properties are generally high in these objects.

In Figure 4.12 we show that the luminosities of all of these objects are larger than the sample median.

These [O III] emission lines are similar to the lines observed in a sample of four extremely dust-reddened quasars at $z \sim 2$ recently identified by Zakamska et al., (2016). The extreme nature of the [O III] emission in these objects led Zakamska et al., (2016) to propose that these objects are being observed transitioning from a dust-obscured, star-burst phase to a luminous, blue quasar. A similar [O III] emission was also observed in J1201+1206 in a sample of five of the most luminous quasars at redshifts $2.3 \lesssim z \lesssim 3.5$ observed by Bischetti et al., (2016).

The four Zakamska et al., (2016) quasars have $5\mu\text{m}$ luminosities of $\sim 10^{47}$ erg/s, which is comparable to maximum luminosity of our sample. The [O III] velocity widths of the Zakamska et al., (2016) objects are extreme in relation to our sample, matched in 5 micron luminosity. The quasars in our sample have very modest amounts of dust reddening ($E(B-V) \sim 0.03$ on average). These findings therefore appear to support the idea that strong feedback is occurring in this population of heavily reddened quasars.

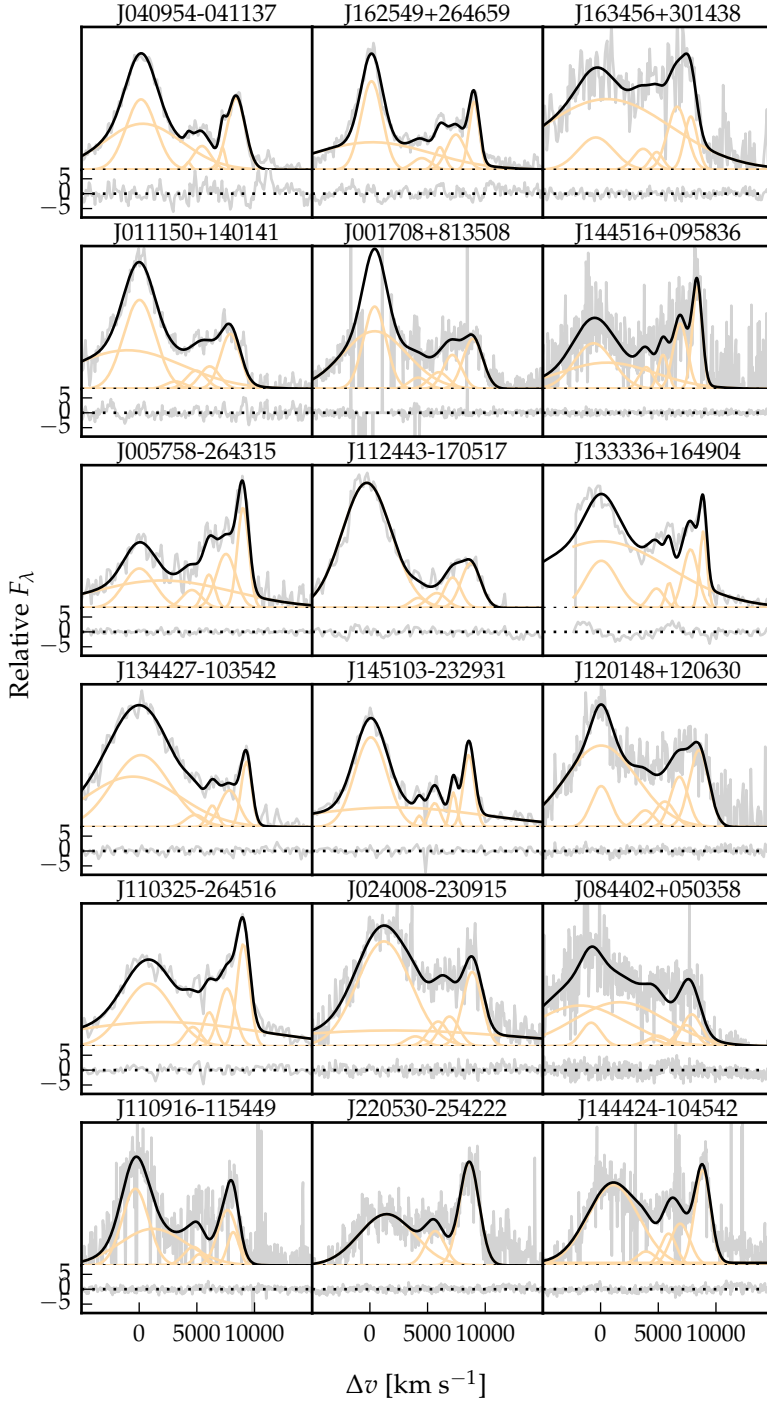


Figure 4.11: Model fits to the continuum- and Fe II-subtracted H β /[O III] emission in 18 quasars with extreme [O III] emission profiles. The data is shown in grey, the best-fitting model in black, and the individual model components in orange. The peak of the [O III] emission is used to set the redshift, and Δv is the velocity shift from the rest-frame transition wavelength of H β . Below each spectrum we plot the data minus model residuals, scaled by the errors on the fluxes.

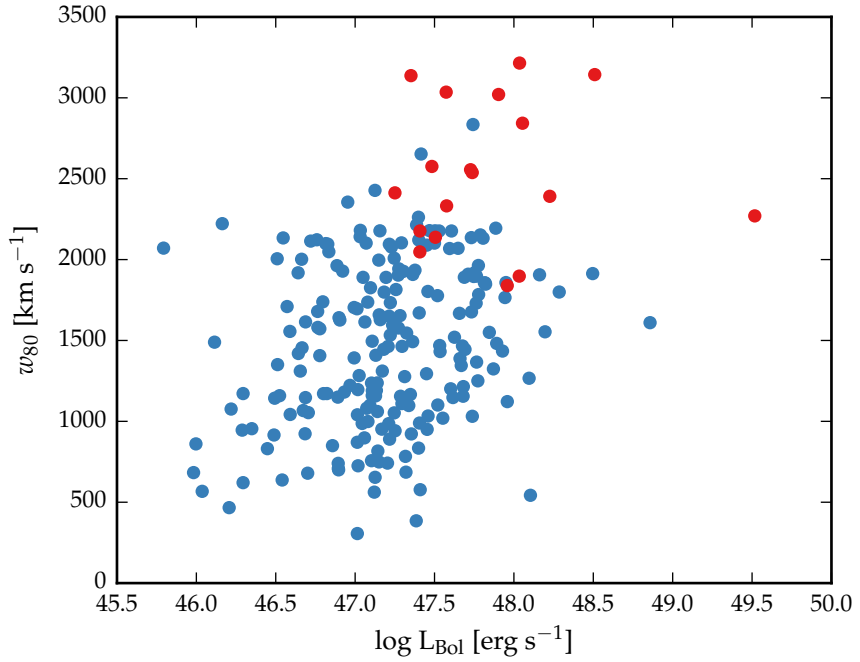


Figure 4.12: [O III] velocity width as a function of quasar bolometric luminosity. Objects with extreme [O III] profiles are shown in red.

4.6.1 [O III] and C IV outflows are linked

In Chapter 3 we looked in detail at properties of the C IV emission in luminous, high-redshift quasars. In many objects C IV is broad and blueshifted, which we interpret as evidence of strong outflows in the quasar BLR. These outflows can reach many thousands of km s^{-1} . However, to quench star formation quasar-driven outflows must break out to galactic scales.

Earlier, we saw that the [O III] EQW has a very strong dependence on the C IV blueshift. [O III] is undetected in XX per cent of quasars with C IV blueshifts greater than 2000 km s^{-1} .

In Figure 4.13 we show the the [O III] blueshift as a function of the C IV blueshift. The [O III] blueshift is defined as $v_{10} - v_{\text{peak}}$. For the C IV blueshift we use v_{50} as a measure of the line location, and again use the peak of the [O III] emission to define the systemic redshift. We use the C IV velocity centroid measurements we derived in Chapter 3. We take a subset of quasars with [O III] EQW $> 8 \text{ \AA}$. This removes most of the quasars with large C IV blueshifts, since [O III] is on average very weak in these quasars. We also remove objects where the fractional uncertainty on v_{10} exceeds 50 per cent (XX quasars).

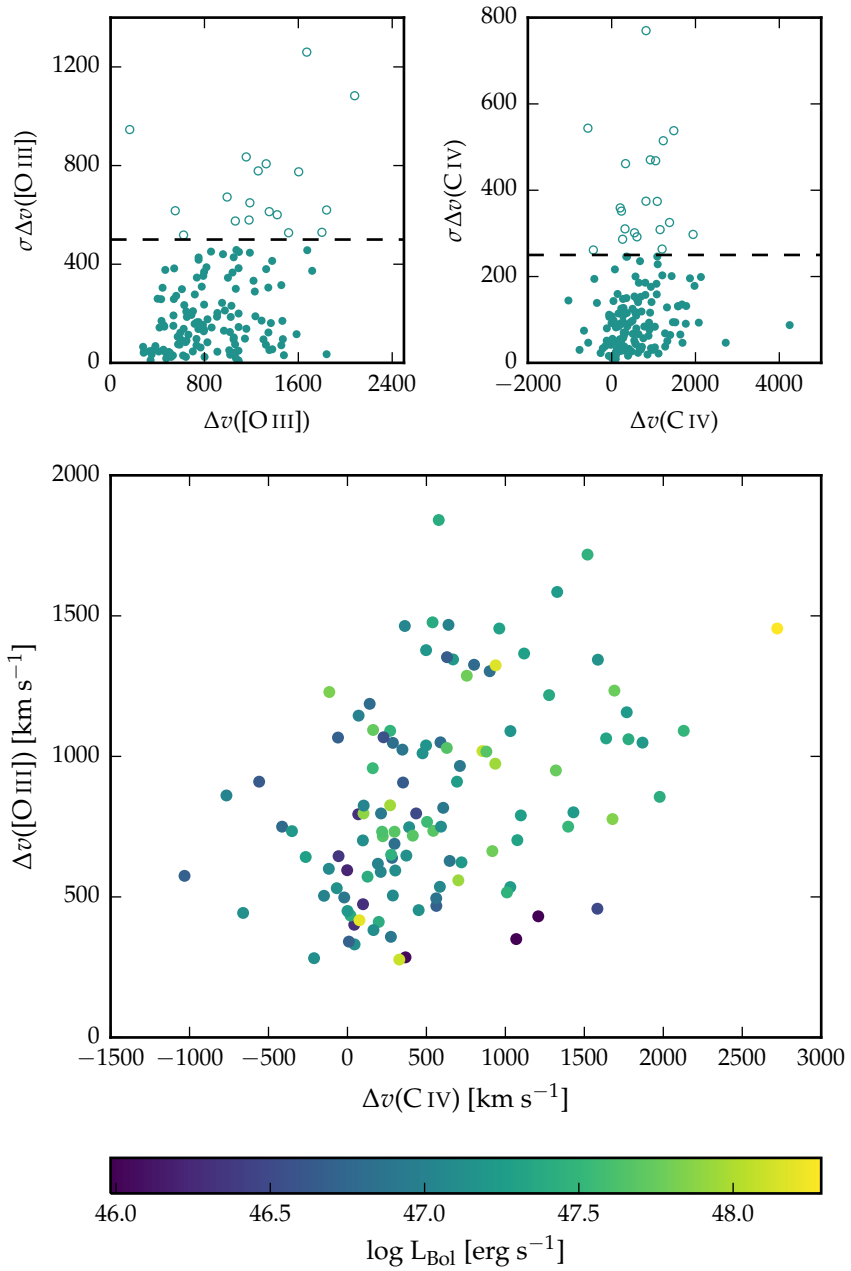


Figure 4.13: The relation between the blueshifts of C IV and [O III].

There is a clear and strong correlation. [O III] is more blueshifted in quasars with large C IV blueshifts. This suggests a direct connection between the gas kinematics in the broad and narrow line regions.

We considered a number of alternative approaches to parametrising both the [O III] line shape and the systemic redshift. As expected, very similar trends are observed when the [O III] line shape is parametrized using $v_{25} - v_{\text{peak}}$, $v_{50} - v_{\text{peak}}$, $w_{80} = v_{90} - v_{10}$, or the relative asymmetry R. The same trend is also observed when the systemic redshift is defined using the peak of the H β emission.

The blueshifting of C IV is known to correlate with luminosity (Richards et al., 2011). In [O III], the blueshifted wing becomes relatively more prominent as the luminosity of the quasar increases (Shen and Ho, 2014). Therefore, it is plausible that the correlation between the C IV and [O III] blueshifts is a secondary effect that is driven by the correlation of each with the luminosity. However, no strong luminosity-dependent trends are apparent in Figure 4.13. We find that both the [O III] and C IV blueshifts are correlated with the luminosity, but that these correlations are much weaker than the correlation between the [O III] and C IV blueshifts.

It has been known for some time that the [O III] EQW is anti-correlated with the strength of optical Fe II, and this trend is thought to be driven by the Eddington ratio. Shen and Ho, (2014) showed that the amplitude of the core [O III] emission decreases faster than the wing component as the Eddington ratio increases. Therefore, the [O III] emission is weaker and more blueshifted in high accretion rate quasars. In Chapter 3 we found that all quasars with strong BLR outflows have high Eddington ratios. In this section, we show that the C IV and [O III] blueshifts are directly linked. This suggests a direct connection between the gas kinematics in the broad and narrow line regions.

Discuss cuts

*We don't show
extreme objects*

*Similar correlations
have been
tentatively found in
lower redshift
quasars and AGN
(Zamanov et al.,
2002).*

4.7 DISCUSSION

4.7.1 Static NLR is removed by outflows

Is the AGN NLR absent in objects where outflows have reached kilo-parsec scales, sweeping up the low-density material responsible for the [O III]-emission? If the BLR outflows can escape, they are very fast and wouldn't need long to clear out the

NLR gas. Estimate a time-scale for how long the NLR would take to be cleared given typical size of galaxy and velocity of outflow.

READ ZAKAMSKA DISCUSSION

4.8 INDEPENDENT COMPONENT ANALYSIS

In this section, we discuss consider an alternative approach to the analysis presented in the bulk of this Chapter. We use an independent component analysis (ICA) to separate the spectrum in to a linear combination of statistically independent sub-components. Each individual spectrum can then be reconstructed with a linear combination of these components. The goal of this section is to determine whether or not the relative weights of the different components can be used in place of more commonly used emission line parameters to understand the physical processes occurring in these quasars.

Issues with the parametric model fitting approach adopted above include sensitivity to S/N. We also found the empirical template to be a poor match to the Fe II emission observed in a number of quasars.

4.8.1 *The technique*

ICA is a blind source separation technique for separating a signal in to linearly mixed statistically independent subcomponents. Unlike the more widely-used principle component analysis technique, ICA produces non-negative components which allows for a physical interpretation of the components and weights. ICA has been successfully applied to model the spectra of emission-line galaxies (Allen et al., 2013) and BAL quasars (Allen et al., 2011). The quasar spectra can be thought of as a set of observations, \mathbf{x} , which are made up of statistically independent components, \mathbf{c} , that are combined by some mixing matrix, \mathbf{W} :

$$\mathbf{x} = \mathbf{W}\mathbf{c} \quad (4.2)$$

ICA reverses this process and describes how the observed data are generated. Both the independent components and the mixing matrix are unknown, but can be found by solving:

$$\mathbf{c} = \mathbf{W}^{-1}\mathbf{x}. \quad (4.3)$$

Ask Paul for details.

The components were solved for using a sample of 2,154 SDSS quasars at redshifts XX. At these redshifts the SDSS spectrograph covers the rest-frame region XX-XXÅ where H β and [O III] lie. The individual spectra were first adjusted to give the same overall shape as a model quasar template spectrum. Six positive independent components and four additional components that could be negative were found to be sufficient to reconstruct the spectrum, without over-fitting. Each quasar spectrum x_j can then be represented as a linear combination of the independent components:

$$x_j = \sum_{i=1}^{10} c_{ij} W_{ij} \quad (4.4)$$

4.8.1.1 *Fitting procedure*

Each of the individual ICA components has been adjusted to give the same overall shape as a quasar template spectrum. We approximate the overall shape of this template by fitting a single power-law to emission line free windows at 4200-4230, 4435-4700 and 5100-5535 Å. We then flatten each of the ICA components by dividing by this power-law. An identical process is performed on each spectrum we fit, so that both the components and the spectrum to be fitted have essentially zero shape. For each quasar in our sample we perform a variance-weighted least-squares minimisation to determine the optimum value of the components weights. The first six component weights are constrained to be non-negative, and the fit is done in logarithmic wavelength space, so that each pixel corresponds to a fixed velocity width. The relative shift of the ICA components is also allowed to vary in the optimisation procedure, to account for errors in the systemic redshifts used to transform the spectra in to rest-frame wavelengths.

4.8.2 *Quality of fits*

*Look at chi-squared distribution?
Doesn't seem that reliable.*

In general, the ICA components are able to reconstruct the spectra of the objects in our sample. We also find that that in some cases, the ICA reconstructions are superior at modelling the Fe II emission than the Boroson and Green, (1992) template.

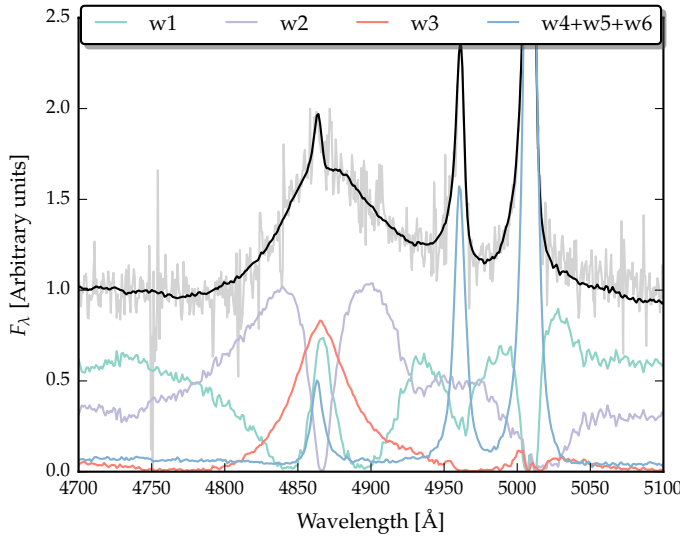


Figure 4.14: $\text{H}\beta/\text{[O III]}$ emission $\text{J}002952+020607$. The ICA reconstruction is shown in black, and the spectrum in grey. The first three components, and the sum of components four, five and six are shown individually.

Table 4.4: Physical interpretation of the ICA components.

Component	Origin
w_1	Fe II
w_2	$\text{H}\beta$
w_3	$\text{H}\beta$
w_4	$\text{[O III]} \text{ core}$
w_5	$\text{[O III]} \text{ core}$
w_6	$\text{[O III]} \text{ wing}$

4.8.3 Physical interpretation of ICA components

Although the ICA analysis is not based on any physics, there appears to be a direct correspondence between the individual components and the different emission features which contribute to the spectra (Fig. 4.14). This correspondence is summarised in Table 4.4. The component w_1 seems to correspond to Fe II emission, the components w_2 and w_3 to broad $\text{H}\beta$ emission, the components w_4 and w_5 to narrow [O III] emission at the systemic redshift, and the component w_6 to broad, blueshifted [O III] emission.

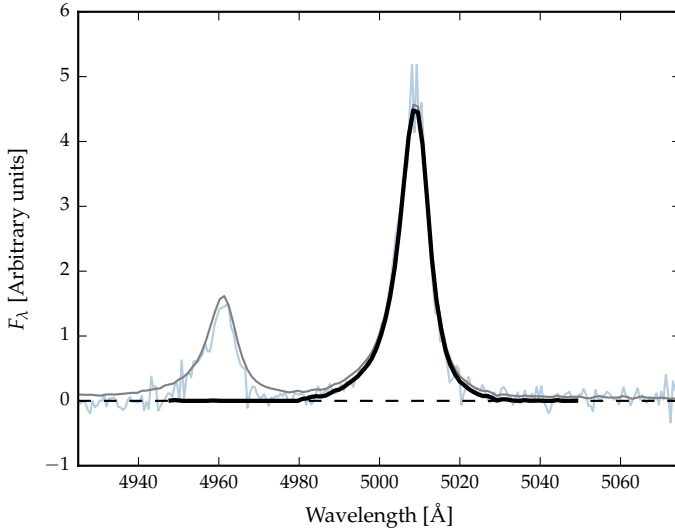


Figure 4.15: [O III] emission in J002952+020607. The data is shown in blue, and the ICA spectrum in grey. The first three ICA components have been subtracted from both the ICA composite and the data. The black curve shows the reconstructed [O III] profile.

4.8.3.1 Reconstructing the [O III] profile

In order to measure non-parametric line parameters, e.g. v_{10} , we must first reconstruct the [O III] emission. It is fortunate that most of the [O III] emission is in just three of the ICA components; the remaining three contribute very little. Therefore, we can set the first three weights to zero to leave only the [O III] emission. The four correction components are also included.

We define the boundaries of [O III] $\lambda 5008$ as being between 4950 and 5500\AA. The blue limit is close to the peak of the [O III] $\lambda 4960$ line, and so to recover the intrinsic profile we instead use the blue wing of [O III] $\lambda 4960$. We use the emission from 4980-5050\AA, and from $4900-(4980-(5008.2-4960.3))$. The blue window is then shifted by $(5008.2-4960.3)$ to reconstruct the blue wing of the [O III] $\lambda 5008$ line. We then subtract a constant, because the flux does not always go to zero (suggests that there is probably flux which is not due to [O III] emission in components four to six).

An examples of a reconstructed [O III] emission line is shown in Figure 4.15. At present I am summing the flux all the way from 4950\AA. However, this is quite a lot of flux to sum up, and we can't ascribe this flux to the wing of the [O III] emission with any certainty. This is borne out by the fact that there are quite

large differences between, for example, v_{10} measured from the Gaussian fit and v_{10} measured from the ICA fit.

Unfortunately, there are systematic differences between the line-width estimates from the Gaussian reconstructions and the ICA reconstructions, particularly for broad-line objects. The current way of doing the ICA reconstruction of the [O III] line ignores any cross-talk between the components and there is potentially flux being ascribed to the line that could be coming from some other component. We can solve this by finding some more representative broad [O III] lines in SDSS from which to derive the components as well as producing a set of components for [O III] only. Therefore we don't use these reconstructions and leave this for future work.

4.8.4 ICA fits

In Figure 4.16 we show the relative weights of each of the six positive ICA components. Also shown are the same measurements for a sample of low-redshift, low-luminosity AGN. We want to examine whether or not there are systematic differences between these two samples.

We see that [O III] core emission is weaker in the more luminous sample, but the strength of the wing component is similar. Shen and Ho, (2014) showed that the strength of the core [O III] component decreases with quasar luminosity and optical Fe II strength faster than the wing component, leading to overall broader and more blueshifted profiles as luminosity and Fe II strength (or C IV blueshift) increases. Shen and Ho, (2014) suggested that a stable NLR is being removed by the outflowing material. Similarly, Zhang et al., (2011) found that the more the peak of the [O III] line is blueshifted, the more the core component decreases dramatically, while the blue wing changes much less. Therefore, there is an anti-correlation between the strength of the core component and the relative strength of the wing component (Figure 4.18).

To show this phenomenon more clearly, we plot the relative [O III] strength and the [O III] wing/core ratio in the high/low luminosity samples (Figure 4.18). We see that [O III] is weaker in the high luminosity sample, but that the wing component is much stronger relative to the core component. .

*Similar to
behaviour of C IV?
Would suggest
that the mechanism
producing the two
correlations is the
same*

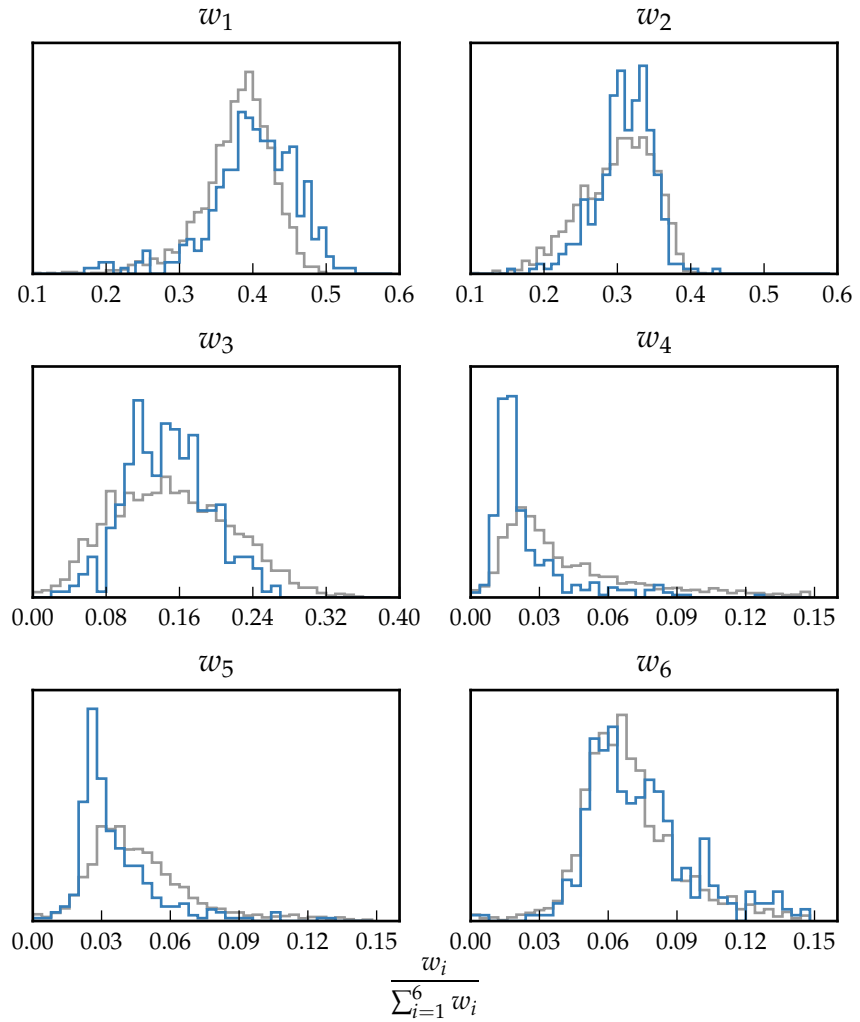


Figure 4.16: The relative weight in each of the six positive ICA components for the high-luminosity (blue) and low luminosity samples (grey). In the high-luminosity sample Fe II emission is stronger (component w_1). The core [O III] emission (components w_4 , w_5) is weaker but the strength of the blueshifted wing (w_6) is the same.

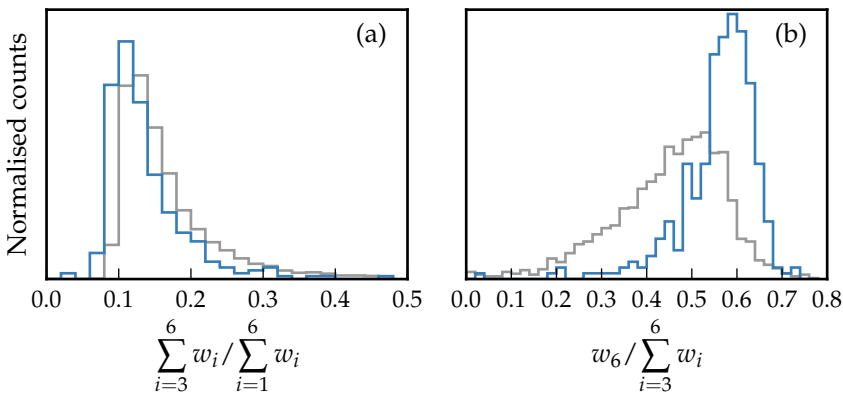


Figure 4.17: The relative weight in the three ICA components corresponding to [O III] emission (*left*) and the relative weight of the component most closely related to blueshifted [O III] emission relative to all three [O III] components (*right*). [O III] emission is weaker in the high-luminosity sample, but the relative contribution from the blueshifted component to the total [O III] emission is higher.

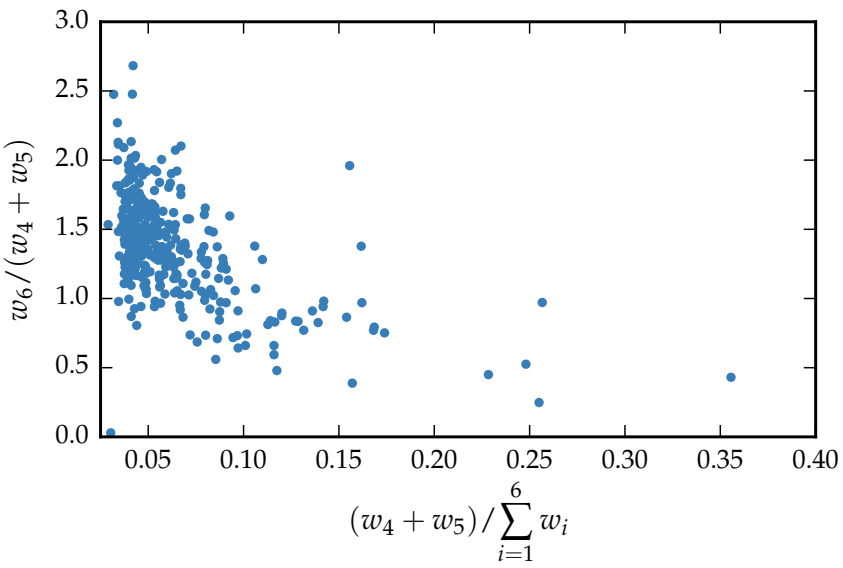


Figure 4.18: Weight in the [O III] wing relative to the weight in the [O III] core emission versus the strength of the core [O III] emission. The blue-asymmetry of the [O III] emission increases as the strength of the core component decreases.

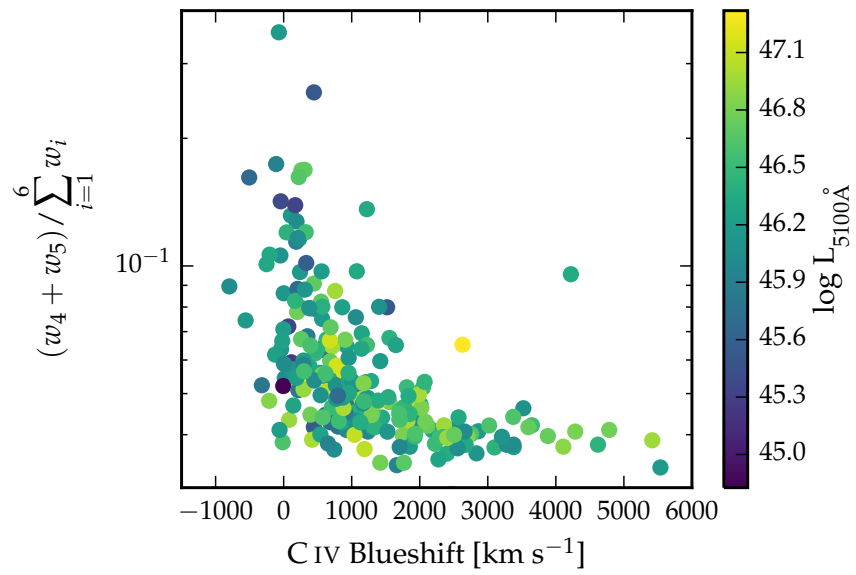


Figure 4.19: The ICA component weight w_4 , which is a proxy for the strength of core [O III], as a function of the C IV blueshift. The C IV blueshift is measured relative to the near-infrared ICA redshift.

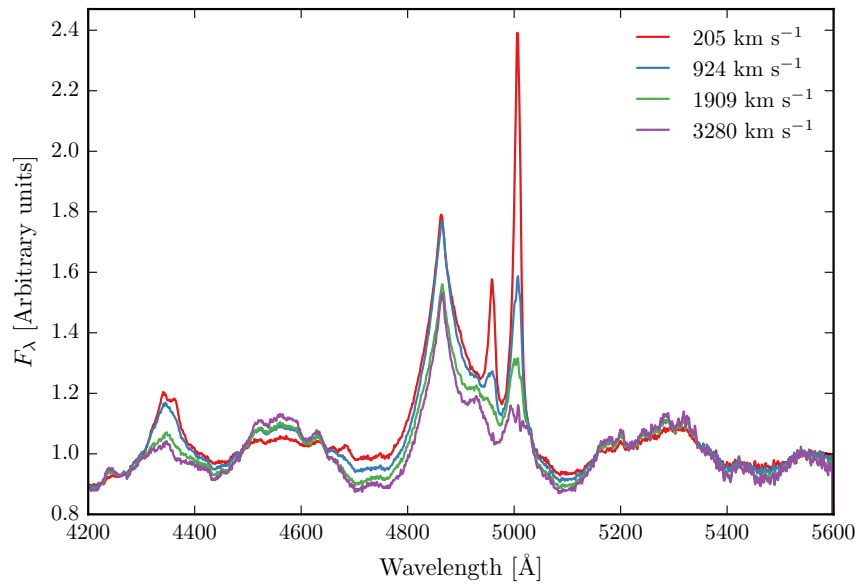


Figure 4.20: Median ICA-reconstructed spectra as a function of the C IV blueshift.

4.8.4.1 *EV1 correlations*

In Figure 4.19 we show how the [O III] strength varies as a function of the C IV blueshift. There is a very well defined relation: when C IV is strongly blueshifted [O III] is very weak. This is very similar to what we found when we used Gaussian functions to model the emission. The correlation between C IV blueshift and [O III] EQW is shown in a different way in Figure 4.20. Here we divide our sample in to four bins according to the C IV blueshift. From the quasars in each C IV blueshift bin we then find then generate an ICA spectrum using the median weights from each quasar. The differences in the spectra as a function of the C IV blueshift are dramatic. [O III] becomes progressively weaker and more blueshifted. The anti-correlation with Fe III and the blue-ward Fe II also clear, but there is no change in the redward Fe II.

4.8.4.2 *Updating EV1*

The ICA can be thought of as update on EV1. The spectral diversity is encapsulated in the EV1 components. Most of the variance in EV1 is the anti-correlation between the strengths of [O III] and Fe II. So at one end we have objects with strong Fe II and weak [O III], and at the other end objects with weak Fe II and strong [O III]. Other properties, including the C IV blueshift and the H β FWHM, also change systematically. Our work shows that the ICA component weights change systematically along the EV1 sequence.

Accurate systemic redshift estimates are essential in a number of applications, and researchers have devoted a large amount of telescope time to obtaining near-infrared spectra to access [O III] for this purpose. HI, CO and absorption line measures of the host galaxy rest frame suggest that [O III] usually gives consistent results within 200 km s^{-1} (de Robertis 1985; Whittle 1985; Wilson & Heckman 1985; Condon et al. 1985; Stripe 1990; Alloin et al. 1992; Evans et al. 2001). However, our work shows that at high luminosities this can result in large errors (profile can be dominated by blueshifted component, Fe II emission can be improperly subtracted, or [O III] might not be detected at all. [O III] is weaker and broader so it is more difficult to detect and measure [O III] accurately for these luminous quasars (to for instance obtain reliable redshift estimates based on [O III])

*Just present this as
an idea for future
work right at the
end rather than
having this
sandwiched in the
middle.*

4.8.5 Future work

Pros:

It is less sensitive to the spectral S/N, and the component weights do not need to be constrained. It is therefore much simpler to apply than fitting multiple Gaussians.

Cons:

The components were calculated using a set of lower-redshift, lower-luminosity AGN, and quasar spectra are known to vary systematically as a function of luminosity. For example, the [O III] line is typically broader in more luminous quasars. Because there are so few objects with very broad [O III] in the low-redshift sample, the ICA reconstruction fails to reproduce the broadest [O III] profiles in our sample.

Cross-talk between components.

The size of the narrow line region is roughly expected to scale as $L^{0.5}$ (e.g. Netzer et al., 2004). However, for high luminosity quasars with strong [O III] this gives NLR sizes which are unreasonably large (~ 100 kpc; Netzer et al., 2004).

See extra text from Brotherton paper. I could be confused here, but I think the Netzer argument goes that the nlr size increase with luminosity because there are more ionising photons. but then you run out of nlr to ionise. the luminosity of the quasar keeps increasing but the luminosity of the nlr flattens out. so the eqw starts to decrease. but we see a huge scatter in eqw at high luminosities. we can relate this to the C IV blueshift, which I don't think Netzer will have been able to.

We see a correlation between the [O III] velocity width and asymmetry. As the line gets broader it gets more blue-asymmetric. One interpretation of this is that the strength of the narrow core is decreasing, leading to a broader and more blueshifted profile (e.g. Shen and Ho, 2014).

[O III] is broader, which is consistent with these quasars having more massive BHs. [O III] also shows stronger blue asymmetries, suggesting that outflows are stronger/more prevalent at these higher luminosities/redshifts. The luminous blueshifted broad wing and the extremely broad profile reveals high-velocity outflowing ionized gas. Our results therefore suggest that kilo-parsec-scale outflows in ionized gas are common in this sample of high-luminosity, high-redshift quasars.

5

SED PROPERTIES

5.1 INTRODUCTION

AGN emit strongly over many decades in frequency (Figure 5.1). At different frequencies, the emission originates from processes occurring in different regions of the AGN. Hard X-ray emission is dominated by Compton up-scattering of accretion disk photons by electrons in a hot corona (e.g. Sunyaev and Titarchuk, 1980), UV/optical by thermal accretion disc emission, IR by dust at a wide range of temperatures, and radio by synchrotron emission in relativistic jets.

Significant diversity is observed in the SEDs of individual objects. However, the systematic study of the dependence of the SED shape on physical parameters has, until very recently, been limited by the difficulty in obtaining a large sample of quasars with good multi-wavelength coverage and large dynamic range in luminosity and redshift. However, we are able to take advantage of a number of recent, sensitive, wide-field photometric surveys, including SDSS (in the UV/optical), UKIDSS (in the NIR) and WISE (in the mid-infrared). We will combine this information with the BH mass and mass-normalised accretion rate estimates and outflow diagnostics which we developed in Chapters 3 and 4. We will determine whether there are SED-related systematics as a function of outflow signatures and BH mass or Eddington ratio.

Since the physical processes that power AGN are generally understood only qualitatively, almost all AGN SED templates are empirical. The empirical template of Elvis et al., (1994) is still the most commonly cited, despite many additions and updates (e.g. Polletta et al., 2000; Kuraszkiewicz et al., 2003; Risaliti and Elvis, 2004; Richards et al., 2006a; Polletta et al., 2007; Lusso et al., 2010; Shang et al., 2011; Marchese et al., 2012; Trichas et al., 2012). However, these composite spectra are often constructed from quasars with a huge range in luminosity as a function of wavelength. In addition, the presence of significant host galaxy at optical wavelengths in low-redshift objects is an additional complication which has not always been taken care of adequately. There is therefore a strong rationale for taking

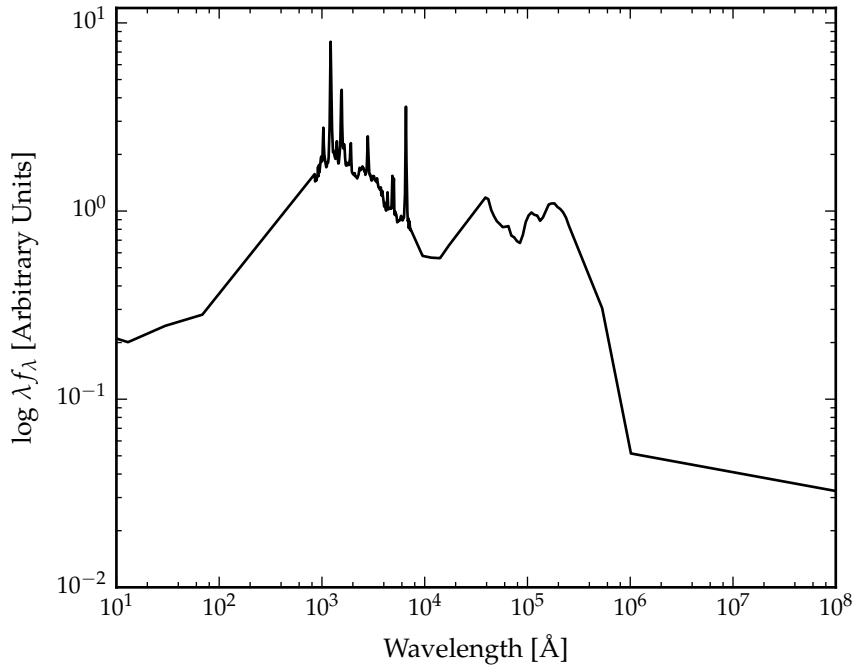


Figure 5.1: Median radio-loud SED from Shang et al., (2011).

a parametric approach to modelling quasar SEDs. This is the approach we take in this chapter. We then investigate whether the systematic dependence of the model parameters on quasar properties including the BH mass, luminosity, accretion rate and outflow diagnostics.

5.2 DATA

5.2.1 SDSS DR7

We use the Seventh Data Release (DR7) of the SDSS spectroscopic quasar catalogue (Schneider et al., 2010), which includes 105,783 objects across $\sim 9,380$ deg 2 . The SDSS obtained images in five broad optical band-passes: u , g , r , i and z (Table 5.1). We use BEST point-spread function magnitudes. Although the SDSS asinh magnitude system is intended to be on the AB system (Oke and Gunn, 1983), the photometric zero-points are known to be slightly off the AB standard. According to the documentation¹, the u band zero-point is in error by 0.04 mag ($u_{\text{AB}} = u_{\text{SDSS}} - 0.04$) while the z band is in error by 0.02

¹ <http://classic.sdss.org/dr7/algorithms/fluxcal.html>

Survey	Band	$\lambda_{\text{eff}} [\mu\text{m}]$	AB offset	$A_{\text{filter}}/E(B-V)$
SDSS	u	0.3543	0.913	4.875
	g	0.4770	-0.081	3.793
	r	0.6231	0.169	2.721
	i	0.7625	0.383	2.099
	z	0.9134	0.542	1.537
UKIDSS	Y	1.0305	0.641	1.194
	J	1.2483	0.941	0.880
	H	1.6313	1.378	0.569
	K	2.2010	1.897	0.352
WISE	W1	3.4	2.691	0.182
	W2	4.6	3.331	0.130
	W3	12.0		
	W4	22.0		

Table 5.1: Available photometry, effective wavelength, Vega to AB magnitude offsets, conversino from $E(B-V)$ to extinction.
Need W3/W4 offsets.

($z_{\text{AB}} = z_{\text{SDSS}} + 0.02$). The g, r and i zero-points are consistent with the AB system.

According to the online documentation², the magnitude of Vega in the SDSS magnitude system is $u = 0.94$, $g = -0.08$, $r = 0.17$, $i = 0.40$ and $z = 0.57$. Vega is estimated to have a magnitude $V = 0.03$ in the Vega magnitude system. We use this information to estimate the zero-point offsets from the native SDSS magnitude system to the Vega system, given in Table 5.1.

5.2.2 UKIDSS Large Area Survey

We use the tenth data release (DR10) of the UKIRT Infrared Deep Sky Survey (UKIDSS; Lawrence et al., 2007) Large Area Survey (ULAS) which has observed $\sim 3,200 \text{ deg}^2$ in four NIR band-passes: Y, J, H and K. We use ‘apermag3’ magnitudes, which are aperture corrected magnitudes in a $2''$ diameter aperture. UKIDSS magnitudes are given in the Vega system. We adopt the Vega to AB zero-point offsets derived by Hewett et al., (2006); these are given in Table 5.1.

Update this once I confirm with Paul SDSS->AB->Vega conversions

Find out why Paul’s AB offsets (given in the table) are slightly different.

² <http://classic.sdss.org/dr4/algorithms/sdssUBVRITransform.html>

5.2.3 WISE All-WISE Survey

The Wide-field Infrared Explorer (WISE; Wright et al., 2010) mapped the entire sky in four mid-IR bands: W1, W2, W3 and W4. The WISE AllWISE Data Release ('AllWISE') combines data from the nine-month cryogenic phase of the mission that led to the 'AllSky' data release with data from the NEOWISE program (Mainzer et al., 2011). We use the profile-fitting magnitudes ('w1mpro', 'w2mpro' etc.) WISE magnitudes are given in the Vega system, and Vega to AB conversion factors are given in the WISE Explanatory Supplement (Cutri et al., 2013).

Find out why Paul's AB offsets (given in the table) are slightly different.

Require S/N > 5?

Confirm with Paul how this is calculated

5.2.4 Galactic extinction correction

5.2.5 Cross-matching

Cross-matching the SDSS catalogue to the UKIDSS catalogue (with a 2" matching radius) and to the WISE catalogue (with a 3" matching radius) leaves 36,607 objects.

We include only the ZZ quasars with i band magnitudes brighter than 19.1, i.e. the quasars selected by the main SDSS quasar selection algorithm for quasars with colours consistent with being at redshifts $z < 3$ (Richards et al., 2002). Broad absorption line (BAL) quasars typically have redder spectra than non-BAL quasars. We therefore exclude these objects from our sample using the catalogue of BALs generated by Allen et al., (2011). The redshift and luminosity distribution of the final sample, containing XX quasars, is shown in Figure 5.2.

5.2.6 Completeness

For a given i magnitude, a quasar with a blue spectrum is more likely to be undetected at longer wavelengths than a quasar with a red spectrum. Therefore, as we allow fainter quasars into our sample we will be biased towards objects with redder spectra. We verified that above the $i = 19.1$ limit the sample is 95% complete in all band-passes (excluding WISE W3 and W4).

This section needs clarification.

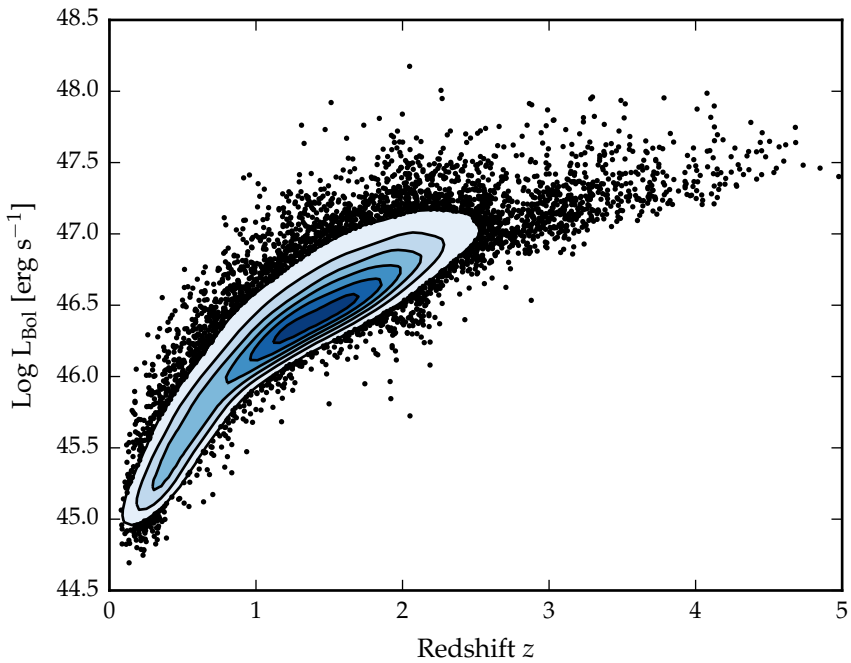


Figure 5.2: Distribution of our sample in the redshift-luminosity plane. **Remake with new sample**

5.2.7 Generating the quasar catalogue

5.3 QUASAR SED

We have 19,853 quasars with photometric data from SDSS, UKIDSS and WISE. Our quasars cover the redshift range $0.2 < z < 4$, and so this data covers the rest-frame wavelength range from 800Å to 3.8μm. In this region the SED is dominated by the accretion disc, emission lines and thermal emission from the hottest ($T \sim 1200\text{K}$) dust. Host galaxy emission is also significant for quasars at redshifts $z \lesssim 1$, and the effect of dust extinction at the AGN redshift is another factor which must be considered. In this section, we describe how we have modelled emission from these different physical processes. The model spectrum is shown in Figure 5.3, with each of the main components indicated.

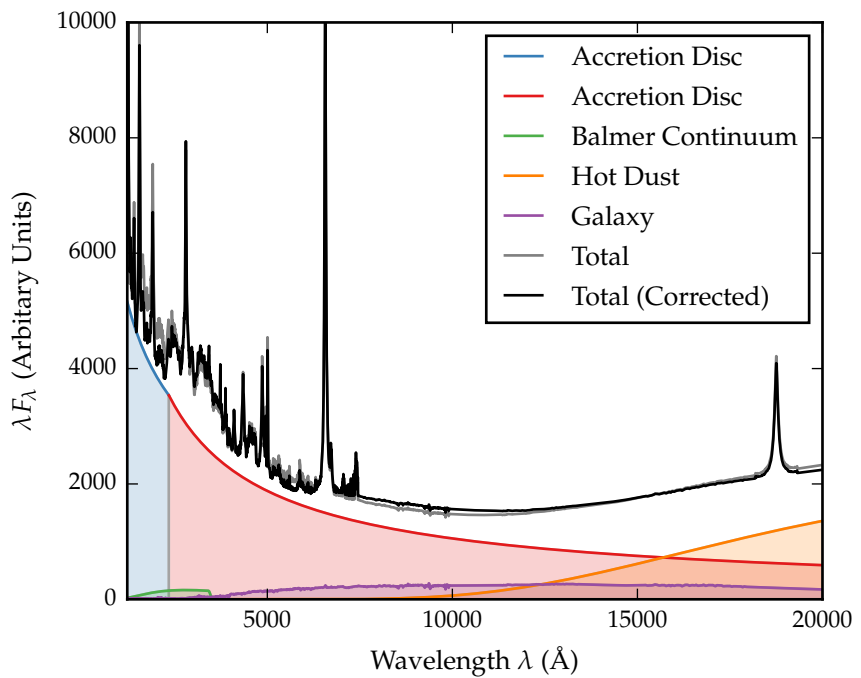


Figure 5.3: Model quasar spectrum at $z = 1$, showing the contributions to the total flux from the blue power-law slope, red power-law slope, Balmer continuum, blackbody, emission line spectrum and host galaxy. **Make sure it is immediately clear in every caption what is being shown in the figure.**

5.4 SED MODEL

5.4.1 Accretion Disc

Thermal accretion disc emission in the 0.1 - 1 μm region is characterised by a broken power-law with three free parameters: a break-wavelength λ_{break} , a blue power-law index α_{blue} for wavelengths shorter than the break wavelength, and a red power-law index α_{red} for wavelengths longer than the break wavelength.

5.4.2 Balmer Continuum

High order Balmer lines, optically thin Balmer continuum emission, two-photon emission and Fe II emission blend together to form a distinct feature in quasar spectra at $\sim 3000\text{\AA}$. We simulate the Balmer continuum we use the empirical model given by Grandi, (1982):

$$F(\lambda) = C_{\text{BC}} \times B_\lambda(T_e)(1 - e^{-\tau_\lambda}); \quad \lambda \leq \lambda_{\text{BE}} \quad (5.1)$$

where C_{BC} is a normalisation factor, $B_\lambda(T_e)$ is the Planck function, $T_e = 13150\text{K}$ is the effective temperature, $\lambda_{\text{BE}} = 3460\text{\AA}$ is the wavelength at the Balmer edge, and $\tau_\lambda = \tau_{\text{BE}} (\lambda_{\text{BE}}/\lambda)^{-3}$ is the optical depth with $\tau_{\text{BE}} = 45$ the optical depth at λ_{BE} . This function is convolved with a Gaussian with $\sigma = 5000\text{km s}^{-1}$ to simulate the effect of bulk velocity shifts comparable to those present in broad AGN emission lines.

5.4.3 Hot Dust

Thermal emission from hot dust, which dominates the SED at wavelengths longer than $1\mu\text{m}$, is modeled using a blackbody

$$F_\lambda = C_{\text{BB}} \times \frac{2hc^2}{\lambda^5} \frac{1}{e^{\frac{hc}{\lambda k_B T_{\text{BB}}}} - 1}, \quad (5.2)$$

with two free parameters: the temperature T_{BB} and normalisation.

5.4.4 Emission Lines

We use an emission line template taken from Francis et al., (1991), which has been extended by Maddox and Hewett, (2006)

to include the H α and Pa α emission lines ³. All emission lines, with the exception of H α , are scaled using a single free parameter C_{EL} , which preserves relative EQWs:

$$F_\lambda = C_{\text{EL}} \times \frac{F_{\lambda,\text{el}}}{F_{\lambda,\text{cont}}} \times F_\lambda; \quad \lambda < 4700\text{\AA} \text{ and } \lambda > 7000\text{\AA} \quad (5.3)$$

where $F_{\lambda,\text{el}}$ is the emission line template, $F_{\lambda,\text{cont}}$ is the continuum flux in the template, and F_λ is the continuum flux in the SED model. H α , one of the strongest broad emission lines, is scaled separately:

$$F_\lambda = C_{\text{EL}} \times C_{H\alpha} \times \left(\frac{L(z)}{L(z_{\text{nrm}})} \right)^{-\beta} \times \frac{F_{\lambda,\text{el}}}{F_{\lambda,\text{cont}}} \times F_\lambda; \quad 4700\text{\AA} < \lambda < 7000\text{\AA} \quad (5.4)$$

The luminosity dependence of the H α EQW (i.e. the Baldwin effect) is parametrised with a power-law with slope $\beta = 0.04$. The redshift dependence of the mean AGN luminosity $L(z)$ for the SDSS quasar catalogue has been determined empirically.

5.4.5 Host Galaxy

Emission from the host galaxy is important for AGN at redshifts $z \lesssim 1$, particularly in the region around the 1 μm inflection point in the quasar SED. We use a $z = 0$ Sb template from Mannucci et al., (2001), which does not evolve with redshift. The template is scaled by a multiplicative factor C_{Gal} and added to the AGN SED. We define a new parameter, η , the fractional contribution from the host galaxy to the total flux in the interval 4000 and 5000 \AA :

$$\eta \equiv \frac{C_{\text{Gal}} F_{\text{Gal}}}{F_{\text{AGN}} + C_{\text{Gal}} F_{\text{Gal}}}, \quad (5.5)$$

where F_{Gal} and F_{AGN} are the flux of the galaxy and AGN respectively. Rearranging for the scaling factor C_{Gal} gives:

$$C_{\text{Gal}} = \frac{\eta}{1 - \eta} \frac{F_{\text{AGN}}}{F_{\text{Gal}}}. \quad (5.6)$$

³ The spectrum is not significantly different from the Vanden Berk et al., (2001) SDSS composite

The fractional contribution to the total emission from the host galaxy decreases as the AGN luminosity increases and, in a flux-limited sample, the mean AGN luminosity increases as the redshift increases. Therefore, the size of the host galaxy contribution to the SED is diminished for AGN at high redshifts ($z \gtrsim 1$). At the same time, the shapes of the AGN and galaxy SEDs are very different. The galaxy SED peaks at $\sim 1\mu\text{m}$, and falls away towards shorter wavelengths. On the other hand, the AGN SED continues to increase shortward of $1\mu\text{m}$. Therefore, the contrast between the AGN and galaxy luminosity increases as the redshift increases. We parametrize the AGN luminosity dependence of the host galaxy luminosity as a power-law:

$$\frac{L_{\text{Gal}}}{L_{\text{AGN}}} = L_{\text{AGN}}^{\beta-1} \quad (5.7)$$

with slope $\beta = 0.42$ (Croom et al., 2004). The galaxy scaling factor C_{Gal} becomes

$$C_{\text{Gal}} = \frac{\eta}{1-\eta} \frac{F_{\text{AGN}}}{F_{\text{Gal}}} \left[\frac{L_{\text{Gal}}(z)}{L_{\text{AGN}}(z)} \right] \left[\frac{L_{\text{Gal}}(z_{\text{nrm}})}{L_{\text{AGN}}(z_{\text{nrm}})} \right]^{-1} \quad (5.8)$$

$$= \frac{\eta}{1-\eta} \frac{F_{\text{AGN}}}{F_{\text{Gal}}} \left[\frac{L_{\text{AGN}(z)}}{L_{\text{AGN}(z_{\text{nrm}})}} \right]^{\beta-1}, \quad (5.9)$$

where z_{nrm} is an arbitrary redshift at which the fractional contribution from the host galaxy is by definition η .

5.4.6 Dust Extinction

The selection criteria of the SDSS DR7Q catalogue are sensitive to quasars with moderate amounts of dust reddening at the redshift of the quasar, and so we included the effect of dust extinction in our model. We use an extinction curve appropriate for the quasar population which has been derived by Paul Hewett. To derive the quasar extinction curve, UKIDSS photometry was used to provide an $E(B-V)$ ⁴ estimate, via the magnitude displacement of each quasar from the locus of un-reddened objects. At redshifts $2 < z < 3$ the reddening measure is made at rest-frame wavelengths 3500-7000Å, where Galaxy, LMC and SMC extinction curves are very similar. The SDSS spectra of the same objects are then employed to generate an empirical extinction

⁴ $E(B-V) = A(B) - A(V)$

curve in the ultraviolet, down to 1200Å. The resulting curve has no 2200Å feature and rises rapidly with decreasing wavelength but is not as steep as the SMC curve. The extinctions curves give the colour excess $E(B - \lambda) = A$ relative to the colour excess $E(B - V)$ as a function of wavelength λ . The ratio of total to selective extinction, R , is defined as:

colour excess $E(B - V)$ is related to the extinction in the V band, $A(V)$, via the ratio R ,

$$R_V = \frac{A(V)}{E(B - V)} \quad (5.10)$$

where we assume $R_V = 3$. Hence the extinction at a wavelength lambda $A(\lambda)$ is

$$A(\lambda) = E(B - V) \times \left[\frac{E(\lambda - V)}{E(B - V)} + R \right] \quad (5.11)$$

where the colour excess $E(B - V)$ is a free parameter in our model. The attenuation of the flux at a given wavelength is then:

$$F_\lambda = F_\lambda 10^{-A(\lambda)/2.5} \quad (5.12)$$

in the rest frame of the quasar.

5.4.7 Empirical Correction

Describe Paul's empirical correction.

5.5 THE 'STANDARD' SED MODEL

- Given the same parameters, my model and Paul's look identical
- I'm generating model colours using my model and Paul's best-fit parameters, and Paul's correction
- Do my model colours look the same as Paul's? (i.e. is there a bug in my code?)
- Can I generate the same median colours as Paul? (i.e. what sample is being used? what magnitudes?)

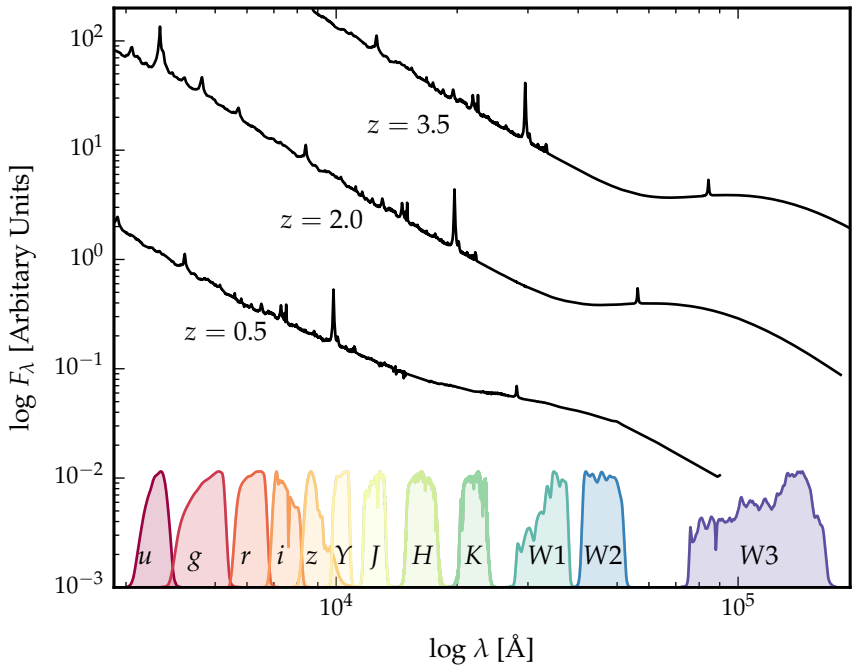


Figure 5.4: Model quasar spectrum at three different redshifts (each arbitrarily scaled), and throughput functions for SDSS, UKIDSS and WISE band-passes.

- **Can I do my own fit to the data?**

We will begin by fitting a single SED model to all 19,853 quasars, encompassing a range of redshifts, luminosities, accretion rates etc. The free parameters in our model are the blue power-law slope, the red power-law slope, the power-law break wavelength, the blackbody temperature, the blackbody normalisation, the emission line EQW scaling, the H α scaling and the fractional contribution from the host galaxy to the total flux. The reddening E(B – V) is fixed to zero, since a large fraction of SDSS quasars have very small amounts of dust reddening (Richards et al., 2003). We generate a set of model observed spectra at redshifts from $z = 0.25$ to $z = 3.75$ in intervals of $\Delta z = 0.1$. The SED model is shown at three different redshifts in Figure 5.4. The predicted broadband magnitude of the model is given by integrating the spectrum over the throughput for each of the bands.

$$m_\lambda(P) = -2.5 \log(f_\lambda(P)) - m_0(P), \quad (5.13)$$

where $m_0(P)$ is the zero-point magnitude of band P and the mean flux density $f_\lambda(P)$ is given by

$$f_\lambda(P) = \frac{\int P(\lambda) f_\lambda(\lambda) \lambda d\lambda}{\int P(\lambda) \lambda d\lambda} \quad (5.14)$$

where $P(\lambda)$ is the dimensionless throughput function of the band-pass. Magnitudes are calculated in the AB system (Oke & Gunn 1983), in which case the zero-point flux per unit wavelength is

$$\frac{f_\lambda(\lambda)}{\text{erg cm}^{-2} \text{s}^{-1} \text{\AA}^{-1}} = 0.1087 \left(\frac{\lambda}{\text{\AA}} \right)^{-2}. \quad (5.15)$$

We divide our quasar sample into the same redshift bins. In each bin we normalise the quasar SEDs in the SDSS i band, and then calculate the median SED. The model SED in each redshift bin is similarly normalised. The chi-squared statistic is then minimised using the ‘nelder-mead’ algorithm ([reference](#)).

Our SED model is valid only up to $\lambda \sim 3\mu\text{m}$ in the quasar rest frame (the approximate wavelength of the peak in hot dust emission); beyond this additional contributions to the total flux from cooler dust will become significant. This prevents us from using the two longest wavelength WISE bands in the fit. We also exclude the SDSS u and g band-passes from the fit at $z > 2.7$ and $z > 3.7$ respectively, where these bands start to be affected by Ly α forest absorption.

5.6 RESULTS

Re-do fit

Need to show individual quasars.

The best-fitting parameters from the fit are shown in Table 5.2. The colours ($u - g$, $g - r$, etc.) of the median SED, the individual quasars, and the best-fitting model are plotted as a function of redshift in Figs. 5.5 and 5.6. Most of the large variations that can be seen in the median colours of the quasars as a function of redshift are due to strong emission lines being redshifted into and out of the band-passes. Take away message is that a single, fairly simple parametric is able to reproduce the median colours of tens of thousands of AGN with a large dynamic range in redshift and luminosity. However, there is a significant scatter about the median model, which we will investigate in the next section? Does any part of this scatter have a systematic dependence on properties of the BH (mass, accretion rate) or outflow diagnostics.

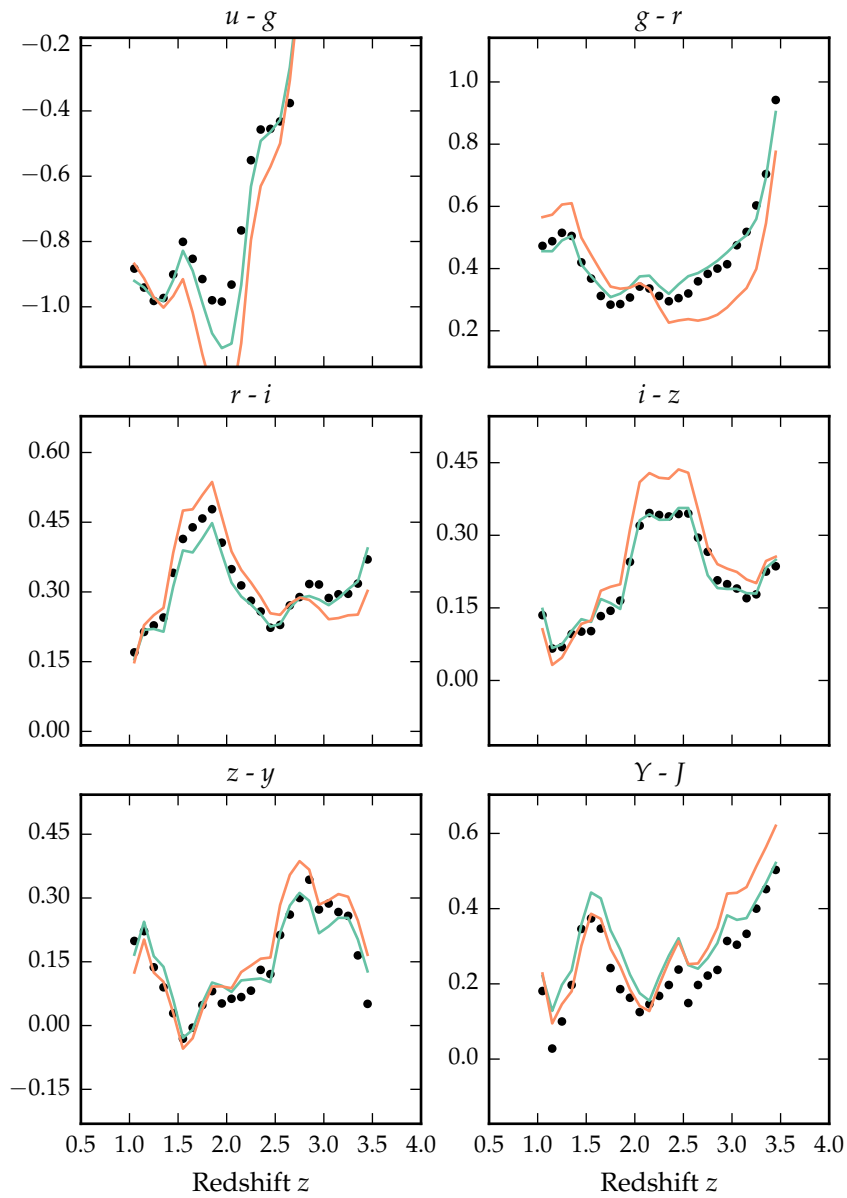


Figure 5.5: Colours of median quasar SED and best-fitting model, with and without correction. **Corrected** is in orange, uncorrected in green. Check with Paul. Correction often makes colours a lot worse. Once got to the bottom of this just show with correction. Is Lyman forest absorption / lyman limit important for the quasars shown here?

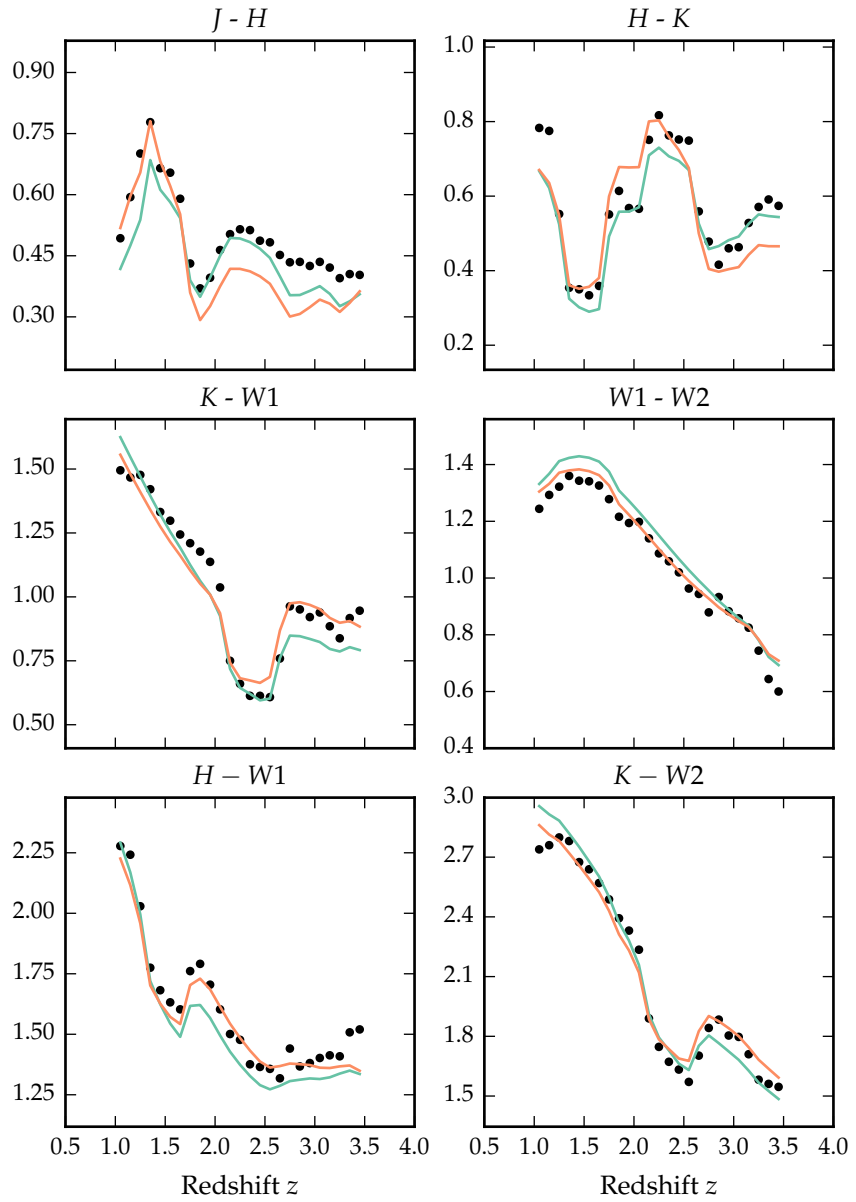


Figure 5.6: Colours of median quasar SED (black circles), individual objects (grey points), best-fitting model (black line) as a function of redshift.

Parameter	Symbol	Value
Blue power-law index	α_{blue}	0.58
Red power-law index	α_{red}	-0.04
Power-law break	λ_{break}	2945
Blackbody temperature	T_{BB}	1216 K
Blackbody normalisation	C_{BB}	0.22
Emission line scaling	C_{EL}	0.63
H α emission line scaling	$C_{\text{H}\alpha}$	0.63
Galaxy fraction	η	0.29
E(B-V)	E(B-V)	0.00

Table 5.2: Model parameters.

5.7 DISCUSSION OF FIT

In Figure 5.7 we show the difference between the magnitudes from the best-fitting model and the median magnitudes from the sample. We have transformed the effective wavelengths of the band-passes to the rest frame of the quasars in each redshift bin, to give the residuals as a function of rest-frame wavelength. We represent the residuals measured in each band-pass using a different coloured line. Differences between residuals from different band-passes at the same rest-frame wavelength could indicate redshift evolution of the typical quasar SED.

The residuals indicate that over a large redshift range the model does a fairly good at reproducing the median observed colours of the sample. Most discrepancies are at the < 0.1 mag level. A single model is effective at reproducing the median colours, suggesting that the properties of a typical quasar do not change significantly over a wide range of redshifts and luminosities. Many authors have found no significant dependence of the mean SED on properties such as redshift, bolometric luminosity, BH mass, or accretion rate (e.g. Elvis et al., 2012; Hao et al., 2013). On the other hand, there is significant intra-sample variation.

5.8 HOT DUST

The spread in the KW1W2 colours (Figure 5.8), probing the rest-frame \sim 1-2 micron region, is significant and strongly suggests

No: be quantitative

Make sure this is emphasised as a new result.

Need individual points on plot to show this.

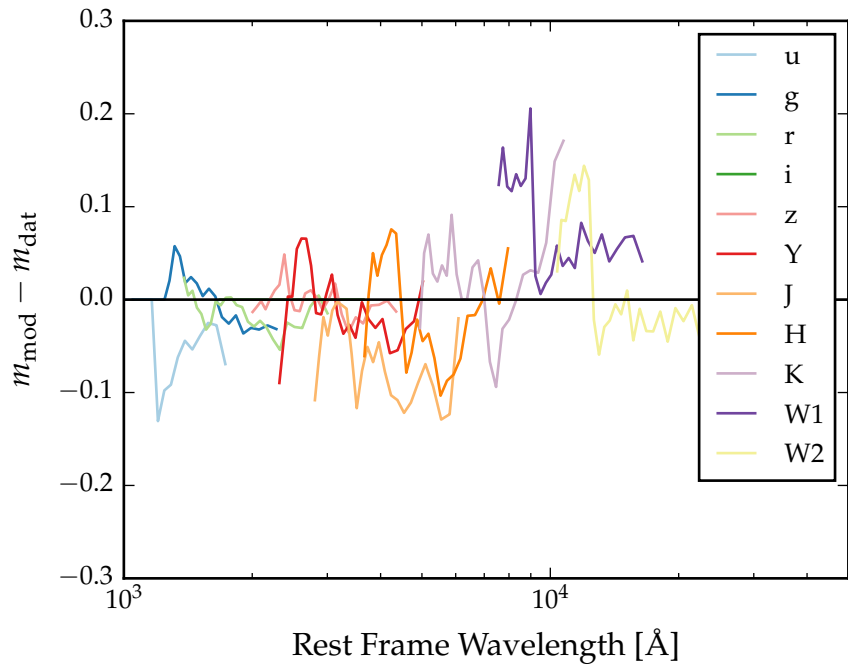


Figure 5.7: Residuals from fit as a function of rest-frame wavelength.
Need more info in caption.

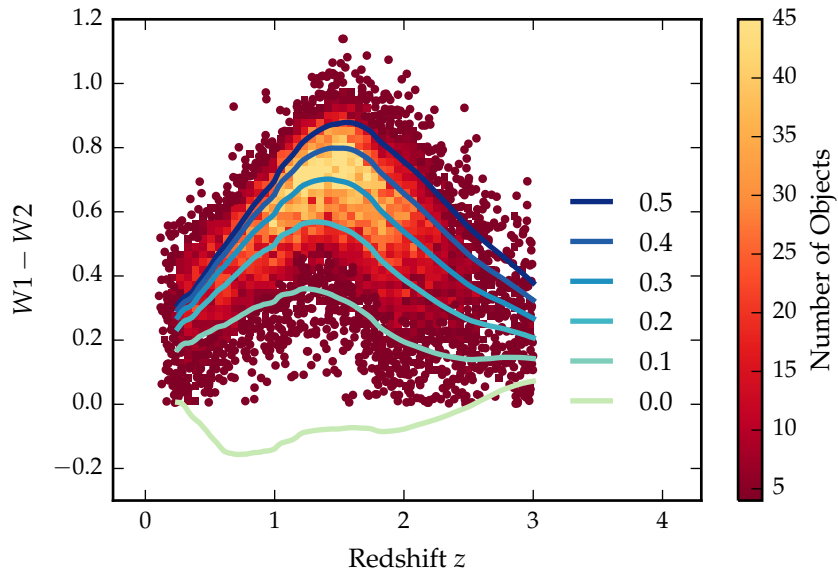


Figure 5.8: $W_1 - W_2$ colours of sample as a function of redshift.
Above a certain density threshold points are represented by a density plot. On top we plot the colours of our standard SED model, with a fixed temperature and a varying NIR ($1 - 3 \mu\text{m}$) to UV ratio.

the presence of real variation in the hot dust temperature and luminosity among the quasars.

5.8.1 *Parametrising the hot dust emission*

We characterise the hot dust properties of our sample in terms of the temperature and luminosity of a blackbody. We choose to parametrise the luminosity in terms of the NIR to UV luminosity ratio (which is proportional to the covering factor of hot dust ($L_{\text{NIR}}/L_{\text{Bol}}$) used in other studies (Roseboom et al., 2013)). The UV and NIR luminosity are calculated between 2000 and 9000Å and 1 and 3 μm respectively.

If the hot dust emission is dominated by emission from the inner edge of a torus, then the temperature is related to the distance from the dust to the central source. If the inner edge of the torus is further from the accretion disc, then the dust will be cooler. If instead the dust is in an outflows, then the interpretation of the dust temperature is less clear. The value of ($L_{\text{NIR}}/L_{\text{Bol}}$) is related to the covering factor of the hot dust.

Some previous studies (e.g. Wang et al., 2013; Zhang et al., 2014) have instead parametrised the NIR emission using a power-law ($\propto \lambda^{\beta_{\text{NIR}}}$), with $\beta \simeq 0.5$. We tested this parametrisation, and evaluated it's effectiveness relative to using a blackbody. We normalise the power-law at 9000Å, where its flux is set equal to the flux of the UV/optical model. The NIR power-law slope is fit between ~1 and 2.4μm (with the exact wavelength region being fit depending on the redshift of the quasar). We found large residuals in the best-fitting model which varied systematically as a function of $\lambda_{\text{eff}}/(1+z)$. This suggests that the power-law model is a poor fit to the shape of the NIR emission. One needs to take care in looking at trends with luminosity given the observed-frame band-pass information on the rest-frame SED can produce some strong systematics with redshift, particularly if the SED-model is not a good fit to the actual SED. A similar conclusion was reached by Gallagher et al., (2007).

5.8.2 *Sample*

Our goal is to determine the temperature and abundance of the hot dust component in individual quasars. These properties will be measured by fitting a model to the SDSS-UKIDSS-WISE photometry. Constraining a T~1200K blackbody component in

Sub-sample	Number of AGN	Data	Redshift range
Low-z	5,910	ugrizYJHKW1W2	$1 < z < 1.5$
High-z	1,989	ugrizYJHKW1W2W3	$2 < z < 2.7$

Table 5.3: Summary of sub-samples.

the SED model requires photometric data covering $\sim 1\text{--}3\mu\text{m}$ in the rest-frame of the quasar.

The observed-frame wavelength coverage of the available band-pass limits the redshift range of the quasars which can be used. We consider only quasars at redshifts $z > 1$ where the relative host galaxy contribution to the SED is negligible. At redshifts $1 \lesssim z \lesssim 1.5$ the available ugrizYJHKW1W2 photometry provides good coverage of the rest-frame SED up to $\sim 2\mu\text{m}$. At $z \sim 1.5$ the W2 band-pass is shifted to $\sim 1.8\mu\text{m}$; at higher redshifts W2 is probing much shorter wavelengths than the peak of a $T \sim 1200\text{K}$ blackbody. Because the shape of the blackbody is not well constrained by the available photometry, the uncertainty on the blackbody temperature measurement increases sharply for quasars at redshifts $z \gtrsim 1.5$.

For the quasars at $z \sim 1$, the WISE W₃ band is probing rest-frame wavelengths of $\sim 5\text{--}6\mu\text{m}$. This region of the SED is dominated by emission from cooler, more distant dust, which is not accounted for in our model. However, at redshifts $z \gtrsim 2$ the WISE W₃ band-pass probes sufficiently short wavelengths to be useful in constraining the shape of the hot blackbody component. Therefore, for quasars at redshifts $z > 2$ we again have sufficient constraints from the ugrizYJHKW1W2W3 photometry to determine the temperature and normalisation of the blackbody component. There are few objects in our sample with redshifts $z > 2.7$, because the SDSS DR7 quasar selection algorithm is highly incomplete at these redshifts. Therefore we set $z = 2.7$ as the upper limit on the redshift of our sample. Because of these constraints, our sample is divided into two parts: one at low redshifts ($1 < z < 1.5$) and the other at higher redshifts ($2 < z < 2.7$).

We impose a lower-limit signal-to-noise ratio ($S/N > 5$) magnitudes in the K, W1 and W2 band-passes for the low-z sample and $S/N > 5$ in the W1, W2, and W3 band-passes for the high-z sample to ensure reliable photometry. This gives us 5,910 quasars in our low-z sample and 1,989 quasars in our high-z sample.

We will hold most model parameters fixed, and vary only the blackbody parameters which parametrise the NIR emission. Therefore, we need to define a sub-sample of objects which we know are well fit by our standard SED model in the UV/optical region. This means excluding objects with extreme emission line EQWs and/or significant dust extinction. We use the $i - K$ colours of the quasars as a measure of the overall colour of the quasars as it provides the longest baseline in wavelength without being affected by absorption in the Ly α forest at high redshifts. A significant amount of the scatter in $i - K$ can be attributed to intrinsic variations in the UV power-law slopes of the individual quasars, which is why we allow a negative reddening. However, there is a clear ‘red tail’ to the colour distribution which can be explained by dust reddening at the redshift of the quasar. We discarded from our sample quasars with $i - K$ colours redder than our standard model with dust reddening $E(B-V) = 0.075$ and bluer than $E(B-V) = -0.075$ (Figure 5.9). Following this cut we are left with 4,615 quasars in our low- z sample and 1,692 quasars in our high- z sample.

The SDSS and UKIDSS photometry are separated by 3-4 years in the source rest-frame. Therefore, some of the $i - K$ scatter could be due to temporal variations in the brightness of the targets. However, the red-asymmetry of the $i - K$ colours about the un-reddened SED model suggests that this effect is sub-dominant to intrinsic colour differences.

5.8.3 Diversity in hot dust properties

In Figure 5.8 we plot the $W1 - W2$ colours of the sample as a function of redshift at $z < 3$. In this redshift range the $W1$ and $W2$ band-passes are probing the $1.2 - 2.8\mu\text{m}$ and $1.6 - 3.8\mu\text{m}$ region of the rest frame SED respectively. For reference, the peak wavelength is at $2.4\mu\text{m}$ for a blackbody radiating at 1200K . At any given redshift we see a ~ 0.5 mag dispersion in the $W1 - W2$ colours.

On the same axes in Figure 5.8 we have plotted the $W1 - W2$ colours derived from our SED model with a fixed blackbody temperature (1216K) and a ratio of NIR to UV luminosity ranging from 0.0 to 1.0, with the other model parameters held constant. We conclude that even with the sample restricted to be uniform in its UV/optical properties, we still get an significant spread in $W1 - W2$ colours, which we can use to learn about the diversity of NIR properties in our sample. In the rest of

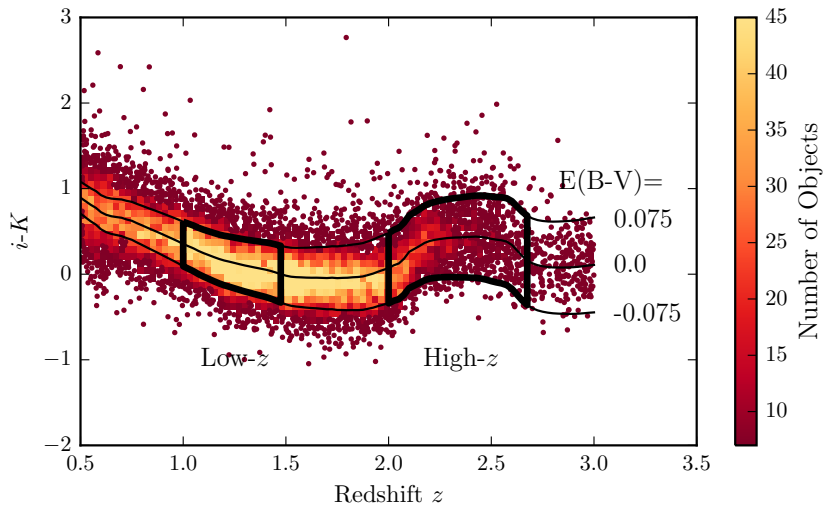


Figure 5.9: $i - K$ colours of non-BALQSO DR7Q quasars with $i > 19.1$ as a function of redshift. The lines show the colours of our model with varying amounts of dust extinction. Quasars with extinction $|E(B - V)| > 0.075$ are excluded.

in this chapter we will characterise the hot dust properties of our sample, and test its relation to quasar properties such as luminosity, black-hole mass and normalised accretion rate, and outflow-properties.

5.9 FITTING PROCEDURE

We will fit a model to the individual quasar SEDs, allowing the temperature and normalisation of the black body component to vary. The model spectrum is redshifted to the redshift of the quasar being fit and is then multiplied by the ugrizYJHMW1W2W3 throughput functions and normalised appropriately to give AB magnitudes. We minimise the chi-squared statistic using the minimisation is done using the ‘nelder-mead’ algorithm. To avoid significant absorption in the Ly α forest at high- z , we restrict our fitting to wavelengths greater than 2000Å; when the effective wavelength of a band-pass falls below this limit the band-pass is excluded from the fit. W3 is only used for the quasars at redshifts $2 < z < 2.7$.

*2000Å is quite large
given the Ly-alpha
forest impacts from
1216Å.*

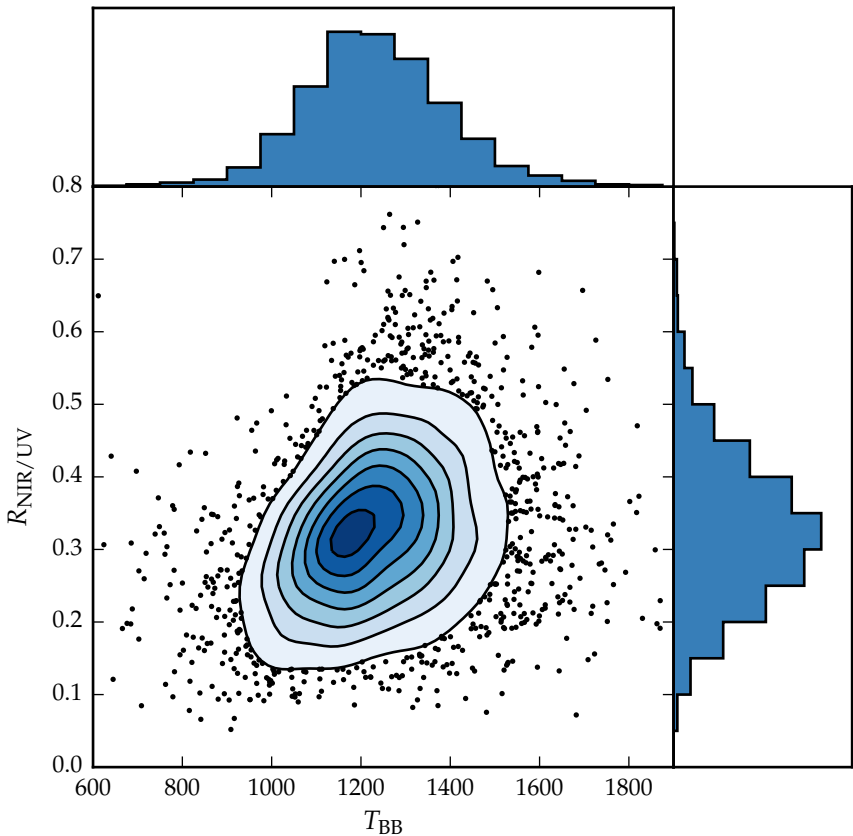


Figure 5.10: Ratio of NIR to UV luminosity ($R_{\text{NIR/UV}}$) against temperature (T_{BB}) for low- z sample. The density of points is shown in more dense regions of the space, and individual objects in less dense regions.

5.10 RESULTS

In Figure 5.10 we see that the two parameters are clearly correlated. For a lower temperature blackbody the NIR to UV luminosity ratio is larger. Such a correlation is to be expected: as the blackbody temperature is lowered, the peak shifts to longer-wavelengths (following Wien's displacement law). Because of this degeneracy we need to be very careful to separate out real trends of $R_{\text{NIR/UV}}$ with other quasar properties from indirect trends resulting from a mutual dependence on T_{BB} .

In Figure 5.10 we show that there is significant range of temperature and normalisation present in our sample. However, we need to quantify how much of this is due simply to uncertainties in the fits stemming from uncertainties in the photometry. In order to achieve this we took our standard SED model with

Show some example
fits? Show
overlaid
data/model with
alpha=0.1?

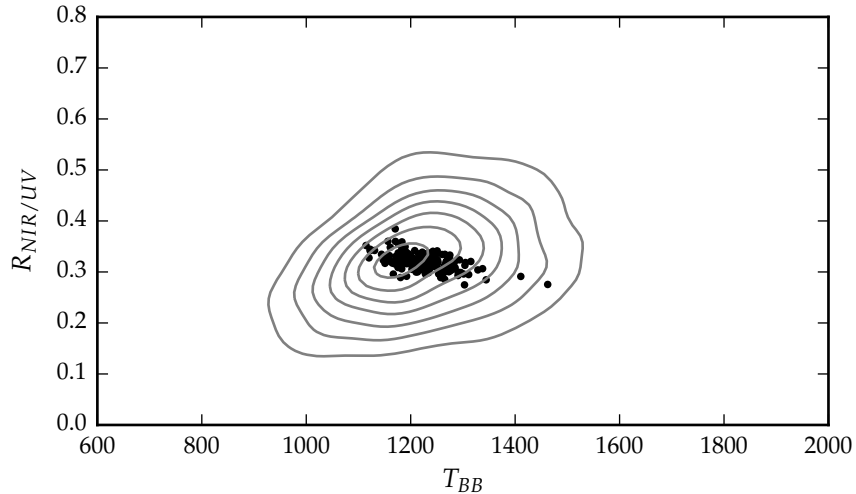


Figure 5.11: Ratio of NIR to UV luminosity ($R_{\text{NIR/UV}}$) against temperature (T_{BB}). The grey contours show equally-spaced lines of constant probability density generated using a Gaussian kernel-density estimator on our data sample. The black points are for our mock data.

a single temperature and normalisation blackbody component, and generated 200 mock SEDs with a brightness distribution similar to that of our real sample. We estimated the mean uncertainty of the magnitudes in the K, W1, and W2 band-passes as a function of apparent brightness. We then sampled the K, W1, and W2 magnitudes from Gaussian distributions, with a mean equal to the magnitude of the model SED, and the width equal to the mean uncertainty at the appropriate brightness. Finally, we fit these mock SEDs using our standard fitting procedure. The results are shown in the Figure below, on top of the results from our real sample (shown as grey contours). We can see that uncertainty in the photometry introduces a significant scatter to the temperature, but that this scatter is significantly less than the intrinsic scatter in the data. This demonstrates that there is a real distribution of hot dust temperatures and luminosities in our sample.

5.10.1 Correlations with quasar properties

We now look for correlations between the properties of the blackbodies we have fitted to the hot dust emission and other properties of the quasar such as redshift, BH mass, normalised accretion rate (Eddington ratio), and outflow diagnostics.

Calculate new BH masses and redo this section.

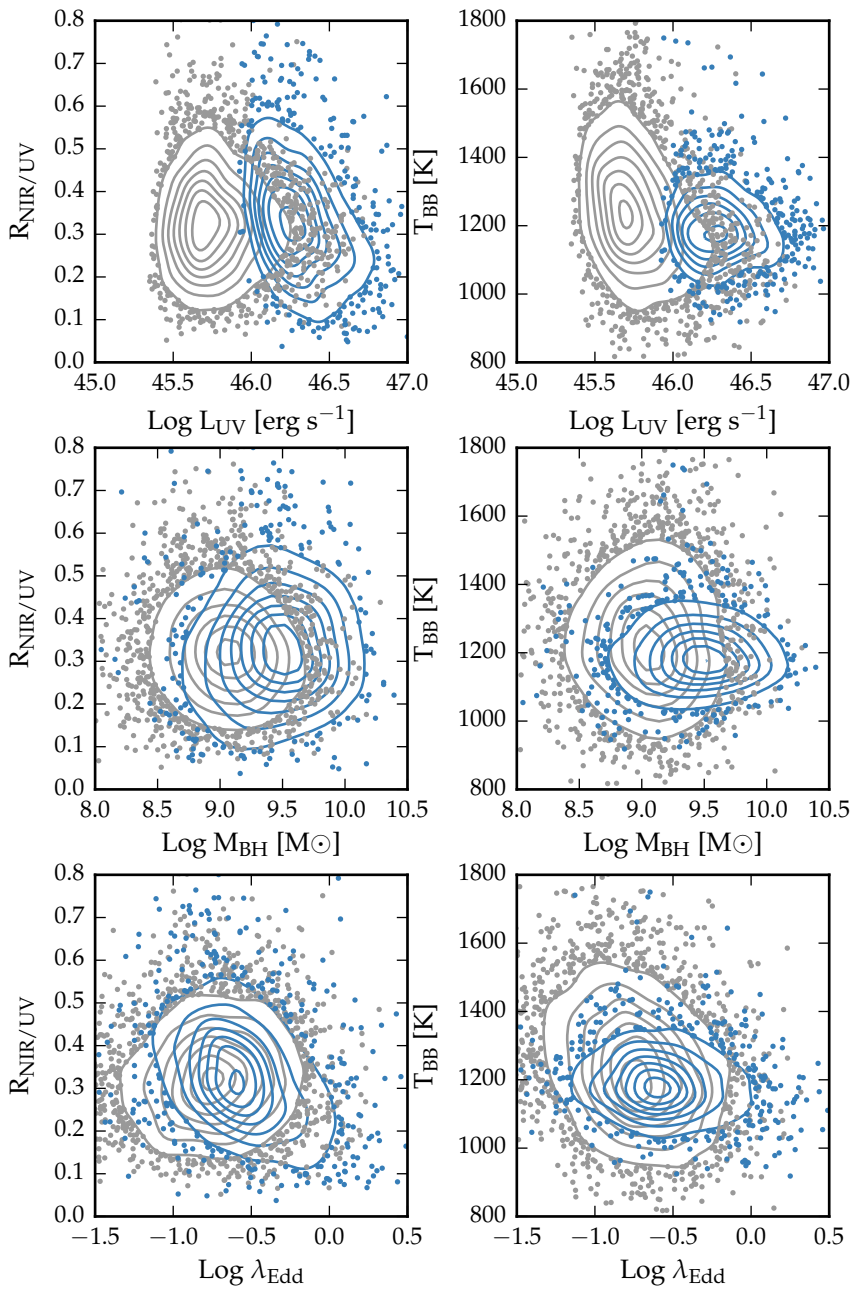


Figure 5.12: Best-fit blackbody temperature against UV luminosity (left), black-hole mass (centre) and Eddington ratio (right) for $1 < z < 1.5$ sample (black) and $2 < z < 2.7$ sample (black). In region of high-density we represent the density with contours generated using a Gaussian kernel density estimation. **Needs re-making with new BH masses. Maybe just show as one sample?**

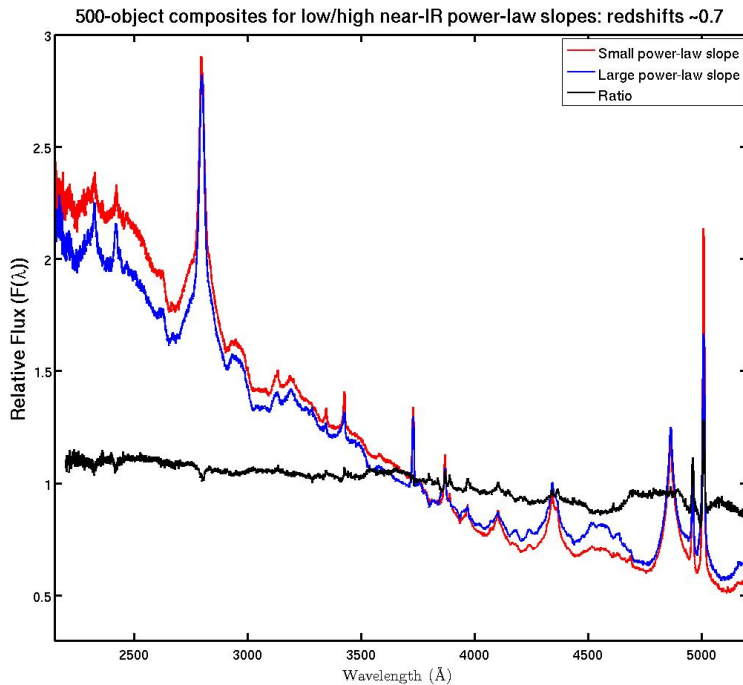


Figure 5.13: Composite SDSS spectra for objects at $z \sim 0.7$. We have divided sample into objects with objects best-fit by small (red line) and large (red line) values of β . **Remake if possible.**

5.10.1.1 Composite spectra

Is there a connection between the hot dust properties and EV₁? To test this we can divide the quasar sample by hot dust properties, and then generate composite spectra. The EV₁ original EV₁ correlates - Fe II, H β , [O III] - are at around 4000-6000 \AA . The SDSS spectra are probing shorter wavelengths at redshifts $z \gtrsim 1$. Recall that our sample does not include any quasars at redshifts $z < 1$, where the host galaxy emission starts to become significant.

Need to decide what to do here. If I say host galaxy is significant using the power-law slope won't help. Use blackbody fits instead?

The $z < 0.8$ SDSS spectrum composite comparison for the small and large β_{NIR} sub-samples (Figure ??) is a very direct illustration of EV₁. Hot dust emission increases with Fe II EW. We also note that the amount of hot dust correlates with the Si III/C III] emission ratios. The Si III/C III] ratio is generally considered to be a good indicator of density and is one of the primary EV₁ correlates. The relative flux ratio of Si III to C III] increases when C IV is more blue-shifted (Richards et al., 2011). The Mg II emission line has exactly the same profile/shape for

the two samples (apparent changes in Mg II seen in Fig. 5.13 are the result of changes in Fe II at wavelengths just short-ward of the line). Finally, we note that objects with more hot dust are slightly redder.

Shen and Ho, (2014) also find that torus emission is enhanced in quasars with larger R_{FeII} . They suggests that this may be caused by more efficient disc winds that facilitate the formation of a dusty torus.

5.10.1.2 High- z

In Fig. 5.14 we show how the ratio of NIR to UV luminosity depends on the blueshift and rest-frame EQW of the C IV line. C IV blueshifts are calculated as in Section XX. We see that the NIR to UV luminosity ratio is strongly correlated with the blue-shift of the C IV emission line. A similar trend was noted by Wang et al., (2013). Interestingly, we note strong similarities to the object subsets selected according to their C IV-emission properties in Richards et al., (2011) (see Figures 11 & 12). We note that the correlation between the hot dust and the C IV emission properties will lead to apparent correlations between the host dust and the BH mass.

5.11 DISCUSSION

Roseboom et al., (2013) studied a similar sample of luminous type 1 quasars. They, like us, modelled the NIR emission using a blackbody and modelled the emission at longer wavelengths using a clumpy torus model. They find that while $L_{1-5\mu\text{m}}/L_{\text{IR}}$ appears relatively insensitive to L_{bol} and L_{IR} , a strong correlation appears between $L_{1-5\mu\text{m}}/L_{\text{IR}}$ and $L_{\text{IR}}/L_{\text{bol}}$ (i.e. the dust covering factor). They explain this correlation by postulating that as the covering factor of the torus decreases, the maximum inclination at which a type 1 quasar would be seen increases. An increase in the inclination will mean direct sight lines to more of the inner wall of obscuring material closest to the accretion disc.

Mor and Trakhtenbrot, (2011) also looked at the hot dust properties of a sample of $0.75 < z < 2$ quasars, with photometry from SDSS and WISE. They modelled the NIR emission with hot clouds of pure graphite dust. They reported an anti-correlation between the covering factor of hot dust clouds and the quasar bolometric luminosity. Like us, they neglect cooler

*Need to re-do this
and understand
why beta-related
trend is apparently
stronger than with
the blackbody
parameters.*

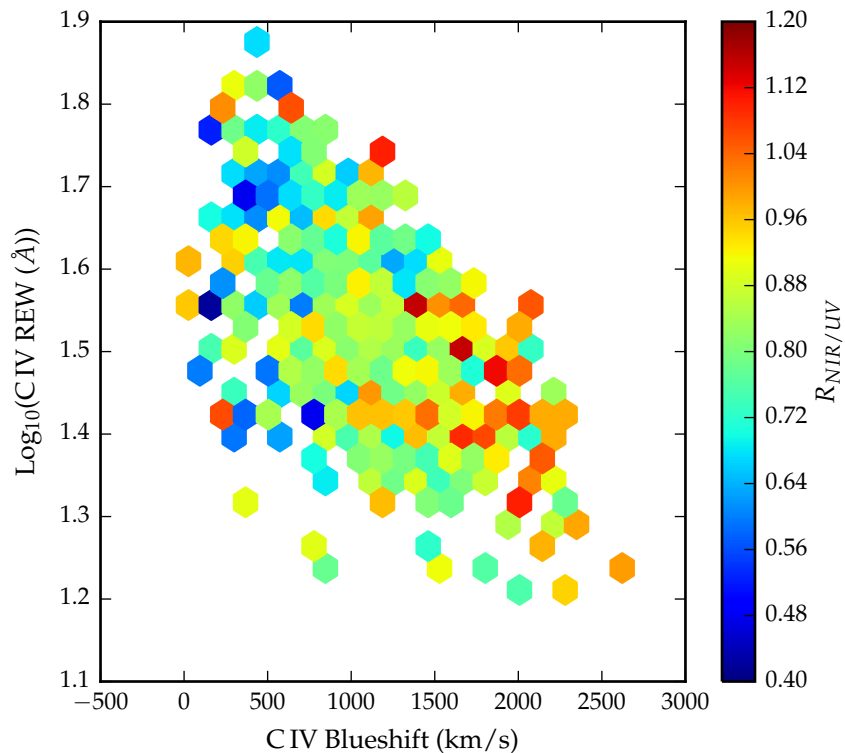


Figure 5.14: Rest-frame EQW and blueshift of the C IV line for 7,115 SDSS DR7 quasars. The colours of the hexagons denote the median hot dust ($T \simeq 1200$ K) abundance for all quasars at a given EQW and blueshift. Quasars with the most extreme outflow signatures are predominantly hot-dust rich. Only bins containing a minimum of two objects are plotted.

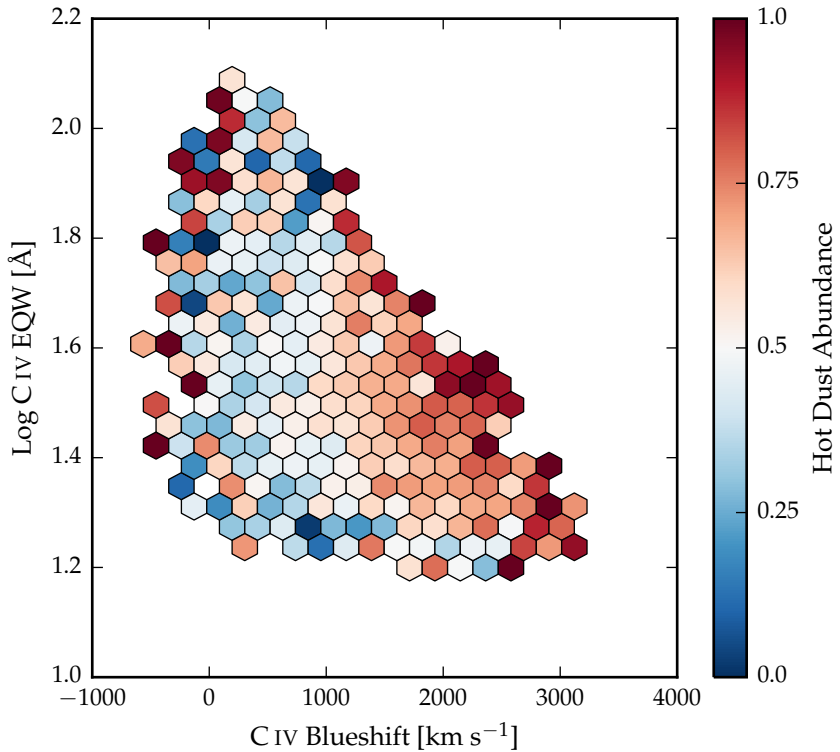


Figure 5.15: Rest-frame EQW and blueshift of the C_{IV} line for 7,115 SDSS DR7 quasars. The colours of the hexagons denote the median hot dust ($T \approx 1200$ K) abundance for all quasars at a given EQW and blueshift. Quasars with the most extreme outflow signatures are predominantly hot-dust rich. Only bins containing a minimum of two objects are plotted. [Change hot dust abundance](#).

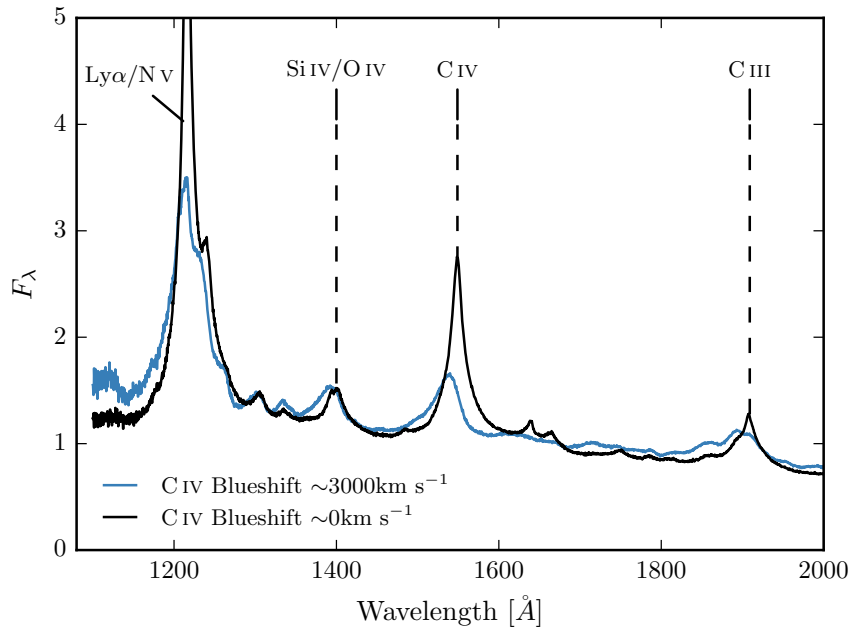


Figure 5.16

dust components which will dominate the SED at longer wavelengths. As we have discovered (see Figure residual plot), the missing flux decreases with redshift because we observe shorter rest-frame wavelengths when the observed spectrum is redshifted to a greater degree. This will induce an anti-correlation between the luminosity of the hot dust component and the luminosity of the quasar (which is correlated with redshift). At $z=0.75$, the W3 band-pass (the longest in their fits) is sensitive to flux from $6.9\mu\text{m}$; at this wavelength we expect the contribution from cooler dust to dominate over the hot dust. It is possible that this effect could explain the tension with our own result that $R_{\text{NIR/UV}}$ does not depend on the quasar luminosity in our low- z sample.

Shen and Ho, (2014) quantify the relative torus emission using the $r - W1$ colour for a sample of $0.4 < z < 0.8$ SDSS quasars. At these redshifts $W1$ is observing between 1.9 and 2.4 microns in the rest-frame of the quasar, which suggests that they are sensitive to the same component of hot dust which we are investigating. They observe a mild trend of decreasing relative torus emission as the quasar luminosity increases. We note that their use of the $r - W1$ at much higher redshifts may be

problematic, as the W1 flux will be increasingly dominated by direct emission from the accretion disc.

Gallagher et al., (2007) undertook a similar investigation for a much smaller sample of 234 radio-quiet quasars.

Reverberation measurements of nearby AGNs suggest the NIR emission is dominated by hot dust very close to the central source (few tens of light days; e.g. Minezaki et al., 2004; Suganuma et al., 2006). The hot dust signature could contain information about inner face of an obscuring torus structure and/or constrain the dust content of an accretion disc wind. Several studies have shown that the luminosity of the NIR excess emission correlates with that of the central engine with a slope close to unity e.g. Gallagher et al., 2007, suggesting that the dust is reprocessing radiation from the accretion disc.

Outflows may emerge from the outer region of the accretion disc or even the innermost region of the torus, in which the gas clouds are dusty and relatively cold. Indeed, there is observational evidence for dusty outflows close to the central engine (e.g. Bowler et al., 2014). The dust is heated by the central engine, and radiates in the NIR band. Wang et al., (2013), fitting the NIR emission with a single power-law, found that objects with strong outflow signatures (blue-shifted C IV) have more hot dust emission relative to the accretion disc emission in a large sample of $z \sim 2$ non-BAL quasars. It could be that this correlation is induced by a third factor that simultaneously affects outflows and dust emission, for instance the inclination angle or metallicity. Alternatively the dust could be intrinsic to outflows and may have a non-trivial contribution to the outflow acceleration (e.g. Fabian, 2012). Also found by Shen and Ho, (2014).

Several other investigations have drawn attention to the rest-frame NIR SEDs, with populations of ‘dust free’ objects postulated (Hao et al., 2010; Hao et al., 2011; Jiang et al., 2010; Mor and Trakhtenbrot, 2011)

*Paul: yes, but not
very dusty in
context of cold
dusty clouds, ~ 0.01
mag per ‘cloud’.*

5.11.1 *Eddington ratio*

Wang et al., Zhang et al., and Mor & Trakhtenbrot find no significant dependence of the amount of hot dust on the Eddington ratio. Is this because the Eddington ratio is wrong or because it’s more complicated? (can high accretion objects with no evidence for strong outflows.)

5.11.2 Spectral properties

In the dusty wind model - first proposed by Konigl and Kartje, (1994) and later developed by, amongst others, Everett, (2005), Elitzur and Shlosman, (2006), Keating et al., (2012) - the ‘torus’ is the dusty part of a magneto-hydrodynamic wind beyond the dust sublimation radius. The MHD wind is roughly polar, and so the hot dust forms a vertical ‘wall’ around the accretion disc. UV photons from the accretion disc accelerate the wind via radiation line driving. That flattens the geometry of the wind and exposes more surface area that is viewable on a relatively face-on line of sight. The radiation pressure is increased at higher luminosities and/or accretion rates. This can flatten the geometry of the wind, thereby increasing the range of angles for which the inner edge of the dusty wind - where dust is at its sublimation temperature - can be observed. A direct prediction is therefore that in quasars with high accretion rates and strong outflows, the emission from hot dust should be enhanced.

5.12 FURTHER WORK

What more is needed to test model(s)?

5.12.1 Hot-Dust-Poor Quasars

The near-IR emission from AGN is generally explained by thermal emission from dust grains at the edge of the dusty torus closest to the accretion disk. The dust is heated to its sublimation temperature (1300-2000K Barvainis, 1992) by emission from the accretion disc. However, Hao et al., (2010) reported that 6% (at $z \lesssim 2$) to 20% (at $2 \lesssim z \lesssim 3.5$) of the quasars in the X-ray selected XMM-COSMOS Type 1 AGN sample (Brusa et al., 2010) have an unusually small amount of hot dust emission, despite having normal accretion disc spectra. They infer a torus covering factor of $\sim 2\%$ to 30% for these ‘hot dust poor’ (HDP) quasars, well below the $\sim 75\%$ predicted by unified models (e.g. Krolik and Begelman, 1988). Hao et al., (2011) found that HDP quasars were just as common in the Richards et al., (2006a) Spitzer/SDSS sample ($8.7\% \pm 2.2\%$) and the Elvis et al., (1994) Palomar-Green-quasar-dominated sample ($9.5\% \pm 5.0\%$). Either the hot dust is destroyed (dynamically or by radiation), or the dust is not centred on the SMBH, which could happen during a major merger (e.g. Blecha et al., 2011). Alternatively, misaligned

accretion disks, which will result from discrete isotropic accretion events (Volonteri, Sikora, and Lasota, 2007), will lead to a wider range of covering factors (Lawrence and Elvis, 2010).

At higher redshifts, Jiang et al., (2010) found two HDP quasars in a sample of 21 at $z \sim 6$. They find that at $z \sim 6$ the hot dust abundance is roughly proportional to the black hole mass, indicating that the two grow at about the same rate. The two HDP quasars also have the smallest SMBH masses, and may be too young to have formed a significant amount of hot dust.

6

CONCLUSIONS / FUTURE WORK

Put some stuff from research proposals here

6.1 FUTURE: RED QUASARS

Punctuated fuelling episodes, e.g. driven by galaxy mergers, satellite accretion and even secular processes, almost certainly lead to AGN experiencing activity-, outflow- and obscuration-dominated cycles with some overlap between phases. However, quantitatively, it remains unclear how these phases relate to the fundamental properties of the accreting black-hole (e.g. mass (M_{BH})), bolometric luminosity (L_{bol}) and Eddington ratio (L/L_{Edd}) and the elements of the non-spherical geometry).

BIBLIOGRAPHY

- Alatalo, K. et al. (2011). "Discovery of an Active Galactic Nucleus Driven Molecular Outflow in the Local Early-type Galaxy NGC 1266." In: *ApJ* 735, 88, p. 88. arXiv: [1104.2326](#).
- Alexander, D. M. and R. C. Hickox (2012). "What drives the growth of black holes?" In: *New Astron. Rev.* 56, pp. 93–121. arXiv: [1112.1949](#).
- Alexander, D. M., A. M. Swinbank, I. Smail, R. McDermid, and N. P. H. Nesvadba (2010). "Searching for evidence of energetic feedback in distant galaxies: a galaxy wide outflow in a $z \sim 2$ ultraluminous infrared galaxy." In: *MNRAS* 402, pp. 2211–2220. arXiv: [0911.0014](#).
- Allen, J. T., P. C. Hewett, N. Maddox, G. T. Richards, and V. Belokurov (2011). "A strong redshift dependence of the broad absorption line quasar fraction." In: *MNRAS* 410, pp. 860–884. arXiv: [1007.3991](#).
- Allen, J. T., P. C. Hewett, C. T. Richardson, G. J. Ferland, and J. A. Baldwin (2013). "Classification and analysis of emission-line galaxies using mean field independent component analysis." In: *MNRAS* 430, pp. 3510–3536. arXiv: [1301.5930](#).
- Aller, M. C. and D. O. Richstone (2007). "Host Galaxy Bulge Predictors of Supermassive Black Hole Mass." In: *ApJ* 665, pp. 120–156. arXiv: [0705.1165](#).
- Antonucci, R. (1993). "Unified models for active galactic nuclei and quasars." In: *ARA&A* 31, pp. 473–521.
- Arav, N., M. Moe, E. Costantini, K. T. Korista, C. Benn, and S. Ellison (2008). "Measuring Column Densities in Quasar Outflows: VLT Observations of QSO 2359-1241." In: *ApJ* 681, 954-964, pp. 954–964. arXiv: [0807.0228](#).
- Assef, R. J. et al. (2011). "Black Hole Mass Estimates Based on C IV are Consistent with Those Based on the Balmer Lines." In: *ApJ* 742, p. 93. arXiv: [1009.1145](#).
- Baldwin, J. A. (1977). "Luminosity Indicators in the Spectra of Quasi-Stellar Objects." In: *ApJ* 214, pp. 679–684.
- Barth, A. J. et al. (2011). "The Lick AGN Monitoring Project 2011: Reverberation Mapping of Markarian 50." In: *ApJ* 743, L4, p. L4. arXiv: [1111.0061](#).
- Barvainis, R. (1992). "Dust reverberation - A model for the infrared variations of Fairall 9." In: *ApJ* 400, pp. 502–509.

- Baskin, A. and A. Laor (2005a). "What controls the CIV line profile in active galactic nuclei?" In: *MNRAS* 356, pp. 1029–1044. arXiv: [astro-ph/0409196](#).
- (2005b). "What controls the [OIII] $\lambda 5007$ line strength in active galactic nuclei?" In: *MNRAS* 358, pp. 1043–1054. arXiv: [astro-ph/0501436](#).
- Begelman, M. C. (1985). "Accretion disks in active galactic nuclei." In: *Astrophysics of Active Galaxies and Quasi-Stellar Objects*. Ed. by J. S. Miller, pp. 411–452.
- Bentz, M. C. et al. (2009). "The Lick AGN Monitoring Project: Broad-line Region Radii and Black Hole Masses from Reverberation Mapping of H β ." In: *ApJ* 705, pp. 199–217. arXiv: [0908.0003](#).
- Bischetti, M. et al. (2016). "The WISSH Quasars Project I. Powerful ionised outflows in hyper-luminous quasars." In: *ArXiv e-prints*. arXiv: [1612.03728](#).
- Blandford, R. D. and C. F. McKee (1982). "Reverberation mapping of the emission line regions of Seyfert galaxies and quasars." In: *ApJ* 255, pp. 419–439.
- Blandford, R. D. and D. G. Payne (1982). "Hydromagnetic flows from accretion discs and the production of radio jets." In: *MNRAS* 199, pp. 883–903.
- Blecha, L., T. J. Cox, A. Loeb, and L. Hernquist (2011). "Recoiling black holes in merging galaxies: relationship to active galactic nucleus lifetimes, starbursts and the M_{BH}- σ_* relation." In: *MNRAS* 412, pp. 2154–2182. arXiv: [1009.4940](#).
- Bonnet, H. et al. (2004). "First light of SINFONI at the VLT." In: *The Messenger* 117, pp. 17–24.
- Boroson, T. A. and R. F. Green (1992). "The emission-line properties of low-redshift quasi-stellar objects." In: *ApJS* 80, pp. 109–135.
- Boroson, T. (2005). "Blueshifted [O III] Emission: Indications of a Dynamic Narrow-Line Region." In: *AJ* 130, pp. 381–386. arXiv: [astro-ph/0505127](#).
- Bowler, R. A. A., P. C. Hewett, J. T. Allen, and G. J. Ferland (2014). "Line-driven radiative outflows in luminous quasars." In: *MNRAS* 445, pp. 359–377. arXiv: [1408.5808](#).
- Boyle, B. J. and R. J. Terlevich (1998). "The cosmological evolution of the QSO luminosity density and of the star formation rate." In: *MNRAS* 293, pp. L49–L51. arXiv: [astro-ph/9710134](#).

- Brandt, W. N. and G. Hasinger (2005). "Deep Extragalactic X-Ray Surveys." In: *ARA&A* 43, pp. 827–859. arXiv: [astro-ph/0501058](#).
- Brotherton, M. S. (1996). "The Profiles of H beta and [O iii] lambda 5007 in Radio-loud Quasars." In: *ApJS* 102, p. 1. arXiv: [astro-ph/9507067](#).
- Brotherton, M. S. and P. J. Francis (1999). "The Intermediate Line Region and the Baldwin Effect." In: *Quasars and Cosmology*. Ed. by G. Ferland and J. Baldwin. Vol. 162. Astronomical Society of the Pacific Conference Series, p. 395. eprint: [astro-ph/9811088](#).
- Brotherton, M. S., V. Singh, and J. Runnoe (2015). "Orientation and quasar black hole mass estimation." In: *MNRAS* 454, pp. 3864–3871. arXiv: [1509.06468](#).
- Brotherton, M. S., J. C. Runnoe, Z. Shang, and M. A. DiPompeo (2015). "Bias in C IV-based quasar black hole mass scaling relationships from reverberation mapped samples." In: *MNRAS* 451, pp. 1290–1298. arXiv: [1504.03427](#).
- Brusa, M. et al. (2010). "The XMM-Newton Wide-field Survey in the Cosmos Field (XMM-COSMOS): Demography and Multiwavelength Properties of Obscured and Unobscured Luminous Active Galactic Nuclei." In: *ApJ* 716, pp. 348–369. arXiv: [1004.2790](#).
- Brusa, M. et al. (2015). "X-shooter reveals powerful outflows in z~1.5 X-ray selected obscured quasi-stellar objects." In: *MNRAS* 446, pp. 2394–2417. arXiv: [1409.1615](#).
- Cappellari, M., E. K. Verolme, R. P. van der Marel, G. A. Verdoes Kleijn, G. D. Illingworth, M. Franx, C. M. Carollo, and P. T. de Zeeuw (2002). "The Counterrotating Core and the Black Hole Mass of IC 1459." In: *ApJ* 578, pp. 787–805. arXiv: [astro-ph/0202155](#).
- Carniani, S. et al. (2015). "Ionised outflows in z ~ 2.4 quasar host galaxies." In: *A&A* 580, A102, A102. arXiv: [1506.03096](#).
- Cicone, C. et al. (2014). "Massive molecular outflows and evidence for AGN feedback from CO observations." In: *A&A* 562, A21, A21. arXiv: [1311.2595](#).
- Cimatti, A., M. Brusa, M. Talia, M. Mignoli, G. Rodighiero, J. Kurk, P. Cassata, C. Halliday, A. Renzini, and E. Daddi (2013). "Active Galactic Nucleus Feedback at z ~ 2 and the Mutual Evolution of Active and Inactive Galaxies." In: *ApJ* 779, L13, p. L13. arXiv: [1311.4401](#).
- Coatman, L., P. C. Hewett, M. Banerji, and G. T. Richards (2016). "CIV emission-line properties and systematic trends

- in quasar black hole mass estimates." In: *MNRAS* 461, pp. 647–665. arXiv: [1606.02726](#).
- Coatman, L., P. C. Hewett, M. Banerji, G. T. Richards, J. F. Hennawi, and J. X. Prochaska (2017). "Correcting C IV-based virial black hole masses." In: *MNRAS* 465, pp. 2120–2142. arXiv: [1610.08977](#).
- Collin, S., T. Kawaguchi, B. M. Peterson, and M. Vestergaard (2006). "Systematic effects in measurement of black hole masses by emission-line reverberation of active galactic nuclei: Eddington ratio and inclination." In: *A&A* 456, pp. 75–90. arXiv: [astro-ph/0603460](#).
- Crenshaw, D. M., S. B. Kraemer, A. Boggess, S. P. Maran, R. F. Mushotzky, and C.-C. Wu (1999). "Intrinsic Absorption Lines in Seyfert 1 Galaxies. I. Ultraviolet Spectra from the Hubble Space Telescope." In: *ApJ* 516, pp. 750–768. arXiv: [astro-ph/9812265](#).
- Croom, S. M., R. J. Smith, B. J. Boyle, T. Shanks, L. Miller, P. J. Outram, and N. S. Loaring (2004). "The 2dF QSO Redshift Survey - XII. The spectroscopic catalogue and luminosity function." In: *MNRAS* 349, pp. 1397–1418. arXiv: [astro-ph/0403040](#).
- Cutri, R. M. et al. (2013). *Explanatory Supplement to the AllWISE Data Release Products*. Tech. rep., p. 1.
- Dall'Aglio, A., L. Wisotzki, and G. Worseck (2008). "An unbiased measurement of the UV background and its evolution via the proximity effect in quasar spectra." In: *A&A* 491, pp. 465–481. arXiv: [0807.5089](#).
- Dawson, K. S. et al. (2013). "The Baryon Oscillation Spectroscopic Survey of SDSS-III." In: *AJ* 145, p. 10. arXiv: [1208.0022](#).
- Dekker, H., S. D'Odorico, A. Kaufer, B. Delabre, and H. Kotzlowski (2000). "Design, construction, and performance of UVES, the echelle spectrograph for the UT2 Kueyen Telescope at the ESO Paranal Observatory." In: *Optical and IR Telescope Instrumentation and Detectors*. Ed. by M. Iye and A. F. Moorwood. Vol. 4008. Proc. SPIE, pp. 534–545.
- Denney, K. D. (2012). "Are Outflows Biasing Single-epoch C IV Black Hole Mass Estimates?" In: *ApJ* 759, p. 44. arXiv: [1208.3465](#).
- Denney, K. D. et al. (2010). "Reverberation Mapping Measurements of Black Hole Masses in Six Local Seyfert Galaxies." In: *ApJ* 721, pp. 715–737. arXiv: [1006.4160](#).

- Denney, K. D., R. W. Pogge, R. J. Assef, C. S. Kochanek, B. M. Peterson, and M. Vestergaard (2013). “C IV Line-width Anomalies: The Perils of Low Signal-to-noise Spectra.” In: *ApJ* 775, p. 60. arXiv: [1303.3889](#).
- Di Matteo, T., V. Springel, and L. Hernquist (2005). “Energy input from quasars regulates the growth and activity of black holes and their host galaxies.” In: *Nature* 433, pp. 604–607. arXiv: [astro-ph/0502199](#).
- Dunn, J. P., M. Bautista, N. Arav, M. Moe, K. Korista, E. Costantini, C. Benn, S. Ellison, and D. Edmonds (2010). “The Quasar Outflow Contribution to AGN Feedback: VLT Measurements of SDSS J0318-0600.” In: *ApJ* 709, pp. 611–631. arXiv: [0911.3896](#).
- Edge, A., W. Sutherland, K. Kuijken, S. Driver, R. McMahon, S. Eales, and J. P. Emerson (2013). “The VISTA Kilo-degree Infrared Galaxy (VIKING) Survey: Bridging the Gap between Low and High Redshift.” In: *The Messenger* 154, pp. 32–34.
- Eisenhauer, F. et al. (2003). “SINFONI - Integral field spectroscopy at 50 milli-arcsecond resolution with the ESO VLT.” In: *Instrument Design and Performance for Optical/Infrared Ground-based Telescopes*. Ed. by M. Iye and A. F. M. Moorwood. Vol. 4841. Proc. SPIE, pp. 1548–1561. arXiv: [astro-ph/0306191](#).
- Elias, J. H., R. R. Joyce, M. Liang, G. P. Muller, E. A. Hileman, and J. R. George (2006). “Design of the Gemini near-infrared spectrograph.” In: *Society of Photo-Optical Instrumentation Engineers (SPIE) Conference Series*. Vol. 6269. Proc. SPIE, p. 62694C.
- Elitzur, M. and I. Shlosman (2006). “The AGN-obscuring Torus: The End of the ‘Doughnut’ Paradigm?” In: *ApJ* 648, pp. L101–L104. arXiv: [astro-ph/0605686](#).
- Elvis, M. (2000). “A Structure for Quasars.” In: *ApJ* 545, pp. 63–76. arXiv: [astro-ph/0008064](#).
- Elvis, M., B. J. Wilkes, J. C. McDowell, R. F. Green, J. Bechtold, S. P. Willner, M. S. Oey, E. Polomski, and R. Cutri (1994). “Atlas of quasar energy distributions.” In: *ApJS* 95, pp. 1–68.
- Elvis, M. et al. (2012). “Spectral Energy Distributions of Type 1 Active Galactic Nuclei in the COSMOS Survey. I. The XMM-COSMOS Sample.” In: *ApJ* 759, 6, p. 6. arXiv: [1209.1478](#).
- Everett, J. E. (2005). “Radiative Transfer and Acceleration in Magnetocentrifugal Winds.” In: *ApJ* 631, pp. 689–706. arXiv: [astro-ph/0506321](#).

- Everett, J., S. Gallagher, and S. Keating (2009). "Blowing Away the "Torus": Dusty Winds in AGN." In: *American Institute of Physics Conference Series*. Ed. by S. Heinz and E. Wilcots. Vol. 1201. American Institute of Physics Conference Series, pp. 56–59.
- Fabian, A. C. (2012). "Observational Evidence of Active Galactic Nuclei Feedback." In: *ARA&A* 50, pp. 455–489. arXiv: [1204.4114](#).
- Feldman, F. R., D. W. Weedman, V. A. Balzano, and L. W. Ramsey (1982). "Emission-line widths in galactic nuclei." In: *ApJ* 256, pp. 427–434.
- Ferrarese, L. and H. Ford (2005). "Supermassive Black Holes in Galactic Nuclei: Past, Present and Future Research." In: *Space Sci. Rev.* 116, pp. 523–624. arXiv: [astro-ph/0411247](#).
- Ferrarese, L. and D. Merritt (2000). "A Fundamental Relation between Supermassive Black Holes and Their Host Galaxies." In: *ApJ* 539, pp. L9–L12. arXiv: [astro-ph/0006053](#).
- Feruglio, C., R. Maiolino, E. Piconcelli, N. Menci, H. Aussel, A. Lamastra, and F. Fiore (2010). "Quasar feedback revealed by giant molecular outflows." In: *A&A* 518, L155, p. L155. arXiv: [1006.1655](#).
- Font-Ribera, A. et al. (2013). "The large-scale quasar-Lyman α forest cross-correlation from BOSS." In: *J. Cosmology Astropart. Phys.* 5, 018, p. 018. arXiv: [1303.1937](#).
- Foreman-Mackey, D., D. W. Hogg, D. Lang, and J. Goodman (2013). "emcee: The MCMC Hammer." In: *PASP* 125, pp. 306–312. arXiv: [1202.3665](#).
- Francis, P. J., P. C. Hewett, C. B. Foltz, F. H. Chaffee, R. J. Weymann, and S. L. Morris (1991). "A high signal-to-noise ratio composite quasar spectrum." In: *ApJ* 373, pp. 465–470.
- Gallagher, S. C., D. C. Hines, M. Blaylock, R. S. Priddey, W. N. Brandt, and E. E. Egami (2007). "Radio through X-Ray Spectral Energy Distributions of 38 Broad Absorption Line Quasars." In: *ApJ* 665, pp. 157–173. arXiv: [0705.0538](#).
- Gallagher, S. C., J. E. Everett, S. K. Keating, A. R. Hill, and R. P. Deo (2012). "Looking for the Wind in the Dust." In: *AGN Winds in Charleston*. Ed. by G. Chartas, F. Hamann, and K. M. Leighly. Vol. 460. Astronomical Society of the Pacific Conference Series, p. 199. arXiv: [1201.5018](#).
- Gallagher, S. C., J. E. Everett, M. M. Abado, and S. K. Keating (2015). "Investigating the structure of the windy torus in quasars." In: *MNRAS* 451, pp. 2991–3000. arXiv: [1505.04219](#).

- Gaskell, C. M. (1982). "A redshift difference between high and low ionization emission-line regions in QSOs - Evidence for radial motions." In: *ApJ* 263, pp. 79–86.
- Gavignaud, I. et al. (2008). "Eddington ratios of faint AGN at intermediate redshift: evidence for a population of half-starved black holes." In: *A&A* 492, pp. 637–650. arXiv: [0810.2172](#).
- Gebhardt, K. et al. (2000). "A Relationship between Nuclear Black Hole Mass and Galaxy Velocity Dispersion." In: *ApJ* 539, pp. L13–L16. arXiv: [astro-ph/0006289](#).
- Graham, A. W., P. Erwin, N. Caon, and I. Trujillo (2001). "A Correlation between Galaxy Light Concentration and Supermassive Black Hole Mass." In: *ApJ* 563, pp. L11–L14. arXiv: [astro-ph/0111152](#).
- Grandi, S. A. (1982). "The 3000 Å bump in quasars." In: *ApJ* 255, pp. 25–38.
- Greene, J. E. and L. C. Ho (2005a). "A Comparison of Stellar and Gaseous Kinematics in the Nuclei of Active Galaxies." In: *ApJ* 627, pp. 721–732. arXiv: [astro-ph/0503675](#).
- (2005b). "Estimating Black Hole Masses in Active Galaxies Using the H α Emission Line." In: *ApJ* 630, pp. 122–129. arXiv: [astro-ph/0508335](#).
- Greene, J. E., N. L. Zakamska, X. Liu, A. J. Barth, and L. C. Ho (2009). "The Growth of Black Holes: Insights from Obscured Active Galaxies." In: *ApJ* 702, pp. 441–459. arXiv: [0907.1086](#).
- Greene, J. E., N. L. Zakamska, L. C. Ho, and A. J. Barth (2011). "Feedback in Luminous Obscured Quasars." In: *ApJ* 732, 9, p. 9. arXiv: [1102.2913](#).
- Grier, C. J. et al. (2012). "Reverberation Mapping Results for Five Seyfert 1 Galaxies." In: *ApJ* 755, 60, p. 60. arXiv: [1206.6523](#).
- Gültekin, K. et al. (2009). "The M- σ and M-L Relations in Galactic Bulges, and Determinations of Their Intrinsic Scatter." In: *ApJ* 698, pp. 198–221. arXiv: [0903.4897](#).
- Hainline, K. N., R. Hickox, J. E. Greene, A. D. Myers, and N. L. Zakamska (2013). "SALT Long-slit Spectroscopy of Luminous Obscured Quasars: An Upper Limit on the Size of the Narrow-line Region?" In: *ApJ* 774, 145, p. 145. arXiv: [1307.5852](#).
- Hamann, F., T. A. Barlow, V. Junkkarinen, and E. M. Burbidge (1997). "High-Resolution Spectra of Intrinsic Absorption Lines in the Quasi-stellar Object UM 675." In: *ApJ* 478, pp. 80–86.

- Hao, H. et al. (2010). “Hot-dust-poor Type 1 Active Galactic Nuclei in the COSMOS Survey.” In: *ApJ* 724, pp. L59–L63. arXiv: [1009.3276](#).
- Hao, H., M. Elvis, F. Civano, and A. Lawrence (2011). “Hot-dust-poor Quasars in Mid-infrared and Optically Selected Samples.” In: *ApJ* 733, 108, p. 108. arXiv: [1011.0429](#).
- Hao, H. et al. (2013). “A quasar-galaxy mixing diagram: quasar spectral energy distribution shapes in the optical to near-infrared.” In: *MNRAS* 434, pp. 3104–3121. arXiv: [1210.3044](#).
- Harrison, C. M. et al. (2012). “Energetic galaxy-wide outflows in high-redshift ultraluminous infrared galaxies hosting AGN activity.” In: *MNRAS* 426, pp. 1073–1096. arXiv: [1205.1801](#).
- Harrison, C. M., D. M. Alexander, J. R. Mullaney, and A. M. Swinbank (2014). “Kiloparsec-scale outflows are prevalent among luminous AGN: outflows and feedback in the context of the overall AGN population.” In: *MNRAS* 441, pp. 3306–3347. arXiv: [1403.3086](#).
- Harrison, C. M., D. M. Alexander, J. R. Mullaney, J. P. Stott, A. M. Swinbank, V. Arumugam, F. E. Bauer, R. G. Bower, A. J. Bunker, and R. M. Sharples (2016). “The KMOS AGN Survey at High redshift (KASHz): the prevalence and drivers of ionized outflows in the host galaxies of X-ray AGN.” In: *MNRAS* 456, pp. 1195–1220. arXiv: [1511.00008](#).
- Heckman, T. M. and P. N. Best (2014). “The Coevolution of Galaxies and Supermassive Black Holes: Insights from Surveys of the Contemporary Universe.” In: *ARA&A* 52, pp. 589–660. arXiv: [1403.4620](#).
- Heckman, T. M., G. K. Miley, and R. F. Green (1984). “The kinematics of the narrow-line region in active galaxies and quasars. III - Correlations with the broad-line region and radio emission.” In: *ApJ* 281, pp. 525–534.
- Heckman, T. M., G. K. Miley, W. J. M. van Breugel, and H. R. Butcher (1981). “Emission-line profiles and kinematics of the narrow-line region in Seyfert and radio galaxies.” In: *ApJ* 247, pp. 403–418.
- Hennawi, J. F. et al. (2006a). “Binary Quasars in the Sloan Digital Sky Survey: Evidence for Excess Clustering on Small Scales.” In: *AJ* 131, pp. 1–23. arXiv: [astro-ph/0504535](#).
- Hennawi, J. F. et al. (2006b). “Quasars Probing Quasars. I. Optically Thick Absorbers near Luminous Quasars.” In: *ApJ* 651, pp. 61–83. arXiv: [astro-ph/0603742](#).

- Hennawi, J. F. et al. (2010). "Binary Quasars at High Redshift. I. 24 New Quasar Pairs at $z \sim 3\text{-}4$." In: *ApJ* 719, pp. 1672–1692. arXiv: [0908.3907](#).
- Hennawi, J. F., J. X. Prochaska, S. Cantalupo, and F. Arrigoni-Battaia (2015). "Quasar quartet embedded in giant nebula reveals rare massive structure in distant universe." In: *Science* 348, pp. 779–783. arXiv: [1505.03786](#).
- Hewett, P. C. and C. B. Foltz (2003). "The Frequency and Radio Properties of Broad Absorption Line Quasars." In: *AJ* 125, pp. 1784–1794. arXiv: [astro-ph/0301191](#).
- Hewett, P. C. and V. Wild (2010). "Improved redshifts for SDSS quasar spectra." In: *MNRAS* 405, pp. 2302–2316. arXiv: [1003.3017](#).
- Hewett, P. C., S. J. Warren, S. K. Leggett, and S. T. Hodgkin (2006). "The UKIRT Infrared Deep Sky Survey ZY JHK photometric system: passbands and synthetic colours." In: *MNRAS* 367, pp. 454–468. arXiv: [astro-ph/0601592](#).
- Higginbottom, N. and D. Proga (2015). "Coronae and Winds from Irradiated Disks in X-Ray Binaries." In: *ApJ* 807, p. 107. arXiv: [1504.03328](#).
- Hodapp, K. W. et al. (2003). "The Gemini Near-Infrared Imager (NIRI)." In: *PASP* 115, pp. 1388–1406.
- Hogg, D. W., J. Bovy, and D. Lang (2010). "Data analysis recipes: Fitting a model to data." In: *ArXiv e-prints*. arXiv: [1008.4686](#).
- Hoyle, F. and W. A. Fowler (1963). "On the nature of strong radio sources." In: *MNRAS* 125, p. 169.
- Jackson, N. and I. W. A. Browne (1991). "Optical Properties of Quasars - Part Two - Emission Line Geometry and Radio Properties." In: *MNRAS* 250, p. 422.
- Jarvis, M. J. and R. J. McLure (2006). "Orientation dependency of broad-line widths in quasars and consequences for black hole mass estimation." In: *MNRAS* 369, pp. 182–188. arXiv: [astro-ph/0603231](#).
- Jiang, L. et al. (2010). "Dust-free quasars in the early Universe." In: *Nature* 464, pp. 380–383. arXiv: [1003.3432](#).
- Kaspi, S., P. S. Smith, H. Netzer, D. Maoz, B. T. Jannuzi, and U. Giveon (2000). "Reverberation Measurements for 17 Quasars and the Size-Mass-Luminosity Relations in Active Galactic Nuclei." In: *ApJ* 533, pp. 631–649. arXiv: [astro-ph/9911476](#).
- Kaspi, S., W. N. Brandt, D. Maoz, H. Netzer, D. P. Schneider, and O. Shemmer (2007). "Reverberation Mapping of High-

- Luminosity Quasars: First Results." In: *ApJ* 659, pp. 997–1007. arXiv: [astro-ph/0612722](#).
- Keating, S. K., J. E. Everett, S. C. Gallagher, and R. P. Deo (2012). "Sweeping Away the Mysteries of Dusty Continuous Winds in Active Galactic Nuclei." In: *ApJ* 749, 32, p. 32. arXiv: [1202.4681](#).
- Kelly, B. C. and Y. Shen (2013). "The Demographics of Broad-line Quasars in the Mass-Luminosity Plane. II. Black Hole Mass and Eddington Ratio Functions." In: *ApJ* 764, p. 45. arXiv: [1209.0477](#).
- Kelly, B. C., M. Vestergaard, X. Fan, P. Hopkins, L. Hernquist, and A. Siemiginowska (2010). "Constraints on Black Hole Growth, Quasar Lifetimes, and Eddington Ratio Distributions from the SDSS Broad-line Quasar Black Hole Mass Function." In: *ApJ* 719, pp. 1315–1334. arXiv: [1006.3561](#).
- Kim, M., L. C. Ho, C. J. Lonsdale, M. Lacy, A. W. Blain, and A. E. Kimball (2013). "Evidence for Active Galactic Nucleus Driven Outflows in Young Radio Quasars." In: *ApJ* 768, L9, p. L9. arXiv: [1303.7194](#).
- King, A. L. et al. (2015). "Simulations of the OzDES AGN reverberation mapping project." In: *MNRAS* 453, pp. 1701–1726. arXiv: [1504.03031](#).
- King, A. (2003). "Black Holes, Galaxy Formation, and the $M_{\text{BH}} - \sigma$ Relation." In: *ApJ* 596, pp. L27–L29. arXiv: [astro-ph/0308342](#).
- King, A. and K. Pounds (2015). "Powerful Outflows and Feedback from Active Galactic Nuclei." In: *ARA&A* 53, pp. 115–154. arXiv: [1503.05206](#).
- Kollatschny, W. and M. Zetzl (2011). "Broad-line active galactic nuclei rotate faster than narrow-line ones." In: *Nature* 470, pp. 366–368.
- (2013). "The shape of broad-line profiles in active galactic nuclei." In: *A&A* 549, A100, A100. arXiv: [1211.3065](#).
- Kollmeier, J. A. et al. (2006). "Black Hole Masses and Eddington Ratios at $0.3 < z < 4$." In: *ApJ* 648, pp. 128–139. arXiv: [astro-ph/0508657](#).
- Konigl, A. and J. F. Kartje (1994). "Disk-driven hydromagnetic winds as a key ingredient of active galactic nuclei unification schemes." In: *ApJ* 434, pp. 446–467.
- Kormendy, J. and L. C. Ho (2013). "Coevolution (Or Not) of Supermassive Black Holes and Host Galaxies." In: *ARA&A* 51, pp. 511–653. arXiv: [1304.7762](#).

- Kormendy, J. and D. Richstone (1995). "Inward Bound—The Search For Supermassive Black Holes In Galactic Nuclei." In: *ARA&A* 33, p. 581.
- Kratzer, R. M. and G. T. Richards (2015). "Mean and Extreme Radio Properties of Quasars and the Origin of Radio Emission." In: *AJ* 149, p. 61.
- Krawczyk, C. M., G. T. Richards, S. S. Mehta, M. S. Vogeley, S. C. Gallagher, K. M. Leighly, N. P. Ross, and D. P. Schneider (2013). "Mean Spectral Energy Distributions and Bolometric Corrections for Luminous Quasars." In: *ApJS* 206, p. 4. arXiv: [1304.5573](#).
- Krolik, J. H. and M. C. Begelman (1988). "Molecular tori in Seyfert galaxies - Feeding the monster and hiding it." In: *ApJ* 329, pp. 702–711.
- Kuraszkiewicz, J. K. et al. (2003). "The Far-Infrared Spectral Energy Distributions of X-Ray-selected Active Galaxies." In: *ApJ* 590, pp. 128–148. arXiv: [astro-ph/0302572](#).
- Lau, M. W., J. X. Prochaska, and J. F. Hennawi (2016). "Quasars Probing Quasars. VIII. The Physical Properties of the Cool Circumgalactic Medium Surrounding $z \sim 2\text{--}3$ Massive Galaxies Hosting Quasars." In: *ApJS* 226, 25, p. 25. arXiv: [1510.06018](#).
- Lawrence, A. and M. Elvis (2010). "Misaligned Disks as Obscurers in Active Galaxies." In: *ApJ* 714, pp. 561–570.
- Lawrence, A. et al. (2007). "The UKIRT Infrared Deep Sky Survey (UKIDSS)." In: *MNRAS* 379, pp. 1599–1617. arXiv: [astro-ph/0604426](#).
- Lee, K.-G. et al. (2013). "The BOSS Ly α Forest Sample from SDSS Data Release 9." In: *AJ* 145, 69, p. 69. arXiv: [1211.5146](#).
- Leighly, K. M. (2004). "Hubble Space Telescope STIS Ultraviolet Spectral Evidence of Outflow in Extreme Narrow-Line Seyfert 1 Galaxies. II. Modeling and Interpretation." In: *ApJ* 611, pp. 125–152. arXiv: [astro-ph/0402452](#).
- Liu, G., N. L. Zakamska, J. E. Greene, N. P. H. Nesvadba, and X. Liu (2013). "Observations of feedback from radio-quiet quasars - II. Kinematics of ionized gas nebulae." In: *MNRAS* 436, pp. 2576–2597. arXiv: [1305.6922](#).
- Luo, B. et al. (2015). "X-ray Insights into the Nature of PHL 1811 Analogs and Weak Emission-line Quasars: Unification with a Geometrically Thick Accretion Disk?" In: *ApJ* 805, p. 122. arXiv: [1503.02085](#).

- Lusso, E. et al. (2010). "The X-ray to optical-UV luminosity ratio of X-ray selected type 1 AGN in XMM-COSMOS." In: *A&A* 512, A34, A34. arXiv: [0912.4166](#).
- Lynden-Bell, D. (1969). "Galactic Nuclei as Collapsed Old Quasars." In: *Nature* 223, pp. 690–694.
- Lynden-Bell, D. and M. J. Rees (1971). "On quasars, dust and the galactic centre." In: *MNRAS* 152, p. 461.
- MacLeod, C. L. et al. (2010). "Modeling the Time Variability of SDSS Stripe 82 Quasars as a Damped Random Walk." In: *ApJ* 721, pp. 1014–1033. arXiv: [1004.0276](#).
- MacLeod, C. L. et al. (2016). "A systematic search for changing-look quasars in SDSS." In: *MNRAS* 457, pp. 389–404. arXiv: [1509.08393](#).
- Maddox, N. and P. C. Hewett (2006). "Simulating wide-field quasar surveys from the optical to near-infrared." In: *MNRAS* 367, pp. 717–731. arXiv: [astro-ph/0512325](#).
- Mainzer, A. et al. (2011). "Preliminary Results from NEOWISE: An Enhancement to the Wide-field Infrared Survey Explorer for Solar System Science." In: *ApJ* 731, 53, p. 53. arXiv: [1102.1996](#).
- Manchado, A. et al. (1998). "LIRIS: a long-slit intermediate-resolution infrared spectrograph for the WHT." In: *Infrared Astronomical Instrumentation*. Ed. by A. M. Fowler. Vol. 3354. Proc. SPIE, pp. 448–455.
- Mannucci, F., F. Basile, B. M. Poggianti, A. Cimatti, E. Daddi, L. Pozzetti, and L. Vanzi (2001). "Near-infrared template spectra of normal galaxies: k-corrections, galaxy models and stellar populations." In: *MNRAS* 326, pp. 745–758. arXiv: [astro-ph/0104427](#).
- Marchese, E., R. Della Ceca, A. Caccianiga, P. Severgnini, A. Corral, and R. Fanali (2012). "The optical-UV spectral energy distribution of the unabsorbed AGN population in the XMM-Newton Bright Serendipitous Survey." In: *A&A* 539, A48, A48. arXiv: [1111.4409](#).
- Marconi, A. and L. K. Hunt (2003). "The Relation between Black Hole Mass, Bulge Mass, and Near-Infrared Luminosity." In: *ApJ* 589, pp. L21–L24. arXiv: [astro-ph/0304274](#).
- Marziani, P. and J. W. Sulentic (2012). "Estimating black hole masses in quasars using broad optical and UV emission lines." In: *New Astron. Rev.* 56, pp. 49–63. arXiv: [1108.5102](#).
- Marziani, P., R. K. Zamanov, J. W. Sulentic, and M. Calvani (2003). "Searching for the physical drivers of eigenvector

- 1: influence of black hole mass and Eddington ratio." In: *MNRAS* 345, pp. 1133–1144. arXiv: [astro-ph/0307367](#).
- Marziani, P., J. W. Sulentic, G. M. Stirpe, S. Zamfir, and M. Calvani (2009). "VLT/ISAAC spectra of the H β region in intermediate-redshift quasars. III. H β broad-line profile analysis and inferences about BLR structure." In: *A&A* 495, pp. 83–112. arXiv: [0812.0251](#).
- Marziani, P., J. W. Sulentic, I. Plauchu-Frayn, and A. del Olmo (2013). "Is MgII λ 2800 a reliable virial broadening estimator for quasars?" In: *A&A* 555, A89, A89. arXiv: [1305.1096](#).
- McGill, K. L., J.-H. Woo, T. Treu, and M. A. Malkan (2008). "Comparing and Calibrating Black Hole Mass Estimators for Distant Active Galactic Nuclei." In: *ApJ* 673, pp. 703–714. arXiv: [0710.1839](#).
- McLure, R. J. and M. J. Jarvis (2002). "Measuring the black hole masses of high-redshift quasars." In: *MNRAS* 337, pp. 109–116. arXiv: [astro-ph/0204473](#).
- McMahon, R. G., M. Banerji, E. Gonzalez, S. E. Koposov, V. J. Bejar, N. Lodieu, R. Rebolo, and VHS Collaboration (2013). "First Scientific Results from the VISTA Hemisphere Survey (VHS)." In: *The Messenger* 154, pp. 35–37.
- Mejía-Restrepo, J. E., B. Trakhtenbrot, P. Lira, H. Netzer, and D. M. Capellupo (2016). "Active galactic nuclei at z~1.5 - II. Black hole mass estimation by means of broad emission lines." In: *MNRAS* 460, pp. 187–211. arXiv: [1603.03437](#).
- Minezaki, T., Y. Yoshii, Y. Kobayashi, K. Enya, M. Suganuma, H. Tomita, T. Aoki, and B. A. Peterson (2004). "Inner Size of a Dust Torus in the Seyfert 1 Galaxy NGC 4151." In: *ApJ* 600, pp. L35–L38. arXiv: [astro-ph/0311338](#).
- Moe, M., N. Arav, M. A. Bautista, and K. T. Korista (2009). "Quasar Outflow Contribution to AGN Feedback: Observations of QSO SDSS J0838+2955." In: *ApJ* 706, pp. 525–534. arXiv: [0911.3332](#).
- Moorwood, A., J.-G. Cuby, and C. Lidman (1998). "SOFI sees first light at the NTT." In: *The Messenger* 91, pp. 9–13.
- Moorwood, A. et al. (1998). "ISAAC sees first light at the VLT." In: *The Messenger* 94, pp. 7–9.
- Mor, R. and B. Trakhtenbrot (2011). "Hot-dust Clouds with Pure-graphite Composition around type-I Active Galactic Nuclei." In: *ApJ* 737, L36, p. L36. arXiv: [1105.3198](#).
- Mullaney, J. R., D. M. Alexander, S. Fine, A. D. Goulding, C. M. Harrison, and R. C. Hickox (2013). "Narrow-line region gas

- kinematics of 24 264 optically selected AGN: the radio connection." In: *MNRAS* 433, pp. 622–638. arXiv: [1305.0263](#).
- Murray, N., J. Chiang, S. A. Grossman, and G. M. Voit (1995). "Accretion Disk Winds from Active Galactic Nuclei." In: *ApJ* 451, p. 498.
- Nardini, E. et al. (2015). "Black hole feedback in the luminous quasar PDS 456." In: *Science* 347, pp. 860–863. arXiv: [1502.06636](#).
- Nesvadba, N. P. H., M. D. Lehnert, F. Eisenhauer, A. Gilbert, M. Tecza, and R. Abuter (2006). "Extreme Gas Kinematics in the z=2.2 Powerful Radio Galaxy MRC 1138-262: Evidence for Efficient Active Galactic Nucleus Feedback in the Early Universe?" In: *ApJ* 650, pp. 693–705. arXiv: [astro-ph/0606530](#).
- Nesvadba, N. P. H., M. D. Lehnert, C. De Breuck, A. M. Gilbert, and W. van Breugel (2008). "Evidence for powerful AGN winds at high redshift: dynamics of galactic outflows in radio galaxies during the "Quasar Era"." In: *A&A* 491, pp. 407–424. arXiv: [0809.5171](#).
- Nesvadba, N. P. H., F. Boulanger, P. Salomé, P. Guillard, M. D. Lehnert, P. Ogle, P. Appleton, E. Falgarone, and G. Pineau Des Forets (2010). "Energetics of the molecular gas in the H₂ luminous radio galaxy 3C 326: Evidence for negative AGN feedback." In: *A&A* 521, A65, A65. arXiv: [1003.3449](#).
- Netzer, H. (2015). "Revisiting the Unified Model of Active Galactic Nuclei." In: *ARA&A* 53, pp. 365–408. arXiv: [1505.00811](#).
- Netzer, H. and B. M. Peterson (1997). "Reverberation Mapping and the Physics of Active Galactic Nuclei." In: *Astronomical Time Series*. Ed. by D. Maoz, A. Sternberg, and E. M. Leibowitz. Vol. 218. Astrophysics and Space Science Library, p. 85. arXiv: [astro-ph/9706039](#).
- Netzer, H., O. Shemmer, R. Maiolino, E. Oliva, S. Croom, E. Corbett, and L. di Fabrizio (2004). "Near-Infrared Spectroscopy of High-Redshift Active Galactic Nuclei. II. Disappearing Narrow-Line Regions and the Role of Accretion." In: *ApJ* 614, pp. 558–567. arXiv: [astro-ph/0406560](#).
- Oke, J. B. and J. E. Gunn (1983). "Secondary standard stars for absolute spectrophotometry." In: *ApJ* 266, pp. 713–717.
- Onken, C. A. and J. A. Kollmeier (2008). "An Improved Method for Using Mg II to Estimate Black Hole Masses in Active Galactic Nuclei." In: *ApJ* 689, p. L13. arXiv: [0810.1950](#).

- Onken, C. A. and B. M. Peterson (2002). "The Mass of the Central Black Hole in the Seyfert Galaxy NGC 3783." In: *ApJ* 572, pp. 746–752. arXiv: [astro-ph/0202382](#).
- Pâris, I. et al. (2012). "The Sloan Digital Sky Survey quasar catalog: ninth data release." In: *A&A* 548, A66, A66. arXiv: [1210.5166](#).
- Pâris, I. et al. (2014). "The Sloan Digital Sky Survey quasar catalog: tenth data release." In: *A&A* 563, A54. arXiv: [1311.4870](#).
- Pâris, I. et al. (2017). "The Sloan Digital Sky Survey Quasar Catalog: Twelfth data release." In: *A&A* 597, A79. arXiv: [1608.06483](#).
- Park, D., J.-H. Woo, K. D. Denney, and J. Shin (2013). "Calibrating C-IV-based Black Hole Mass Estimators." In: *ApJ* 770, p. 87. arXiv: [1304.7281](#).
- Perna, M. et al. (2015). "Galaxy-wide outflows in $z \sim 1.5$ luminous obscured quasars revealed through near-IR slit-resolved spectroscopy." In: *A&A* 574, A82, A82. arXiv: [1410.5468](#).
- Peterson, B. M. (1993). "Reverberation mapping of active galactic nuclei." In: *PASP* 105, pp. 247–268.
- (1997). *An Introduction to Active Galactic Nuclei*.
- (2010). "Toward Precision Measurement of Central Black Hole Masses." In: *Co-Evolution of Central Black Holes and Galaxies*. Ed. by B. M. Peterson, R. S. Somerville, and T. Storchi-Bergmann. Vol. 267. IAU Symposium, pp. 151–160. arXiv: [1001.3675](#).
- (2011). "Masses of Black Holes in Active Galactic Nuclei: Implications for NLS1s." In: *ArXiv e-prints*. arXiv: [1109.4181](#).
- (2014). "Measuring the Masses of Supermassive Black Holes." In: *Space Sci. Rev.* 183, pp. 253–275.
- Peterson, B. M. et al. (2004). "Central Masses and Broad-Line Region Sizes of Active Galactic Nuclei. II. A Homogeneous Analysis of a Large Reverberation-Mapping Database." In: *ApJ* 613, pp. 682–699. arXiv: [astro-ph/0407299](#).
- Plotkin, R. M. et al. (2015). "Detection of Rest-frame Optical Lines from X-shooter Spectroscopy of Weak Emission Line Quasars." In: *ApJ* 805, p. 123. arXiv: [1503.07523](#).
- Polletta, M., T. J.-L. Courvoisier, E. J. Hooper, and B. J. Wilkes (2000). "The far-infrared emission of radio loud and radio quiet quasars." In: *A&A* 362, pp. 75–96. arXiv: [astro-ph/0006315](#).

- Polletta, M. et al. (2007). "Spectral Energy Distributions of Hard X-Ray Selected Active Galactic Nuclei in the XMM-Newton Medium Deep Survey." In: *ApJ* 663, pp. 81–102. arXiv: [astro-ph/0703255](#).
- Prochaska, J. X. and J. F. Hennawi (2009). "Quasars Probing Quasars. III. New Clues to Feedback, Quenching, and the Physics of Massive Galaxy Formation." In: *ApJ* 690, pp. 1558–1584. arXiv: [0806.0862](#).
- Proga, D., J. M. Stone, and T. R. Kallman (2000). "Dynamics of Line-driven Disk Winds in Active Galactic Nuclei." In: *ApJ* 543, pp. 686–696. arXiv: [astro-ph/0005315](#).
- Rafiee, A. and P. B. Hall (2011). "Supermassive Black Hole Mass Estimates Using Sloan Digital Sky Survey Quasar Spectra at $0.7 < z < 2$." In: *ApJS* 194, 42, p. 42. arXiv: [1104.1828](#).
- Reichard, T. A., G. T. Richards, P. B. Hall, D. P. Schneider, D. E. Vanden Berk, X. Fan, D. G. York, G. R. Knapp, and J. Brinkmann (2003). "Continuum and Emission-Line Properties of Broad Absorption Line Quasars." In: *AJ* 126, pp. 2594–2607. arXiv: [astro-ph/0308508](#).
- Richards, G. T. (2006). "AGN Outflows in Emission and Absorption: The SDSS Perspective." In: *AGN Winds in the Caribbean*. arXiv: [astro-ph/0603827](#).
- Richards, G. T., D. E. Vanden Berk, T. A. Reichard, P. B. Hall, D. P. Schneider, M. SubbaRao, A. R. Thakar, and D. G. York (2002). "Broad Emission-Line Shifts in Quasars: An Orientation Measure for Radio-Quiet Quasars?" In: *AJ* 124, pp. 1–17. arXiv: [astro-ph/0204162](#).
- Richards, G. T. et al. (2003). "Red and Reddened Quasars in the Sloan Digital Sky Survey." In: *AJ* 126, pp. 1131–1147. arXiv: [astro-ph/0305305](#).
- Richards, G. T. et al. (2006a). "Spectral Energy Distributions and Multiwavelength Selection of Type 1 Quasars." In: *ApJS* 166, pp. 470–497. arXiv: [astro-ph/0601558](#).
- Richards, G. T. et al. (2006b). "The Sloan Digital Sky Survey Quasar Survey: Quasar Luminosity Function from Data Release 3." In: *AJ* 131, pp. 2766–2787. arXiv: [astro-ph/0601434](#).
- Richards, G. T., N. E. Kruczak, S. C. Gallagher, P. B. Hall, P. C. Hewett, K. M. Leighly, R. P. Deo, R. M. Kratzer, and Y. Shen (2011). "Unification of Luminous Type 1 Quasars through CIV Emission." In: *AJ* 141, p. 167. arXiv: [1011.2282](#).
- Risaliti, G. and M. Elvis (2004). "A Panchromatic View of AGN." In: *Supermassive Black Holes in the Distant Universe*.

- Ed. by A. J. Barger. Vol. 308. Astrophysics and Space Science Library, p. 187. arXiv: [1011.2282](#).
- Roseboom, I. G., A. Lawrence, M. Elvis, S. Petty, Y. Shen, and H. Hao (2013). "IR-derived covering factors for a large sample of quasars from WISE-UKIDSS-SDSS." In: *MNRAS* 429, pp. 1494–1501. arXiv: [1205.4543](#).
- Ross, N. P. et al. (2013). "The SDSS-III Baryon Oscillation Spectroscopic Survey: The Quasar Luminosity Function from Data Release Nine." In: *ApJ* 773, p. 14. arXiv: [1210.6389](#).
- Runnoe, J. C., M. S. Brotherton, Z. Shang, and M. A. DiPompeo (2013a). "Rehabilitating C IV-based black hole mass estimates in quasars." In: *MNRAS* 434, pp. 848–861. arXiv: [1306.3521](#).
- Runnoe, J. C., M. S. Brotherton, Z. Shang, B. J. Wills, and M. A. DiPompeo (2013b). "The orientation dependence of quasar single-epoch black hole mass scaling relationships." In: *MNRAS* 429, pp. 135–149. arXiv: [1211.3984](#).
- Runnoe, J. C., M. S. Brotherton, M. A. DiPompeo, and Z. Shang (2014). "The behaviour of quasar C IV emission-line properties with orientation." In: *MNRAS* 438, pp. 3263–3274. arXiv: [1312.7500](#).
- Rupke, D. S. N. and S. Veilleux (2013). "Breaking the Obscuring Screen: A Resolved Molecular Outflow in a Buried QSO." In: *ApJ* 775, L15, p. L15. arXiv: [1308.4988](#).
- Salpeter, E. E. (1964). "Accretion of Interstellar Matter by Massive Objects." In: *ApJ* 140, pp. 796–800.
- Schmidt, M. (1963). "3C 273 : A Star-Like Object with Large Red-Shift." In: *Nature* 197, p. 1040.
- Schneider, D. P. et al. (2010). "The Sloan Digital Sky Survey Quasar Catalog. V. Seventh Data Release." In: *AJ* 139, p. 2360. arXiv: [1004.1167](#).
- Shang, Z. et al. (2011). "The Next Generation Atlas of Quasar Spectral Energy Distributions from Radio to X-Rays." In: *ApJS* 196, 2, p. 2. arXiv: [1107.1855](#).
- Shen, Y. (2013). "The mass of quasars." In: *Bulletin of the Astronomical Society of India* 41, pp. 61–115. arXiv: [1302.2643](#).
- (2016). "Rest-Frame Optical Properties of Luminous $1.5 < z < 3.5$ Quasars: The H β -[O III] Region." In: *ApJ* in press. arXiv: [1512.00005](#).
- Shen, Y. and L. C. Ho (2014). "The diversity of quasars unified by accretion and orientation." In: *Nature* 513, pp. 210–213. arXiv: [1409.2887](#).

- Shen, Y. and X. Liu (2012). "Comparing Single-epoch Virial Black Hole Mass Estimators for Luminous Quasars." In: *ApJ* 753, p. 125. arXiv: [1203.0601](#).
- Shen, Y., J. E. Greene, M. A. Strauss, G. T. Richards, and D. P. Schneider (2008). "Biases in Virial Black Hole Masses: An SDSS Perspective." In: *ApJ* 680, pp. 169–190. arXiv: [0709.3098](#).
- Shen, Y. et al. (2011). "A Catalog of Quasar Properties from Sloan Digital Sky Survey Data Release 7." In: *ApJS* 194, p. 45. arXiv: [1006.5178](#).
- Shen, Y. et al. (2015). "The Sloan Digital Sky Survey Reverberation Mapping Project: Technical Overview." In: *ApJS* 216, p. 4. arXiv: [1408.5970](#).
- Shen, Y. et al. (2016). "The Sloan Digital Sky Survey Reverberation Mapping Project: Velocity Shifts of Quasar Emission Lines." In: *ArXiv e-prints*. arXiv: [1602.03894](#).
- Silk, J. and M. J. Rees (1998). "Quasars and galaxy formation." In: *A&A* 331, pp. L1–L4. arXiv: [astro-ph/9801013](#).
- Simcoe, R. A. et al. (2010). "The FIRE infrared spectrometer at Magellan: construction and commissioning." In: *Ground-based and Airborne Instrumentation for Astronomy III*. Vol. 7735. Proc. SPIE, p. 773514.
- Skrutskie, M. F. et al. (2006). "The Two Micron All Sky Survey (2MASS)." In: *AJ* 131, pp. 1163–1183.
- Stern, J. and A. Laor (2012). "Type 1 AGN at low z - II. The relative strength of narrow lines and the nature of intermediate type AGN." In: *MNRAS* 426, pp. 2703–2718. arXiv: [1207.5543](#).
- Stockton, A. (1976). "The Structure and Spectrum of Nebulosity Associated with the QSO 4c 37.43." In: *ApJ* 205, p. L113.
- Suganuma, M., Y. Yoshii, Y. Kobayashi, T. Minezaki, K. Enya, H. Tomita, T. Aoki, S. Koshida, and B. A. Peterson (2006). "Reverberation Measurements of the Inner Radius of the Dust Torus in Nearby Seyfert 1 Galaxies." In: *ApJ* 639, pp. 46–63. arXiv: [astro-ph/0511697](#).
- Sulentic, J. W., P. Marziani, and D. Dultzin-Hacyan (2000). "Phenomenology of Broad Emission Lines in Active Galactic Nuclei." In: *ARA&A* 38, pp. 521–571.
- Sulentic, J. W., T. Zwitter, P. Marziani, and D. Dultzin-Hacyan (2000). "Eigenvector 1: An Optimal Correlation Space for Active Galactic Nuclei." In: *ApJ* 536, pp. L5–L9. arXiv: [astro-ph/0005177](#).

- Sulentic, J. W., G. M. Stirpe, P. Marziani, R. Zamanov, M. Calvani, and V. Braito (2004). "VLT/ISAAC spectra of the H β region in intermediate redshift quasars." In: *A&A* 423, pp. 121–132. arXiv: [astro-ph/0405279](#).
- Sulentic, J. W., P. Repetto, G. M. Stirpe, P. Marziani, D. Dultzin-Hacyan, and M. Calvani (2006). "VLT/ISAAC spectra of the H β region in intermediate-redshift quasars. II. Black hole mass and Eddington ratio." In: *A&A* 456, pp. 929–939. arXiv: [astro-ph/0606309](#).
- Sulentic, J. W., R. Bachev, P. Marziani, C. A. Negrete, and D. Dultzin (2007). "C IV λ 1549 as an Eigenvector 1 Parameter for Active Galactic Nuclei." In: *ApJ* 666, pp. 757–777. arXiv: [0705.1895](#).
- Sunyaev, R. A. and L. G. Titarchuk (1980). "Comptonization of X-rays in plasma clouds - Typical radiation spectra." In: *A&A* 86, pp. 121–138.
- Tilton, E. M. and J. M. Shull (2013). "Ultraviolet Emission-line Correlations in HST/COS Spectra of Active Galactic Nuclei: Single-epoch Black Hole Masses." In: *ApJ* 774, p. 67. arXiv: [1307.6560](#).
- Trakhtenbrot, B. and H. Netzer (2012). "Black hole growth to $z = 2$ - I. Improved virial methods for measuring M_{BH} and L/L_{Edd} ." In: *MNRAS* 427, pp. 3081–3102. arXiv: [1209.1096](#).
- Tremaine, S. et al. (2002). "The Slope of the Black Hole Mass versus Velocity Dispersion Correlation." In: *ApJ* 574, pp. 740–753. arXiv: [astro-ph/0203468](#).
- Trichas, M. et al. (2012). "The Chandra Multi-wavelength Project: Optical Spectroscopy and the Broadband Spectral Energy Distributions of X-Ray-selected AGNs." In: *ApJS* 200, 17, p. 17. arXiv: [1204.5148](#).
- Turnshek, D. A. (1988). "BAL QSOs: Observations, Models and Implications for Narrow Absorption Line Systems." In: *QSO Absorption Lines: Probing the Universe*. Ed. by J. C. Blades, D. A. Turnshek, and C. A. Norman, p. 17.
- Urry, C. M. and P. Padovani (1995). "Unified Schemes for Radio-Loud Active Galactic Nuclei." In: *PASP* 107, p. 803. arXiv: [astro-ph/9506063](#).
- Vanden Berk, D. E. et al. (2001). "Composite Quasar Spectra from the Sloan Digital Sky Survey." In: *AJ* 122, pp. 549–564. arXiv: [astro-ph/0105231](#).
- Veilleux, S. et al. (2013). "Fast Molecular Outflows in Luminous Galaxy Mergers: Evidence for Quasar Feedback from Herschel." In: *ApJ* 776, 27, p. 27. arXiv: [1308.3139](#).

- Venemans, B. P., F. Walter, L. Zschaechner, R. Decarli, G. De Rosa, J. R. Findlay, R. G. McMahon, and W. J. Sutherland (2016). "Bright [C ii] and Dust Emission in Three $z > 6.6$ Quasar Host Galaxies Observed by ALMA." In: *ApJ* 816, 37, p. 37. arXiv: [1511.07432](#).
- Vernet, J. et al. (2011). "X-shooter, the new wide band intermediate resolution spectrograph at the ESO Very Large Telescope." In: *A&A* 536, A105, A105. arXiv: [1110.1944](#).
- Veron, M. P. (1981). "On the width and profile of nuclear emission lines in galaxies." In: *A&A* 100, pp. 12–19.
- Véron, P., A. C. Gonçalves, and M.-P. Véron-Cetty (2002). "The "red shelf" of the H β line in the Seyfert 1 galaxies RXS J01177+3637 and HS 0328+05." In: *A&A* 384. arXiv: [astro-ph/0201240](#).
- Vestergaard, M. (2002). "Determining Central Black Hole Masses in Distant Active Galaxies." In: *ApJ* 571, pp. 733–752. arXiv: [astro-ph/0204106](#).
- (2004). "Early Growth and Efficient Accretion of Massive Black Holes at High Redshift." In: *ApJ* 601, pp. 676–691. arXiv: [astro-ph/0309521](#).
- Vestergaard, M. and P. S. Osmer (2009). "Mass Functions of the Active Black Holes in Distant Quasars from the Large Bright Quasar Survey, the Bright Quasar Survey, and the Color-selected Sample of the SDSS Fall Equatorial Stripe." In: *ApJ* 699, pp. 800–816. arXiv: [0904.3348](#).
- Vestergaard, M. and B. M. Peterson (2006). "Determining Central Black Hole Masses in Distant Active Galaxies and Quasars. II. Improved Optical and UV Scaling Relationships." In: *ApJ* 641, pp. 689–709. arXiv: [astro-ph/0601303](#).
- Vestergaard, M., X. Fan, C. A. Tremonti, P. S. Osmer, and G. T. Richards (2008). "Mass Functions of the Active Black Holes in Distant Quasars from the Sloan Digital Sky Survey Data Release 3." In: *ApJ* 674, pp. L1–L4. arXiv: [0801.0243](#).
- Vestergaard, M., K. Denney, X. Fan, J. J. Jensen, B. C. Kelly, P. S. Osmer, B. M. Peterson, and C. A. Tremonti (2011). "Black hole mass estimations: limitations and uncertainties." In: *Narrow-Line Seyfert 1 Galaxies and their Place in the Universe*, p. 38.
- Vogt, S. S. et al. (1994). "HIRES: the high-resolution echelle spectrometer on the Keck 10-m Telescope." In: *Instrumentation in Astronomy VIII*. Ed. by D. L. Crawford and E. R. Craine. Vol. 2198. Proc. SPIE, p. 362.

- Volonteri, M., M. Sikora, and J.-P. Lasota (2007). "Black Hole Spin and Galactic Morphology." In: *ApJ* 667, pp. 704–713. arXiv: [0706.3900](#).
- Vrtilek, J. M. (1985). "Seyfert galaxy narrow-line regions. II - Kinematic models." In: *ApJ* 294, pp. 121–133.
- Wang, H., F. Xing, K. Zhang, T. Wang, H. Zhou, and S. Zhang (2013). "Outflow and Hot Dust Emission in High-redshift Quasars." In: *ApJ* 776, p. L15. arXiv: [1309.4465](#).
- Wang, J.-G., X.-B. Dong, T.-G. Wang, L. C. Ho, W. Yuan, H. Wang, K. Zhang, S. Zhang, and H. Zhou (2009). "Estimating Black Hole Masses in Active Galactic Nuclei Using the Mg II $\lambda 2800$ Emission Line." In: *ApJ* 707, pp. 1334–1346. arXiv: [0910.2848](#).
- Weedman, D. W. (1970). "High-Velocity Gas Motions in Galactic Nuclei." In: *ApJ* 159, p. 405.
- Weymann, R. J., S. L. Morris, C. B. Foltz, and P. C. Hewett (1991). "Comparisons of the emission-line and continuum properties of broad absorption line and normal quasi-stellar objects." In: *ApJ* 373, pp. 23–53.
- White, R. L., R. H. Becker, D. J. Helfand, and M. D. Gregg (1997). "A Catalog of 1.4 GHz Radio Sources from the FIRST Survey." In: *ApJ* 475, pp. 479–493.
- Whittle, M. (1985). "The narrow line region of active galaxies. I - Nuclear forbidden line profiles. II - Relations between forbidden line profile shape and other properties." In: *MNRAS* 213, pp. 1–31.
- Williams, R. J., R. Maiolino, Y. Krongold, S. Carniani, G. Cresci, F. Mannucci, and A. Marconi (2016). "An ultra-dense fast outflow in a quasar at z=2.4." In: *ArXiv e-prints*. arXiv: [1605.08046](#).
- Wilson, J. C. et al. (2004). "Mass producing an efficient NIR spectrograph." In: *Ground-based Instrumentation for Astronomy*. Ed. by A. F. M. Moorwood and M. Iye. Vol. 5492. Proc. SPIE, pp. 1295–1305.
- Wisotzki, L., N. Christlieb, N. Bade, V. Beckmann, T. Köhler, C. Vanelle, and D. Reimers (2000). "The Hamburg/ESO survey for bright QSOs. III. A large flux-limited sample of QSOs." In: *A&A* 358, pp. 77–87. arXiv: [astro-ph/0004162](#).
- Wright, E. L. et al. (2010). "The Wide-field Infrared Survey Explorer (WISE): Mission Description and Initial On-orbit Performance." In: *AJ* 140, 1868, pp. 1868–1881. arXiv: [1008.0031](#).

- Wu, X.-B., R. Wang, M. Z. Kong, F. K. Liu, and J. L. Han (2004). “Black hole mass estimation using a relation between the BLR size and emission line luminosity of AGN.” In: *A&A* 424, pp. 793–798. arXiv: [astro-ph/0403243](#).
- York, D. G. et al. (2000). “The Sloan Digital Sky Survey: Technical Summary.” In: *AJ* 120, pp. 1579–1587. arXiv: [astro-ph/0006396](#).
- Zakamska, N. L. and J. E. Greene (2014). “Quasar feedback and the origin of radio emission in radio-quiet quasars.” In: *MNRAS* 442, pp. 784–804. arXiv: [1402.6736](#).
- Zakamska, N. L., F. Hamann, I. Pâris, W. N. Brandt, J. E. Greene, M. A. Strauss, C. Villforth, D. Wylezalek, R. M. Alexandroff, and N. P. Ross (2016). “Discovery of extreme [O III] $\lambda 5007$ Å outflows in high-redshift red quasars.” In: *MNRAS* 459, pp. 3144–3160. arXiv: [1512.02642](#).
- Zamanov, R., P. Marziani, J. W. Sulentic, M. Calvani, D. Dultzin-Hacyan, and R. Bachev (2002). “Kinematic Linkage between the Broad- and Narrow-Line-emitting Gas in Active Galactic Nuclei.” In: *ApJ* 576, pp. L9–L13. arXiv: [astro-ph/0207387](#).
- Zamfir, S., J. W. Sulentic, P. Marziani, and D. Dultzin (2010). “Detailed characterization of H β emission line profile in low-z SDSS quasars.” In: *MNRAS* 403, pp. 1759–1786. arXiv: [0912.4306](#).
- Zhang, K., X.-B. Dong, T.-G. Wang, and C. M. Gaskell (2011). “The Blueshifting and Baldwin Effects for the [O III] $\lambda 5007$ Emission Line in Type 1 Active Galactic Nuclei.” In: *ApJ* 737, 71, p. 71. arXiv: [1105.1094](#).
- Zhang, S., H. Wang, T. Wang, F. Xing, K. Zhang, H. Zhou, and P. Jiang (2014). “Outflow and Hot Dust Emission in Broad Absorption Line Quasars.” In: *ApJ* 786, p. 42. arXiv: [1403.3166](#).
- van der Marel, R. P. and M. Franx (1993). “A new method for the identification of non-Gaussian line profiles in elliptical galaxies.” In: *ApJ* 407, pp. 525–539.